

---

**Photoinduced molecular dynamics in  
increasingly complex systems:**

*From ultrafast transient absorption  
spectroscopy to nanoscopic models*

**Uwe Megerle**

---



Dissertation

München 2011



---

**Photoinduced molecular dynamics in  
increasingly complex systems:**

*From ultrafast transient absorption  
spectroscopy to nanoscopic models*

**Uwe Megerle**

---

Dissertation  
an der Fakultät für Physik  
der Ludwig-Maximilians-Universität  
München

vorgelegt von  
Uwe Megerle  
aus Bukarest

München, im Januar 2011

Erstgutachter: Prof. Dr. E. Riedle

Zweitgutachter: Prof. Dr. J. Rädler

Tag der mündlichen Prüfung: 04.04.2011

## Kurzfassung

Lichtinduzierte Prozesse bilden ein stetig wachsendes, interdisziplinäres Forschungsfeld, das sich von der Physik über die Chemie und Biologie bis in die Materialwissenschaften hinein zieht. Die transiente Absorptionsspektroskopie hat sich in den letzten Jahrzehnten als ideales Werkzeug herausgestellt, um die Grundlagen der Primär- und Folgeprozesse nach optischer Anregung in Echtzeit zu beobachten und auf molekularer Ebene zu verstehen. Im Rahmen der vorliegenden Arbeit wurde ein neuartiges transientes Absorptionsspektrometer mit Vielkanaldetektion konzipiert und aufgebaut. Zusammen mit dem in Kalziumfluorid erzeugten ultrabreiten Abfragespektrum von 290 – 750 nm und einem eigens entwickelten prismenbasierten Polychromator bietet die gleichzeitige Detektion von über 500 Kanälen ein viel umfassenderes Bild der nanoskopischen Prozesse als bisher. Bei einer spektralen Auflösung von 50 – 100  $\text{cm}^{-1}$  und einer Zeitauflösung unter 50 fs konnte die Nachweisgrenze für Änderungen der optischen Dichte zu Werten unterhalb von  $10^{-4}$  OD verschoben werden.

Die spektroskopisch untersuchten molekularen Systeme beleuchten jeweils verschiedene Facetten photoinduzierter Reaktionsmechanismen und weisen Möglichkeiten für ihre gezielte Steuerung auf. Der fundamentale Prozess des intramolekularen Elektronentransfers wurde in zwei kernsubstituierten Naphtalendiimiden untersucht, die je eine Arylaminogruppe sowie ein gegenüberliegendes Chloratom bzw. eine Alkylaminogruppe als weiteren Kernsubstituenten aufweisen. Während die vollständige Ladungstrennung nach optischer Anregung in beiden Molekülen ähnlich abläuft, findet die Rekombination bei zwei Aminosubstituenten als Folge der größeren Energielücke zum Grundzustand sechsmal langsamer statt. Damit lässt sich über die Kernsubstitution die Lebenszeit des ladungstrennten Zustands beeinflussen.

Das Wechselspiel zwischen intramolekularem Elektrontransfer und der Solvation durch polare Lösungsmittelmoleküle wurde anhand zweier donor-substituierter Triarylborane untersucht. Dabei konnte gezeigt werden, dass die Anwesenheit von drei äquivalenten Donoreinheiten in einem symmetrischen Molekül die energetische Relaxation des Gesamtsystems um bis zu 90% gegenüber der Referenzsubstanz beschleunigt. Zusätzlich zur Umorientierung der Lösungsmittelmoleküle gemäß der geänderten Ladungsverteilung im angeregten Zustand kann hier auch eine intramolekulare Umverteilung der Anregung auf die drei Subchromophore stattfinden. Das Dipolmoment wird dadurch mobil und kann auf die lokale Solvationsschale reagieren. Multichromophore mit mehreren aktiven Einheiten können demnach benutzt werden um ladungstrennte Zustände schneller zu stabilisieren.

Eine noch stärker ausgeprägte Abhängigkeit der intramolekularen Ladungsverteilung von der Solvation wurde am Beispiel des Kristallviolett-lactons gefunden. Auch hier führt die optische Anregung direkt in einen ladungstrennten Zustand und löst eine Relaxation des polaren Lösungsmittels aus. Dadurch wird ein zweiter, stärker polarer Zustand energetisch abgesenkt. Seine Population wird direkt vom Solvationsprozess kontrolliert, sowohl in der Dynamik als auch im Ausmaß, da die Polarität des Lösungsmittels über die Zugänglichkeit des zweiten ladungstrennten Zustandes entscheidet. Dies konnte durch vergleichende Messungen in verschiedenen Lösungsmitteln quantitativ überprüft werden.

In flavinbasierten Systemen bleibt die Ladungsverteilung bei der optischen Anregung mit sichtbarem Licht im Wesentlichen unverändert. Im angeregten Zustand ist Flavin allerdings ein starkes Oxidationsmittel, das in der Natur und in künstlichen Systemen Elektrontransferreaktionen antreibt. In DNA-Haarnadelstrukturen konnte so die Photooxidation nahe gelegener Basenpaare erreicht und der nachfolgende intramolekulare Ladungstransport durch die DNA untersucht werden. In Abhängigkeit von der Basensequenz wurden dabei langlebige ladungstrennte Zustände mit Lebenszeiten über 1 ns und Ausbeuten bis zu 14 % nachgewiesen.

Die Bedeutung einer effizienten Ladungstrennung erschließt sich aus der Studie der flavinkatalysierten Photooxidation von Benzylalkohol zu Benzaldehyd. Die spektroskopische Aufklärung des Reaktionsmechanismus ergab, dass der intermolekulare Elektronentransfer vom Alkohol zum Flavin im Singlettzustand durch die schnelle Rekombination in 50 ps einen Verlustkanal darstellt. In ausreichend verdünnter Lösung ist die diffusive Annäherung der Reaktionspartner langsamer als die Interkonversion des Flavins in den Tripletzustand. Hier ist der Rückelektrontransfer spinverboten und findet auf der Mikrosekundenskala statt. Die deutliche Lebenszeitverlängerung des ladungsgetrenten Zustandes ermöglicht einen effizienten Protontransfer als produktive Folgereaktion hin zum Benzaldehyd. Aufgrund des komplexen Reaktionsschemas ergibt sich für niedrige und hohe Substratkonzentrationen eine sehr geringe Quantenausbeute, während für 25 mM das Optimum gefunden wird. Der genaue Verlauf der Reaktionseffizienz konnte mithilfe eines selbst entwickelten LED-basierten Aufbaus zur Messung absoluter Ausbeutewerte experimentell gezeigt und durch die quantitative Analyse der nicht-exponentiellen Diffusionsdynamik auch präzise modelliert werden.

## Publications

This thesis is based on the following publications reprinted in the appendices A1-A7:

- 1 Sub-50 fs broadband absorption spectroscopy with tunable excitation: putting the analysis of ultrafast molecular dynamics on solid ground**  
*U. Megerle, I. Pugliesi, C. Schriever, C. F. Sailer, E. Riedle*  
Applied Physics B: Lasers and Optics 96, 215-231 (2010).
- 2 Laboratory apparatus for the accurate, facile and rapid determination of visible light photoreaction quantum yields**  
*U. Megerle, R. Lechner, B. König, E. Riedle*  
Photochemical & Photobiological Sciences 9, 1400-1406 (2010).
- 3 Influence of core-substitution on the ultrafast charge separation and recombination in arylamino core-substituted naphthalene diimides**  
*I. Pugliesi, U. Megerle, S.-L. Suraru, F. Würthner, E. Riedle, S. Lochbrunner*  
Chemical Physics Letters 504, 24-28 (2011).
- 4 Symmetry-dependent solvation of donor-substituted triarylboranes**  
*U. Megerle, F. Selmaier, C. Lambert, E. Riedle, S. Lochbrunner*  
Physical Chemistry Chemical Physics 10, 6245-6251 (2008).
- 5 The key role of solvation dynamics in intramolecular electron transfer: time-resolved photophysics of crystal violet lactone**  
*U. Schmidhammer, U. Megerle, S. Lochbrunner, E. Riedle, J. Karpiuk*  
Journal of Physical Chemistry A 112, 8487-8496 (2008).
- 6 Unraveling the flavin-catalyzed photooxidation of benzylic alcohol with transient absorption spectroscopy from sub-pico- to microseconds**  
*U. Megerle, M. Wenninger, R.-J. Kutta, R. Lechner, B. König, B. Dick, E. Riedle*  
Physical Chemistry Chemical Physics 13, 8869-8880 (2011).
- 7 Flavin-induced DNA photooxidation and charge movement probed by ultrafast transient absorption spectroscopy**  
*M. Wenninger, D. Fazio, U. Megerle, C. Trindler, S. Schiesser, E. Riedle, T. Carell*  
ChemBioChem 12, 703-706 (2011).





# Contents

<b>1. Introduction .....</b>	<b>1</b>
<b>2. Instrumental and interpretational methods.....</b>	<b>7</b>
2.1 Principles of transient absorption spectroscopy .....	7
2.2 Design of the femtosecond broadband pump-probe spectrometer .....	9
2.3 Behavior of rate models on artificial data involving spectral shifts .....	15
<b>3. Quantitative modeling of molecular dynamics .....</b>	<b>21</b>
3.1 Applicability of simple rate models to intramolecular charge transfer:	
Fluorescence quenching in naphthalene diimides .....	21
3.2 Spectral decomposition to model band shifts:	
Solvation dynamics of donor-substituted triarylboranes .....	27
3.3 From absorption changes to state populations:	
Solvent-controlled intramolecular electron transfer in crystal violet lactone.....	31
3.4 Band integrals, diffusion model and species associated spectra:	
flavin-catalyzed photooxidation of benzylic alcohol .....	35
3.5 Anisotropy, temperature and absolute quantum yields:	
additional concepts used in related studies.....	43
<b>4. Conclusion and outlook.....</b>	<b>49</b>
<b>References.....</b>	<b>55</b>
<b>Appendices A1-A7 .....</b>	<b>59</b>
<b>List of LabView programs</b>	
<b>Danksagung</b>	
<b>Curriculum vitae</b>	



## 1. Introduction

“Curiosity is the very basis of education and if you tell me that curiosity killed the cat, I say only the cat died nobly.”

Arnold Edinborough

The impulse to ask questions and seek answers has always been an essential trait of mankind. Besides the practical questions of how to kill the mammoth or stay out of the rain, this has also implied from the very beginning the desire to understand the basic principles in nature. Starting off from anthropocentric questions such as “where do we come from, why are we here, where are we going?”, this led to scientific subjects like “what are the building blocks of matter, how did the universe evolve, what processes take place in living organisms?”. The same curiosity that dragged man to handle fire is also at the heart of modern fundamental research. It is the aim to bring light into the darkness.

In this context, “light” is not just a metaphor. In fact, finding answers to the above questions has often involved experiments where light acted as a scientific tool and/or as a direct observable. Thereby, the variety of subjects spans a huge range. On the one hand, light is used in astronomy to investigate objects on the largest spatial and temporal scales we know of. On the other hand, light microscopy has opened the way to study ever smaller structures. Both disciplines in their modern form are closely related to Galileo Galilei (1564-1642) who is sometimes called the first physicist [1]. His technological improvements of optical instruments extended the measurable world to beyond what is seen with the bare eye.

In his tradition, physicists over the centuries have made use of more and more regions of the electromagnetic spectrum to reveal previously hidden facts. A prominent example are X-rays which not only found rich application in medicine due to their penetration through soft tissue. The shorter wavelength compared to visible light also allows for the resolution of much smaller structures down to the atomic level. The discovery and systematic study of this radiation in the wavelength range from 0.01 to 10 nm earned W. C. Röntgen the first Nobel prize in physics in 1901. Since then, approximately one fourth of all Nobel prizes in physics were awarded for theories or experiments whose subject was directly linked to electromagnetic radiation. Most recently, C. K. Kao, W. S. Boyle and G. E. Smith were honored in 2009 for their achievements concerning the transmission of light in optical fibers and the invention of the CCD sensor for light detection.

A major break-through for optical experiments was the first demonstration of a laser by T. H. Maiman fifty years ago [2]. While he first denoted his device “a solution seeking a problem”, it soon became a ubiquitous tool in scientific and industrial applications. In the past decades, the advent of pulsed lasers has triggered the evolution of a new field of fundamental research called femtochemistry. Starting with the seminal work of A. Zewail (Nobel prize in chemistry 1999) [3], scientists were now able to gather information not only on molecular length scales, but also on the relevant ultrashort time scales. The world record of timing con-

trol so far has been achieved by stabilizing the phase of near infrared laser pulses with a precision of 12 attoseconds =  $1.2 \times 10^{-17}$  seconds [4]. This is a factor of two below the atomic unit of time which is considered to be the characteristic order of magnitude at which the fastest inner-atomic processes may occur.

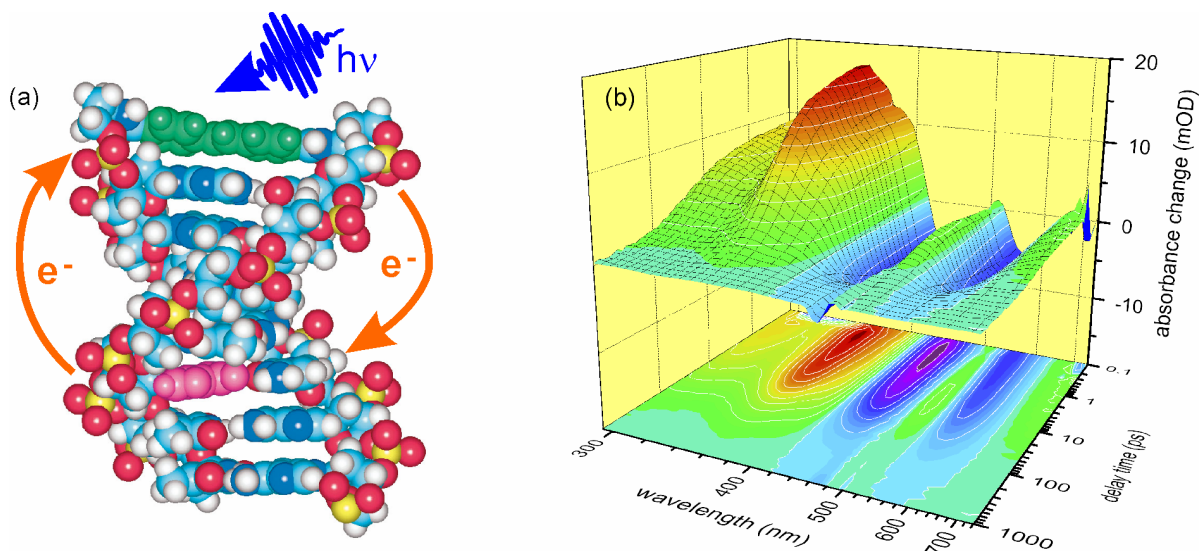


**Fig. 1.1 Electron transfer in DNA: (a)** Structure of a stilbene-capped DNA hairpin. After photoexcitation of the stilbene chromophore (green), intramolecular electron transfer from a deoxyguanosine base (magenta) is observed, followed by back electron transfer. Adapted from ref. [5] with permission from AAAS. **(b)** Transient absorption changes after excitation at 480 nm of a similar DNA hairpin with a flavin cap. The signal decay within some tens of picoseconds indicates the quenching of the flavin excitation by ultrafast electron transfer from neighboring DNA bases (see section 3.5).

The basis of chemistry is the somewhat larger scale involving the interaction of several atoms or molecules. Here, the fastest processes occur on a timescale of 10-100 femtoseconds =  $10^{-14}$ - $10^{-13}$  seconds. The elementary reaction steps comprise charge or energy transfer events, structural reorganizations, bond breaking and bond formation as well as translation and rotation of molecules or their subunits. In many cases, these processes cause changes in the absorption properties of the sample. In a pump-probe scheme, femtosecond light pulses allow on the one hand the definition of a starting point for an ultrafast reaction and on the other hand the monitoring of the induced absorption changes in real-time. In systematic experiments and with the help of theoretical models one can then deduce detailed nanoscopic pictures of the fundamental chemical processes.

A large variety of questions from different scientific disciplines has been addressed with ultrafast time-resolved spectroscopy. Prominent examples from biology were the identification of the primary processes in the perception of light in the eye [6, 7] or during the photosynthetic conversion of light into chemical energy [8]. In material science, femtosecond spectroscopy is used for instance to analyze the charge separation in plastic solar cells [9], the artificial complement of the photosynthetic apparatus. In chemistry, the properties of intra- and intermolecular electron transfer as the simplest chemical reaction were also inten-

sively investigated with transient absorption experiments [10]. In the overlap region between biology and chemistry are found the studies on electron/hole transport in DNA strands [11] as shown in Fig. 1.1. A largely debated aspect of these investigations is the question whether DNA can be described as a molecular wire [12] or rather as an insulator [13]. This leads inevitably into the realm of physics which is also touched by many photochemical studies. One reason for this is that the fastest intermolecular chemical reactions are often limited by diffusion (see Fig. 1.2). The quantitative modeling of their dynamics therefore requires thermodynamic considerations. These examples underline the distinct interdisciplinarity of ultrafast transient absorption spectroscopy.

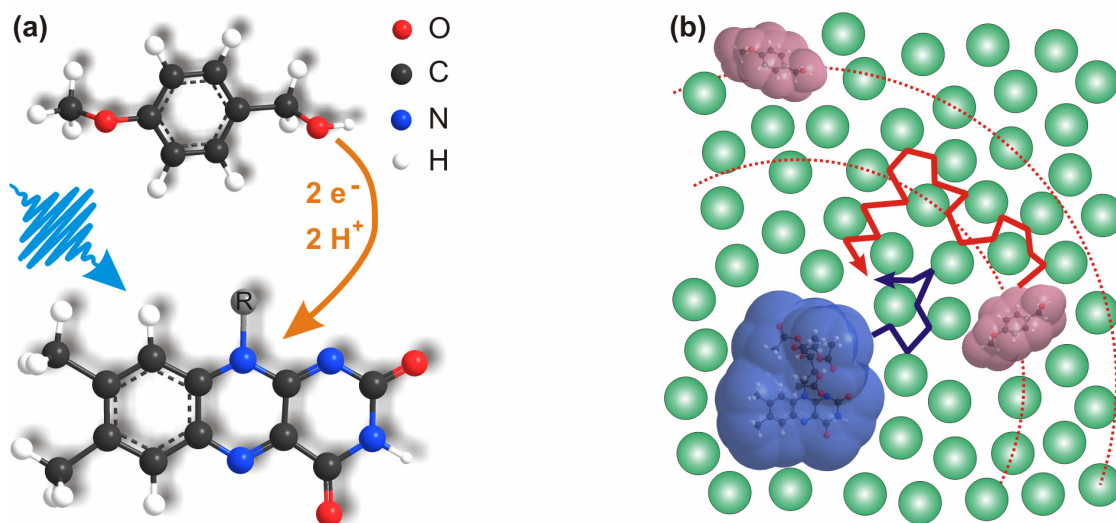


**Fig. 1.2 Diffusion controlled reaction:** (a) After photoexcitation, riboflavin tetraacetate (bottom) can oxidize methoxybenzyl alcohol (top) to the corresponding aldehyde by the transfer of two electrons and protons. (b) In dilute solutions, the reaction proceeds only after the partners have diffused together through a random walk. The visualization of the reactants corresponds to the solvent accessible surface. For details of the model see section 3.4.

Despite the daily increasing number of publications in this field and the new insights gathered over the years, it is still not possible to reliably predict molecular behavior on the ultrafast timescale from theoretical considerations alone. Even simple two-atomic molecules are too complicated for a full quantum mechanical description. The approximations needed for larger, chemically relevant molecular systems therefore generally require experimental proof. The more data become available, the more efficient is then the refinement of the theoretical models.

Following the footsteps of Galilei, any cutting-edge experiment is intrinsically connected to constant improvements and new developments of measuring instruments. The past two decades have witnessed the upgrowth of ultrafast light sources that are freely tunable from the deep UV into the mid-IR. They allow for a selective triggering of various photochemical processes and dramatically enlarge the scope of ultrafast transient absorption spectroscopy. In parallel, ultrabroad supercontinua generated in optically nonlinear materials give access to a wide spectral probing range. Recent advancements in detector electronics have opened the

way to a multichannel detection at high read-out frequencies that exploits the full potential of the broadband probe pulses.

In the framework of this thesis, two transient absorption spectrometers with a novel multichannel detection have been designed and set up. They combine for the first time all state-of-the-art concepts and components, from mechanics over optics to software codes. The implications of this new instrument on data recording, post-processing and modeling are described in chapter 2 after a short review of the basic principles of transient absorption spectroscopy. Compared to the classical pump-probe experiment where kinetic information is only obtained at single wavelengths, the multichannel detection provides a 2D data set with transient absorption spectra along one axis and their temporal evolution along the other. This permits new analytic methods such as global fits or the mapping of logarithmically differentiated absorption changes for a quantitative visualization of the dynamics.

With the instrumental and interpretational tools at hand, chapter 3 summarizes the study of prototypical molecular systems. They are chosen following the reductionistic approach, i.e. the attempt to understand the nature of complex systems by reducing them to their fundamental interactions and constituents. Thereby, the focus lies on the complexity of the modeling and the interpretation. While moving from simple to more and more advanced systems, the aim is to identify the concepts of how to approach ultrafast transient absorption data, what questions are to be asked and what possibilities exist to answer them. Eventually, the interest is to derive from the observed changes in the optical density information on a selected molecular ensemble, its internal state comprising electronic excitation or geometric conformation, its specific surrounding, its interaction with other molecules and the dynamics of these processes.

In section 3.1, the ultrafast charge separation and recombination in two differently substituted naphthalene diimides is compared using a relatively simple biexponential rate model in a global least-square fit. The resulting nanoscopic model involves only intramolecular processes such as the twisting of structural subunits of the chromophores and the associated energy level differences.

In contrast, the study on two donor-substituted triarylboranes described in section 3.2 explicitly considers the interplay between intramolecular processes and the response of the environment in the form of solvation, i.e. the dynamic energetic lowering of the excited state by reorganization of the polar solvent molecules. Here, the observed dynamics can be modeled by a decomposition of the transient spectra into individual bands that are subject to spectral shifts with a characteristic time constant.

The topic of solvation is revisited in section 3.3 by the investigation of crystal violet lactone. Here, the complexity is increased by the presence of two excited states with different polarities. The time dependent population of both states can be calculated from the transient absorption changes. The kinetic modeling with a time-dependent rate allows the unequivocal proof that the dynamic transition between the two states by intramolecular electron transfer is controlled by the solvent.

The next step in complexity is to study true bimolecular reactions such as the photocatalytic oxidation of benzylic alcohol by a flavin derivative (section 3.4). The evaluation of the direct reaction between the excited flavin catalyst and the alcohol substrate uses and extends

the concepts developed for the simpler systems. While a biexponential global rate model can be applied if the alcohol is used as solvent, the intermolecular electron transfer in dilute solution is described with a diffusion model (see Fig. 1.2) that implies time-dependent rates. The influence of spectral band shifts due to solvation is minimized by the use of band integrals. Extracting absorption spectra of the intermediates from the applied modeling allows for the first time a detailed insight into the sequence of events during the photocatalytic reaction. This example demonstrates that the understanding of application-oriented photochemical reactions is associated with a relatively high level of complexity.

Chapter 3 is completed with section 3.5 where additional concepts for the investigation and interpretation of ultrafast molecular dynamics are pointed out. For instance, the evolution of the anisotropy induced by the linearly polarized excitation pulse can prove the proposed energy transfer mechanism between orthogonal subunits of a multichromophore. Another example is the determination of absolute quantum yields for a specific reaction channel from the quantitative analysis of spectral amplitudes at different delay times.

In the last chapter the various approaches to obtain a complete picture of the ultrafast nanoscopic processes are summarized in a general strategy. Some envisaged improvements of the fit routines are outlined and an outlook on further technological developments is given that are to increase the precision of the transient absorption experiments and to even enlarge the range of photochemical processes that can be examined. Finally, the key findings from the presented molecular studies are summarized and potential systems for future investigations are discussed.

The reprints of the publications that underlie this thesis can be found in the appendix. They comprise two technical reports (A1 and A2) with details on the assembly and operation of the transient spectrometer and an LED-based apparatus for quantitative illumination. The photochemistry oriented publications (A3-A7) provide additional information on the chemical background as well as on potential applications of the investigated molecular samples. Both aspects are mostly left out from this presentation in favor of an overarching conceptual discussion.





## 2. Instrumental and interpretational methods

### 2.1 Principles of transient absorption spectroscopy

The modern version of ultrafast transient absorption (TA) spectroscopy is a direct successor of the flash photolysis technique developed by R. G. W. Norrish and G. Porter around 1950 [14, 15]. In their experiments, which earned them the Nobel prize in chemistry in 1967, they used light bursts with millisecond durations from discharge lamps to trigger fast chemical reactions. The course of the reaction was monitored by taking photographs of the absorption of the sample at different delay times after the excitation. Thereby, the sample was exposed to a second light flash with a continuous spectrum that was dispersed in a polychromator before illuminating the photoplates.

The basic idea behind this is that different intermediate states of the photoinduced reaction have different absorption bands as shown in Fig. 2.1. Thus, the comparison of the intensities transmitted through the excited ( $I^*$ ) and the unpumped sample ( $I_0$ ) provides information on the nature of intermediate and product states as well as on their population dynamics. They are recorded in terms of the induced changes of the optical density (OD) according to:

$$\Delta OD(\lambda, \Delta t) = -\log \left( \frac{I^*(\lambda, \Delta t)}{I_0(\lambda)} \right). \quad (2.1)$$

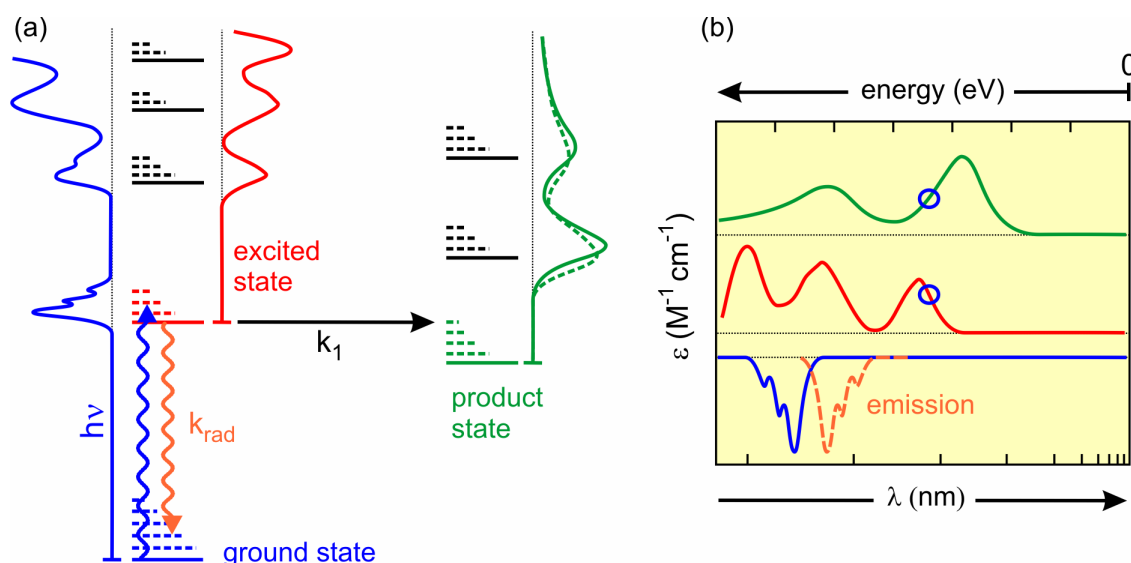


**Fig. 2.1 Fundamentals of TA spectroscopy:** (a) Schematic photoreaction process showing the connection between the energetic position of resonances and molecular absorption and emission bands. (b) Differences between the species spectra are used as fingerprints to identify the reaction mechanism by monitoring changes of the optical density after photoexcitation.

In general, the observed TA spectra consist of three contributions: ground state bleach (GSB), stimulated emission (SE) and product or excited state absorption (ESA). The ESA contributes positive absorption changes ( $\Delta OD > 0$ ) in spectral regions that correspond to resonant transitions of the states that are populated after the optical excitation. A negative signal

in the TA data ( $\Delta OD < 0$ ) can be observed in the spectral region of the fluorescence where the intensity of the transmitted probe light is increased due to stimulated emission. The diminished population of the ground state after the excitation gives rise to a higher transmitted intensity in the ground state absorption bands since less molecules absorb light at these specific frequencies. The GSB therefore also contributes a negative signal to the TA spectra. The GSB signature is specifically suited to quantify the fraction of molecules that populate an intermediate or product state of the photochemical reaction: Its persistence indicates that not all of the excited molecules have relaxed back to the ground state.

The schematic absorption bands shown in Fig. 2.1 illustrate the need for broad spectral coverage to study a large variety of molecular systems and processes. The more spectral signatures are observed, the more accurate are the identification of intermediates and the overall interpretation of the reaction dynamics. In contrast, probing with monochromatic light can conceal the transfer between two states if the wavelength happens to lie near an isosbestic point. There, the absorption of the precursor and the successor state is of equal strength and no change in the optical density is observed during the transition. An example for an isosbestic point is marked with blue circles in the absorption spectra of the excited (red) and the product state (green) in Fig. 2.1b. However, in broadband TA studies, isosbestic points are important indicators for a direct conversion between two species without intermediates (see section 3.3).

An important point to note is that not all changes in the TA signals necessarily reflect transitions between different electronic states or chemical species. For instance, the hot product state that is formed with a rate  $k_1$  from the first excited state in Fig. 2.1a (dotted green line) will be subject to vibrational cooling, i.e. the dissipation of vibrational energy to other normal modes of the molecule and to the surrounding solvent. This causes a spectral narrowing and a peak shift of the absorption bands of this state (solid green line) with time. Similar spectral band shifts are observed during the solvation process, i.e. the relaxation of polar solvent molecules after a change of the charge distribution in the excited solute (see section 3.2). Thus, a careful investigation of the TA spectra is required before the temporal evolution of the absorption changes can be connected to the dynamics of the state populations during a photophysical or photochemical reaction.

## 2.2 Design of the femtosecond broadband pump-probe spectrometer

In contrast to the classical flash photolysis technique, ultrafast pump-probe spectrometers at first used two essentially monochromatic laser pulses for pump and probe. Then, the sample molecules had to be chosen such that their electronic transitions were in resonance with the given laser lines. A major improvement over this concept has become possible with the advent of spectrally ultrabroad probe pulses that are compatible with femtosecond time resolutions. Nowadays, this allows one the combination of a polychromator and a multiplex detection for pump-probe spectroscopy also on the ultrafast timescale. Thus, it is possible to obtain not only kinetic traces at individual wavelengths, but rather transient spectra over the whole sampled time range. The experimental layout of such a broadband femtosecond pump-probe spectrometer is shown in Fig. 2.2.

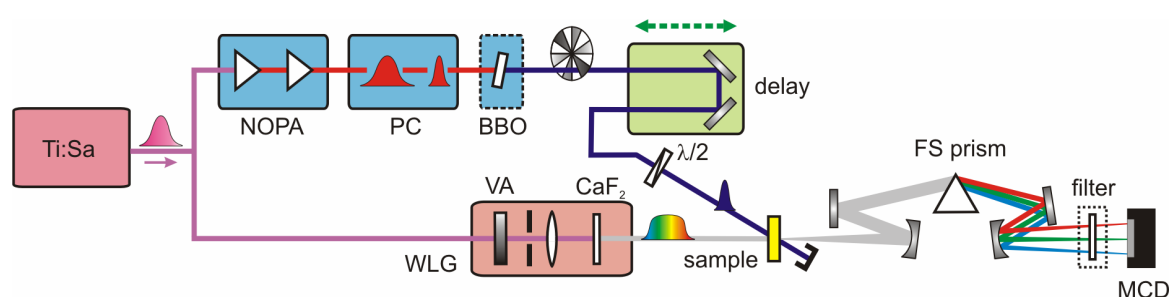


**Figure 2.2** Schematic of the femtosecond broadband absorption spectrometer. NOPA: non-collinear optical parametric amplifier; PC: prism compressor; BBO:  $\beta$ -barium borate crystal; WLG: white light generation; VA: variable attenuator; FS: fused silica; MCD: multichannel detector.

A detailed description of all conceptual developments and technical components for the assembly and operation of this spectrometer according to the state of the art is given in the following invited publication (appendix A1):

### **Sub-50 fs broadband absorption spectroscopy with tunable excitation: putting the analysis of ultrafast molecular dynamics on solid ground**

*U. Megerle, I. Pugliesi, C. Schrieber, C. F. Sailer, E. Riedle*

*Applied Physics B: Lasers and Optics* 96, 215-231 (2010).

The spectrometer is operated at 1 kHz and based on a commercial Ti:sapphire amplifier. A noncollinear parametric amplifier and frequency doubling are used to provide pump tuning from the UV to the NIR [16-22]. A  $\text{CaF}_2$  based single filament white light [23-33] allows for 290 to 750 nm probing. The multichannel detection is operated at the full 1 kHz rate and chopping of the pump light avoids the use of a reference channel. The resulting high detection sensitivity of better than  $\Delta\text{OD} = 10^{-4}$  allows for the simultaneous recording of the spectral features of electronic states and species with differing transition strengths.

A prism-based polychromator is employed to avoid the order sorting problem with the more than octave wide probe spectrum and to enhance the throughput. Flow cells with

200  $\mu\text{m}$  windows and down to 120  $\mu\text{m}$  sample thickness reduce the coherent artifact [34-36] and the group velocity mismatch [37]. This results in an overall sub-50 fs temporal resolution. This timescale can be regarded as an upper limit for electronic dephasing processes. The homogeneous line broadening associated with a 50 fs lifetime is  $106\text{ cm}^{-1}$ , which perfectly matches the spectral resolution of our instrument of  $50 - 100\text{ cm}^{-1}$ .

### Data post-processing

On the one hand, the multichannel detection that was developed in the framework of this thesis literally widens the horizon for the study of molecular dynamics. On the other hand, it also requires a larger set of post processing routines to convert the raw data to physically meaningful information. In general, the path from the technical performance of an experiment in the lab to the final nanoscopic understanding of the photochemical system is a multistep process including many non-trivial considerations.

The first important intermediate in this intellectual process is to obtain a correct two-dimensional  $\Delta\text{OD}$ -map that contains all the relevant (and accessible) information on a given sample. This implies for example the proper assignment of a wavelength to each pixel of the multichannel detector. For our home-built prism polychromator this is assured by a routinely performed measurement of the transmission of a set of multiband and longpass filters. Their known spectra are then used for the wavelength calibration of the spectrometer.

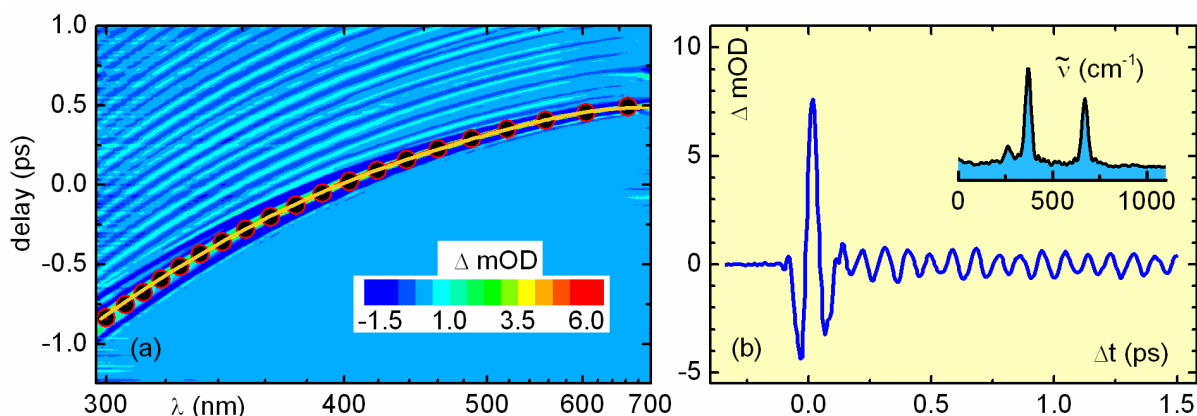


**Fig. 2.3** (a) Transient absorption of pure chloroform after 600 nm excitation. The polynomial fit (orange curve) to the center of the coherent artifact (filled circles) is used for the chirp correction of the TA data matrix. (b) Kinetic trace at 450 nm showing the coherent artifact at time zero and subsequent oscillatory signals from impulsive Raman scattering. Inset: The Fourier transform spectrum shows maxima at the Raman active modes of chloroform at 260, 370 and  $670\text{ cm}^{-1}$  corresponding to vibrational periods of 128, 90 and 50 fs.

Another decisive issue is to bring the TA data on a single common time axis to allow for proper modeling of the molecular dynamics signatures [38-41]. Due to the chirp of the  $\text{CaF}_2$  continuum, the temporal overlap between pump and probe in the raw data spans a range of  $\sim 1.5\text{ ps}$  between the UV and near IR white light components (see Fig. 2.3a). In most cases, we use the coherent artifact [36, 42-43] that results from the interaction of pump and probe in the sample to determine the time zero  $t_0$  at selected wavelengths (see Fig. 2.3b). The exact

value of  $t_0$  for each wavelength is best obtained by fitting a Gaussian function and/or its first and second derivative to the artifact [44]. This is also the best way to determine the wavelength-dependent cross correlation time  $\tau_{CC}(\lambda)$  or the effective time resolution of the experiment. The time-zero points  $t_0(\lambda)$  are then used to interpolate the whole data set to a common, physically meaningful time scale. The highest precision is usually achieved when the data for the chirp correction are measured directly before or after the actual experiment in the pure solvent. Otherwise, fast molecular signals can intermingle with the coherent artifact. In addition, the amplitude of the artifact will be reduced in the presence of sample molecules since a sizeable fraction of the pump photons are absorbed [36]. Both effects can render the assignment of  $t_0(\lambda)$  – and also of  $\tau_{CC}(\lambda)$  – erroneous. Only for samples without sub-ps dynamics and/or high initial amplitudes after excitation, the chirp correction can be performed using the TA raw data of the sample itself.

### **Choice of experimental parameters**

In experimental physics in general and in TA spectroscopy in particular one has to be aware of the fact that the perfect measurement is an illusion. In practice, it will not be possible to tune each and every parameter of the instrument independently to the absolute optimum and to record all information in one heroic experiment. Even if technical aspects such as the finite long-term stability of the laser or the reciprocal dependence of some parameters are left aside: In many cases the complete picture of a photochemical process can only be gained if information from several experiments is combined. As will be shown in the next sections, this can include measurements in different solvents, at different concentrations, with different sampled time scales, and so on. It is therefore crucial to keep in mind the specific questions to be addressed and to concentrate on the optimization of the parameters that are relevant to answer them.

This often requires a step-wise approach where one starts with relatively rough “overview measurements” and moves towards the final picture in several iterations of data analysis and refined experimental conditions. For example, if measurements in low dispersion cuvettes suffer from small signal amplitudes but show no sub-ps dynamics, one might work with a larger sample thickness thus sacrificing unneeded time resolution for a better signal-to-noise ratio. It is therefore not meaningful to define a fixed set of parameters that are required for an ideal experiment, but rather to adapt them to the spectroscopic problem. Due to the deliberately open layout of the pump-probe spectrometer and the flexibility of the control software, there are many options for specific optimizations: the central wavelength, spectral width, duration and energy of the excitation pulse, the relative polarization between pump and probe, the external angle at which they intersect inside the sample, the spot sizes at this position, the sample thickness, its flow-rate and temperature, the noise reduction in the most relevant spectral range of the probe white light, the spectral window that is detected, the scan range of the delay time, the number and spacing of the sampled time points, the number of averages per spectrum and repeated scans, the referencing method. The criteria for a reasonable choice in some of these options will be explicitly discussed in the following sections on the basis of the molecular systems investigated in the framework of this thesis.

### Additional tools, modifications and extensions

To make a photochemical reaction accessible for TA spectroscopy, an essential prerequisite is a reasonable quantum yield of the reaction, typically a few percent are required. Sometimes, a macroscopic chemical conversion is reached by cumulative effects over longer times despite a very low quantum yield of the initial photoprocess [45]. However, the data acquired in a TA experiment are an average over single events. If the process of interest has a low quantum yield, the signal will be dominated by the side reactions and it will be hard to filter out the desired information. Unfortunately, many reports on photochemical reactions lack an accurate determination of their photoefficiency. Therefore, we built and successfully tested an opto-electronic device for quantitative illumination (see Fig. 2.4) that allows for the accurate, rapid and facile determination of absolute quantum yields for visible light photoreactions under the conditions of a chemical synthesis laboratory.

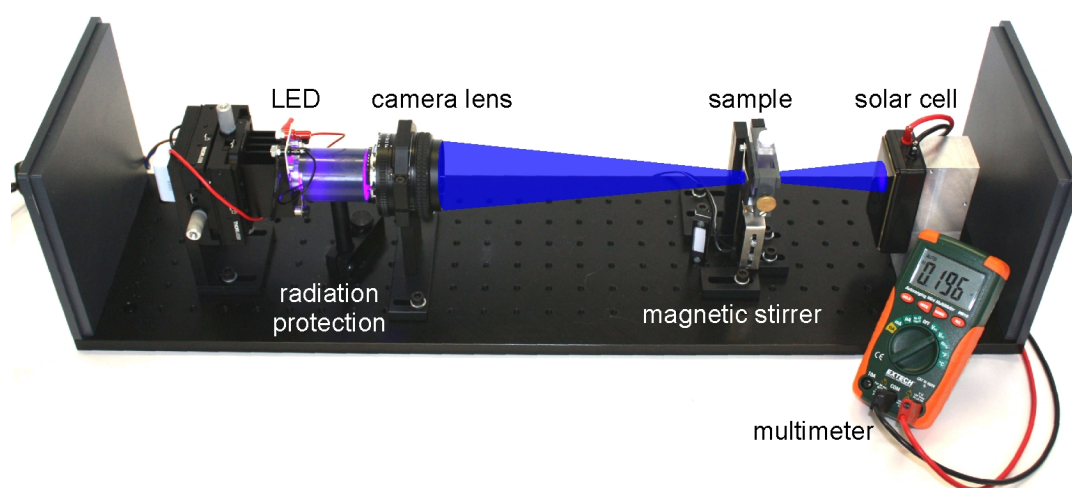


**Fig. 2.4** Compact and portable setup for quantitative illumination using a high-power light emitting diode as light source and a multimeter connected to a solar cell as light detector.

The method builds on the use of high power light emitting diodes whose output can be imaged efficiently and in a controlled fashion into the sample by a photographic lens. The transmitted light is monitored by a home-built solar cell detector that converts the incident radiant power into a voltage drop across an external resistor which is then displayed with a multimeter. After the irradiation of the reaction mixture with a well defined number of photons, the chemical product yield can be quantified by any suitable and established analytical technique, e.g. gas chromatography (GC) or high performance liquid chromatography (HPLC). All information on the assembly, operation and performance of the device is given in the following publication (appendix A2):

#### **Laboratory apparatus for the accurate, facile and rapid determination of visible light photoreaction quantum yields**

*U. Megerle, R. Lechner, B. König, E. Riedle*

*Photochemical & Photobiological Sciences* 9, 1400-1406 (2010).

Thus, the quantum yield of a photoreaction can be optimized prior to the TA study by systematic modification of external parameters such as the solvent, the pH value or the concentrations of the reaction partners. In collaborations between synthetic chemists and spectroscopists, these initial tests can constitute a shortcut that allows for a faster focusing on the most relevant experiments and thereby add to a more effective project management.

In the same context of acquiring “external” information, it is important to note that for many ultrafast photochemical studies one has to consider also slower processes extending to the nanosecond regime and beyond. Even though the TA setup described above is not originally designed to access this timescale, there are some modifications that allow getting a grasp of the nanosecond range.

For instance, the TA signature of long-lived triplet species can be obtained under the same experimental conditions as the fs-ps-spectra by redirecting the pump light. When the prism compressor after the NOPA and the delay line are omitted and the excitation pulses are directly focused into the sample [46], the optical path difference between pump and probe can be enlarged significantly. In our setup this resulted in a fixed time delay of 12 ns. Since this is larger than typical fluorescence lifetimes, the absorption of any product species or molecules in the triplet state is no longer influenced by the stimulated emission and can be investigated directly. Of course, this method yields only a static picture. To really record dynamics from nano- to milliseconds one has to move over to different spectroscopic methods such as laser flash photolysis [47] or Streak-camera measurements [48]. Nevertheless, the single spectrum at a ns delay time can be essential for the comparability of TA data obtained with different instruments (see section 3.4 and appendix A6).

For the recording of a ns-spectrum with visible excitation pulses, the subtraction of stray light from the pump becomes an issue. Usually, the signature of the pump stray light is obtained from the TA data at negative delay times. During the data post processing, its contribution can be subtracted from the data at positive delay times to obtain the unperturbed spectra. When the delay line is omitted, the stray light contribution has to be measured by periodically blocking the probe white light with a second chopper wheel, i.e. with an extended referencing method [46].

In the near future a similar approach will also be used to improve the “standard” experiments. There, we frequently observe a slight change of the stray light contribution over time that can originate from long term laser variations, sample precipitation inside the cuvette and/or imperfections of the delay line adjustment. To correct for this we will implement a computer-controlled shutter in the probe beam path and adapt the data acquisition software to record the pure stray light in regular intervals. This will hopefully allow for a more efficient stray light subtraction and increase the precision of fits in the spectral region of the excitation wavelength.





### 2.3 Behavior of rate models on artificial data involving spectral shifts

A numerical data analysis involving multiple exponential decays or rates is the most extensively used model in TA studies – and far beyond them. A rate model is based on two assumptions: (i) the complete reaction can be described as a sequence of well defined intermediate states and (ii) the number of molecules  $-dN_i$  leaving a certain state in a small time interval  $dt$  is proportional to the total population  $N_i$  of this state.

$$-\frac{dN_i}{dt} = k_i \cdot N_i . \quad (2.2)$$

The constant of proportionality  $k_i$  is called the rate of the process and represents the probability that an individual molecule leaves the ensemble within  $dt$ . Its inverse corresponds to the lifetime  $\tau_i$  of the state. The solution to this first-order differential equation is

$$N_i(t) = N_{i,0} \cdot \exp(-k_i t) + \text{const.} = N_{i,0} \cdot \exp\left(\frac{-t}{\tau_i}\right) + \text{const.} , \quad (2.3)$$

where  $N_{i,0}$  is the initial population of the state at  $t = 0$ . The application of a rate model to molecular dynamics is achieved through fitting the observed kinetics with one or more exponential functions multiplied with the step function  $\theta(t)$  and convoluted with the instrumental response function (IRF):

$$F(t) = \text{IRF} \otimes \left\{ \theta(t) \cdot \left[ \sum_i A_i \exp\left(\frac{-t}{\tau_i}\right) + \text{const.} \right] \right\} + \text{artifact} . \quad (2.4)$$

Despite the ubiquitous use of exponential fit functions, there are limitations that one has to be aware of. Most importantly, fitting with exponentials does not yield directly interpretable results if the underlying process cannot be described by a rate model. In TA spectroscopy, the most prominent examples for this are spectral diffusion processes. For an absorption or emission band that shifts due to solvation or vibrational cooling (see Fig. 2.1a), the obtained “rate constants” strongly depend on the probe wavelength and in the best case convey a rough feeling of the time scale for the spectral shift.

A more detailed illustration of this issue is shown in Fig. 2.5 with artificial solvation data. The left hand side shows the situation of an absorption band with constant integral strength, whose maximum shifts from 440 to 450 nm with an exponential behavior of  $\tau_{\text{shift}} = 2$  ps, i.e. the solvation timescale of a typical non-protic polar solvent such as DMSO [49]. The first approach to model the data are single-channel fits where only the kinetics at one specific wavelength are considered at a time and the process is repeated  $N$  times for the  $N$  available channels. If a monoexponential function is used in such an analysis, the fits (i) do in general not agree perfectly with the artificial data and (ii) only yield the correct “shift time” for two channels in the rising and falling edge of the band. Near the position of the maximum, e.g. at 445 nm, the kinetics features both a rise and a decay which is of course not describable with a monoexponential function and leads to diverging time constants (see Fig. 2.5b). The corresponding residual shown in Fig. 2.5d demonstrates the significant deviation between data and fit, which for a real TA experiment would be one order of magnitude larger than the

typical noise. Moreover, the obtained time constants rise from  $\sim 1$  to 3.5 ps when moving across the band. This corresponds to a relative error of more than 50%, which is a typical value for this situation.

In contrast to single-channel fits, the availability of a 2D data set from the multichannel detection allows for the application of a global fit routine [50]. This means that the kinetics at all wavelengths are fitted simultaneously with one common set of time constants  $\tau_i$ . The global analysis yields for each time constant a decay associated difference spectrum (DADS) [51] that is computed algebraically by a projection of the experimental kinetic traces on the exponential decays.

With one finite time constant, the global analysis of the artificial shift data yields a point symmetric DADS with the shape of the first derivative of the band (see Fig. 2.5c). This indicates the decay in the blue and the rise in the red spectral region due to the redshift of the band. In contrast to the single-channel fit, the global analysis nicely reproduces the 2 ps time constant for the shift as a consequence of the intrinsic weighted average of the kinetics at individual wavelengths.

In TA studies one often has to deal with decay processes on the same or at least similar timescales as the spectral shifts. This situation is illustrated with the artificial data on the right hand side of Fig. 2.5. Here, a 4 ps decay was added to the 2 ps redshift of the band. In this case, the monoexponential fit at individual wavelengths yields a generally quite poor agreement with the data. The fitted time constants also show a much wider variation from below 1.5 to almost 16 ps when moving from the red to the blue edge (see Fig. 2.5f), i.e. a relative error up to 400%. The most meaningful result is now obtained near the center at 445 nm, where the 4 ps decay time can be reproduced. Introducing a second time constant, i.e. using a biexponential fit, is not helpful in this case. Due to very high correlations up to 100% between the corresponding four parameters (amplitudes and time constants), the fit results depend very much on the starting values – especially for noisy data – and an evaluation is not reasonable.

In contrast to the single channel fit, the global fit algorithm does not suffer from these high correlations. Since the spectral signatures of the shift and the decay are very different (see Fig. 2.5g), the two parameters of the biexponential fit, i.e. the time constants, are only weakly correlated: in this example the off-diagonal value of the variance-covariance matrix is 0.31. As a consequence, the biexponential global fit is again superior to the single-channel evaluation. It typically reproduces the decay time constant with an accuracy of a few percent. The error for the shift timescale is larger and increases the closer the two time constants get. In general, a somewhat smaller value than the actual shift time is found. If the decay and the shift happen on separate timescales, the global fit reproduces both time constants with an equally high precision.

An interesting point to note is that the global analysis also yields a reasonable result for a monoexponential fit (see Fig. 2.5g). It is then comparable to an analysis of the spectrally integrated kinetics. In the band integral, the spectral shift does not appear and thus only the 4 ps decay time is obtained. Again, the weighted average over the individual wavelengths provides a meaningful fit result even though the fit function agrees very badly with individual kinetic traces or transient spectra of the original data.

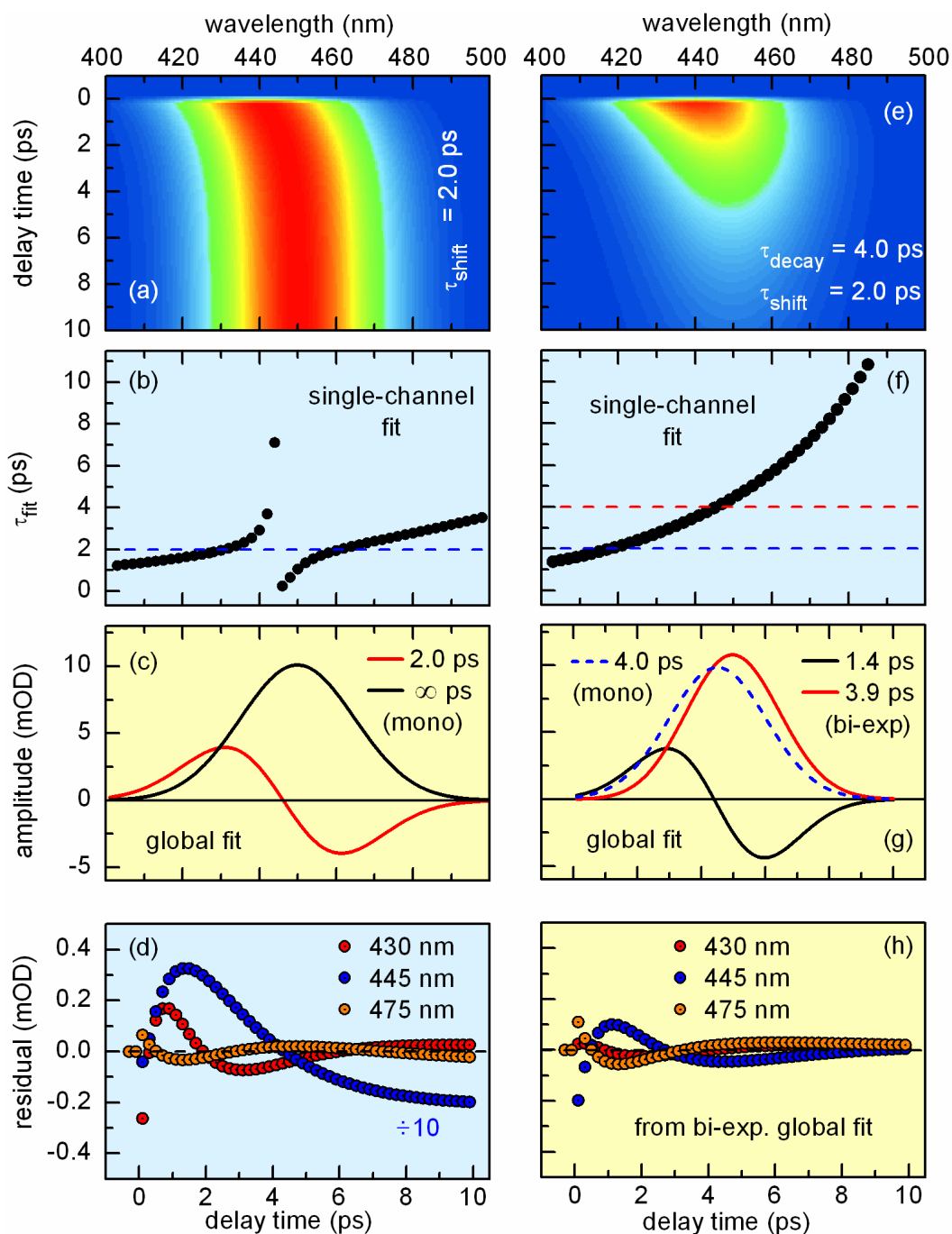


**Fig. 2.5 Spectral shifts and rate models:** (a) Artificial data showing the 10 nm redshift of a Gaussian absorption band (35 nm FWHM) within 2 ps. (b) Decay or rise times obtained from a monoexponential fit to single wavelength channels. The according amplitudes closely resemble the amplitude spectra from a global fit shown in (c). The global fit nicely reproduces the 2 ps time for the shift, even though the individual exponential fits show significant residuals (d). If a 4 ps decay is added to the simulation (e) the monoexponential single-channel fit again yields smaller decay times in the blue wing of the band and higher ones in the red wing (f). The times now tend to diverge not around the central wavelength, but towards the long wavelength region. The global fit (g) is once more superior and yields a  $\sim 4$  ps decay time for a monoexponential model and in addition a somewhat underestimated solvation time when a biexponential model is applied. The residuals from different time traces (h) still show significant deviations between data and fit.

An approach to visualize the TA dynamics unbiased by a specific model was proposed by Satzger and Zinth [52]. First, the TA data have to be recorded (or interpolated) on a time scale that has linear spacing on the logarithmic scale, i.e. exponentially increasing step sizes. Then the kinetic traces at each wavelength are differentiated on the logarithmic scale. On a logarithmic time scale, an exponential rise or decay has an inflection point at  $t = \tau$ . Thus, the involved time constants show up as maxima or minima in the logarithmically differentiated absorption changes (LDAC). As shown explicitly in ref. [52] and [53], the method works best with pure exponential processes on well separated time scales. Serious complications arise in the presence of noise which is strongly amplified by the differentiation. Then, significant averaging has to be applied to the data before the calculation of the LDAC signal. Even though this prevents a very detailed numeric analysis, the qualitative visualization of the data helps to choose reasonable starting values for a fit algorithm. Even more importantly, the LDAC signal can be used to check the consistency of fit results and to identify deviations from a simple rate model as caused for instance by spectral shifts.

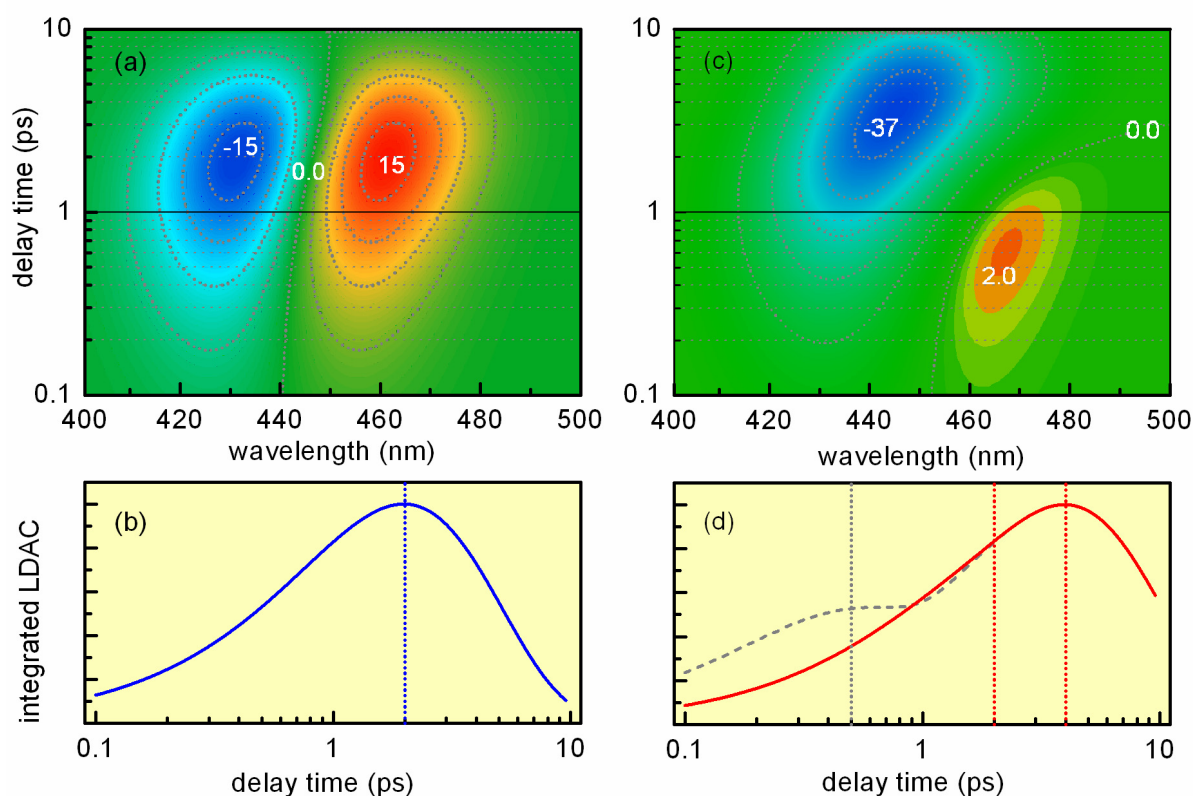


**Fig. 2.6 Analytic visualization of TA data:** (a) and (c): Logarithmically differentiated absorption changes (LDAC) of the artificial data of Fig. 2.5a and Fig. 2.5e. (b) The spectral integral of the absolute LDAC signal shows a maximum at the solvation time of 2 ps. (d) For close lying solvation (2 ps) and decay (4 ps) times, the spectral integral (red line) does not allow to extract both times. If the timescales are further separated (0.5 ps and 4 ps), both the shift and the decay time (dashed lines) can be identified from the LDAC integral.

The LDAC signals from the artificial data of Fig. 2.5 are shown in Fig. 2.6. In the case of a pure redshift of the absorption band, one obtains a “tilted”, nearly symmetric LDAC signal with two local extrema of equal absolute value (Fig. 2.6a). Their position in time-direction

corresponds to the 2 ps time constant of the spectral shift. This is seen more clearly if the absolute LDAC value at each delay time is summed over the whole spectrum. The resulting integrated LDAC shown in Fig. 2.6b consists of a broad peak with a maximum at  $\Delta t = 2$  ps.

If the 4 ps decay is added to the artificial data, the LDAC signal becomes less clear (see Fig. 2.6c). The new minimum corresponding to the decay of the band is superimposed on the shift signature resulting in a complex pattern with a deep global minimum at  $\Delta t > 1$  ps and a relatively small local maximum at  $\Delta t < 1$  ps. The large difference in amplitude demonstrates the importance of an interactively adaptable color coding in the LDAC software in order to prevent small signatures from being overlooked. The decay time constant of a few ps is reasonably visualized by the position of the global minimum. However, since the local maximum is shifted to smaller delay times, the 2 ps timescale for the spectral shift is practically not recognizable. This also holds for the spectral integral of the absolute LDAC signal shown in Fig. 2.6d. A second maximum in the integral becomes visible only if the shift and decay times are further apart, e.g. 0.5 and 4 ps.

The simulations presented above are an idealized situation. In actual TA experiments, one will face several complications. First, solvation itself is known to occur on multiple time-scales [49] for the common solvents. Thus, the dynamics of the spectral shift will also be multiexponential. Secondly, in most cases the analysis will suffer from the overlap of several bands corresponding to different molecular transitions. These bands might show different decay dynamics and different shift amplitudes (see section 3.2). Last but not least, the presence of noise can also severely influence the fit results and for example disturb the symmetric spectral characteristics found for some of the parameters. Nevertheless it is useful to keep in mind the typical signatures shown in Fig. 2.5 and 2.6 in order to reach a faster and more profound understanding when modeling actual TA data. The analysis of the artificial data also helps to estimate the accuracy of fitted parameters.

In addition to the limited applicability of rate models when spectral shifts are involved, another common mistake is to assume that a successful exponential fit unambiguously reveals the sequence of events for multistep processes. The order of the individual reaction steps does not necessarily follow the order of the decay rates, i.e. the highest rate (or the smallest time constant) cannot automatically be associated to the first process or the smallest one to the last [54-56]. Furthermore, the system might show branching where two or more decay pathways exist from one intermediate. Thus, several reaction schemes are in principle compatible with an experimentally determined set of rates. However, each of them leads to different species associated spectra (SAS), i.e. absorption spectra of the intermediate or product states. They are given by linear combinations of the DADS and depend on the specific rate model. Using information from other sources, such as steady state absorption spectra, it is in most cases possible to decide on which model is the most probable one.



### 3. Quantitative modeling of molecular dynamics

#### 3.1 Applicability of simple rate models to intramolecular charge transfer: Fluorescence quenching in naphthalene diimides

From the point of view of the interpretation of the TA spectra, the ultrafast emission quenching of core-substituted naphthalene diimides (NDI) is a relatively simple example. One reason is that intramolecular processes are essentially sufficient to explain the observed dynamics. At least for measurements in one selected solvent, interactions of the sample molecules with the environment do not have to be taken into account explicitly. The final mechanism can be well described by the two-step rate model shown in Fig. 3.1.

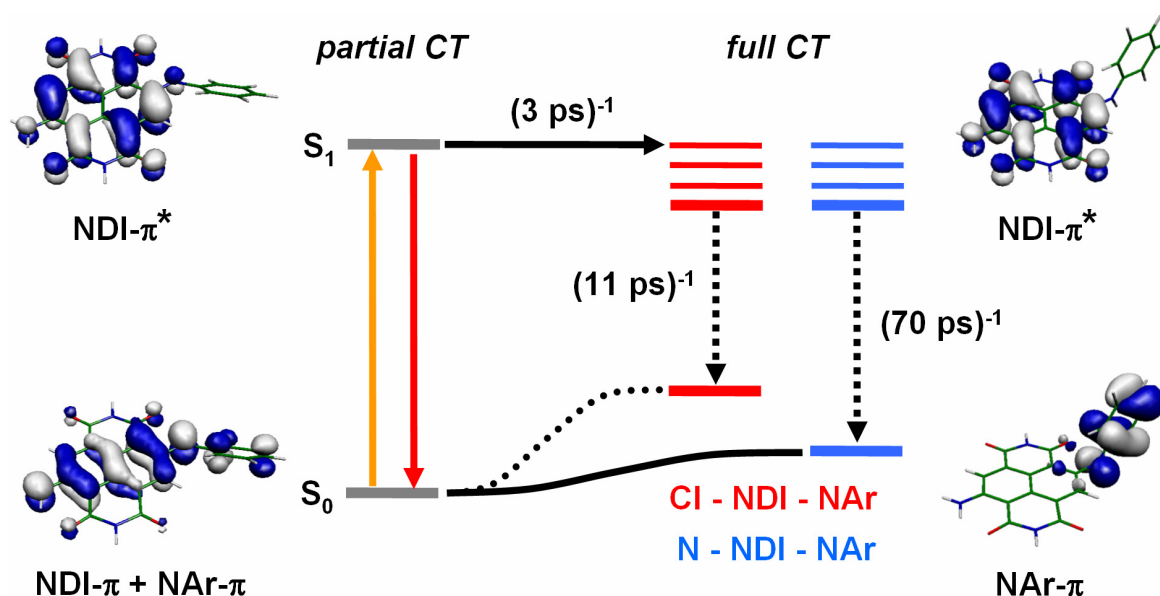


**Fig. 3.1** Molecular orbitals and relative energies of the electronic states involved in the charge separation and charge recombination process of arylamino core-substituted NDIs. For N-NDI-NAr (blue lines), a larger energy gap is found between the  $S_1$  and  $S_0$  states in the full CT geometry as compared to CI-NDI-NAr (red lines), resulting in a longer lifetime of the full CT state.

In a comparative study we investigated two arylamino core-substituted NDIs shown in Fig. 3.2, one with an additional amino-group attached to the NDI core (N-NDI-NAr) and one with a chloro-substituent at the same position (CI-NDI-NAr). In both NDIs, the optical excitation with visible light corresponds to a partial charge transfer (CT) from the arylamino substituent to the NDI core. Quantum chemical calculations show that the molecules in the excited state relax to a full CT state and thereby twist the arylamino substituent out of the plane of the NDI chromophore. Experimentally we determine a similar time constant of about 3 ps for the excited state charge separation for both compounds. In contrast, the rate associated with the subsequent charge recombination strongly depends on the nature of the second core substituent. We find a roughly sixfold larger lifetime of the full CT state for N-NDI-NAr (70 ps) than for CI-NDI-NAr (11 ps). The reason for this difference is the larger  $S_1$ - $S_0$  energy gap of N-NDI-NAr in the full CT geometry compared to CI-NDI-NAr as re-

vealed by *ab initio* calculations. In the following, the steps leading from the TA spectra to such a model are described in detail. The experimental and theoretical findings and their interpretation are also summarized in the following publication (appendix A3):

**Influence of core-substitution on the ultrafast charge separation and recombination in arylamino core-substituted naphthalene diimides**

*I. Pugliesi, U. Megerle, S.-L. Suraru, F. Würthner, E. Riedle, S. Lochbrunner*

*Chemical Physics Letters* 504, 24-28 (2011).

The panels in the first row of Fig. 3.2 show the steady state absorption and emission spectra of N-NDI-NAr and Cl-NDI-NAr in chloroform solution. As in many cases, these spectra provide the key information for the interpretation of the TA data shown in the panels of the second row of Fig. 3.2. For example, the striking fingerprint structure in the TA spectra around 350 nm can clearly be attributed to the ground state bleach (GSB) signature of a higher transition of the NDI chromophore that is superimposed on a relatively structureless, but stronger excited state absorption (ESA). The plateau-like ESA signature can also be inferred from the signal in the 400 – 500 nm range that is exclusively due to ESA transitions.

Similarly, the comparison of the TA data in Fig. 3.2b with the steady state spectra of N-NDI-NAr reveals that the ~ 650 nm band with negative absorption change is a superposition of the ground state bleach and the stimulated emission (SE). The narrowing of this band with increasing delay time and the shift of the minimum to shorter wavelengths can then be readily assigned to a faster decay of the SE signal than of the GSB signal. The vanishing SE is a clear indication for the population of the full CT state. The local minimum at  $\Delta t \geq 10$  ps coincides perfectly with the steady state absorption maximum at 617 nm indicating a negligible contribution of the ESA in this spectral region. This is supported by *ab initio* calculations on the corresponding anion (see appendix A3) which also explain the stronger overlap of the ESA with the GSB and SE signatures of Cl-NDI-NAr (see Fig. 3.2f). In this case, almost the whole visible region is dominated by the ESA. Negative absorption changes are only found for short delay times and  $\lambda \geq 650$  nm which unambiguously identify them as SE signatures. Their fast disappearance while ESA and GSB signatures are still present suggests a qualitatively similar quenching process as in N-NDI-NAr.

To obtain a quantitative description, the TA data can be smoothed\* and differentiated on the logarithmic scale to obtain the two-dimensional LDAC signal of both compounds (see Fig. 3.2c and g). In the spectral region of the SE, both LDAC signals show a broad distribution of time constants in the range up to a few picoseconds. The positive amplitude (warm colors) indicates a rise in the TA data, i.e. a quenching of the negative SE. The slightly tilted shape of the LDAC signature resembles the data shown in Fig. 2.6. It can therefore be taken as an indication for a spectral shift occurring on a timescale similar to the quenching process. This is in line with the reported solvation times of chloroform [49]: 0.3 ps (36%) and

---

\* In this case, smoothing is not only necessary to reduce noise, but also to average out the oscillatory signal contributions at early delay times that arise from impulsive Raman scattering in chloroform, see Fig. 1.2b.



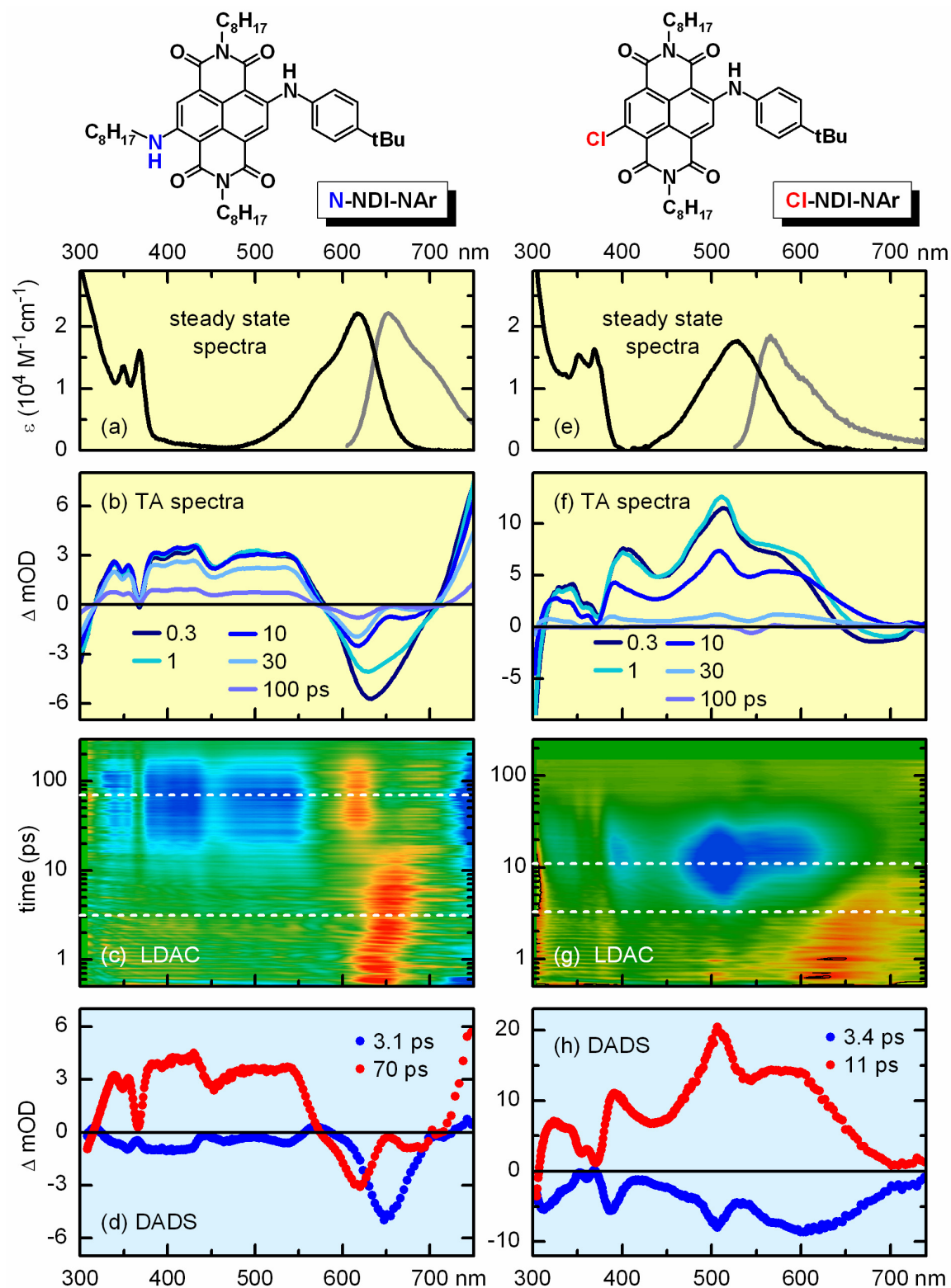


**Fig. 3.2 Global analysis based on a rate model:** Steady state and transient absorption spectra of N-NDI-NAr (a, b) and Cl-NDI-NAr (e, f) in chloroform solution. The dashed lines in the LDAC spectra (c, g) indicate the time constants found in the global fit. Cold colors in the LDAC spectra represent negative derivatives, i.e. decays of the TA signal, whereas warm colors represent positive derivatives, i.e. a rise of the TA signal. (d, h): Decay associated difference spectra (DADS) obtained from a biexponential global analysis.

4.2 ps (64%). In addition, the broad distribution indicates that the quenching process is not well described by a rate model. Indeed, the quantum chemical calculations suggest a barrierless adiabatic charge separation as quenching mechanism, i.e. a smooth process on the excited state potential energy surface rather than a sequence of well defined states.

In contrast to the complex situation in the SE spectral region, the interpretation of the dynamics for the other spectral signatures seems more straightforward. For N-NDI-NAr (Fig. 3.2c), the larger part of the spectrum shows an evolution on the timescale of several tens of ps. This is seen from the distinct minima (blue) at this delay time for  $\lambda < 550$  nm and above 700 nm. From the straight vertical shape of this LDAC signal one can infer that spectral shifts are not present on this timescale. This also holds for the local LDAC maximum observed in the same time range around 620 nm. Together, this indicates a concerted decay of ESA and GSB and the return of the system to the ground state within several tens of ps. As shown in Fig. 3.2g, the corresponding dominant evolution for Cl-NDI-NAr clearly happens on a much shorter timescale around 10 ps. Hence, the major result of the comparative TA study on the differently substituted NDIs, i.e. the different lifetime of the charge separated state, is already quantitatively seen in the LDAC signal.

A more accurate analysis leading to numerical values of the lifetimes is achieved with a global analysis. From the LDAC signals it is obvious that at least two time constants are necessary for a reasonable modeling of the data. For N-NDI-NAr, the biexponential global fit yields time constants of 3.1 and 70 ps. The corresponding DADS shown in Fig. 3.2d support the model described above. The fast time constant is essentially restricted to the SE spectral region, whereas the amplitude of the 70 ps component reproduces the ESA + GSB spectrum. From the DADS it is clear that the fast process is indeed the first relaxation step in the sequence of events after the photoexcitation.

The agreement between the biexponential fit and the experimental data is generally very good. The only exception is the SE region around 650 nm. The deviations there can be readily understood from the temporal coincidence of spectral shifts and decay processes which themselves are multi- or rather nonexponential. The 3 ps time constant can therefore be understood as a benchmark for the speed of the charge separation process. The fact that the fast decay time is only prominent in a relatively narrow spectral window might also contribute to the limited accuracy of the 3 ps time constant [52]. The separation and precise modeling of the involved processes on the sub-10 ps timescale might in principle be possible. However, the significant effort is disproportionate to the possible benefit as the key aspects of the charge separation are already understood at this point. In addition, the focus of this study is the lifetime of the charge separated state, i.e. the difference in the charge recombination rate of N-NDI-NAr and Cl-NDI-NAr.

In line with this notion, the global fit to the TA data of Cl-NDI-NAr is also restricted to two exponential contributions despite the resulting small discrepancies between data and fit. Adding a third exponential leads to strong correlations and compensation effects between two of the parameters and is not helpful for the interpretation. In general, the discussion of the TA, LDAC and DADS of Cl-NDI-NAr is complicated by the stronger spectral overlap of ESA, GSB and SE and the closer proximity of solvation, charge separation and charge re-

combination times. The most relevant parameter, however, the lifetime of the charge separated state, is consistently determined to  $\sim 10$  ps in both the LDAC and the global analysis.

In summary, the study of the photoinduced charge separation and recombination in the two core-substituted NDIs shows the necessity to combine different approaches to obtain the final nanoscopic model of the molecular process. This includes the comparison of transient spectra at different delay times with the steady-state spectra, the consideration of *ab initio* calculations, visualization methods such as LDAC and global fits with several exponential functions. Even though the application of a two-step rate model is a slight simplification of the actual dynamics in this case, especially of the adiabatic charge separation, it succeeds to describe the essential processes and allows for a simple comparison of the two systems. Naturally, the acceptable level of approximation depends on the specific problem. Here for example, the details of any solvation or vibrational relaxation dynamics do not contribute decisively to the overall picture. It is therefore sufficient to identify the reasons for the small deviations between model and experiment and to concentrate the discussion primarily on the central questions that needed to be answered. In this manner we found that arylamino core-substituted NDIs show a different charge separation mechanism than the previously studied arylsulfanyl core-substituted NDIs [57]. There, the first step corresponds to a planarization of the substituents and an associated partial electron transfer that is not necessary for the amino compounds described here: Their optically excited state already possesses a partial CT character and a quasi planar configuration. Our study also revealed that the second core-substituent opposite the arylamino group does not change the charge separation time significantly. However, it has a strong influence on the charge recombination step leading back into the electronic ground state. Exchanging the chloro substituent for an alkylamino group leads to a sixfold increase of the excited state lifetime from 11 ps to 70 ps as a consequence of the larger energy gap. These findings show how the choice of core-substituents allows for the tuning of the charge separation and recombination processes in NDI chromophores.



### 3.2 Spectral decomposition to model band shifts:

#### Solvation dynamics of donor-substituted triarylboranes

In contrast to the situation for the NDIs, the locally excited state of carbazole-substituted triarylboranes (TABs) already possesses a full CT character. This can be deduced from the clear solvatochromic shift of the lowest energy absorption band [58]. As shown in Fig. 3.3, the steady state fluorescence of donor-substituted TABs is subject to an even more pronounced shift that indicates the emergence of a highly polar excited state from a relatively nonpolar ground state. This strong charge redistribution upon photoexcitation makes TABs ideal candidates to study solute-solvent-correlated dynamics. By using TABs with multiple donor substituents, we investigated in particular the influence of molecular symmetry and the related charge mobility to the solvation dynamics. The results of this study are summarized in the following publication (appendix A4):

#### Symmetry-dependent solvation of donor-substituted triarylboranes

*U. Megerle, F. Selmaier, C. Lambert, E. Riedle, S. Lochbrunner*

Physical Chemistry Chemical Physics 10, 6245-6251 (2008).

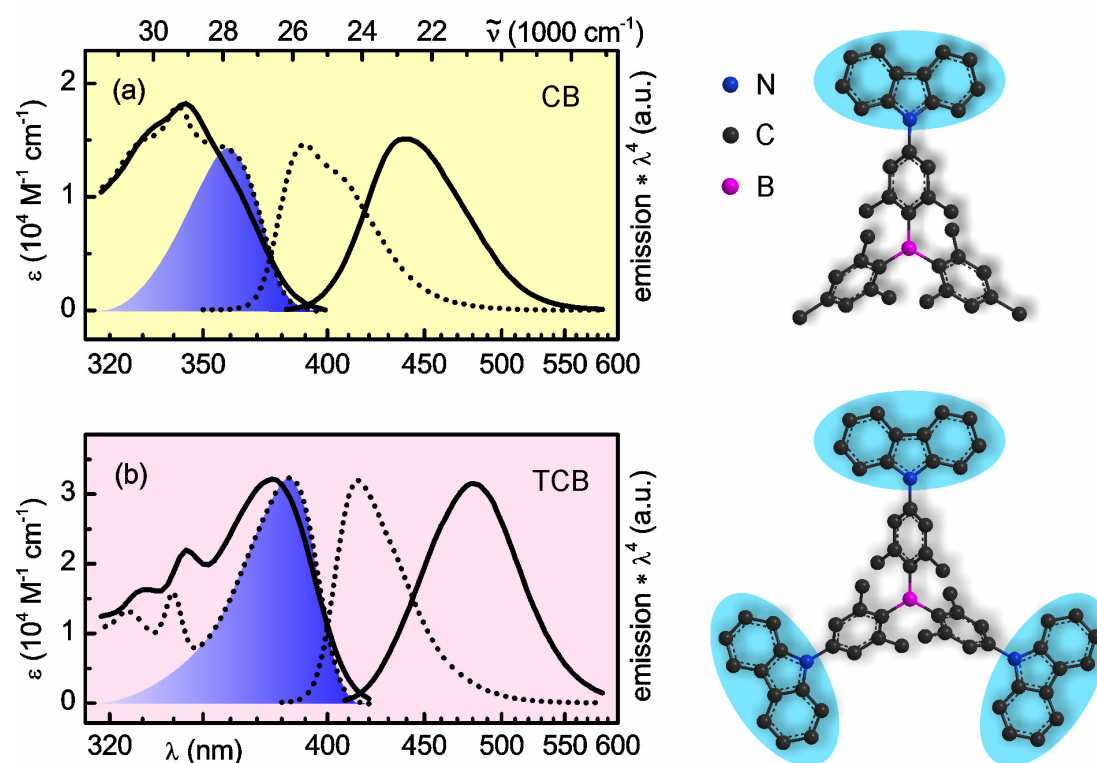


**Fig. 3.3** Steady-state absorption and emission spectra of (a) CB and (b) TCB in the nonpolar solvent cyclohexane (dotted lines) and the polar solvent benzonitrile (solid lines). The CT-absorption (shaded area) corresponds to an electron transfer from a carbazole moiety (blue ellipse in the chemical structure) to the boron center.

In our investigation we compared the single carbazole-substituted borane (CB) shown in Fig. 3.3a and its highly symmetric counterpart, the triple carbazole-substituted borane (TCB) shown in Fig. 3.3b. For all polar solvents under study we found an accelerated solvation process for TCB compared to the less symmetric CB. We explained these findings by the possibility of an intramolecular charge delocalization over the different carbazole sites of TCB. This allows for a response of the excited state dipole moment of TCB to the local field of the solvation shell. In contrast to CB, where the relaxation is only possible by motions of the solvent molecules, the TCB system thus acquires an additional efficient pathway to reach the minimum energy configuration.

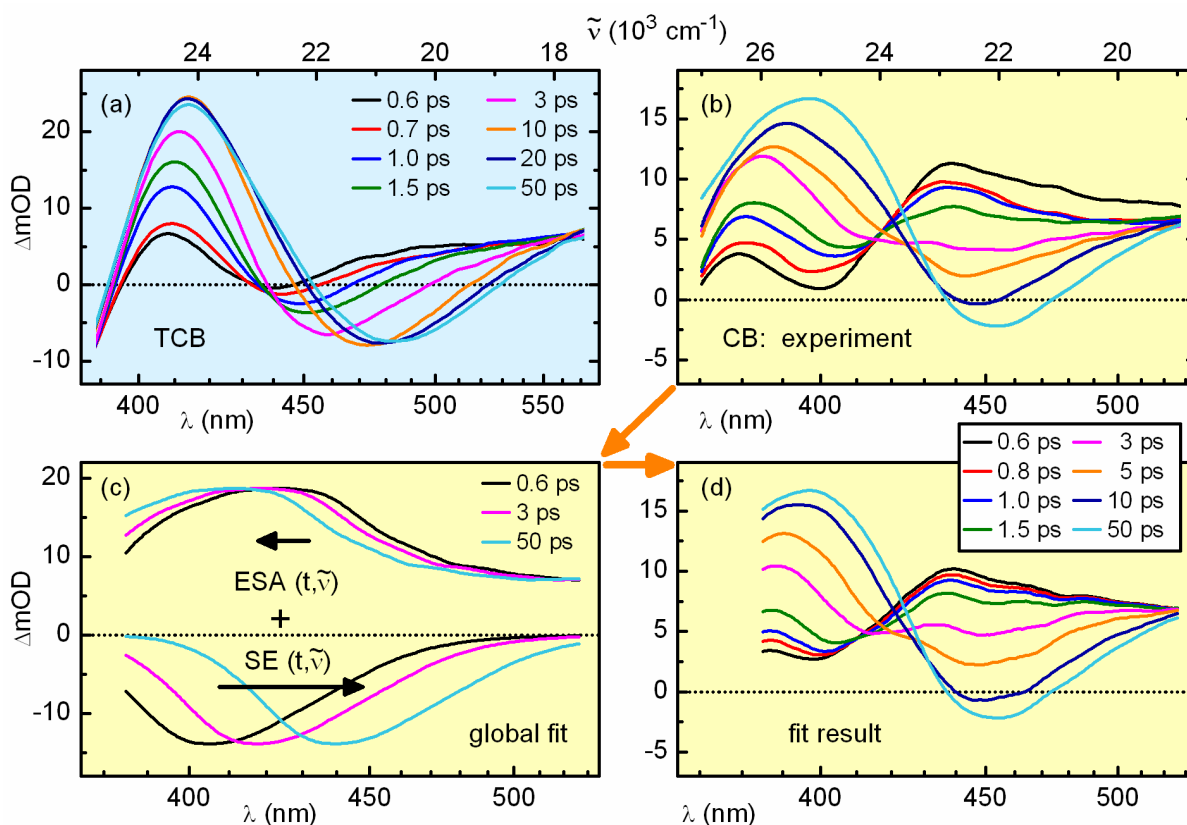


**Fig. 3.4 Spectral decomposition to model solvatochromic band shifts:** (a) TA spectra of TCB in benzonitrile solution after 360 nm excitation. The spectral evolution is governed by the redshift of the stimulated emission band. The more complicated TA spectra of CB (b) can be decomposed into a strongly shifting SE band and a slightly shifting broad ESA band (c). The reconstructed transient spectra (d) resulting from this minimal parameter global fit are in very good agreement with the experimental curves.

These results are based on the evaluation of the solvation dynamics of the two chromophores, i.e. the kinetics of the spectral shifts observed in the ultrafast TA experiments. The occurrence of strong band shifts in polar media can already be predicted from the cw spectra. By comparing the cw emission maxima in the nonpolar cyclohexane (dotted lines in Fig. 3.3) with, for example, the ones in benzonitrile (solid lines), one can expect a dynamic Stokes shift of up to  $3000\text{ cm}^{-1}$  for the stimulated emission bands of CB and TCB in a time-resolved study. The dynamics of the band shift can be estimated using the solvent response

times from the extensive study by Maroncelli and coworkers on a coumarin dye [49]. Typically, the characteristic times for the solvation lie in the ps range. Since the investigated TABs were designed as long-lived emitters and charge transport materials for organic light emitting diodes (OLEDs), the excited state has a lifetime on the order of nanoseconds [58] which implies that only the onset of a deactivation will be observed in the time range of our experiment.

Indeed, the TA spectra we obtained after 360 nm excitation of CB and TCB in polar solvents show a strong evolution on the ps timescale (see Fig. 3.4a and b). In cyclohexane however, the TA spectra remain virtually unchanged for several tens of picoseconds. Only for larger delay times approaching the ns fluorescence lifetime does the decay to the ground state cause the signals to decrease. This slow, collective decay is also observed in polar environments. However, since its dynamics is (i) understood and (ii) completely separated from the ps evolution, it can be neglected for the further discussion.

Intuitively, the interpretation of the TCB spectra is easier. As seen in Fig. 3.4a, the observed spectral evolution is clearly governed by a red-shifting SE band. The  $\sim 7$  mOD change in the amplitude of the local minimum between 0.6 and 50 ps can be understood from the superposition with the falling edge of an ESA band in this region. On the other hand, the CB spectra in Fig. 3.4b on first sight suggest a reaction from a species absorbing around 440 nm to one absorbing around 400 nm. This, however, would require an isosbestic point in between, which is not observed. A closer look also reveals the occurrence of spectral shifts: for example, the local minimum around 450 nm shifts by  $\sim 10$  nm between 3 and 50 ps. From the discussion above it is much more likely that for CB as well solvation is the only driving force for the spectral changes.

To validate this assumption we aimed for a quantitative modeling of the TA data. As shown in section 2.3 with artificial data, exponential fits to kinetic traces at fixed wavelengths are not suitable to describe the dynamics of spectral shifts. For the TA data of CB and TCB in polar solvents, a reasonable parameterization requires up to three exponential components with strongly varying time constants depending on the probe wavelength. We therefore followed a different approach and decomposed the TA spectra in a global fit routine.

In the case of a non-reactive system, the three signals contributing to the TA spectra are the stimulated emission (SE), the excited state absorption (ESA) and the ground state bleach (GSB). Here as in most cases, the GSB is not subject to spectral shifts: it represents the absorption of ground state molecules that is not time-dependent. The global fit of the solvation dynamics is therefore restricted to  $\lambda > 400$  nm for TCB and to  $\lambda > 385$  nm for CB. For the spectral signatures of ESA and SE we assume an evolution that comprises an exponential shift of the spectral bands with time on the energy scale (see Fig. 3.4c):

$$\begin{aligned} \text{ESA}(t, \tilde{\nu}) &= \text{ESA} \left( \infty, \left[ \tilde{\nu} - \Delta\tilde{\nu}_{\text{ESA}} \cdot e^{-t/\tau} \right] \right); \\ \text{SE}(t, \tilde{\nu}) &= \text{SE} \left( \infty, \left[ \tilde{\nu} - \Delta\tilde{\nu}_{\text{SE}} \cdot e^{-t/\tau} \right] \right). \end{aligned} \quad (3.1)$$

As always for the modeling of TA spectra, one should try to use previous knowledge to limit the parameter range as much as possible. First of all, the SE signature must coincide with the known steady-state emission spectrum in the respective solvent at  $t \rightarrow \infty$ , i.e. at quasi-equilibrium. The spectral shape of the ESA for large delay times can then be inferred from the final transient spectrum by subtracting the steady state emission with a proper scaling factor<sup>\*</sup>. Secondly, the dynamics of the shift should be the same for ESA and SE. Therefore, a common time constant  $\tau$  can be used reflecting the averaged solvation dynamics of the system. Moreover, the solvation model requires that the SE is initially blue-shifted, accounting for the unfavorable energetic situation directly after the excitation. As a consequence,  $\Delta\tilde{\nu}_{SE}$  will always have a positive sign. Since the dipole moment of the higher electronic states contributing to the ESA band is unknown at first,  $\Delta\tilde{\nu}_{ESA}$  can in principal have both signs.

All of this was implemented in a least-square fit algorithm written in LabView. The transient spectra resulting from this fit are in very good agreement with the experimental curves, including in particular the rather complex CB spectra (see Fig. 3.4d). As expected, the shift amplitudes for the SE band are on the order of several  $1000\text{ cm}^{-1}$  and the corresponding shift times are in the same regime as the average solvation times known from literature [49], at least for the less symmetric CB. The consistently shorter times found for TCB led to the model of symmetry-dependent intramolecular contributions to the solvation as described above and in appendix A4.

It is worth noting that the TA spectra of CB in benzonitrile are a striking example that even complicated looking spectral evolutions might have fairly simple explanations. One only has to take into account what is known from independent sources, e.g. from cw spectroscopy, literature, TA experiments in a nonpolar solvent or with a related molecule such as TCB, to rule out any unlikely processes. In the case of CB, the existence of several discrete intermediate states and the interconversion between them could be excluded from the discussion, even though the apparent rise and decay features in the TA spectra would suggest such a scheme on first glance. Instead, the solvation induced band shifts sufficed to reproduce the TA signatures.

---

<sup>\*</sup> For a quantitative analysis, the spontaneous steady state emission spectra have to be corrected for the spectral sensitivity of the fluorimeter and converted to cross sections for stimulated emission by multiplication with  $\lambda^4$ .



### 3.3 From absorption changes to state populations:

#### Solvent-controlled intramolecular electron transfer in crystal violet lactone

The interplay of solvation and intramolecular charge transfer is also the key aspect in the TA study of crystal violet lactone (CVL) that is summarized in the following publication (appendix A5):

**The key role of solvation dynamics in intramolecular electron transfer: time-resolved photophysics of crystal violet lactone**

*U. Schmidhammer, U. Megerle, S. Lochbrunner, E. Riedle, J. Karpiuk*

Journal of Physical Chemistry A 112, 8487-8496 (2008)

In analogy to the TABs, the evaluation of the solvatochromic behavior together with *ab initio* calculations could identify the nature of the CT states involved in the absorption and emission process [59]. As shown in Fig. 3.5a, the interesting extension in this case is that the emission can occur from two different CT states depending on the solvent polarity. Both CT states are characterized by a negative charge on the lactone ring and a positive charge on one of the differently situated dimethylaniline groups (Fig. 3.5b)

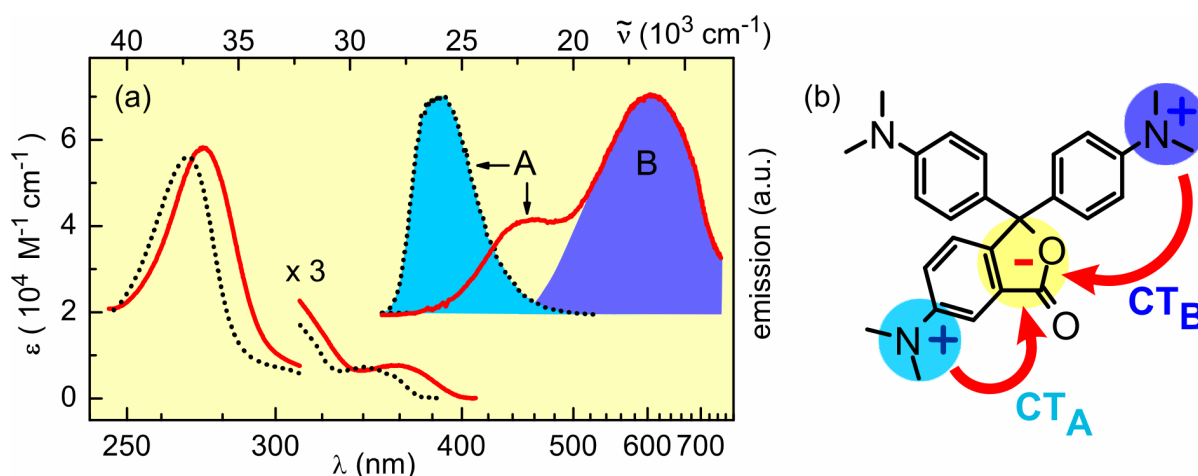


**Fig. 3.5** (a) Steady-state absorption and emission spectra of CVL in nonpolar (n-hexane, dotted lines) and polar (acetonitrile, solid lines) solvent. In the latter, CVL shows a dual fluorescence (A and B) from the two charge transfer states shown in (b). In nonpolar media, the  $CT_B$  state is not accessible and emission is only seen in the A-band.

We showed that in this system the intramolecular ET between the initially excited  $CT_A$  state and the highly polar  $CT_B$  state proceeds with a time-dependent rate that is controlled by the solvent. Within the timescale of the solvation process, the relative energetics of the two states changes from a higher lying  $CT_B$  state to the opposite situation in the quasi-equilibrium. The intrinsic ET reaction is probably as fast as in the structurally analogous malachite green lactone (on the 100 fs time scale). Nevertheless, the slower solvation dynamics is decisive for the actual ET rate and the final population distribution.

From the steady-state spectra, one could expect qualitatively similar TA signals for CVL as for the TABs. In particular, the strong CT character of the emission would suggest significant spectral shifts in polar solvents. However, the stimulated emission is completely outweighed by the excited state absorption at all delay times and over the whole spectral range (see Fig. 3.6a). In contrast to the  $S_1 \rightarrow S_0$  transition, the transitions contributing to the ESA obviously comprise only minor changes of the static dipole moment. The most striking evidence for this is that instead of spectral shifts a clear isosbestic point is observed around 500 nm. By comparison of the CVL spectra with data from related molecules, we can identify the initial double-peaked signature with the  $CT_A$  state whereas the final single-peaked spectrum with a maximum at 470 nm corresponds to the  $CT_B$  state. The isosbestic point then indicates the direct interconversion between these two states by intramolecular ET. In contrast to the situation in the core-substituted NDIs (see section 3.1), the back-ET in CVL proceeds on the nanosecond timescale [59] and is practically not observed in the ultrafast experiments. From this one can infer a larger energy gap between the  $S_1$  state and the ground state, even after the stabilization of the excited CT states by the solvation process. The larger energy gap is in line with the UV absorption of CVL being shifted by roughly  $10000\text{ cm}^{-1}$  or 1.2 eV compared to the visible CT absorption band of the NDIs.

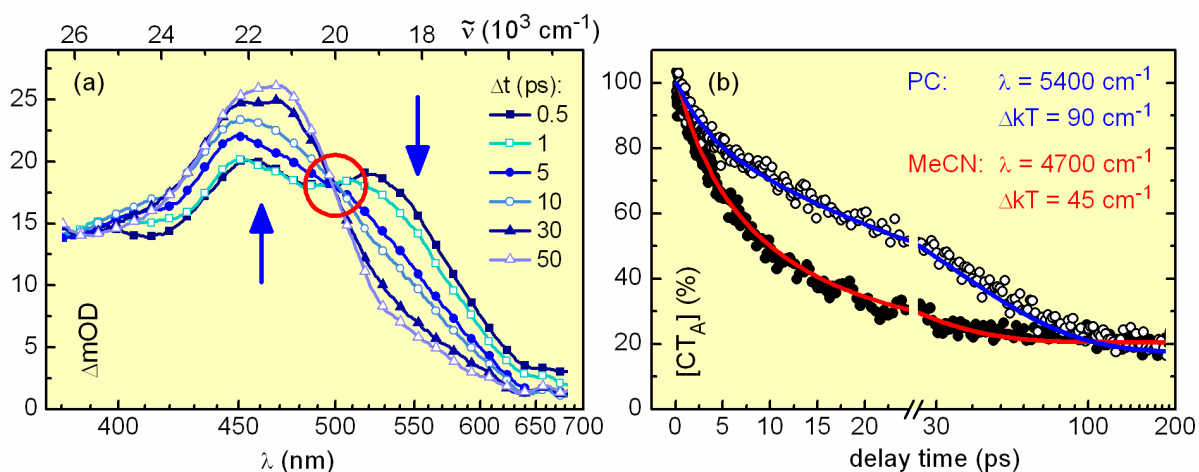


**Fig. 3.6 From kinetic traces to population dynamics:** (a) TA spectra of CVL in propylene carbonate (PC) after 370 nm excitation. The isosbestic point corresponding to the  $CT_A \rightarrow CT_B$  conversion is marked by a red circle. (b) Relative population of the  $CT_A$  state in PC (open circles) and acetonitrile (closed circles). The solid lines show the simulation of the population dynamics using the time-dependent rate determined from Marcus theory.

The kinetics of the intramolecular ET from  $CT_A$  to  $CT_B$  can best be monitored in the rise of the 470 nm maximum or in the decay of the long wavelength band around 550 nm. As expected from the observation of the isosbestic point, the rise and decay dynamics are correlated in each of the investigated solvents. Within the experimental accuracy we always find the same exponential time constants in both bands (see appendix A5). However, the observed biexponential behavior has no straightforward explanation, even if the multiexponential characteristics of solvation processes are taken into account. Most evidently, the second

time constant is always significantly larger than the slowest solvation process [49]. Therefore, the exponential fit merely serves as a parameterization of the kinetic traces.

The reason for the failure of a kinetic model based on exponential fits is again the fact that the underlying process is only poorly described with a static rate model. When the relative energetics between  $CT_A$  and  $CT_B$  change, the barrier between them is also subject to changes. This in turn affects the rate for the population transfer from  $CT_A$  to  $CT_B$  and back. The first step towards a quantitative kinetic modeling is therefore to extract the relative population of the involved states from the TA data.

Since effectively only the two CT states contribute to the observed signal at a given wavelength and we know that the  $CT_B$  state is not populated directly by the optical excitation,  $\Delta OD(t)$  is given by

$$\begin{aligned}\Delta OD(t) &= c_A(t) \cdot \varepsilon_A \cdot d + c_B(t) \cdot \varepsilon_B \cdot d \\ &= c_A(t) \cdot \varepsilon_A \cdot d + [c_A(0) - c_A(t)] \cdot \varepsilon_B \cdot d,\end{aligned}\quad (3.2)$$

where  $d$  is the sample thickness,  $c_X(t)$  is the concentration of molecules in state  $CT_X$  and  $\varepsilon_X$  is the extinction coefficient of this state at the investigated wavelength. The normalized population  $\tilde{c}_A(t)$  of the  $CT_A$  state can then be expressed as

$$\tilde{c}_A(t) = \frac{c_A(t)}{c_A(0)} = \frac{\Delta OD(t)/c_A(0) - \varepsilon_B \cdot d}{d(\varepsilon_A - \varepsilon_B)}.\quad (3.3)$$

The unknown extinction coefficients can be eliminated using the amplitudes  $A_0$  at  $t = 0$  and  $A_\infty$  at  $t > 100$  ps together with the calculable\* fraction  $x = c_A(\infty)/c_A(0)$  of the  $CT_A$  population after the solvation, i.e. in quasi-equilibrium:

$$\begin{aligned}\Delta OD(0) &= c_A(0) \cdot \varepsilon_A \cdot d = A_0; \\ \Delta OD(\infty) &= x \cdot c_A(0) \cdot \varepsilon_A \cdot d + (1-x) \cdot c_A(0) \cdot \varepsilon_B \cdot d = A_\infty.\end{aligned}\quad (3.4)$$

Substituting these expressions into the equation for the normalized  $CT_A$  population yields:

$$\tilde{c}_A(t) = \frac{\Delta OD(t) \cdot (1-x) - A_\infty + A_0 \cdot x}{A_0 - A_\infty}.\quad (3.5)$$

Thus, we can use the fit amplitudes from the above mentioned exponential parameterization to convert the kinetic traces at individual wavelengths to the physically more relevant population dynamics (see Fig. 3.6b). This paves the way for a quantitative description of the solvent-dependent ET.

The model includes the determination of a number of microscopic and thermodynamic quantities such as the initial separation between the two CT states, the total amount of energetic lowering caused by the solvent reorganization and an estimate for the solvation and local heat dissipation timescales. The proper combination of these considerations leads to a knowledge of the energetics at each point in time and therefore allows the application of the

---

\* The final population in the  $CT_A$  and  $CT_B$  state corresponds to a Boltzmann distribution and depends on the energy difference between the states after solvation. This can be inferred from the analysis of the solvatochromism, see equation 1 and 2 in appendix A5.

Marcus theory [60, 61] to determine a time-dependent ET rate  $k_{\text{ET}}(t)$ . With this the population dynamics can be found by numerical integration of the rate equation

$$\frac{d\tilde{c}_A}{dt} = -k_{\text{ET}}^+(t) \cdot \tilde{c}_A + k_{\text{ET}}^-(t)(1 - \tilde{c}_A), \quad (3.6)$$

where the plus sign refers to the forward and the minus sign to the backward ET. The results for the depopulation of the  $\text{CT}_A$  state in propylene carbonate and acetonitrile are shown in Fig. 3.6b as solid lines. The agreement with the experimental data is remarkable given that all kinetic information used in the model is taken from independent sources. The only parameters that are adjusted are the reorganization energy  $\lambda$  and the initial increase in local temperature  $\Delta kT$ . The significantly higher value of the latter in PC is due to the high polarity of this solvent. Thus, the absorption band of CVL in PC is redshifted compared to MeCN and the same excitation wavelength leads to a higher excess energy.

The analysis of the intramolecular ET of CVL demonstrates that even clear spectral signatures might sometimes require non-standard modeling to reach a deeper understanding. In this regard, CVL is the counter-example to the TABs described above, especially CB, where rather complicated spectral evolutions could be explained by a fairly simple model. In both cases, the continuous characteristics of the solvation process impede the application of a classic rate model implying discrete states with time-independent energies and constant rates for the transitions between them. For CVL, the application of the time-dependent rate model not directly to kinetic TA traces but to the derived state population was decisive to prove the control of the ET by the solvent, both in terms of energetics and dynamics. The consideration of both these aspects explains why simple exponential fits to kinetic traces fail to reproduce the known solvation times. The obtained time-constants are therefore not particularly relevant for the final description of the process.

### 3.4 Band integrals, diffusion model and species associated spectra: flavin-catalyzed photooxidation of benzylic alcohol

The photoinduced charge transfer reactions presented in the previous sections are intramolecular processes, even though the environment, i.e. the solvent molecules, can have significant influence. The next level of complexity is to study true bimolecular reactions where electrons and/or atoms are exchanged between different species. A prominent example are photocatalytic redox reactions that are involved in many important chemical and biological processes such as water splitting or photosynthesis.

In nature, the most ubiquitous cofactors of redox enzymes are flavin derivatives that can be reduced and oxidized by one- and two-electron-transfer reactions [62]. The strong absorption of flavin up to  $\sim 500$  nm also makes it an ideal candidate for synthetic chemical photocatalysis using visible light. Due to the largely different absorption spectra of the three redox states of flavin which also depend significantly on the protonation state [63-66], the course of the reaction can be monitored very well by TA spectroscopy.

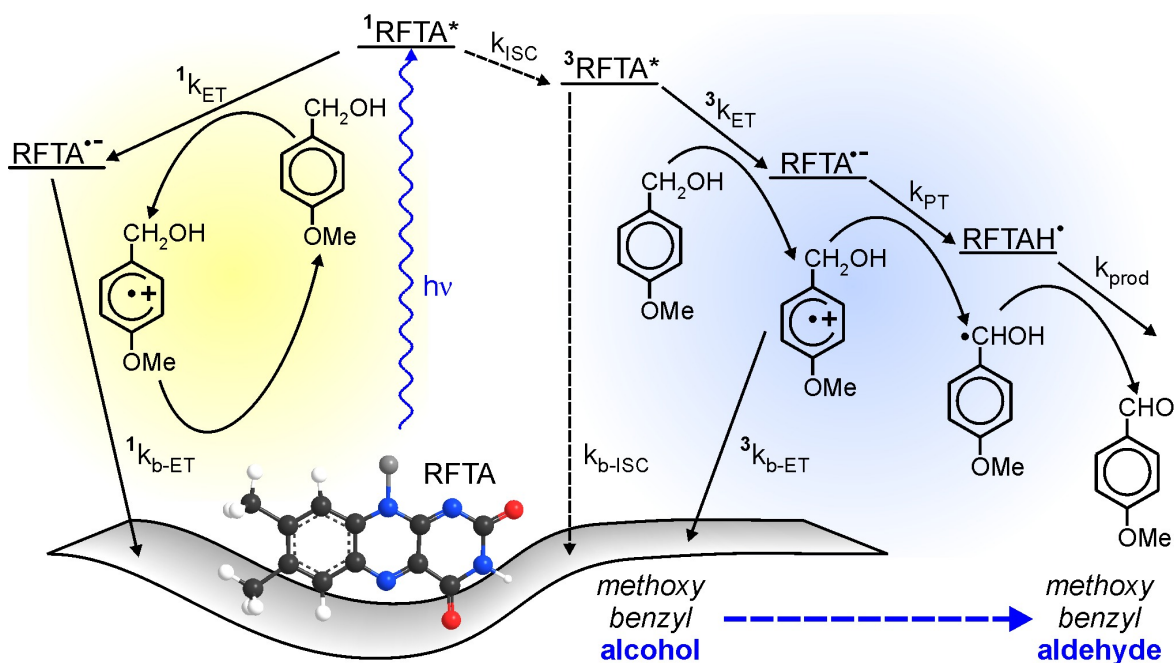


**Fig. 3.7** Scheme of the oxidation mechanism of MBA. The non-productive singlet channel (yellow) brings the excited RFTA back to the ground state by diffusion controlled electron transfer from MBA ( $^1k_{ET}$ ) and fast charge recombination ( $^1k_{b-ET}$ ). In the triplet manifold (blue), the charge recombination ( $^3k_{b-ET}$ ) is much slower allowing for a finite product yield via a sequence of electron and proton transfer events.

The favorable properties of flavin are exploited by using riboflavin tetraacetate (RFTA) as photocatalyst in our study on the oxidation of methoxybenzyl alcohol (MBA) to benzaldehyde. The resulting mechanism of the photoreaction is shown in Fig. 3.7. We found that the key intermediate is the triplet state of RFTA and that the productive reaction proceeds on the microsecond timescale via a sequence of electron and proton transfer events. If, however,

the initial ET from MBA to RFTA occurs in the singlet state, the reaction does not lead to significant product formation. Since the back-ET is now spin-allowed, the charge recombination is more than five orders of magnitude faster than in the triplet state which impedes any further reaction steps. Thus, in dilute solution, the diffusion controlled rate for an encounter of MBA with RFTA has to be on the order of the intersystem crossing rate of RFTA to avoid the singlet loss channel. The detailed discussion of the experimental results and their implications on the photocatalytic reaction are given in the following publication (appendix A6):

**Unraveling the flavin-catalyzed photooxidation of benzylic alcohol with transient absorption spectroscopy from sub-pico- to microseconds**

*U. Megerle, M. Wenninger, R.-J. Kutta, R. Lechner, B. König, B. Dick, E. Riedle*

*Physical Chemistry Chemical Physics* 13, 8869-8880 (2011).

As suggested by the scheme in Fig. 3.7, the basis for the description of the reaction mechanism is again a rate model. However, for some of the involved processes additional issues have to be considered that go beyond the classic assumptions of rate models. In the case of RFTA dissolved in pure MBA, the situation is analogous to the fluorescence quenching in the NDIs (see section 3.1). As shown in Fig. 3.8a, the decay of the SE observed as negative signal between 520 and 630 nm is much faster than the decay of the GSB (415-485 nm) and the ESA in the rest of the spectrum. These signatures decay to baseline with a time constant of 50 ps as found from a biexponential global analysis (see Fig. 3.8b). This process is well described by a rate model as seen from the LDAC spectrum shown in Fig. 3.8c. Similar to the situation for the NDIs, relatively well defined extrema are obtained at the spectral position of the ESA and the GSB. Accordingly, the time constant of 50 ps is very stable in the fit algorithm, even if the fast SE decay is modeled differently.

The assignment of one exponential time constant to the fast emission quenching is complicated by the fact that it proceeds on the same timescale as the spectral shifts of ESA and SE caused by solvation. In addition, the quenching process might require some rotational diffusion of the molecules to reach a significant overlap of the wavefunctions and therefore an efficient ET from MBA to RFTA\* [61]. The initial distribution of relative orientations would then translate into a distribution of rates. In similar situations, an empirical function of the form  $A \exp\left(-\sqrt{t/\tau}\right)$  has successfully been applied to model the kinetics [67-69]. This stretched exponential function also reproduces very well the fast components of our data set. For the typical ET time  $\tau$  a value of 3.6 ps is obtained, nearly identical to the result of 3.8 ps from the pure exponential fit. The DADS of the stretched exponential contribution is also very similar to the blue spectrum in Fig. 3.8b. The standard deviation between fit and data can be reduced further by replacing the stretched exponential with two simple exponential functions. This fit results in two comparably strong contributions for the fast ET with time constants of  $\tau_1=0.43$  and  $\tau_2=6.8$  ps, i.e. an average ET time of 3.6 ps. Independent of the model function of choice one can therefore conclude that the intrinsic bimolecular ET rate  $^1k_{\text{ET}}$  between MBA and RFTA in direct contact is on the order of  $(4 \text{ ps})^{-1} = 2.5 \times 10^{11} \text{ s}^{-1}$ .

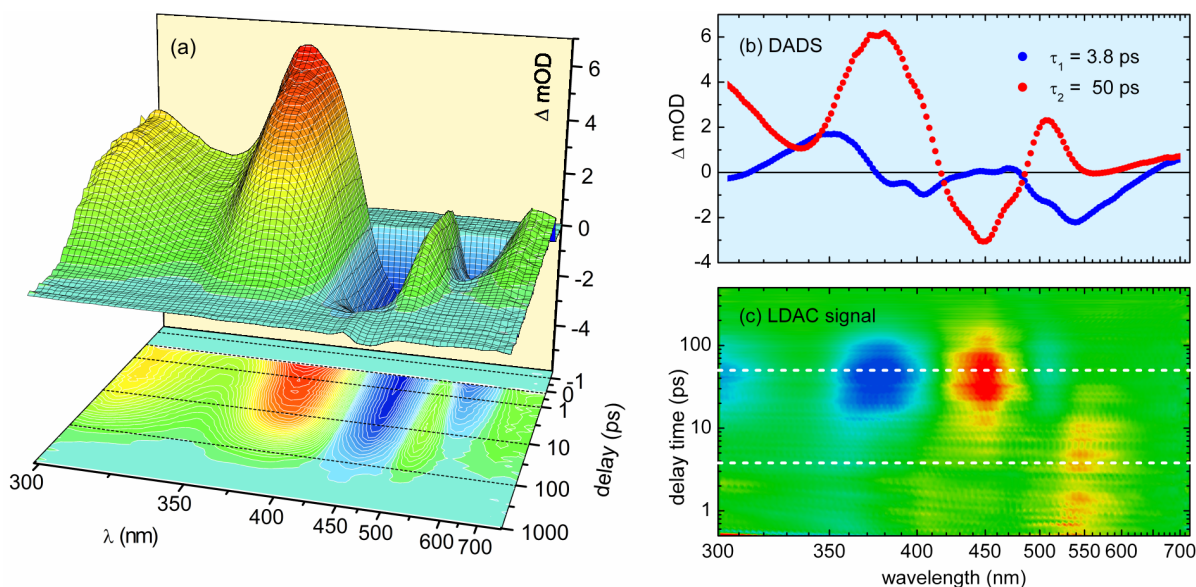


**Fig. 3.8 Global analysis of a bimolecular reaction:** (a) TA spectra of RFTA in pure MBA after excitation at 480 nm. The few-ps decay of the SE around 560 nm reflects the initial ET from the alcohol to the flavin. The concerted decay of all other signatures with  $\tau_2 = 50$  ps (biexponential global fit, b) indicates a full charge recombination without product formation. The dispersive shape of the DADS of the fast component (blue curve in b) reveals the presence of spectral shifts on the few-ps timescale. This is corroborated by the tilted maximum of the LDAC signal in the SE region and the weak shift signatures for  $\Delta t < 10$  ps between 350 and 450 nm (c).

As expected, the ET rate changes when RFTA and MBA are dissolved in an external solvent thus effectively reducing the MBA concentration around any RFTA molecule. Then, the two reaction partners have to diffuse to close proximity before an ET can occur. As shown in Fig. 3.9a, even at the high MBA concentration of 1.6 M a significant SE signal is still observed at long delay times up to 100 ps. It is also interesting to note that the overall decay of ESA and GSB is now proceeding on a similar timescale as the quenching of the SE. The fact that the three major bands are clearly separated from each other makes the TA data of RFTA very well suited for the application of band integrals to evaluate the population dynamics [70]. The integral  $\int d\lambda \cdot \Delta OD / \lambda$  over the whole band is directly proportional to the transition dipole moment squared [71, 72] and to the population of the respective electronic state. Thus, band integrals minimize distortions from spectral diffusion, broadening or narrowing that occur in the analysis of kinetic traces at single wavelengths. This is helpful since the existent solvation and vibrational relaxation processes are not of interest in this study. The integration limits marked by the shaded areas in Fig. 3.9a are set to 300–409 nm for the ESA band, 409–486 nm for the GSB and 525–625 nm for the SE band. These values do not exactly represent the outer limits of the bands, but they comprise the spectral regions where the respective transitions dominate the TA signals. It was found that slight alterations of the integration limits do not change significantly the resulting dynamics of the population/oscillator strength that are shown in Fig. 3.9b–d for three different MBA concentrations.

### 3. Quantitative modeling of molecular dynamics

Based on the knowledge of the system it is clear that the observed dynamics has to be fitted with a diffusion model. On the sub-nanosecond timescale, the rate at which RFTA\* and MBA diffuse together to form an encounter pair is time dependent [73, 74]. The transient effect originates from a changing concentration of MBA quenchers around the ensemble of excited RFTAs. After the optical excitation, the RFTA\* molecules with nearby quenchers will react first, leaving behind an ensemble of RFTA\* with a larger average distance to the next MBA. The diffusion rate therefore decreases continuously until the depletion of MBA around the remaining RFTA\* is balanced by the diffusion of bulk MBA towards the RFTA\* molecules.

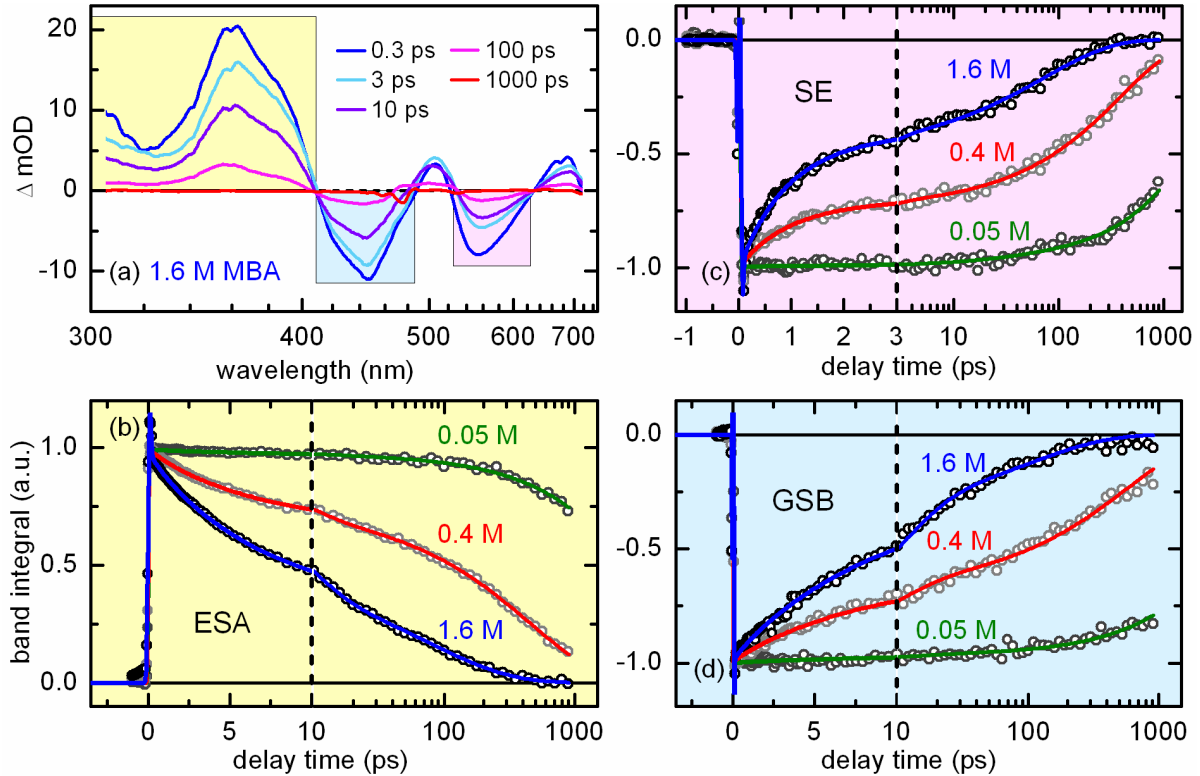


**Fig. 3.9 Band integrals to monitor reaction dynamics:** (a) TA spectra of RFTA and 1.6 M MBA dissolved in MeCN/H<sub>2</sub>O (50:50, v/v). The shaded areas indicate the spectral regions used for the band integrals of ESA (yellow), GSB (blue) and SE (red). (b-d) The obtained population dynamics (circles) reveal a faster relaxation at higher MBA concentrations and can be fitted consistently with a diffusion model and one additional fast component (solid lines, see text).

An analytical expression for the population dynamics of excited RFTA can be obtained using the approximations of the Smoluchowski theory. There, the quencher molecules are treated as an initially homogeneous continuum outside the spherical chromophore that, at large distance from the chromophore, is not affected by the reaction. Furthermore, one assumes an infinite reaction rate upon contact of RFTA and MBA. The resulting expression for the concentration of RFTA\* as a function of time can be used directly to model the TA data in dilute solutions:

$$\Delta OD(t) = \Delta OD(0) \cdot \exp \left\{ -\frac{t}{\tau_{fl}} - 10^3 N_A \cdot 4 \pi R_{int} D \cdot [MBA]_0 \cdot \left( 1 + \frac{2R_{int}}{\sqrt{\pi Dt}} \right) \cdot t \right\}. \quad (3.7)$$



Here,  $\tau_{fl}$  is the fluorescence lifetime of RFTA,  $R_{int}$  is the interaction distance of RFTA and MBA,  $D = D_{RFTA} + D_{MBA}$  is the mutual diffusion constant and  $[MBA]_0$  is the initial or bulk concentration of MBA. Mathematically, the diffusion function is of the form  $A \exp\left(-t/\tau_1 - \sqrt{t/\tau_2}\right)$  and therefore related to the stretched exponential. For the typical values of  $D = 100 \text{ \AA}^2/\text{ns}$  and  $R_{int} = 6 \text{ \AA}$ , the term  $2R_{int}/\sqrt{\pi Dt}$  becomes smaller than 1 for  $t > 0.5 \text{ ns}$ . That means that for small MBA concentrations and accordingly slow quenching dynamics in the ns regime, the TA data can be fitted in good approximation with a mono-exponential function. Then, the transient effect in the diffusion rate that is responsible for the stretched exponential behavior becomes negligible.

The diffusion model consistently describes the predominant contribution to the dynamics observed in the three major TA bands of RFTA for all MBA concentrations. However, at high quencher concentrations we find an additional fast component in the dynamics. As seen exemplarily from the dashed curve in Fig. 3.10a, the initially higher ET rate from the diffusion model alone can not account for this contribution. We therefore extended our diffusion fit function by adding a single exponential decay. As discussed in more detail in appendix A6, one can understand the fast contribution in terms of pre-associated RFTA-MBA complexes. Their reaction is not subject to diffusion control but proceeds on the ‘‘intrinsic’’ ET timescale known from the experiments of RFTA in pure MBA.

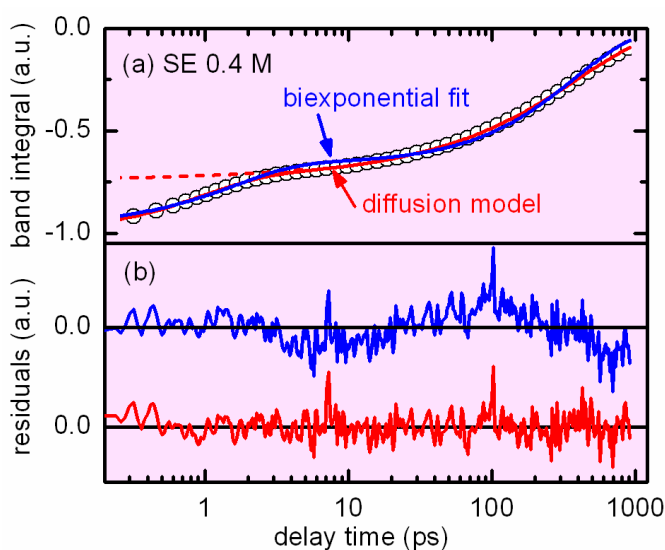


**Fig. 3.10 Fit function beyond standard rate models:**

(a) Circles: SE band integral from Fig. 3.9c at 0.4M MBA; blue line: biexponential fit; solid red line: fit according to the diffusion model described in the text; dashed line: diffusion fit function without the fast exponential contribution.

(b) The residual of the biexponential fit (blue) shows systematic deviations from the data that are not present in the residual of the diffusion fit function (red).

The resulting extended diffusion model is in very good agreement with the data (see solid lines in Fig. 3.9b-d) and yields a consistent and meaningful set of parameters. This includes the relevant microscopic quantities of the diffusion constant and the interaction distance for the ET between MBA and RFTA. In contrast, a simple biexponential fit shows systematic deviations from the data, especially at higher MBA concentrations that show dynamics in the sub-ns regime (see Fig. 3.10b). There, the transient effect in the diffusion rate is significant and causes the nonexponential behavior. Apart from the inferior agreement with the data, the simple multiexponential fit does not allow an equally detailed picture of the molecular processes as obtained from the diffusion model.

Overall, the successful modeling of all TA signatures with the extended diffusion function shows that no significant product formation occurs at high MBA concentrations above 100 mM. Instead, the initial ET reaction of MBA with  $^1\text{RFTA}^*$  is followed by rapid charge recombination. This points to a photooxidation mechanism that involves the triplet state of RFTA as an intermediate. This assumption could be validated by an evaluation of the reaction quantum yield as a function of MBA concentration using the LED-based apparatus described in section 2.2 for quantitative irradiation (see appendix A2).

In flavin compounds, the intersystem crossing is known to proceed with a time constant of 10 – 20 nanoseconds [75]. With the femtosecond TA spectrometer and a limited delay time of 1 ns, one can essentially only observe the excited singlet state of RFTA. However, the triplet spectrum can be obtained with the fs TA setup after redirecting the pump light directly from the NOPA into the sample as described in section 2.2 [46]. This results in a fixed delay time of 12 ns between pump and probe. At this delay time and in the absence of MBA, only ~10% of the initial  $S_1$  population is left and the dominant contribution arises from  $^3\text{RFTA}^*$ . For a better signal-to-noise ratio, this experiment can be performed in a sample cell with a larger optical path length than for the usual fs measurements. In the nanosecond regime, the additional dispersion which deteriorates the time resolution is not relevant. Likewise, the chirp of the probe white light of ~2 ps can be neglected and does not have to be corrected for. With the selected modifications of the fs TA setup it is possible to connect the ultrafast experiments on the singlet state dynamics of RFTA to the measurements on longer timescales that probe the reactions starting from the triplet state.

The reaction dynamics of RFTA and MBA on the nano- to microsecond timescale were monitored in a TA experiment with a Streak camera detection [48] in the group of Prof. Dick at the University of Regensburg. In the absence of MBA, the TA spectrum shows the same triplet signature as observed in the 12 ns experiment. It decays monoexponentially with a time constant of 1.3  $\mu\text{s}$  which is mostly due to the triplet quenching by oxygen in the solution. From the corresponding DADS, the absorption spectrum of  $^3\text{RFTA}^*$  in absolute values, i.e. the extinction coefficient  $\epsilon(\lambda)$ , can be obtained using the GSB signature as an internal standard. This concept is frequently used in other analytical techniques in chemistry such as gas chromatography. There, known amounts of an internal standard are added to the investigated sample to quantify absolute amounts of reaction products.

For the direct deactivation of  $^3\text{RFTA}^*$  to the ground state without side reactions, the DADS corresponds to the difference between the triplet and the ground state spectrum. The extinction spectrum of  $^3\text{RFTA}^*$  shown in Fig. 3.11b is then obtained by first scaling the negative steady state absorption spectrum (Fig. 3.11a) such that it matches the GSB signature and then subtracting it from the DADS. In the presence of MBA, the calculation of species associated spectra (SAS) from the DADS is less straightforward. It involves the solution of the multistep rate model shown on the right hand side of Fig. 3.7. Thereby, the known ground and triplet state spectra are used to determine the absolute absorption spectra of the other intermediates shown in Fig. 3.11d-e. By comparison with reference spectra from the literature shown in Fig. 3.11e-h [63], the intermediates can be unambiguously identified as the radical anion and the protonated neutral radical of flavin. This validates the reaction scheme for the photooxidation in which an initial electron transfer from MBA to RFTA is

followed by a proton transfer. Thus, the net transfer of a hydrogen atom from MBA to RFTA is a two-step process.

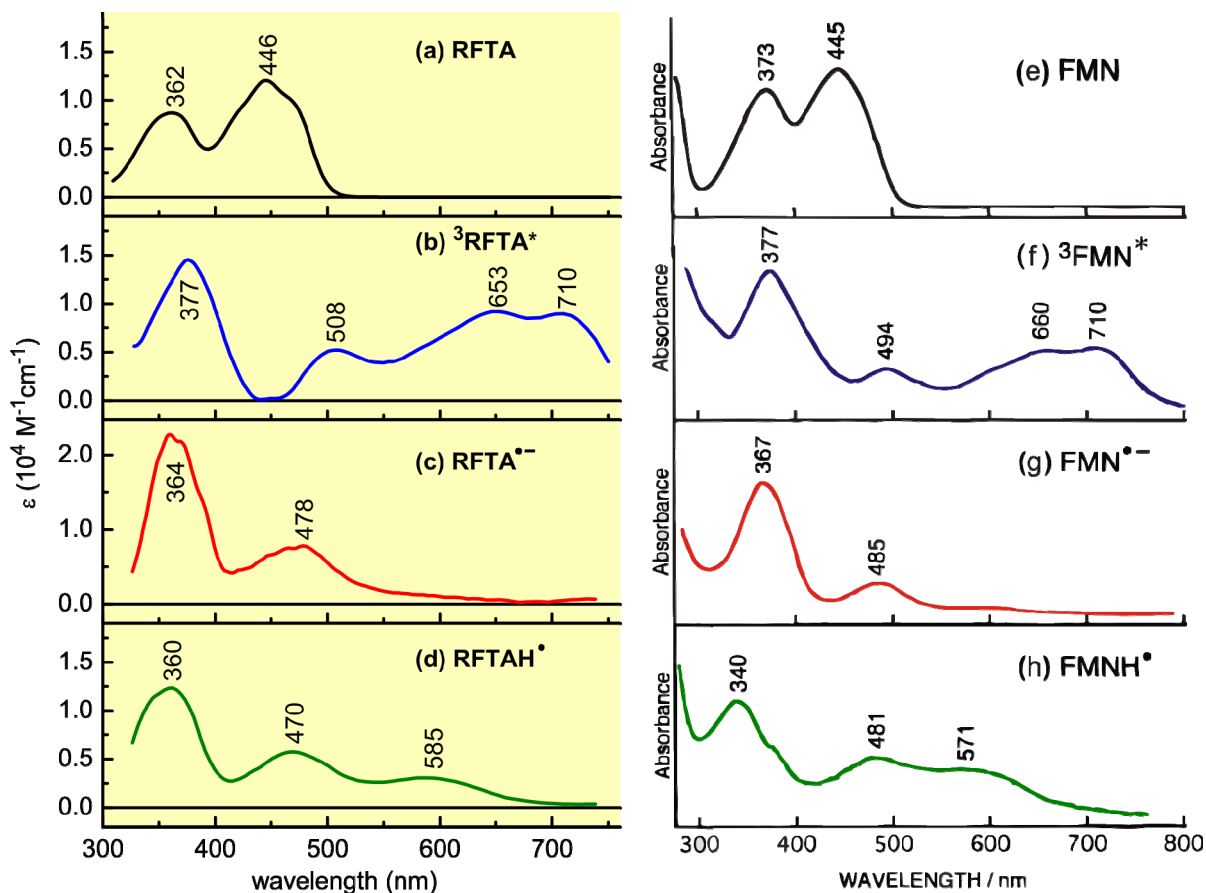


**Fig. 3.11 Identification of intermediates with reference spectra:** Steady state absorption of ground state RFTA in MeCN/H<sub>2</sub>O solution (a). Species associated spectra (SAS) of the first excited triplet state (b), the semiquinone radical anion (c) and the protonated semiquinone (d) of RFTA. The SAS are obtained from the application of the rate model shown in Fig. 3.7 to the  $\mu$ s TA data of RFTA at 0.1M MBA in MeCN/H<sub>2</sub>O solution. (e-h) Reference absorption spectra of the corresponding forms of flavin mononucleotide (FMN) in aqueous solution, reprinted from ref. [63] with permission from Elsevier.

The example of RFTA shows why the calculation of absolute extinction spectra from the rate model analysis is preferred to the qualitative description of spectral signatures such as the position of local maxima. As seen for instance from Fig. 3.11, all intermediate states of flavin have a local absorption maximum around 370 nm. Due to possible spectral shifts from solvation or slightly different substitution, the wavelength at which the maximum is observed might be subject to changes. However, the absolute evaluation shows that the extinction coefficient differs partly by a factor of two. Even though this aspect is often neglected when comparing molecular spectra, it can offer valuable information that helps to distinguish between species with qualitatively similar absorption spectra. This of course requires the report of species spectra on an absolute scale instead of simple  $\Delta$ OD or even arbitrary units scales which is often found in the literature.



### 3.5 Anisotropy, temperature and absolute quantum yields:

#### additional concepts used in related studies

So far, all the presented TA data were measured in a magic angle configuration, i.e. with the pump polarization rotated by  $54.7^\circ$  compared to the horizontally polarized probe light. Under this condition, the transient absorption changes comprise only the pure population dynamics [74, 76]. This rules out orientational effects on the signal that arise from the rotation of the excited chromophores in solution or from changes in the direction of the transition dipole moments. In some cases, however, a polarization sensitive study can provide valuable insights into the molecular processes. A recent example studied in our lab by Igor Pugliesi is the Förster resonant energy transfer (FRET) in an orthogonally arranged perylene diimide dyad (see Fig. 3.12) [77].

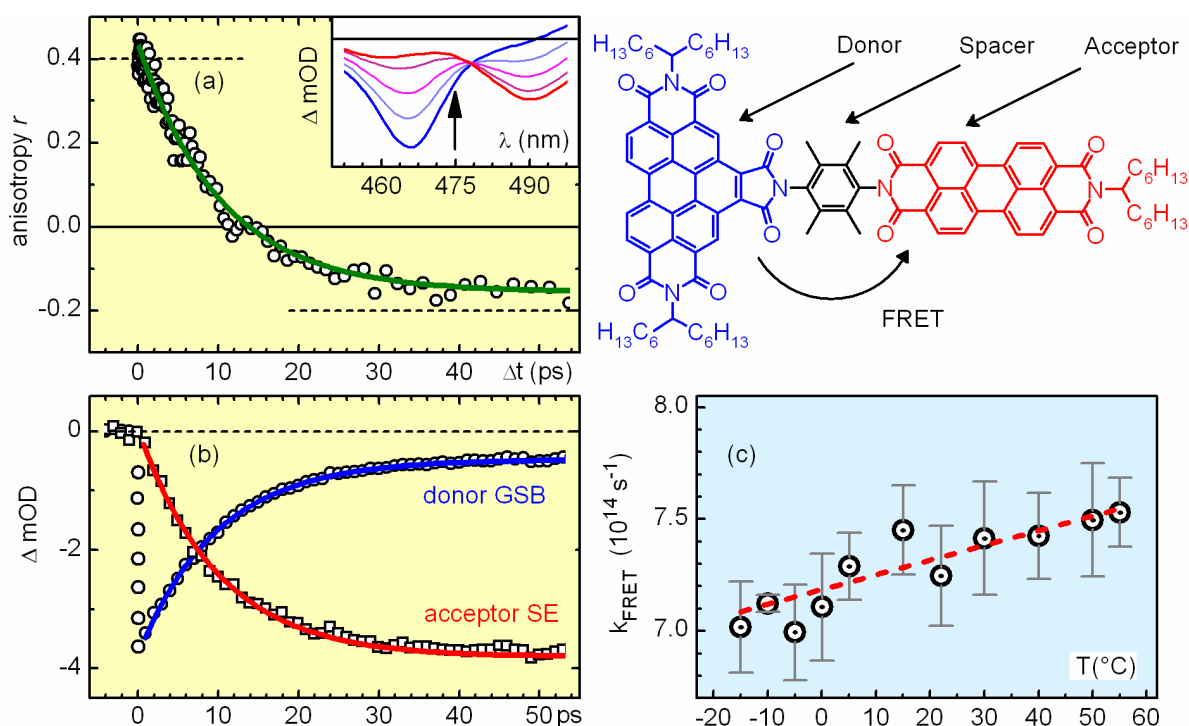


**Fig. 3.12 Anisotropy and temperature effects:** (a) Evolution of the anisotropy (circles) after selective excitation of the donor moiety of the depicted perylene diimide dyad in chloroform.  $r(t)$  was calculated from the TA dynamics at 475 nm near the isosbestic point (inset) and fitted with a monoexponential model (green line,  $\tau = 9$  ps). (b) The same 9 ps dynamics is found in the TA changes (symbols) measured under magic angle polarization in the spectral region of the donor GSB (blue) and the acceptor SE (red) (c) Linear dependence of the FRET rate in toluene on the temperature of the solution. Data from [77].

To obtain orientational information, two TA data sets are measured, one with parallel ( $\Delta OD_{\parallel}$ ) and one with perpendicular ( $\Delta OD_{\perp}$ ) pump and probe polarizations under otherwise identical conditions. From this, one can calculate the anisotropy  $r(t)$  of the excited sample that has been introduced by the linearly polarized pump:

$$r(t) = \frac{\Delta OD_{\parallel} - \Delta OD_{\perp}}{\Delta OD_{\text{total}}} = \frac{\Delta OD_{\parallel} - \Delta OD_{\perp}}{\Delta OD_{\parallel} + 2\Delta OD_{\perp}}. \quad (3.8)$$

Due to the Brownian motion of the molecules in solution, the anisotropy decays to 0 for  $\Delta t \rightarrow \infty$ . In previous experiments it was shown that the rotational diffusion proceeds on the timescale of several hundreds of ps for similar perylene diimide dyes [78]. For the dyad however, a much faster change of the anisotropy is observed (Fig. 3.12a). With a time constant of 9 ps, the anisotropy changes from +0.4 to about -0.2. It can be shown that these are the limiting values for parallel (+0.4) and orthogonal (-0.2) orientation of the pumped and probed transition dipole moments [74]. Thus, the excitation is transferred from the initially excited donor moiety to the orthogonally arranged acceptor moiety. This is confirmed by the population dynamics shown in Fig. 3.12b that is recorded under magic angle configuration. With the same 9 ps time constant found for the anisotropy decay, the GSB of the donor disappears and the SE of the acceptor arises.

In the basic FRET theory, the rate for an energy transfer between orthogonal transition dipole moments is negligible which would result in an efficient suppression of FRET for the perylene diimide dyad. An alternative explanation for the fast energy transfer could be a Dexter-type mechanism, but this was clearly ruled out by the analysis of dyads with longer spacers that also showed efficient energy transfers [77]. It was therefore rationalized that thermally activated low-frequency vibrations of the dyad temporarily distort the perfect orthogonality between donor and acceptor. Together with the close distance between the two subunits, this would allow for an efficient FRET.

This assumption can be proved by performing experiments at different temperatures. The sample circuit used in our TA setup can be connected to an external thermostat that controls the temperature of the sample reservoir, the pump and the flow cell [79]. With this setup, the energy transfer rate of the perylene diimide dyad was determined in the range between -15 and +55 °C using toluene as solvent (melting point -93 °C). The experimentally significant linear increase of the rate demonstrates the activity of a FRET mechanism that is enabled by vibrational distortions of the orthogonal equilibrium conformation.

The active control of the sample temperature is also a critical issue for experiments with biological samples such as DNA strands. An example for this is our study on the photooxidation and charge movement in flavin-capped DNA hairpins that is summarized in the following publication (appendix A7):

**Flavin-induced DNA Photooxidation and Charge Movement Probed by Ultrafast Transient Absorption Spectroscopy**

*M. Wenninger, D. Fazio, U. Megerle, C. Trindler, S. Schiesser, E. Riedle, T. Carell*  
ChemBioChem 12, 703-706 (2011).

In the time resolved experiments, the temperature was kept constant at 10 °C which is well below the melting point of the double helix and assures a well defined geometry of the sample molecules. This is an essential prerequisite for the quantitative comparison of the photo-induced charge transfer processes in DNA hairpins with different base sequences.

The structures of the hairpins used for this study are shown in Fig. 3.13. After excitation, the flavin cap oxidizes the close lying DNA bases on the timescale of several tens of picoseconds. Thereby, an electron is transferred to the flavin from the bases with the lowest oxidation potential, i.e. from a guanine (dG) or less effectively from an adenine (dA). For most of the studied hairpins, the charge recombination is found to be faster than the initial charge separation. However, if one or more (dG:dC) pairs are placed three base pairs away from the flavin, the injected positive charge can hop out of the Coulomb field of the flavin radical anion and a significant fraction of long-lived charge separated states is observed.

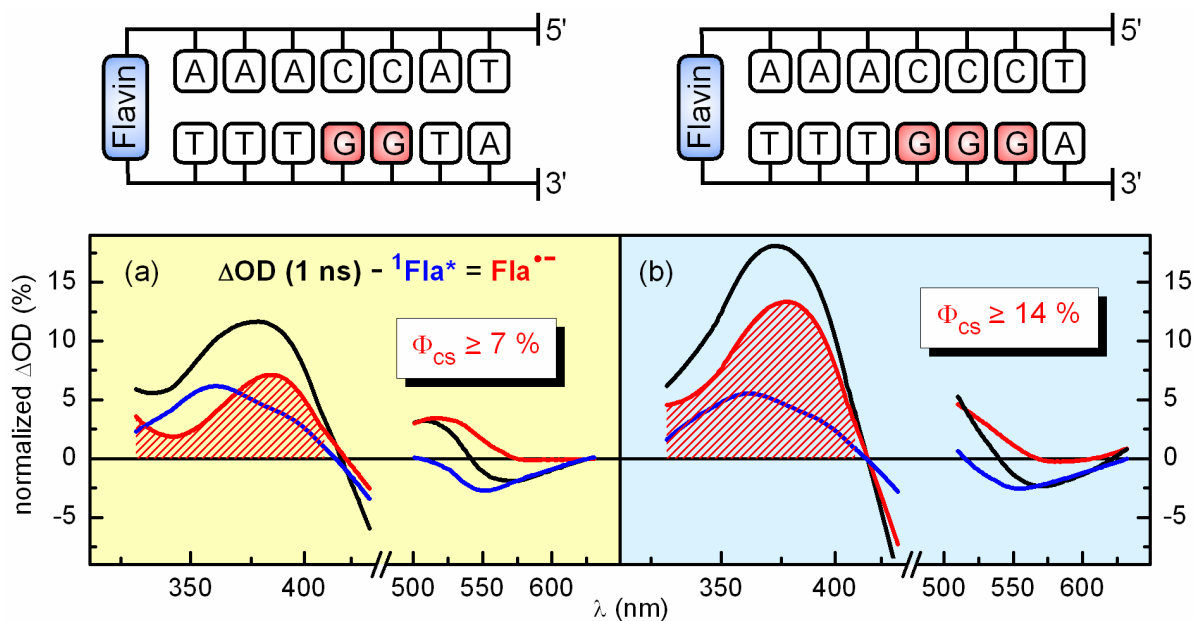


**Fig. 3.13 Absolute quantum yield from internal standard:** Decomposition of the TA spectrum at  $\Delta t = 1$  ns (black line) obtained from a flavin-capped DNA hairpin with a double-(dG:dC)-sequence **(a)** and a triple-(dG:dC)-sequence **(b)** after excitation at 480 nm in buffer solution. The residual contribution from the  $S_1$  state of flavin (blue line) is subtracted to obtain the contribution from the long-lived radical anion of flavin (red line). The quantum yield of charge separation is calculated from the band integrals (shaded area).

The absolute quantum yield of long-lived radical pairs can be calculated from the integral over the TA signal of flavin between 330 and 410 nm. In this spectral region, the transition from the  $S_1$  state to the radical anion of flavin causes a spectral shift of  $\sim 15$  nm, but almost no loss in oscillator strength, in analogy to the situation of RFTA dissolved in pure MBA described in the previous section (see Fig. 3.8). At the maximum delay time of 1 ns, the TA signal still comprises a residual contribution from flavin in the  $S_1$  state as seen from the negative amplitude in the SE region around 550 nm. The negative SE signature together with the redshift of the UV absorption band can be used to identify the fraction of the  $S_1$  contribution (blue line in Fig. 3.13) in the 1 ns TA spectrum (black line). The integrated area under the difference spectrum (red shaded area) corresponds to the sought for long-lived radical anion contribution (red line). The quantum yield of long-lived charge separated states follows directly from the relation of this integral to that obtained immediately after photoexcita-

tion. With this quantitative evaluation method it could be shown that charge trapping is increasing in efficiency from a single over a double to a triple (dG:dC) sequence.

In the absence of internal standards, the calculation of reaction quantum yields relies on the precise determination of the excitation conditions. If the extinction coefficients  $\epsilon_{\text{prod}}$  of the photoproducts are known and their signatures are sufficiently well separated from other signals, the quantum yield  $\Phi(t)$  for a specific product channel can be calculated from the TA changes  $\Delta\text{OD}(t)$  at the corresponding wavelength:

$$\Phi(t) = \frac{c_{\text{prod}}(t)}{c_{\text{exc}}} = \frac{\Delta\text{OD}(t)/\epsilon_{\text{prod}}d}{c_0 \cdot P_{\text{exc}}}. \quad (3.9)$$

Here,  $c_{\text{prod}}(t)$  is the product concentration at delay time  $t$  and  $d$  is the sample thickness. The concentration of initially excited molecules  $c_{\text{exc}}$  is the product between the bulk sample concentration  $c_0$  and the excitation probability  $P_{\text{exc}}$ . The latter is given by the photon density in the focus multiplied by the absorption cross section  $\sigma$  of the sample molecules:

$$P_{\text{exc}} = n_{\text{ph}} \cdot \sigma = \frac{E_{\text{pump}}}{(hc/\lambda) \cdot \pi(D/2)^2} \cdot \epsilon_0 \frac{\ln 10}{N_A}. \quad (3.10)$$

For a sample with an extinction coefficient  $\epsilon_0$  at the excitation wavelength  $\lambda$ ,  $P_{\text{exc}}$  depends on the pump energy  $E_{\text{pump}}$  and the focal diameter  $D$ . Therefore, the calculation of quantum yields requires a nearly symmetric beam profile in the focal plane and a precise determination of its size.

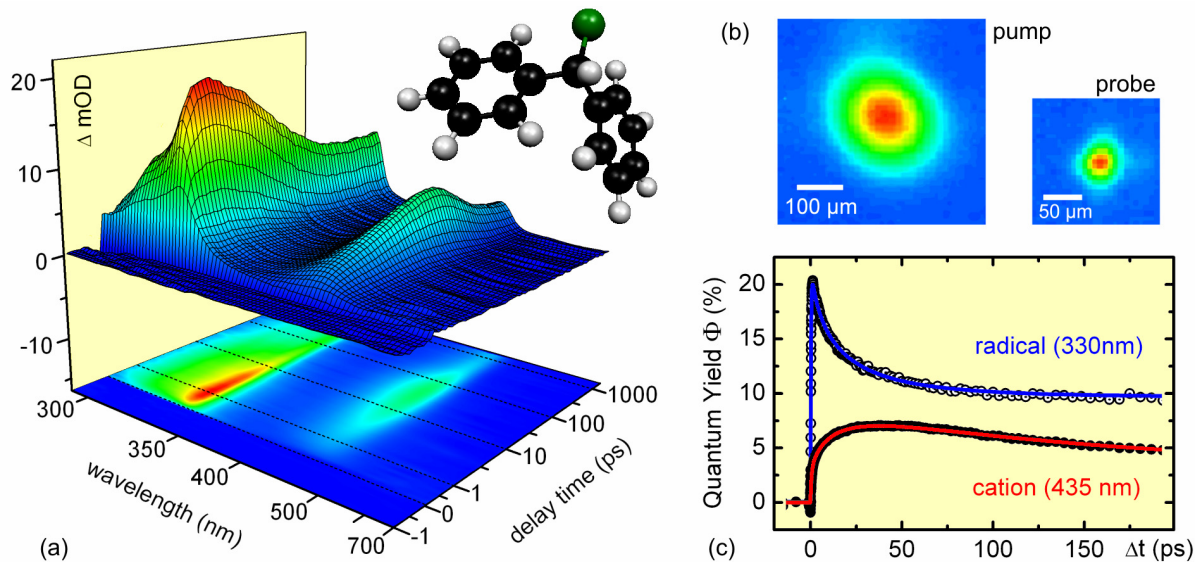


**Fig. 3.14 Quantum yield from excitation conditions:** (a) TA spectra of diphenylmethyl chloride (inset) in acetonitrile. The excitation at 270 nm leads to photodissociation and the formation of radical pairs (330 nm) and ion pairs (435 nm). (b) Typical beam profiles of pump and probe pulses. (c) The absorption changes in the band maxima can be converted to time dependent quantum yields for the two reaction channels by normalization to the number of initially excited molecules. Data from [80].



The photodissociation of diphenylmethyl chloride currently studied by C. Sailer [80] in the framework of his thesis is an example that demonstrates the application of the above mentioned method (see Fig. 3.14). In this case, the absorption of the starting material lies outside the detection range in the UV. On the one hand, this impedes the calculation of quantum yields using the GSB as an internal standard as for the flavin-capped DNA hairpins. On the other hand, it avoids the need for spectral decomposition to obtain the product signatures, especially since the contributions from ESA and SE to the TA spectra are also negligible. Furthermore, the absorption maxima of the two relevant photoproducts, the diphenylmethyl radical and the benzhydrylium cation, are separated by more than 100 nm (see Fig. 3.14a) and their extinction coefficients are precisely known [81]. With the near Gaussian beam profiles typically achieved with our setup (Fig. 3.14b), the calculation of absolute product quantum yields from the TA data is straightforward (Fig. 3.14c).

The concepts described in this section emphasize the fact that TA studies can provide much more information than just the report of exponential decay times. In particular, the interpretation of the TA spectra of DPMC involves many of the analytic methods described in this thesis. Besides the determination of quantum yields, this includes the evaluation of temperature effects, the comparison of systematically varied molecules and solvents, the analysis of band shifts as small as 5 nm, the use of stretched exponential functions to describe an electron transfer between diffusing particles and last but not least the incorporation of theoretical models from quantum chemical calculations. The coalescence of all this information results in very detailed insights into the photodissociation process of DPMC and the subsequent reactions with alcohols that belong to the fastest observed bimolecular reactions in chemistry [80].



## 4. Conclusion and outlook

In this thesis, a comprehensive discussion of methodical concepts has been presented that are used for the interpretation of broadband transient absorption data. On the basis of prototypical molecular systems, various ultrafast intra- and intermolecular processes have been covered and their identification from the observed optical signals has been traced. The presented methods build on the newly designed femtosecond TA spectrometer with an ultrabroad probing range between 290 and 750 nm and a multichannel detection at the kHz repetition rate of the laser system. The investigated molecular systems involve complex, multistep reaction mechanisms on multiple timescales. The key elements are the relation between photoinduced charge transfer events and molecular conformations as well as the interplay of these intramolecular processes with the surrounding solvent molecules. For intermolecular reactions, the decisive role of the intricate diffusion dynamics on the reaction process has been shown by the quantitative modeling of the diffusive approach of the reaction partners. Thereby, the studies of molecular dynamics have both profited from and boosted the ongoing development of the experimental methods.

### Instrumental and interpretational methods

The simultaneous recording of the induced absorption changes throughout the whole spectral range of the CaF<sub>2</sub> supercontinuum required the development and implementation of new experimental components as well as data acquisition and post processing software. The desired high sensitivity and good spectral resolution is best achieved with a home-built prism based polychromator. While showing a higher transmission over the whole spectral range, prisms avoid the order sorting problem of gratings and in addition offer a more balanced spectral resolution that does not decrease quadratically towards the UV. Under realistic experimental conditions, an average sensitivity better than 10<sup>-4</sup> OD and a spectral resolution below 100 cm<sup>-1</sup>, i.e. much below the typical band width around 2000 cm<sup>-1</sup>, could be demonstrated. A decisive factor for this is the high dynamic range of the chosen multichannel sensors of effectively more than 1000:1 combined with their low shot noise limit that falls significantly below the laser excess noise.

The overall time resolution of sub-50 fs is achieved by the use of low dispersion sample cells that reduce deteriorations due to the group velocity mismatch and the coherent artifact at time zero. To exploit this time resolution for global modeling procedures, the 1.5 ps chirp of the white light is corrected for during the data post processing. Furthermore, the suite of programs developed for the data processing contains a wavelength calibration, an optional stray light subtraction and several visualization tools to inspect the raw data and compare the results of different scans individually before averaging.

The final set of processed TA spectra can be analyzed in various ways as shown in this thesis for a number of molecular systems. The specific choice out of the pool of conceptual methods depends on the investigated sample and for each new system certain adaptations will be needed. Still, a general strategy for the interpretation of TA spectra can be extracted:

- Collect as good information as possible from external sources, e.g. from literature, *ab initio* calculations, steady state absorption and emission spectroscopy or complementary experiments of collaboration partners.
- Use the prior knowledge of the investigated system to establish a hypothesis for the molecular processes initiated by the photoexcitation.
- Derive from this provisional model what species should be observed in the optical signal – especially at the extreme delay times, i.e. directly after excitation and towards the end of the accessible time range. Qualitatively compare the corresponding TA signatures to available reference spectra of the expected species.
- Apply quantitative visualization methods such as the logarithmic differentiation of the absorption changes (LDAC) or exponential fits at distinguished spectral positions to get an estimate on the relevant timescales for the dynamics.
- Select a functional model to simulate the temporal evolution of the species populations and convolute it with the spectral information to reproduce the TA measurements. Identify the number of intermediates and consider possible band shifts or narrowing due to solvation or vibrational cooling.
- If the model comes close to the observations, the free parameters such as time constants can be found in a least-square fit to the data. Depending on the complexity of the photochemical reaction, this can include one or several of the developed software modules, e.g. the global fit, spectral decompositions, single channel fit of state populations or anisotropy decays, fit of band shifts or the analysis of band integrals.
- Check the consistency of your quantitative model by comparison to related systems reported by others and to your own reference measurements, e.g. in solvents of different polarity or solvation timescales, at different temperatures or with systematically modified sample molecules.

New challenges within this general strategy may be faced when examining for instance larger biomolecules or intermolecular processes with several reaction partners. This can be accompanied by the need for higher precision to resolve small effects. In this context it will be helpful to routinely generate and visually inspect false color 2D residual maps during each global fit procedure rather than just compare the agreement between data and fit in single spectral or temporal traces. In a 2D plot of the residuals, disregarded but significant contributions should appear more clearly as areas of systematic deviations from zero. Even if an unbiased fit algorithm fails to resolve these components, the restriction to that specific spectral or temporal range and a narrowed parameter space might allow for a quantitative evaluation.

At some stage, qualitatively new analytical techniques for the interpretation may be required. For example, an unsolved problem so far is the implementation of spectral shifts into the global fit algorithm, even though the two effects of shifting and decaying signals can perfectly be treated independently. In its current version, the global fit procedure is based on the separation of time and wavelength properties which is no longer applicable if the species associated spectra become time dependent.

The difficulty can be overcome with the use of spectrotemporal models [51]. There, both the state populations and the corresponding spectra are described by a model that depends on

a set of parameters, e.g. decay times, spectral positions of band maxima or band widths. Ideally, the set of parameters can be limited significantly using a priori knowledge such as the number of intermediate states or the spectral shape of the ground state bleach. The best fit to the data is then found from random parameter sets in an evolutionary learning loop based on the least square criterion [82, 83]. This combination of global analysis with testing of a specific photophysical or photochemical model is often referred to as target analysis [51].

In addition to further developments of the processing software, several technological improvements of the TA spectrometer are also envisaged and partially already implemented. Recently, a second probe beam path has been installed in one of the spectrometers that extends the accessible probing range further into the near IR. In a first version, a second CaF<sub>2</sub> supercontinuum is generated with the 1200 nm output of an optical parametric amplifier. The emerging white light between 400 and 1100 nm is then dispersed in a second prism based polychromator and detected with a second multichannel camera. Due to the overlap of the two CaF<sub>2</sub> spectra between 400 and 700 nm, continuous TA spectra can be obtained in the ultrabroad probing range from 290 to 1100 nm.

In a second step, even these limits can be overcome and the proof of principle has already been made [84]. To reach longer wavelengths, the white light is pumped at 1700 nm and an InGaAs sensor array will be used instead of the silicon based detector. For the accessible probe range between 900 and 1600 nm, the CaF<sub>2</sub> crystal can then be replaced by a YAG or sapphire plate which can be used without the need for translation. On the short wavelength side, first experiments have shown that a CaF<sub>2</sub> continuum ranging to below 250 nm can be generated using the second harmonic of the Ti:sapphire laser at 387 nm as pump. Thus, a continuous probing range of more than 4 eV or 34,000 cm<sup>-1</sup> seems within reach.

The desired extension of the detection window also comprises the temporal dimension. As shown exemplarily for the photooxidation reaction of flavin with benzylic alcohol (section 3.4), many relevant photochemical processes show extensive dynamics in the nano- to microsecond regime. It is therefore planned to use the established detection scheme of the femtosecond setup in combination with a tunable nanosecond laser system for excitation. By electronically delaying the trigger of the nanosecond laser with respect to the femtosecond probe pulse, it should be possible to record TA spectra between a few nanoseconds and 1 ms delay.

This approach offers several advantages over competing concepts such as laser flash photolysis. There, the probe light is either obtained from a classical light source for broad spectral coverage, e.g. from a Xe flash lamp, or from continuous wave lasers which allow the discrimination of unwanted fluorescence signals by reducing the solid angle used for the detection. The femtosecond white light combines both these properties by being spectrally ultrabroad and still laser-like in terms of the divergence. Moreover, leaving the detection scheme unchanged between the experiments on the ultrafast and on the slower timescale yields a much better comparability of the obtained TA spectra.

Last but not least, attempts are being made to further increase the detection sensitivity of the TA spectrometer. One possibility is to abandon the consecutive referencing with one detector for single-shot referencing using two detectors. Therefore, a fraction of the probe light has to be split off before the sample cell, dispersed in a second polychromator and

monitored with a reference detector array. This could improve the signal to noise ratio by at least a factor of three [85], however at the cost of a significantly higher complexity. Due to spatial constraints, the implementation of a reference arm presently excludes the extensions of the spectral coverage mentioned above. It might therefore be more rewarding to try to track down the origin of systematic deviations of the baseline spectrum that appear as pseudo-bands within the confidence interval. The noise around this band structure, i.e. for neighboring pixels at one delay time, is typically 2-3 times smaller than the noise for one pixel at different delay times. Hence, the sensitivity of the measurement could be definitely increased if a way was found to either avoid these band structures or to reliably correct for them in the data processing.

### Dynamics of molecular systems

The TA spectrometers developed in the framework of this thesis represent the state of the art for the study of ultrafast photochemical processes. Even during the development, they could already be applied for a sizeable series of prototypical molecular systems. As a matter of fact, the use of the spectrometers has had a great impact on their development. In a class of naphthalene diimide dyes we investigated the influence of core substituents on the electronic relaxation of the NDIs due to CT processes. For the two compounds with arylamino donor groups attached to the naphthalene core we found an excited state charge separation within 3 ps that is rather insensitive to the second substituent opposite the donor moiety. However, by exchanging the chloro substituent in Cl-NDI-NAr with an alkylamino group, a sixfold slower charge recombination is observed leading to an excited state lifetime of 70 ps in N-NDI-NAr. The variation of the dynamics is a consequence of the increased energy gap as proven by *ab initio* calculations. In previous studies [57] it was shown that introducing a methylene spacer between the linker atom and the electron donor changes the coupling of the optically excited with the charge separated state of NDIs, which significantly slows down the corresponding electron transfer. This indicates that the coupling and the energy gap represent two handles of the system that allow tuning the intramolecular charge separation and recombination process more or less independently from each other.

With a second class of donor-substituted organic chromophores we shifted the focus towards intermolecular processes and studied the symmetry-dependent solvation of triarylboranes. When we compared the single carbazole-substituted triarylborane CB with its highly symmetric triple carbazole-substituted counterpart TCB, we found an accelerated solvation of the latter in all polar environments. The average solvation rates increase by 20–90% depending on the solvent. To rationalize these findings we propose that the electronic excitation in TCB is mobile and can hop between the three subchromophores arranged at 120°. By means of this intramolecular charge redistribution, the excited state dipole moment can respond to the external field of the solvation shell. This leads to a faster energy relaxation compared to the model compound CB with only one active site. In general, this study is an example for the significant dependence of the solvation dynamics on the solute and demonstrates how the availability of several identical active sites in a symmetric molecule can be used to stabilize excited states faster and more efficiently.

The possible extent of the interplay between intramolecular electron transfer and the intermolecular solvation process was observed in the transient absorption study on crystal violet lactone. We found that the solvent polarity dynamically determines the energetics of the two relevant CT states and thereby controls the availability of the various deactivation pathways. The CT state with higher polarity can only be populated if its energy is sufficiently lowered by the solvation of the initially excited CT state. Thus, the intramolecular electron transfer is controlled not only by the dynamics of the solvation, but also by the amount of stabilization achieved on a certain timescale. The experimental findings for CVL highlight that the choice of the surrounding medium constitutes an additional parameter for the active tuning of charge separation and recombination processes, complementary to the above examples of selective substitution and the addition of several active sites.

The lifetime of charge separated states is also at the heart of the two studies on flavin photochemistry. With a flavin derivative incorporated into a DNA hairpin, we observed the sequence dependent formation of long-lived intramolecular CT states. Thereby, the excited flavin acts as electron acceptor and the close lying DNA bases, most prominently the dG:dC base pairs, act as electron donors. In the presence of multiple dG:dC base pairs at sufficient distance from the flavin, the injected hole on a DNA base near the flavin can be withdrawn from the Coulomb field of the flavin radical anion, probably by a hopping mechanism over neighboring base pairs, which impedes the fast charge recombination. This results in the formation of CT states with lifetimes exceeding one nanosecond and quantum yields up to 14 %, depending on the size of the (dG:dC)<sub>n</sub> cassette that stabilizes the dG<sup>•+</sup> state.

The spatial separation of opposite charges using multiple donor or acceptor sites might also improve the efficiency of intermolecular photoreactions such as the flavin-catalyzed oxidation of benzylic alcohol to the corresponding aldehyde. If by aggregation or early diffusive approach the flavin and the alcohol establish contact before the excited flavin can undergo intersystem crossing, the observed electron transfer is unproductive due to a fast charge recombination within 50 ps. In sufficiently dilute solution, more time is needed for a diffusional encounter of the reactants and the productive dynamics proceeds on the nano- to microsecond timescale via the triplet state of flavin. Here, the charge recombination is spin-forbidden and five to six orders of magnitude slower than for the singlet state of the spin-correlated radical ion pair. This allows for a higher efficiency of the successive proton and hydrogen transfer steps. The complex reaction scheme results in low quantum yields of the photoreaction for both too high and too low substrate concentrations, whereas an optimum efficiency of 3 % is found at 25 mM of benzylic alcohol. The prediction of this non-trivial concentration dependence of the reaction efficiency was made possible by the observation and quantitative modeling of the complex diffusion dynamics under selected experimental conditions.

From a global perspective, even the quantum yield at optimized substrate concentrations leaves much room for improvement. As mentioned above, one promising way that is also followed by natural enzymes [86] might be to use multiple redox centers for an efficient and stable charge separation in the singlet state. For the photooxidation of benzylic alcohol, much higher efficiencies were found in experiments using flavin–zinc(II)–cyclen complexes as catalysts containing a substrate binding site [87]. However, in the light of the results pre-

sented here that close proximity of the reactants is counterproductive, it will be interesting to analyze the reaction mechanism of the extended catalyst with TA spectroscopy. This should clarify whether the zinc(II)-cyclen does not rather act as an intermediary redox centre that mediates the electron transfer between the alcohol and the flavin. In related systems, the substrate binding itself will be of increased importance, for instance if a defined geometric orientation of the reactants is needed to reach a high enantioselectivity of the photocatalytic reaction [88]. In such systems which are already being examined in our lab, the mechanistic insights gained from TA spectroscopy can also be very helpful for the targeted design of improved catalysts.

In general, most of the molecular systems mentioned above can be regarded as examples of functional organic materials. Other prominent representatives of this class of molecules are for instance molecular motors, switches and electronics as well as three dimensional  $\pi$ -systems such as carbon nanotubes or fullerenes [89]. Many of them have already been studied with ultrafast time-resolved spectroscopy demonstrating the significance of dynamic effects in the area of novel technological applications. The improved experimental capabilities and methodical approaches presented in this thesis should render further progress in the understanding of the key mechanisms.

Considering the commercial success of organic functional materials, for instance in displays based on organic light emitting diodes (OLEDs), it is highly probable that artificially synthesized molecules with strong potential for applications will constitute a large fraction of the systems investigated in the future with our setups and related ones in other groups. However, from the point of view of fundamental research, it is at least as rewarding to study photoinduced processes directly in biological macromolecules such as the light-driven DNA repair enzymes called photolyases. Their working principle is based on electron transfer cascades through the protein and onto the damaged DNA that are initiated by the absorption of a photon in the flavin cofactor of the enzyme [90]. Thus, they are closely related to the flavin-based studies presented in this thesis. Transient absorption spectroscopy has proven to be capable of resolving the individual intermediates even in such complex systems [91]. With the technological improvements in terms of detection sensitivity, temporal and spectral probing range, multiplex data acquisition and last but not least data analysis software, the scope of accessible biomolecules is dramatically widened. This unique opportunity can be used to reach a deeper insight into the detailed reaction mechanisms of natural light harvesting systems that will certainly be beneficial for the future design of green technologies exploiting the potential of visible light.



## References

- [1] J. MacLachlan, *Galileo Galilei: First Physicist*, Oxford University Press, Oxford, USA, **1999**.
- [2] T. H. Maiman, *Nature* **1960**, *187*, 493-494.
- [3] A. H. Zewail, *J. Phys. Chem. A* **2000**, *104*, 5660-5694.
- [4] S. Koke, C. Grebing, H. Frei, A. Anderson, A. Assion, G. Steinmeyer, *Nature Phot.* **2010**, *4*, 462-465.
- [5] F. D. Lewis, T. F. Wu, Y. F. Zhang, R. L. Letsinger, S. R. Greenfield, M. R. Wasielewski, *Science* **1997**, *277*, 673-676.
- [6] J. Dobler, W. Zinth, W. Kaiser, D. Oesterhelt, *Chem. Phys. Lett.* **1988**, *144*, 215-220.
- [7] R. W. Schoenlein, L. A. Peteanu, R. A. Mathies, C. V. Shank, *Science* **1991**, *254*, 412-415.
- [8] R. Vangronnelle, J. P. Dekker, T. Gillbro, V. Sundstrom, *Biochim. Biophys. Acta* **1994**, *1187*, 1-65.
- [9] C. J. Brabec, N. S. Sariciftci, J. C. Hummelen, *Adv. Funct. Mat.* **2001**, *11*, 15-26.
- [10] P. F. Barbara, T. J. Meyer, M. A. Ratner, *J. Phys. Chem.* **1996**, *100*, 13148-13168.
- [11] F. D. Lewis, R. L. Letsinger, M. R. Wasielewski, *Acc. Chem. Res.* **2001**, *34*, 159-170.
- [12] Y. A. Berlin, A. L. Burin, M. A. Ratner, *Superlatt. Microstruct.* **2000**, *28*, 241-252.
- [13] S. O. Kelley, J. K. Barton, *Science* **1999**, *283*, 375-381.
- [14] R. G. W. Norrish, G. Porter, *Nature* **1949**, *164*, 658-658.
- [15] G. Porter, *Proc. Roy. Soc. Lond. Ser. A* **1950**, *200*, 284.
- [16] T. Wilhelm, J. Piel, E. Riedle, *Opt. Lett.* **1997**, *22*, 1494-1496.
- [17] E. Riedle, M. Beutter, S. Lochbrunner, J. Piel, S. Schenkl, S. Sporlein, W. Zinth, *Appl. Phys. B* **2000**, *71*, 457-465.
- [18] A. Baltuska, T. Kobayashi, *Appl. Phys. B* **2002**, *75*, 427-443.
- [19] G. Cerullo, S. De Silvestri, *Rev. Sci. Instr.* **2003**, *74*, 1-18.
- [20] P. Baum, S. Lochbrunner, E. Riedle, *Appl. Phys. B* **2004**, *79*, 1027-1032.
- [21] P. Baum, M. Breuer, E. Riedle, G. Steinmeyer, *Opt. Lett.* **2006**, *31*, 2220-2222.
- [22] C. Schrieffer, S. Lochbrunner, E. Riedle, D. J. Nesbitt, *Rev. Sci. Instr.* **2008**, *79*, 13107.
- [23] G. Buntinx, R. Naskrecki, O. Poizat, *J. Phys. Chem.* **1996**, *100*, 19380-19388.
- [24] N. P. Ernsting, S. A. Kovalenko, T. Senyushkina, J. Saam, V. Farztdinov, *J. Phys. Chem. A* **2001**, *105*, 3443-3453.
- [25] R. Huber, H. Satzger, W. Zinth, J. Wachtveitl, *Opt. Commun.* **2001**, *194*, 443-448.
- [26] P. Tzankov, I. Buchvarov, T. Fiebig, *Opt. Commun.* **2002**, *203*, 107-113.

- 
- [27] C. Nagura, A. Suda, H. Kawano, M. Obara, K. Midorikawa, *Appl. Opt.* **2002**, *41*, 3735-3742.
- [28] R. R. Alfano, *The supercontinuum laser source*, Springer, Berlin, **2005**.
- [29] J. B. Ashcom, R. R. Gattass, C. B. Schaffer, E. Mazur, *J. Opt. Soc. Am. B* **2006**, *23*, 2317-2322.
- [30] S. Laimgruber, H. Schachenmayr, B. Schmidt, W. Zinth, P. Gilch, *Appl. Phys. B* **2006**, *85*, 557-564.
- [31] I. Buchvarov, A. Trifonov, T. Fiebig, *Opt. Lett.* **2007**, *32*, 1539-1541.
- [32] V. Kartazhev, R. R. Alfano, *Opt. Commun.* **2008**, *281*, 463-468.
- [33] R. S. S. Kumar, K. L. N. Deepak, D. N. Rao, *Phys. Rev. A* **2008**, *78*, 43818.
- [34] K. Ekvall, P. van der Meulen, C. Dhollande, L. E. Berg, S. Pommeret, R. Naskrecki, J. C. Mialocq, *J. Appl. Phys.* **2000**, *87*, 2340-2352.
- [35] M. Ziolk, M. Lorenc, R. Naskrecki, *Appl. Phys. B* **2001**, *72*, 843-847.
- [36] M. Lorenc, M. Ziolk, R. Naskrecki, J. Karolczak, J. Kubicki, A. Maciejewski, *Appl. Phys. B* **2002**, *74*, 19-27.
- [37] I. Z. Kozma, P. Krok, E. Riedle, *J. Opt. Soc. Am. B* **2005**, *22*, 1479-1485.
- [38] S. A. Kovalenko, N. P. Ernsting, J. Ruthmann, *Chem. Phys. Lett.* **1996**, *258*, 445-454.
- [39] V. I. Klimov, D. W. McBranch, *Opt. Lett.* **1998**, *23*, 277-279.
- [40] A. Maciejewski, R. Naskrecki, M. Lorenc, M. Ziolk, J. Karolczak, J. Kubicki, M. Matysiak, M. Szymanski, *J. Mol. Struct.* **2000**, *555*, 1-13.
- [41] M. Raytchev, E. Pandurski, I. Buchvarov, C. Modrakowski, T. Fiebig, *J. Phys. Chem. A* **2003**, *107*, 4592-4600.
- [42] M. Chachisvilis, H. Fidler, V. Sundstrom, *Chem. Phys. Lett.* **1995**, *234*, 141-150.
- [43] M. Rasmusson, A. N. Tarnovsky, E. Akesson, V. Sundstrom, *Chem. Phys. Lett.* **2001**, *335*, 201-208.
- [44] S. A. Kovalenko, A. L. Dobryakov, J. Ruthmann, N. P. Ernsting, *Phys. Rev. A* **1999**, *59*, 2369-2384.
- [45] J. Svoboda, H. Schmaderer, B. König, *Chem. Euro. J.* **2008**, *14*, 1854-1865.
- [46] M. Wenninger, *Spektroskopische Charakterisierung der ultraschnellen Reaktionsmechanismen flavinbasierter Photochemie*, Diplomarbeit, Ludwig-Maximilians-Universität (München), **2010**.
- [47] U. Schmidhammer, S. Roth, E. Riedle, A. A. Tishkov, H. Mayr, *Rev. Sci. Instr.* **2005**, *76*, 93111.
- [48] T. Langenbacher, D. Immeln, B. Dick, T. Kottke, *J. Am. Chem. Soc.* **2009**, *131*, 14274-14280.
- [49] M. L. Horng, J. A. Gardecki, A. Papazyan, M. Maroncelli, *J. Phys. Chem.* **1995**, *99*, 17311-17337.

- 
- [50] P. Fita, E. Luzina, T. Dziembowska, C. Radzewicz, A. Grabowska, *J. Chem. Phys.* **2006**, *125*, 184508.
- [51] I. H. M. van Stokkum, D. S. Larsen, R. van Grondelle, *Biochim. Biophys. Acta* **2004**, *1658*, 262-262.
- [52] H. Satzger, W. Zinth, *Chem. Phys.* **2003**, *295*, 287-295.
- [53] H. Satzger, *Untersuchung initialer Schritte der Peptidfaltung mit Ultrakurzzeitspektroskopie*, Doktorarbeit, Ludwig-Maximilians-Universität (München), **2004**.
- [54] W. Holzzapfel, U. Finkele, W. Kaiser, D. Oesterhelt, H. Scheer, H. U. Stolz, W. Zinth, *Proc. Natl. Acad. Sci. USA* **1990**, *87*, 5168-5172.
- [55] A. R. Holzwarth, M. G. Muller, *Biochem.* **1996**, *35*, 11820-11831.
- [56] M. Beutter, *Erzeugung und Anwendung von sub-30-fs Impulsen vom UV zum Nahinfraroten: Der photochrome Schalter Dihydroazulen/Vinylheptafulven*, Doktorarbeit, Ludwig-Maximilians-Universität (München), **2001**.
- [57] I. Pugliesi, P. Krok, S. Lochbrunner, A. Blaszczyk, C. von Hanisch, M. Mayor, E. Riedle, *J. Phys. Chem. A* **2010**, *114*, 12555-12560.
- [58] R. Stahl, C. Lambert, C. Kaiser, R. Wortmann, R. Jakober, *Chem. Euro. J.* **2006**, *12*, 2358-2370.
- [59] J. Karpiuk, *J. Phys. Chem. A* **2004**, *108*, 11183-11195.
- [60] R. A. Marcus, *J. Chem. Phys.* **1956**, *24*, 966-978.
- [61] R. A. Marcus, N. Sutin, *Biochim. Biophys. Acta* **1985**, *811*, 265-322.
- [62] E. Silva, A. M. Edwards, *Flavins: Photochemistry and Photobiology in Comprehensive Series in Photochemical & Photobiological Sciences* (Eds.: D. P. Häder, G. Jori), Royal Society of Chemistry, Cambridge, **2006**.
- [63] M. Sakai, H. Takahashi, *J. Mol. Struct.* **1996**, *379*, 9-18.
- [64] A. Niemz, J. Imbriglio, V. M. Rotello, *J. Am. Chem. Soc.* **1997**, *119*, 887-892.
- [65] T. B. Melo, M. A. Ionescu, G. W. Haggquist, K. R. Naqvi, *Spectrochim. Acta A* **1999**, *55*, 2299-2307.
- [66] Y. T. Kao, C. Saxena, T. F. He, L. J. Guo, L. J. Wang, A. Sancar, D. P. Zhong, *J. Am. Chem. Soc.* **2008**, *130*, 13132-13139.
- [67] G. Williams, D. C. Watts, *Trans. Farad. Soc.* **1970**, *66*, 80.
- [68] H. Scher, M. F. Shlesinger, J. T. Bendler, *Physics Today* **1991**, *44*, 26-34.
- [69] M. Schlosser, S. Lochbrunner, *J. Phys. Chem. B* **2006**, *110*, 6001-6009.
- [70] A. Weigel, A. L. Dobryakov, M. Veiga, J. L. P. Lustres, *J. Phys. Chem. A* **2008**, *112*, 12054-12065.
- [71] S. J. Strickler, R. A. Berg, *J. Chem. Phys.* **1962**, *37*, 814.
- [72] A. P. Thorne, *Spectrophysics*, Chapman and Hall, London, **1974**.
- [73] S. A. Rice, *Diffusion-limited reactions, Vol. 25*, Elsevier Science Publishers B.V.,

- Amsterdam, **1985**.
- [74] J. R. Lakowicz, *Principles of fluorescence spectroscopy*, 3rd ed., Springer Science+Business Media, New York, **2006**.
- [75] S. D. M. Islam, A. Penzkofer, P. Hegemann, *Chem. Phys.* **2003**, *291*, 97-114.
- [76] H. E. Lessing, A. V. Jena, *Chem. Phys. Lett.* **1976**, *42*, 213-217.
- [77] H. Langhals, A. J. Esterbauer, A. Walter, E. Riedle, I. Pugliesi, *J. Am. Chem. Soc.* **2010**, *132*, 16777-16782.
- [78] P. Krok, *Entwicklung und Kombination neuer zeitlich hochauflösender und hochrepetitiver Systeme und Methoden zur Untersuchung ultraschneller Ladungstransfer- und Schwingungsdynamik in großen Molekülen*, Doktorarbeit, Ludwig-Maximilians-Universität (München), **2008**.
- [79] M. Bock, *Ultraschneller Elektronentransfer in Photolyasen anhand von Flavin-Modellverbindungen*, Bachelorarbeit, Technische Universität (München), **2008**.
- [80] C. F. Sailer, Doktorarbeit, Ludwig-Maximilians-Universität (München), **2011**.
- [81] J. Bartl, S. Steenken, H. Mayr, R. A. McClelland, *J. Am. Chem. Soc.* **1990**, *112*, 6918-6928.
- [82] W. Wohlleben, T. Buckup, J. L. Herek, R. J. Cogdell, M. Motzkus, *Biophys. J.* **2003**, *85*, 442-450.
- [83] J. Savolainen, D. van der Linden, N. Dijkhuizen, J. L. Herek, *J. Photochem. Photobiol. A* **2008**, *196*, 99-105.
- [84] M. Bradler, P. Baum, E. Riedle, *Appl. Phys. B* **2009**, *97*, 561-574.
- [85] A. L. Dobryakov, S. A. Kovalenko, A. Weigel, J. L. Pérez-Lustres, J. Lange, A. Müller, N. P. Ernsting, *Rev. Sci. Instr.* **2010**, *81*, 113106.
- [86] C. C. Page, C. C. Moser, X. Chen, P. L. Dutton, *Nature* **1999**, *402*, 47-52.
- [87] R. Cibulka, R. Vasold, B. König, *Chem. Euro. J.* **2004**, *10*, 6223-6231.
- [88] A. Bauer, F. Westkamper, S. Grimme, T. Bach, *Nature* **2005**, *436*, 1139-1140.
- [89] T. J. J. Müller, U. H. F. Bunz, *Functional organic materials*, Wiley-VCH, Weinheim, **2007**.
- [90] A. Sancar, *Chem. Rev.* **2003**, *103*, 2203-2237.
- [91] A. Lukacs, A. P. M. Eker, M. Byrdin, K. Brettel, M. H. Vos, *J. Am. Chem. Soc.* **2008**, *130*, 14394-14395.

## **Appendix A1**

**Sub-50 fs broadband absorption spectroscopy with tunable excitation:  
putting the analysis of ultrafast molecular dynamics on solid ground**

*U. Megerle, I. Pugliesi, C. Schrieber, C. F. Sailer, E. Riedle*

Applied Physics B: Lasers and Optics 96, 215-231 (2010)



# Sub-50 fs broadband absorption spectroscopy with tunable excitation: putting the analysis of ultrafast molecular dynamics on solid ground

U. Megerle · I. Pugliesi · C. Schrieffer · C.F. Sailer · E. Riedle

Received: 22 May 2009 / Published online: 18 June 2009  
© Springer-Verlag 2009

**Abstract** We give a full description of a state-of-the-art femtosecond transient spectrometer. The setup has been put together under full consideration of all technical and conceptual developments that became available in the last few years. Particular care was taken to avoid any unneeded components and modules.

The spectrometer is operated at 1 kHz and based on a commercial Ti:sapphire amplifier. A noncollinear parametric amplifier and frequency doubling are used to provide pump tuning from the UV to the NIR. A CaF<sub>2</sub> based single filament white light allows for 290 to 720 nm probing. The multichannel detection is operated at the full 1 kHz rate and chopping of the pump light avoids the use of a reference channel. The resulting high detection sensitivity of better than  $\Delta OD = 10^{-4}$  allows for the simultaneous recording of the spectral features of electronic states and species with differing transition strengths.

A prism-based polychromator is employed to avoid the order sorting problem with the more than octave wide probe spectrum and to enhance the throughput. Flow cells with 200  $\mu\text{m}$  windows and down to 120  $\mu\text{m}$  sample thickness reduce the coherent artifact and the group velocity mismatch. This results in an overall sub-50 fs temporal resolution.

**PACS** 07.60.Rd · 42.62.Fi · 78.47.J- · 82.50.Hp · 82.53.Uv

## 1 Introduction

The study of photophysical and photochemical processes crosses the interest of many fields of research in physics, chemistry and biology. Among the experimental approaches developed for this purpose, transient absorption spectroscopy has become a powerful and widely used technique. The process investigated is triggered by exciting the molecules with a short laser pulse. The dynamics of the electronically excited states is then probed by a second light pulse that monitors the photo-induced transmission changes. This concept is not easily transferred to bimolecular reactions, since the observed rate is usually limited by diffusion. Unimolecular processes, however, can easily proceed in the pico- or femtosecond range.

In their early stages, ultrafast studies had to rely on the accidental coincidence of given laser lines—mostly from sub-ps dye lasers—with molecular absorptions, both in the spectrum of the educt and the transient spectrum of the intermediates or products. In prominent cases, this was already sufficient for a crucial breakthrough in understanding the underlying mechanisms [1]. In other situations however, a fair amount of “chemical intuition” had to be added to resolve any ambiguities. Ideally, however, the excitation should not be chosen by technical constraints but according to the sample of interest. To put the analysis on solid ground, all relevant transient signatures should be monitored.

The last two decades have witnessed the upgrowth of low noise and sufficient intensity ultrafast light sources freely tunable from the deep UV into the mid-IR. These sources are typically pumped by amplified Ti:sapphire lasers and are based on optical parametric amplification (OPA). A collinear OPA together with difference frequency mixing gives access to the spectral range from near-IR to mid-IR [2–5] while a noncollinear geometry (NOPA) with the

U. Megerle · I. Pugliesi · C. Schrieffer · C.F. Sailer · E. Riedle (✉)  
Lehrstuhl für BioMolekulare Optik,  
Ludwig-Maximilians-Universität (LMU), Oettingenstr. 67,  
80538 München, Germany  
e-mail: [riedle@physik.lmu.de](mailto:riedle@physik.lmu.de)  
Fax: +49-89-21809202

help of frequency doubling and sum frequency mixing allows for shortest pulses from the UV to the near-IR [6–9]. This development allowed for a selective triggering of photochemical processes, thereby dramatically enlarging the range of molecules that can be properly studied by transient spectroscopy. The spectral width of pulses generated in a NOPA routinely supports pulse lengths below 30 fs ensuring a time resolution on the scale of molecular vibrations.

The available tunability can also be used to probe the transient species developing from the photo-initiation by optical transitions occurring at various wavelengths [10–12]. However, employing probe pulses that cover an ultrabroad spectral range at once greatly simplifies the experiment. The wider the probe spectrum, the more spectral signatures of the transient species involved in a photoprocess can be monitored simultaneously, which significantly facilitates the assignment of the underlying reaction mechanism.

Towards this goal, one approach is to use ultrabroadband NOPA pulses that have a Fourier limit of only a few femtoseconds [13–15]. Combining such a probe pulse with a narrowband NOPA excitation allows one to achieve a time resolution in the sub-10 fs regime [16, 17] which is tailored to the investigation of the fastest photochemical processes.

However, even ultrabroad NOPA pulses can at best extend over 200 THz corresponding to most of the visible but not reaching down to the UV. The alternative approach to cover a much wider range is to use supercontinua. These are generated by focusing an ultrashort laser pulse under proper conditions into optically nonlinear transparent media like gases, liquids, photonic crystal fibers and solids [18]. The properties of the continua and their applicability to transient spectroscopy depend very much on the way they are generated. Even though time-resolved studies have been performed using white light from liquids [19–22] or microstructured fibers [23], the great majority of reported spectrometers relies on supercontinua obtained from bulk materials. The latter have been shown to yield continua with a very broad and smooth spectrum, high temporal and spatial coherence and a very high pulse-to-pulse energy stability. In contrast to broadband NOPA pulses, supercontinua cannot readily be compressed to the Fourier limit. Therefore, extra care has to be taken to reach a temporal resolution significantly better than 100 fs in spectrometers with chirped supercontinuum probing. For many studies this disadvantage is, however, heavily outweighed by the broad probing range [24–31].

The full potential of the broad supercontinua can best be exploited with a multichannel detection system in contrast to approaches where a stepwise scanning of the probe light is employed. In the past, multichannel detection faced some significant technical difficulties by posing high demands on electronics and data acquisition. Commercially available detectors were limited to read-out frequencies well below

the typical repetition rate of the pump system of 1 kHz. This required acquisition times of several minutes to reach sufficient signal-to-noise ratios. Only home-built systems were capable of real single pulse analysis at kHz repetition rates [32–34], however often with a rather small number of channels. Recent advancements in detector electronics have increased the read-out frequencies of arrays containing up to 1024 elements reliably to over 1 kHz. This development has already found its way into first spectroscopic setups [35–38].

Besides the progress in light sources and detectors, many additional advances have allowed transient spectrometers to mature to highly productive scientific instruments. Over the years, a considerable number of publications has been dedicated to the description and characterization of the large variety of pump-probe spectrometers. However, to the reader of spectroscopic journals it is often unclear whether the described setup is historically motivated or specifically built for a certain application. Furthermore, since the spectrometers are constantly improved, many of the contributions tend to focus on the newest developments and therefore concentrate on selected experimental aspects. Thus, a complete description of the setup and the link between the individual features comprising the spectrometer is often lacking.

In this paper we present a summary of all relevant concepts and components that we used to build and run a state-of-the-art femtosecond broadband pump-probe spectrometer, further details can be requested from the authors. From our experience gained over many years of activity in the field, the essential tools are optical parametric amplifiers, low dispersion optics and sample cells, a stable supercontinuum generation combined with a high transmission polychromator and a kHz multichannel detector, and last but not least the proper software for data recording and processing. We believe that a design based on these elements comes closest to the realization of the following principles: tunability of the excitation source, broad spectral coverage, sub-50 fs time resolution, high sensitivity, efficient data acquisition and evaluation, and finally flexibility of the whole setup. The implementation of these principles is crucial for reliable high quality time resolved measurements and essential for a sound analysis of the observed ultrafast molecular dynamics.

## 2 Experimental setup

### 2.1 Design of the pump-probe spectrometer

In this section we give an overview of our femtosecond pump-probe spectrometer before describing the most relevant components in more detail in the following sections. The complete schematic of our setup is shown in Fig. 1. It is directly linked to the actual layout on the optical table since



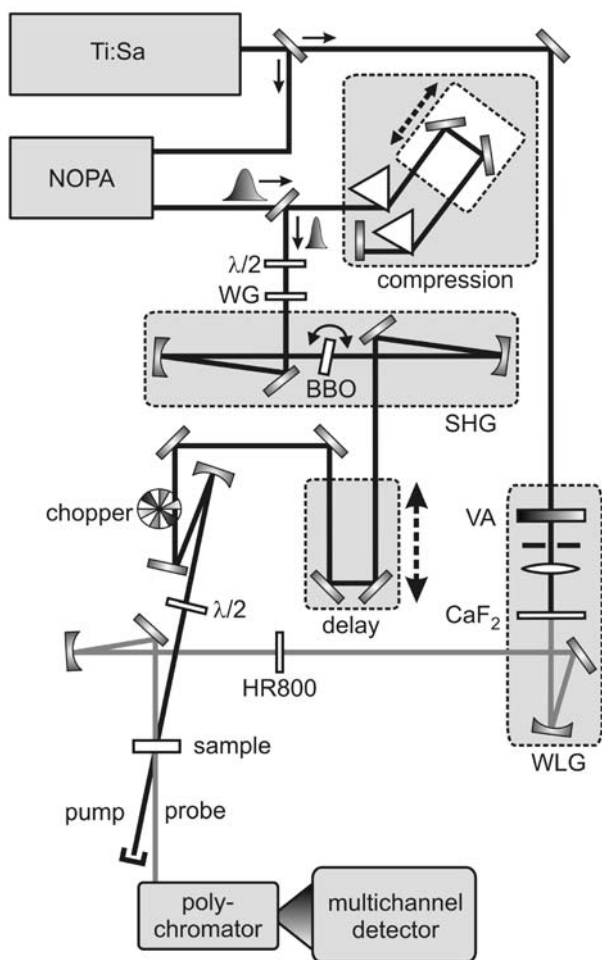


**Fig. 1** Layout of the pump-probe spectrometer. WG: wire-grid polarizer; SHG: second harmonic generation; VA: variable attenuator; WLG: white light generation; HR800: custom-made dielectric mirror to block the CPA fundamental

it depicts essentially all of the employed components. The idea behind the design is on the one hand simplicity reached by omitting redundant optics. On the other hand, we deliberately keep an open layout on the optical table to facilitate the day-to-day operation and optimization. The aim of our setup is not to perform heroic measurements after many days of adjustment but rather to ensure a reliable performance when sensitive chemical samples become available.

As a light source we use a regenerative Ti:Sa amplifier system (CPA 2001; Clark MXR) that delivers 1 mJ-pulses at 775 nm with 150 fs duration and a repetition rate of 1 kHz. The comparatively long pulse duration ensures a stable operation and still is sufficient to perform measurements with highest temporal resolution due to the pulse shortening in the NOPA. For the pump, a fraction of 200–250 μJ is used to operate a two-stage noncollinearly phase-matched optical parametric amplifier (NOPA). The chirped visible output pulses with energies of several μJ are compressed with a sequence of two Brewster prisms. Subsequently, a thin achro-

matic half-wave plate and a wire-grid polarizer (ProFlux™; MOXTEK, Inc.) are used to adjust the pulse energy according to the needs of the spectroscopic experiment. The polarizer is set parallel to the pump polarization and the transmission is controlled by rotating the half-wave plate. If desired, the visible pulses can be frequency doubled in a type-I BBO crystal. Contrary to the simple model of pump-probe spectroscopy, we do not change the delay of the probe pulses but rather the pump pulses are delayed with a retro reflector mounted on a computer controlled linear stage and then focused to the sample. This ensures the most stable operation of the probe continuum and introduces only negligible changes in the pump focus. The polarization of the pump beam can be set with another achromatic half-wave plate which is placed directly before the sample. A reflection on mirrors at a polarization deviating from horizontal or vertical would turn linearly into elliptically polarized light.

As probe pulse we use the white light generated by focusing roughly 1 μJ of the fundamental Ti:Sa beam into a CaF<sub>2</sub> crystal. After passing through the sample at an external angle of ~6° with respect to the pump, the probe is dispersed in a polychromator and focused onto a multichannel detector. A chopper wheel in the pump beam blocks every second excitation pulse such that changes in the optical density (OD) of the sample can be measured according to:

$$\Delta OD(\lambda, \Delta t) = -\log\left(\frac{I^*(\lambda, \Delta t)}{I_0(\lambda)}\right). \tag{1}$$

Here,  $I^*$  and  $I_0$  are the transmitted probe light through the excited and the unpumped sample. With the knowledge of all relevant parameters like beam diameters and sample concentration, the  $\Delta OD$ -signal allows for the determination of absolute values for the photoprocesses, e.g., extinction coefficients or concentrations of the transient species. Thus, the time resolved absorption spectroscopy can not only identify, but also quantify the processes occurring during a photoreaction.

The induced absorption changes can be followed up to times given by the length of the delay line, in our case from  $\Delta t = -0.1$  ns to about 1.7 ns. For longer delays, the alignment of the pump beam becomes more and more difficult, e.g., due to the divergence and the associated change of the pump diameter and also the changing overlap with the probe inside the sample. To record dynamics from ultrafast charge transfer or wavepackets (<100 fs) up to slow population redistributions (>100 ps) within the same experiment we use a quasi-exponential time scale for sampling. The step size is chosen constant between -1 and 1 ps and is then linearly increased with the delay time according to

$$\Delta t(i) = \begin{cases} -1 + \frac{2i}{N} & \text{for } i = 0 \dots N - 1, \\ 10^{-1+i/N} & \text{for } i = N \dots M. \end{cases} \tag{2}$$

Here,  $N$  denotes the number of points between  $-1$  and  $1$  ps and  $M$  is given by the maximum delay time  $\Delta t_{\max}$  by  $M = N(1 + \log \Delta t_{\max})$ . This time scale generates the same number of delay points from  $-1$  to  $1$  ps as between  $1$  and  $10$  ps,  $10$  and  $100$  ps, etc., respectively. If a fit routine is applied to such a data set, the dynamics on every time scale will have equal weighting. The initially linear scan ensures proper correction for the continuum chirp and the exponential sampling in addition minimizes the measurement time. For an appropriate data presentation we usually add some sparsely spaced points at negative delay times and typically start at  $\Delta t = -100$  ps. This also allows for better statistics when analyzing the baseline in terms of sensitivity (see Sect. 4.2).

An important consideration is the choice of the optics in the setup. For the white light probe we only use metal coated planar mirrors for steering and spherical mirrors rather than lenses to avoid additional chirp. For highest throughput UV enhanced aluminium mirrors (RAL UVE; Linos Photonics GmbH & Co. KG<sup>1</sup>) are employed. For the focusing we have turned away from off-axis parabolic mirrors due to the unfavorable surface quality of available samples. We found that much better beam profiles and tenfold lower  $M^2$  values can be achieved with spherical mirrors. To limit the influence of the astigmatism we keep the reflection angles low on all spherical mirrors by placing them in a folded geometry as seen in Fig. 1. We have also tested the use of spherical mirrors off-axis in alternating planes to minimize the astigmatism [39]. However, for most purposes we find no need for this implementation and believe that a slight deterioration for example of the pump and probe foci inside the sample is acceptable (see Sect. 2.4).

For the visible pump pulses an enhanced silver coating (Silflex<sup>TM</sup> MK II; Optics Balzers GmbH (see footnote 1)) is a good choice since it has a very high reflectivity for the whole range from  $450$  nm into the IR. For the UV pump the enhanced aluminium mirrors provide the advantage of broad spectral coverage. For near unity efficiency and separation of the UV from the fundamental we use a few dielectric mirrors.

In contrast to the standard approach, our spectrometer does not include the detection of a reference beam to account for the shot to shot fluctuations of the white light. Instead, we exploit the high correlation between successive pulses (see Sect. 2.3) for the normalization of the probe intensity. This greatly simplifies the setup, since only one multichannel detector needs to be implemented. As shown in Sect. 4.2, the sensitivity still reaches excellent values beyond the  $10^{-4}$

level which is among the best reported sensitivities for femtosecond spectrometers.

All software based operations connected with the spectrometer and the evaluation of the measurements are performed with codes developed in our group utilizing the LabView 8.5 (National Instruments, Inc.) platform. The modules allow the experimenter to have full visual control of all relevant data and highly interactive handling. We find this most important to collect reliable and reproducible molecular dynamics information and to properly interpret the raw signals. The software is routinely adapted to the changing needs and insights.

## 2.2 Ultrashort tunable excitation pulses

As mentioned in the introduction, the need to excite a large variety of molecules at their specific electronic transitions requires a broad tunability of the pump pulses. For true versatility, a continuous tunability is favored over the detached excitation wavelengths reached when higher harmonic generation of the fundamental Ti:Sa output is applied [20, 25, 40–42]. Additionally, the pump pulses should be in the sub-100 fs regime to ensure a sufficient time resolution for the study of ultrafast photophysical and photochemical processes. Last but not least, sufficient energy has to be available to excite a few percent of the illuminated molecules under conditions of weak focusing.

All these requirements can be met by the use of a NOPA which has been described in detail in previous papers [6, 7, 9]. Briefly, less than a  $\mu\text{J}$  of the Ti:Sa fundamental is used for the generation of a visible seed continuum by focusing it into a  $3$  mm sapphire plate. So far, in most applications a focal length of  $30$  mm was used, which goes back to early work [43]. However, recently the importance of the numerical aperture on the quality of the continuum has been shown [44]. We observed that the use of lenses with a longer focal length ( $f = 50$ – $80$  mm) yields broader continua, both in the visible and in the IR [45] and therefore widens the tunability of the NOPA.

For excitation pulses in the UV/Vis range, a selected portion of the white light is amplified in a  $1$  mm thick BBO crystal pumped by tens of  $\mu\text{J}$ s of the second harmonic of the Ti:Sa beam. For better beam profiles and higher pulse energies a second amplification stage with a  $2$  mm BBO and more pump energy can be employed. As shown on the right hand side of Fig. 2, pulses ranging from  $450$ – $760$  nm with Fourier limits below  $30$  fs and energies of several  $\mu\text{J}$ s can easily be obtained by a suitable choice of the angle of non-collinearity between pump and seed and the phase matching angle of the BBO [7].

The spectral width of the NOPA pulses can be tailored depending on the specific needs of the spectroscopic experiment. For instance, spectrally narrow pulses can be obtained

<sup>1</sup>Mention of vendor names and model numbers is for technical communication purposes only and does not necessarily imply recommendation of these units, nor does it imply that comparable units from another vendor would be any less suitable for this application.

by adding chirp to the white light seed without sacrificing output power [46]. If the pump is chirped the output spectra can be broadened to reach shorter Fourier limits down to a few fs [13, 47, 48]. Therefore, the spectra shown in Fig. 2 are to be considered as examples for a typical pump-probe experiment without the particular need for extremely short or spectrally narrow pulses.

At the output of the NOPA the pulses are chirped to roughly 130 fs [49]. However, due to the large spectral width much shorter pulse lengths can be obtained, most easily by the use of a fused silica prism compressor. Above 550 nm the length of the compressor can be substantially shortened with SF10 instead of the fused silica prisms. A very helpful feature shown in Fig. 1 is the use of two mirrors acting as a retro reflector inside the prism compressor. This folding allows for a quick and easy adaptation of the length of the compressor to a change of the NOPA center wavelength. In this way the tunability of the NOPA can really be exploited on a day-to-day-basis requiring only minute changes in the alignment of the whole setup. After the compression, pulse durations below 30 fs are routinely achieved throughout the visible. To characterize these pulses we use a compact dispersion-free autocorrelator [50].

In order to extend the tunability of the NOPA into the UV, the visible pulses are focused into a thin BBO crystal. In contrast to the common approach we have not implemented a second prism compressor for the UV pulses. We found that a compression in the visible is sufficient to reach even sub 20-fs pulses in the UV [47]. The prism compressor for the visible is set to precompensate for the additional chirp introduced by the SHG and the further propagation of the pulse through the setup. For the spectra shown on the left hand side of Fig. 2 we used a 150  $\mu\text{m}$  thick BBO crystal in the SHG. This leads to an increase of the pulse length but has the benefit of a higher conversion efficiency. Again, the specific needs of the spectroscopic experiment can be met by the right choice and alignment of the components in the doubling stage. Together with the SHG, the NOPA allows for a nearly continuous tunability of the excitation pulses from the region of the fundamental at 750 nm down to about 240 nm.

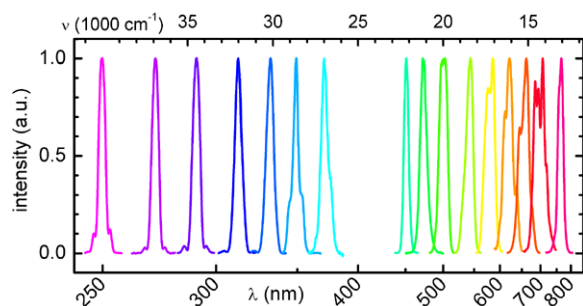


**Fig. 2** Typical output spectra of the NOPA. The spectra below 400 nm were obtained by second harmonic generation in a BBO crystal

### 2.3 Octave spanning low noise supercontinuum probe

A commonly used material for white light generation is a sapphire crystal which is often used not only inside the NOPA but also to generate the probe pulse [26, 51–54]. Figure 3a shows the anti-Stokes side of a sapphire continuum obtained with the Ti:Sa fundamental at 775 nm. The spectroscopically useful range spans from about 420 to 720 nm. As strong spectral modulations and temporal fluctuations are present near the fundamental, this range is usually filtered out (e.g. Calflex™X; Optics Balzers GmbH (see footnote 1)).

As many organic molecules have their lowest transitions in the UV it is helpful to extend the probe to higher photon energies. This allows, e.g., for the direct observation of the ground state bleach. However, even for molecules with transitions in the visible it is often useful to be able to monitor the ground state recovery of higher absorption bands since they do not overlap with the stimulated emission or are distorted by stray light from the excitation pulse.

Recently, calcium fluoride crystals were successfully employed [25, 30, 39, 55–58] to generate an ultrabroad continuum that reaches much further into the UV than the one obtained from sapphire. As can be seen in Fig. 3a, the spectrum of a white light generated in a 5 mm  $\text{CaF}_2$  plate extends from 290 to 720 nm showing an almost flat plateau. The dip at 400 nm is not a feature of the continuum but is due to the dielectric mirror used to block the fundamental (HR800 in Fig. 1). This custom-made mirror is specified to a high reflectivity at 800 nm and a high transmittance (>90%) from 300 to 700 nm.

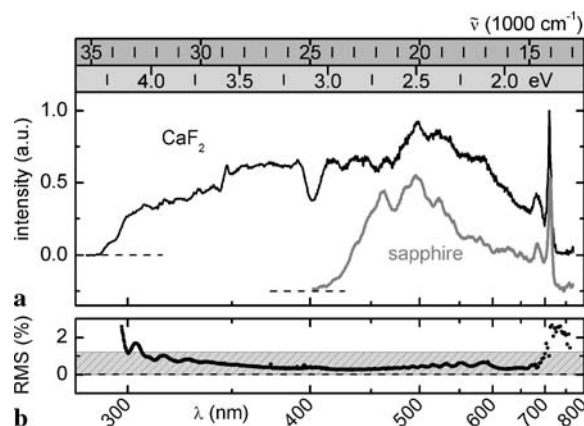


**Fig. 3** (a) White light continua generated in  $\text{CaF}_2$  and in sapphire. The fundamental was suppressed by the HR800 mirror ( $\text{CaF}_2$ ) and a Calflex X filter (sapphire). The spectra were measured with a commercial fiber optic spectrometer and not corrected for its efficiency since a similar efficiency is relevant for the broadband detector. (b) RMS noise of the  $\text{CaF}_2$  continuum evaluated for 2000 consecutive pulses with the multichannel detector. The low frequency contributions have been subtracted prior to the calculation of the RMS values. The shaded area contains 90% of the points

The spectrum of the CaF<sub>2</sub> white light corresponds to an energy window of over 20,000 cm<sup>-1</sup>, which is more than twice the range of the sapphire continuum. Within this window, the modulation of the absolute spectral energy density is less than a factor of ten. In the range from 300–700 nm, the energy density is ~10 pJ/nm and the intensity modulation even decreases to a factor of three. This is considerably better than the modulation found when the white light is generated in other materials like microstructured fibers [23, 59] or gas cells [60–62]. The even distribution of the intensity allows for measurements with a high dynamic range and makes the CaF<sub>2</sub> continuum an ideal probe.

The quality of the CaF<sub>2</sub> white light strongly depends on several experimental parameters. These include the energy of the fundamental, the numerical aperture of the setup, the angle of incidence on the CaF<sub>2</sub> disk, its positioning relative to the focus along the beam and the orientation of the crystal axes with respect to the polarization of the laser.

To adjust the energy of the Ti:Sa fundamental we use a variable attenuator in combination with an iris whose aperture is set to about 5 mm. The latter also controls the diameter of the focus inside the CaF<sub>2</sub> disk. For the focusing we use a 10 cm lens which leads to a numerical aperture of 0.025. As described by Laimgruber et al. [37], the optimization of the focus position starts by placing the focus behind the CaF<sub>2</sub> plate. Then the plate is moved towards the focus until a stable single filament white light is obtained. For a good performance in the UV, the intensity of the fundamental has to be increased till a red ring surrounding the white light is seen on a white card. A further increase in pump energy leads to multifilamentation with even higher UV yield [63], however at the cost of a strongly structured beam profile. This causes significant problems in the beam guidance and therefore we restrict ourselves to the use of a single filament CaF<sub>2</sub> continuum with its near Gaussian profile (see Sect. 2.4).

As even CaF<sub>2</sub> plates of carefully selected quality have an insufficient damage threshold, the crystal has to be continuously moved in order to increase its lifetime. Contrary to our early impressions the possible damage does not occur at the surface but rather inside the bulk material. Several motion techniques are conceivable, e.g., translation, rotation or any combination of both. However, to maintain a linear polarization of the white light across the spectrum and over time, the orientation of the crystal axes relative to the polarization of the fundamental has to be kept constant [64–66]. This can be easily achieved by an eccentric motion of the plate, i.e. a circular translation rather than a classical rotation around the center [37]. For an arbitrary orientation of the CaF<sub>2</sub> crystal the white light is elliptically polarized. The complete extinction behind a polarizer is a good measure to adjust the crystal orientation, which will then remain perfectly linear (parallel to the horizontal pump polarization) and unchanged during the eccentric motion.

As a measure of the stability of the continuum we monitor online the root-mean-square (RMS) of the noise at all wavelength components of the white light using the multichannel detector described in Sect. 2.7. The RMS noise is given by the standard deviation of the intensity distribution of the measured pulse sequence divided by its RMS value. During the adjustment of the white light, one needs a quick feedback for practical reasons. We therefore typically evaluate 200 consecutive pulses corresponding to an update rate of 5 Hz. The obtained RMS spectra are sufficient for a daily optimization routine but this simple calculation generally overestimates the shot to shot noise.

As shown previously [45, 46], the intensity fluctuations of kilohertz laser systems are not purely statistical but are typically dominated by low frequency contributions. This holds not only for the fundamental, but also for the supercontinuum or the NOPA output. The implication that consecutive laser pulses are strongly correlated is exploited by the shot to shot referencing method described in Sect. 2.1. Therefore, a reasonable measure of the relevant white light stability is obtained when the long-term fluctuations are subtracted before calculating the RMS noise. A typical result for a CaF<sub>2</sub> continuum is shown in Fig. 3b. The RMS values lie well below 1.2% for 90% of the channels as marked by the shaded area and only rise slightly at the edges of the spectrum.

One should note that varying the parameters for the continuum generation leads to a changed wavelength dependence of the RMS values. Different settings, e.g., of the numerical aperture or the intensity of the fundamental, can be used to optimize the stability of selected parts of the spectrum. For most purposes an even distribution of the RMS values over the whole range is a good compromise.

#### 2.4 Choice and check of the focusing geometry

For the optical excitation of the molecules only a fraction of the NOPA output energy is used to avoid multi-photon pump processes or saturation of the transition. In most cases an excitation probability below 10% assures a near linear dependence between the pump energy and the observed signal. In its simplest form the excitation probability  $P_{\text{exc}}$  is the product of the photon density  $n_{\text{ph}}$  in the focus and the absorption cross section  $\sigma$  of the sample molecules:

$$P_{\text{exc}} = n_{\text{ph}} \cdot \sigma = \frac{E_{\text{pump}}}{(hc/\lambda) \cdot \pi(D/2)^2} \cdot \varepsilon \frac{\ln 10}{N_A}. \quad (3)$$

For a given sample with an extinction coefficient  $\varepsilon$  at the excitation wavelength  $\lambda$ ,  $P_{\text{exc}}$  can be tuned by changing the focal diameter  $D$  and/or the pump energy  $E_{\text{pump}}$ . While the latter is adjusted by the half-wave plate/wire-grid dyad after the prism compressor, the former can be controlled by a set of irises in the collimated part of the pump beam.

Decreasing their apertures increases the focal diameter and thereby lowers  $P_{exc}$ . Typical values used in our setup are  $E_{pump} = 80\text{--}150$  nJ and  $D = 100\text{--}150$   $\mu\text{m}$  with a spherical mirror of  $R = -1000$  mm ( $f = 500$  mm) employed for focusing. The almost symmetric and near Gaussian beam profile of the NOPA output is well preserved at the focal plane inside the sample despite the slight astigmatism introduced by the spherical mirrors.

For an optimal pump-probe signal the excitation density in the sample should be constant over the probe beam. This is approximately achieved by keeping the waist of the probe beam significantly smaller than that of the pump beam. In our setup, the divergent probe beam after the white light generation is recollimated by a spherical mirror with  $R = -150$  mm. This leads to a beam diameter of 2 mm FWHM. The probe is then focused into the sample by a  $R = -300$  mm mirror resulting in a focal diameter of about 30  $\mu\text{m}$  FWHM. For good pump-probe signals, other combinations of spherical mirrors are also feasible as long as the ratio between pump and probe beam diameters is not too large.

A more detailed analysis of the beam profiles at the position of the sample reveals that the spot sizes vary for different spectral components of the white light (see Fig. 4). To obtain this information we placed nine different bandpass filters with transmissions centered between 350 and 750 nm and a FWHM of 10 nm into the white light beam. While the beam profile of the complete white light is almost circular at the position of the sample (inset in Fig. 4a), the profiles of the spectral components show a moderate elliptic deformation.

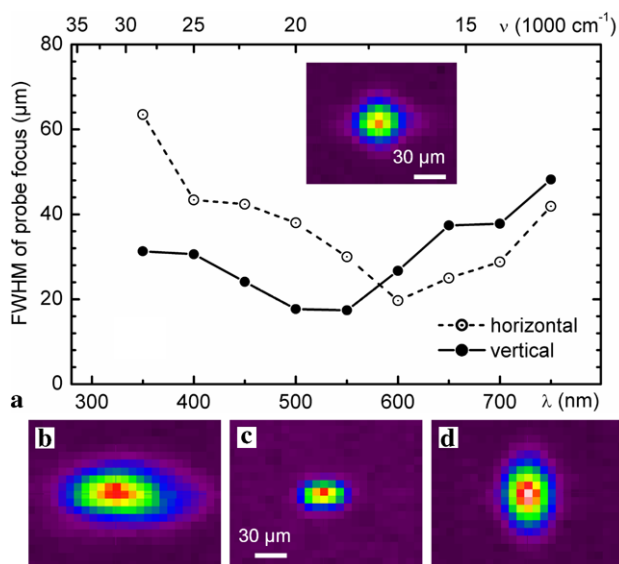


**Fig. 4** White light beam profile at the position of the sample: (a) diameters of the probe focus in vertical (closed circles) and horizontal (open circles) direction for different spectral components. The inset shows the profile of the complete white light continuum. Selected profiles at 350 nm (b), 550 nm (c) and 700 nm (d)

As mentioned previously, this is a consequence of the astigmatism caused by the off-axis use of spherical mirrors. Since we deflect the beam in the plane parallel to the optical table the focus in this plane lies behind the one for the vertical plane. In the propagation direction of the beam the profile turns from a vertical ellipse into a circle and then into a horizontal ellipse. The data shown in Fig. 4 therefore indicate that the circular focal profile of the blue wavelength components lies in front of the sample and that of the red components behind the sample. We believe that the wavelength dependence of the position of the focus is related to the processes involved in the white light generation which include different beam geometries for different wavelengths [43, 67, 68].

### 2.5 Flow cell with thin windows and low sample thickness

Femtosecond pump-transient absorption probe spectroscopy has been applied to a large variety of samples in all three phases: solid [69–71], liquid [72, 73] and gaseous [46, 74]. However, most studies are performed in solution since this is where the majority of the chemically and biologically relevant processes take place. In order to avoid photodegradation or accumulation of photoproducts in the probed volume it is often necessary to exchange the solution continuously, i.e. to use flow cells instead of conventional cuvettes.

In our setup we use a custom-made flow cell which is shown in Fig. 5. The design has been optimized to keep the optical path length through the windows and the sample solution at a minimum. This improves significantly the time resolution due to the decreased contribution from the group velocity mismatch as will be discussed in more detail in Sect. 4.1. In addition, the coherent artifacts produced by nonlinear interaction of the pump and probe pulse in the cell windows are minimized. It is no trivial task to produce thin windows on the order of a few hundred microns that are stable enough for everyday performance in a flow cell.

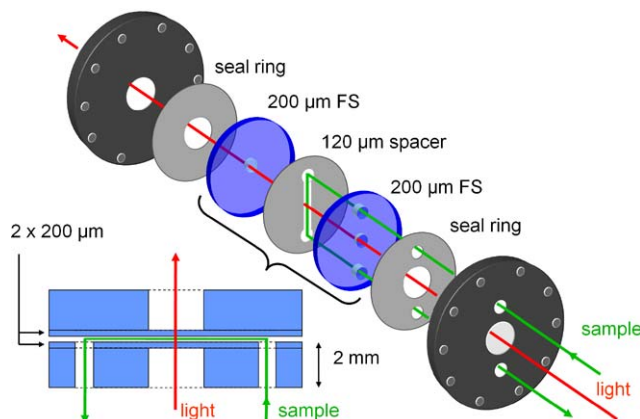


**Fig. 5** Scheme of the custom-made flow cell designed for low dispersion and a small optical path length

To overcome this difficulty, special windows have been designed in cooperation with Hellma GmbH.

Each window consists of two fused silica disks with optically polished surfaces, one of 1.8 mm thickness and the other of only 200  $\mu\text{m}$ . The two disks are fused together under clean-room conditions. The thicker disk has a drilled hole of 2 mm diameter in the middle such that the laser pulses propagate only through 200  $\mu\text{m}$  of glass for each window. The front window has two additional holes in both disks, which allow the sample solution to enter the space between the front and back window. The path length can be adjusted by a Teflon spacer of typically 120  $\mu\text{m}$  thickness which has a channel of  $\sim 2 \times 20$  mm cut out for the sample solution. The flow cell is held together by two stainless steel flanges shown in black in Fig. 5. In comparison to standard absorption cells with an optical path of 1 mm and a window thickness of 1.25 mm our setup represents a considerable reduction of material in the light path without sacrifice of stability. The whole flow cell is mounted on a holder movable in three dimensions. This facilitates the fine adjustment of the cell position with respect to the spatial overlap of pump and probe.

Many spectroscopically interesting chemical and biological samples are the product of a complex synthetic route or purification and are therefore only available in small amounts. In order to reach suitable optical densities in the rather small sample thickness of 120  $\mu\text{m}$  high concentrations are required. This calls for small volumina, which we assure by using a micro annular gear pump (mzr-2921-M2; HNP Mikrosysteme GmbH (see footnote 1)). This device allows for flow rates up to 18 ml/min and an overall sample volume as low as 1 ml.

## 2.6 High transmission prism polychromator

To exploit the full potential of the ultrabroad supercontinuum generated in  $\text{CaF}_2$  we use a multichannel detection scheme with a home-built prism-based polychromator as shown in Fig. 6a. We find that this system best meets the key requirements of an ultrafast spectrometer, namely an effective data acquisition, a simple layout providing a straightforward alignment and a high transmission throughout the whole spectral range, especially in the UV.

The first two aims can be met equally well with a grating based spectrometer like the one we used previously in our lab (Fig. 6b). It can also be utilized as a polychromator and the implementation does not require a significantly larger number of optical components. A prism, however, poses significant advantages over a grating as dispersive element.

The most important one is the high transmission throughout the whole spectral range of the white light, especially when used in a Brewster angle configuration. This fixes the polarization of the probe beam and we choose to set

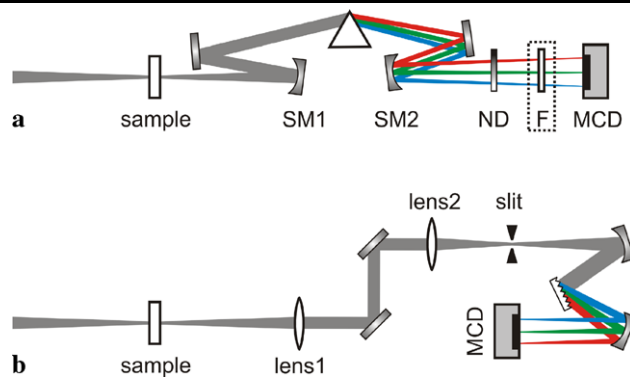


**Fig. 6** Design of a polychromator: **(a)** prism-based polychromator used in our setups, **(b)** standard grating based polychromator for comparison. SM: spherical mirror; ND: neutral density wedge; F: optional filters; MCD: multichannel detector

the relative polarization of pump and probe by a half-wave plate in the pump beam (see Sect. 2.1). The high probe transmission increases the detection sensitivity in the region around and below 300 nm where the continuum has a low intensity. Even for highest quality gratings at their specific blaze wavelength, 10% of the incident light intensity is lost into the zeroth and higher orders of diffraction [75]. Moreover, commercially available gratings will not cover the complete range of the  $\text{CaF}_2$  continuum with high efficiency but will fade strongly towards the edges of the spectrum. Hence, when we replaced the grating (600 lines/mm,  $\lambda_{\text{Blaze}} = 400$  nm) with the prism-based polychromator, we could immediately extend our detection window by  $\sim 15$  nm in the UV.

The second advantage is that prisms avoid the order sorting problem, i.e. the fact that higher orders of a short wavelength component are diffracted in the same direction as the first order of light at twice the respective wavelength. This is of particular importance when the continuum spans more than one octave like the  $\text{CaF}_2$  white light. Then, order sorting filters have to be used to avoid the distorting coincidence of different spectral components on the same pixel of the multichannel detector. However, we found it virtually impossible to purchase a commercial or custom-made filter suitable for our application.

The third advantage of prisms over gratings is the wavelength dependence of the dispersion. For a grating, the dispersion is approximately linear in wavelength leading to a constant wavelength resolution  $\Delta\lambda$ . The consequence, however, is an energy or wavenumber resolution  $\Delta\tilde{\nu}$  that decreases quadratically towards the UV. A typical value of  $\Delta\lambda = 4$  nm for a grating spectrometer corresponds to a resolution of  $\Delta\tilde{\nu} = 80$   $\text{cm}^{-1}$  at 700 nm sufficient for solution phase spectroscopy but to a rather modest resolution of  $440$   $\text{cm}^{-1}$  at 300 nm. In contrast, the dispersion of a prism is a complex function of the wavelength dependent refractive index  $n(\lambda)$  of the prism material (see Sect. 3.1). The steeper

slope of  $n(\lambda)$  towards the UV results in a high energy resolution for the blue side of the spectrum which does not drop dramatically towards the near IR (see Sect. 4.3). Overall, this leads to a more balanced spectral resolution which on average compares very well to standard grating spectrometers.

We use a metal neutral density wedge deposited on a fused silica substrate in front of the detector to balance the intensities of the channels by suppressing the stronger red components near the fundamental relative to the weaker UV components. Simultaneously, the attenuator adjusts the intensity of the white light to the full-well capacity or saturation charge of the detector. For optimal spectral resolution, the multichannel detector has to be placed in the focal plane of the dispersed white light. In the routine alignment of the detector we use a set of small bandwidth interference filters that are inserted into the white light beam path at the position of the sample. The camera is mounted on a linear translation stage in  $z$ -direction and positioned such that the widths of the transmitted profiles are minimized. The curvature of the focal plane arising from spherical aberration is much smaller than the Rayleigh range and therefore does not cause any problems.

The choice of the optics depends on the prism material and on the geometry of the multichannel detector. The prism dispersion together with the total length of the detector area fixes the focal length of the spherical mirror SM2 in Fig. 6a. The focal length of SM2 together with the size of the individual pixels then determines the necessary beam diameter of the collimated white light before the prism. This can be adjusted by the choice of the spherical mirror SM1 once the focusing geometry of the probe light into the sample is fixed. Overall the continuum is imaged once from the output face of the CaF<sub>2</sub> plate into the sample and a second time onto the detector. The ratios of focal lengths determine the magnification and only due to the single filament character of the continuum does the presented simple solution become possible.

In one of our laboratories we use a fused silica prism ( $\alpha = 68.7^\circ$ , side length 1") and a CCD camera with a sensor area of  $\sim 12.5 \times 1.5$  mm and a pixel size of  $24 \times 24$   $\mu\text{m}$ . There, the white light is recollimated after the sample with a  $R = -500$  mm spherical mirror (SM 1 in Fig. 6a) to a diameter of  $\sim 3$  mm. The dispersed spectral components are then focused onto the multichannel detector with a second spherical mirror (SM2,  $R = -400$  mm). Interestingly, the astigmatism is a desirable side effect. By placing the CCD in the sagittal plane one ensures that the white light is spread in vertical direction over all lines of the CCD array without losing spectral resolution. The choice of reflective optics avoids chromatic aberrations that would result from lenses.

## 2.7 kHz multichannel detection with high dynamic range

For the measurement of the photo-induced transmission change alternating measurements of the transmission of the probe continuum through the sample with and without excitation are performed. The high correlation between successive probe pulses [46] can be exploited by chopping the pump pulse at half the laser repetition rate. For a typical amplified femtosecond laser system this requires a kHz read-out frequency of the multichannel detector. Dependent on the employed hardware adapted triggering schemes are needed. The cleanest solution is to trigger the detector at the laser repetition rate. If this is not possible, an asynchronous operation is also conceivable. This requires that the integration time of the detector is set to match the period between the laser pulses as closely as possible, or vice versa. In practice, the detector has to be resynchronized after the read-out of a burst as large as possible. Due to the limited long-term stability of the laser system it is important to keep the total measurement time at a minimum. Typically, the duration of one experiment should not exceed 2–3 hours. By maximizing the duty cycle of the data acquisition more laser pulses can be acquired within the measurement time. Thus, a better signal-to-noise ratio can be achieved. With the advent of fast multicore processors and large memories it is nowadays possible to use high level data acquisition languages such as LabView for a fast data recording and real-time processing and visualization.

Over the past decade, multichannel detectors with ever faster read-out electronics have become commercially available at affordable prices. In our lab we use two types of multichannel detection systems: a photodiode array (PDA) based camera (tec5 AG) which is operated in burst mode and a back-thinned full frame transfer (FFT) CCD camera (2000 series; Ingenieurbüro Stresing) which is triggered synchronously to the laser.

The PDA sensor (NMOS; S3902-512Q; Hamamatsu) consists of 512 pixels,  $50 \times 500$   $\mu\text{m}$  each. Due to the large pixel size, the saturation output charge is  $\sim 6 \times 10^7$  electrons. With a quantum efficiency of 50% at 600 nm, this corresponds to the absorption of  $12 \times 10^7$  photons or an energy density of  $\sim 40$  pJ per pixel at 600 nm. This is about a factor of 5 larger than the actual energy density of our supercontinuum (see Sect. 2.3). Thus, the dynamic range of the PDA cannot be exploited properly. In the UV the situation is even worse since the quantum efficiency of the PDA drops to below 30% and the energy density of the white light decreases. To operate the analog-to-digital converter of the PDA camera in the optimal regime we employ an analog pre-amplifier to scale the PDA output. This, however, increases both signal and noise and probably adds extra electronic noise. In total, we determined from the experiment an effective dynamic range of 1000:1 for the PDA.

The FFT sensor (S7030-0906; Hamamatsu) is a two-dimensional CCD array of  $524 \times 58$  pixels,  $24 \times 24 \mu\text{m}$  each. After illumination, the 58 pixels in the vertical direction are rapidly binned into a reading register. The full-well-capacity of the register is  $6 \times 10^5$  electrons. With a quantum efficiency of 85% at 600 nm, this corresponds to the absorption of  $7 \times 10^5$  photons or an energy density of  $\sim 0.3 \text{ pJ}$  per pixel at 600 nm. Furthermore, the quantum efficiency in the UV is well above 45% for the back-thinned detector. Now the energy in the white light continuum is sufficient throughout the whole spectral range to saturate the detector. Experimentally we measure a dynamic range of 4000:1, i.e. a fourfold increase compared to the PDA. This allows one to extend the detection window towards the UV where the intensity of the white light decreases. We therefore employ the CCD camera preferentially for samples with decisive transient absorption bands in the low wavelength region (see Sect. 5.2).

An often claimed disadvantage of the CCD as compared to a PDA sensor is its lower saturation threshold [76]. This can lead to the unwanted effect that the shot noise becomes higher than the technical laser noise and thereby the detection sensitivity deteriorates. An essential improvement is reached by the vertical binning described above. In our case, the resulting shot noise limit corresponding to the full-well capacity of the CCD reading register is  $1.3 \times 10^{-3}$ . Although quite large, this value is still well below the technical noise of the white light continuum (see Fig. 3b) and therefore does not determine the overall noise of the measurement. For the PDA sensor, the maximum number of generated electrons is about five times smaller than the saturation output charge. This still leads to a shot noise limit of  $2.9 \times 10^{-4}$  which is one order of magnitude better than for the CCD and much below the laser excess noise.

The quality of the spectroscopic data we obtain with these two detection systems is very similar (see Sects. 4 and 5). The differences arise mostly from the fact that the two setups are operated with different laser sources whose performance is never quite the same. Also the two supercontinua generated in  $\text{CaF}_2$  will always have slightly different properties. From our experience, these contributions are larger than the actual differences between the CCD and the PDA based camera and therefore we find both systems equally suitable for the application in ultrafast transient absorption experiments.

### 3 Calibration and data post-processing

#### 3.1 Wavelength calibration

For the wavelength calibration of our home-built prism polychromator we use a filter wheel with five color filters that can be rotated into the probe beam successively. It is important to position the filters for normal incidence of the beam

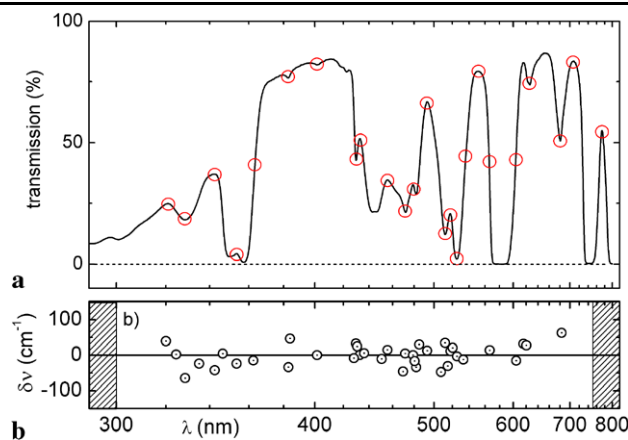


**Fig. 7** (a) Transmission spectrum of the filter BG 36, the red circles exemplarily indicate features that can be used to calibrate the spectrometer. (b) Accuracy of the wavelength calibration as identified by the position of the same features in the recorded spectrum. For details see text

propagation to avoid a parallel shift of the continuum on the detector. To minimize the influence of a small wedge on the filter, the wheel is placed right in front of the camera. The set consists of the three longpass filters WG 320, GG 475 and RG 695 and the two multiband filters BG 20 and BG 36 from Schott. While the strongly modulated spectra of the latter allow for a calibration over the whole near-UV/Vis range (see Fig. 7a), the former serve as additional checks at specific points.

At the beginning of each transient measurement we record the transmission of all filters as a function of the pixel number. The known spectra of the filters can then be used to assign the proper wavelengths to selected pixels. The various maxima, minima and steep slopes of the curves render about 30 wavelength/pixel couples that are used as input data for a fit that correlates each of the 512 pixels to a wavelength  $\lambda_i$ .

The horizontal deflection of a wavelength  $\lambda_i$  with respect to a reference wavelength  $\lambda_0$  corresponds to the pixel number  $N(\lambda_i)$  according to the exit angle  $\theta_{\text{out}}(\lambda)$  from the prism:

$$N(\lambda_i) = M - f \cdot \sin(\theta_{\text{out}}(\lambda_i) - \theta_{\text{out}}(\lambda_0)) + \text{const.} \quad (4)$$

$M$  is the total number of pixels on the detector and  $f$  the focal length of the spherical mirror SM2 in Fig. 6a. The exit angle depends on the index of refraction  $n(\lambda)$  of the prism material which can be calculated from the Sellmeier equation:

$$\theta_{\text{out}}(\lambda) = \arcsin\left(n(\lambda) \cdot \sin\left(\alpha - \arcsin\left(\frac{\sin\theta_{\text{in}}}{n(\lambda)}\right)\right)\right). \quad (5)$$

Here,  $\theta_{\text{in}}$  is the angle of incidence of the white light into the prism and  $\alpha$  is its apex angle.

Only two of the parameters in (4) are fitted with a Levenberg–Marquardt algorithm: the constant offset and the



focal length  $f$ . Although the latter quantity is in principle determined by the radius of curvature of SM2, we also fit this parameter to account for imperfect collimation of the white light and the astigmatism inherent to the setup. After fitting (4) the sought-after function  $\lambda(N_i)$  is obtained by numerically inverting the monotonic function  $N(\lambda_i)$ .

The quality of the calibration procedure is estimated by comparing the spectral position of the most prominent features of the BG 36 spectrum after the calibration with their actual position known from the reference measurement in a standard spectrometer. The results are shown in Fig. 7b. Over the whole range of the white light continuum we find the deviations to be mostly within a  $\pm 50 \text{ cm}^{-1}$  window, which translates to a precision of  $\pm 0.5 \text{ nm}$  at 300 nm and  $\pm 2.5 \text{ nm}$  at 700 nm. This is in the range of the spectral spacing of the pixels.

### 3.2 Chirp correction procedure

Due to the chirp of the white light, the temporal overlap between pump and probe—or time zero—is wavelength dependent. This can be seen in Fig. 8a which shows the raw transient absorption of chloroform excited at 600 nm. The nominal delay of 0 fs is arbitrarily set at 400 nm. The temporal overlap of a certain component of the continuum with the pump pulse results in a coherent artifact (see Sect. 4.1). Its position is marked with filled circles in Fig. 8a and reveals that there is a  $\sim 1.5 \text{ ps}$  temporal dispersion between 300 and 750 nm, in good agreement with the calculated group velocity dispersion due to the optical components in the probe beam. To obtain the transient spectrum at a chosen delay time the raw data have to be corrected for the chirp. In a single-channel detection scheme this can be done online

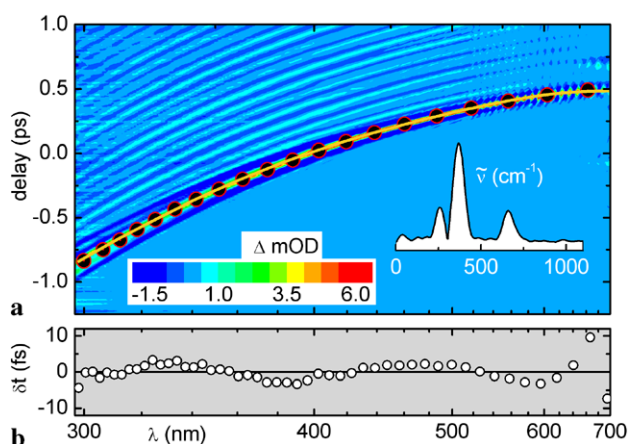


**Fig. 8** (a) Absorption changes of the white light continuum in pure chloroform ( $\lambda_{\text{exc}} = 600 \text{ nm}$ ,  $\tau_{\text{exc}} = 25 \text{ fs}$ ). Orange curve: polynomial fit to the center of the coherent artifact (filled circles). Inset: Fourier transform spectrum of the kinetic trace at 340 nm not including the coherent artifact. (b) Residuum of the polynomial fit to the time zero positions

during the measurement by adjusting the delay of the pump synchronously with the wavelength [72, 77]. For multichannel data acquisition the correction is best carried out after the measurement.

The proper chirp correction requires an accurate determination of the time zero. In degenerate pump-probe experiments, i.e. when the probe is a temporally shifted replica of the pump, one can use spectral interference on the detector to determine the time zero with an accuracy of 1 fs [38]. For nondegenerate broadband probing, the most commonly used methods are based on the coherent artifact [35, 36, 77, 78], even though the evaluation of the oscillatory signals arising from stimulated impulsive Raman scattering [79] has also been proposed [80]. The latter method has two requirements: The phase of the oscillation has to be known and the instrument response function has to be shorter than the vibrational period of the Raman active modes of the solvent molecules. It is therefore most useful for experiments with a time resolution better than  $\sim 50 \text{ fs}$ . With time resolutions between 50 and  $\sim 100 \text{ fs}$  impulsive Raman signals can still be observed for solvents like chloroform or dichloromethane which have low frequency vibrational modes. This case is shown in Fig. 8a where the oscillatory signals of chloroform are seen as stripes above the coherent artifact. The Fourier spectrum reveals three major contributions at 259, 367 and  $662 \text{ cm}^{-1}$  which closely match the known Raman active modes of chloroform.

When using other common solvents such as ethanol, acetonitrile or DMSO, the Raman active oscillations are more difficult to resolve and the determination of the time zero point is most easily done using the coherent artifact. Therefore, in most cases our chirp correction procedure relies on this method. To sufficient accuracy, the coherent artifact in a thin sample cuvette can be modeled by a Gaussian and/or its first and second time derivative [80]. About 20 time zero points are determined by fitting these functions to the raw data at selected wavelengths. We then fit a low order polynomial to these points to interpolate the time zero for the whole data set. This fit typically introduces an error  $\delta t$  of less than  $\pm 5 \text{ fs}$  into the chirp correction as shown in Fig. 8b. As discussed in Sect. 4.1, this is well below the time resolution of our setup. With the help of the chirp correction function the true transient spectra can be reconstructed by linear interpolation of the raw data along the time axis. Only after this chirp correction the molecular dynamics signatures are accessible to proper modeling in global fitting and target analysis [81].

## 4 Performance of the setup

So far we have presented the concept and implementation of our transient spectrometer and discussed the tuning range

for the molecular excitation as well the observation range for the probe light. Now we want to present the achieved performance parameters that are most relevant to the use in molecular and chemical dynamics. As with any other kind of spectroscopy the prime concerns are the spectral and temporal resolution and the sensitivity of the detection.

#### 4.1 Time resolution

A first estimate of the temporal resolution in a broadband experiment can be obtained from the width of the frequently observed coherent artifact [82]. By fitting a Gaussian and possibly its derivatives to the transients this can be done quantitatively. The FWHM of the Gaussian is taken as the time resolution and assumed to be very similar to the result of a crosscorrelation measurement performed in a thin nonlinear crystal. A measurement of the coherent artifact in the pure solvent is routinely obtainable with our setup for the whole spectral range of the white light (see Fig. 9a for ethanol). The single profile at 360 nm shown in Fig. 9b demonstrates the importance of the derivatives. Due to the varying group velocity mismatch [83] between the pump and the spectral components of the probe the width of the artifact varies with the probe wavelength, e.g., from 40 to 130 fs when a 120  $\mu\text{m}$  flow cell is used (see Fig. 9c).

In general, it is complicated to accurately resolve an ultrafast process whose signature coincides with the coherent artifact. It is therefore very helpful to minimize the amplitude and the temporal width of the artifact. Experiments and theoretical considerations have shown that both the cuvette windows and the sample solution contribute to the artifact. For commercial cuvettes the group velocity mismatch can elongate the artifact up to some hundred femtoseconds [84]. Then, in most cases the modeling with standard functions like Gaussians is not possible any more [85, 86]. This makes

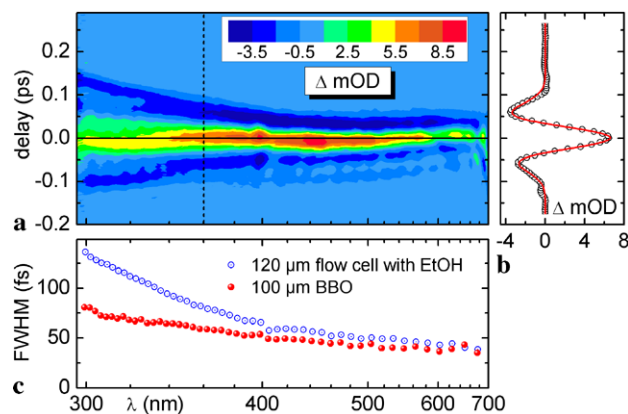


**Fig. 9** Time resolution as a function of wavelength: (a) coherent artifact obtained from a flow cell filled with ethanol ( $\lambda_{\text{exc}} = 510$  nm,  $\tau_{\text{exc}} = 28$  fs); (b) kinetic trace at 360 nm (circles) and Gaussian fit (solid line); (c) FWHM of the coherent artifact of (a) (open circles) and of a 100  $\mu\text{m}$  BBO crystal (filled circles)

the separation of the artifact and the very fastest molecular signatures very challenging and renders the resolution of few femtoseconds dynamics almost impossible for spectral regions far from the pump wavelength. For this very reason our flow cell is designed such that not only the thickness of the sample is kept as low as possible but also the windows are very thin (see Sect. 2.5). The artifact then only extends to several ten femtoseconds before and after time zero and ultrafast processes down to well below the 100 fs level can be observed.

It is interesting to note that the effective time resolution lies below the width of the artifact measured in the presence of windows. A good estimate is obtained by measuring the artifact in a crystal or glass plate whose thickness is comparable to the thickness of the sample solution alone. As shown in Fig. 9c the FWHM of the artifact measured in a 100  $\mu\text{m}$  BBO lies below 80 fs for the whole spectral range. A striking evidence of this discrepancy is the Fourier transform spectrum of the chloroform transients in Fig. 8 where the  $669\text{ cm}^{-1}$  mode is clearly resolved even in regions where the coherent artifact is much longer than the vibrational period of 50 fs. We can therefore estimate the actual time resolution that can routinely be achieved with our setup to be below 50 fs.

#### 4.2 Sensitivity, signal-to-noise ratio and quantitative measurement

To establish the sensitivity of the broadband spectrometer under realistic conditions and to determine the minimal detectable absorption change, we analyzed the noise of typical pump-probe traces like the ones shown in Figs. 8, 9, 12 and 13. For a purely statistical noise distribution the signal-to-noise ratio should increase with the square root of the averaging time. As mentioned in Sect. 2.7, we want to keep the total measurement time below 3 hours. With a laser repetition rate of 1 kHz, this corresponds to a maximum of  $5.4 \times 10^6$  recordable pairs of probe pulses with and without excitation of the sample. Using the quasi-exponential timescale described in Sect. 2.1, 400 sampled points are typically enough to cover the range up to 1 ns. With a duty cycle of the data acquisition of  $\sim 80\%$  this allows for a maximum of  $\sim 10^4$  averages per measured spectrum, usually split into several faster scans to account for any drift of the laser power and to allow for consistency checks. Under these conditions a statistical analysis of the signal before time zero returns a standard deviation, i.e. a detection sensitivity of the instrument of  $1 \times 10^{-4}$  OD over the whole spectral range. With 10 scans and 2000 averages for each we can even reach an average sensitivity of  $4.6 \times 10^{-5}$  OD, some spectral regions being even a factor of 4 better as shown in Fig. 10.

These values hold for both detection systems used in our lab, the PDA based and the CCD camera. This indicates that the dominant contribution to the noise observed in

our pump-probe spectrometer is the laser excess noise and nonstatistical fluctuations, whereas shot noise and electronic noise play only a minor role. In contrast to the standard approach, our setup presently does not include the detection of a reference beam, even though this might push the sensitivity to the  $10^{-6}$  OD level [46]. However, in this regime it would be likely that stimulated impulsive Raman signals are observed even in solvents with low intensity Raman bands. These oscillatory signals can mask the sought-after dynamics of the solute. Thus, at least for studies in liquid phase, a sensitivity of several ten  $\mu$ OD seems to be a practical limit and this is already reached in our comparatively simple setup.

The signal after time zero suffers from two sources of noise: the fundamental noise of the setup determined above and in addition the noise of the pump pulse. The latter does not contribute to the noise of the data in linear fashion, but has to be weighted with the induced transmission change ((9) in Ref. [46]). With maximum absorption changes of a few percent, this results in a contribution of the pump noise that is somewhat smaller than the fundamental noise. Thus, the noise in the data, both before and after time zero, is mainly determined by the uncorrelated fluctuations in the white light continuum. This renders a correction for the fluctuations of the pump light unnecessary. With the high signal-to-noise ratio of presently more than 500:1 we can observe for instance a pure exponential decay over the whole spectral range for over six decay time constants.

The high sensitivity together with the smooth profiles of the pump and probe pulses (see Sect. 2.4) allows us to report quantitative values for the time dependent absorption changes. In many spectroscopic reports only data scaled in arbitrary units are given. This neglects the important information that is contained in the strength of the transient absorptions, e.g., the concentration of the intermediates or their extinction coefficient. The latter is a most powerful tool for the identification of the intermediates.

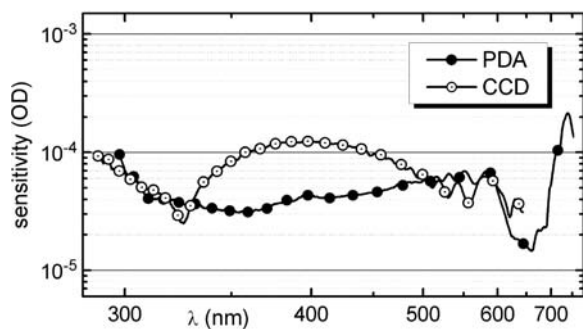


**Fig. 10** Typical detection sensitivities determined from the baseline of 10 accumulated scans with  $2 \times 10^3$  averages per point each. *Filled circles*: PDA based camera; *open circles*: CCD camera. The average sensitivities are  $4.6 \times 10^{-5}$  for the PDA and  $7.6 \times 10^{-5}$  OD for the CCD

### 4.3 Spectral resolution

To determine the spectral resolution of our home-built prism polychromator we measured the line widths of a mercury-neon calibration lamp (Pen-Ray; L.O.T.-Oriol GmbH (see footnote 1)). The obtained line spectrum is shown in Fig. 11a. To ensure that the optical imaging matches that of the white light continuum we placed the lamp in front of a  $50 \mu\text{m}$  pinhole. The latter was positioned at the focus of the continuum in the sample. Since the intensity of the cw-calibration lamp is much lower than that of the white light, we had to increase the integration time of the camera by a factor of 50. Therefore we replaced the kHz trigger from the laser with a 20 Hz TTL signal. After some averaging we obtained sharp lines over the whole spectral region. These lines can be associated to mercury transitions whereas the neon lines only show up shortly after the lamp is turned on and the temperature is still low. In principle the characteristic atomic lines could also be used for the wavelength calibration of the polychromator. However, the implementation in an everyday routine is somewhat more complicated and prone to errors than the use of the calibration filters described in Sect. 3.1.

The mercury lines can be fitted with Gaussian functions whose widths are plotted in Fig. 11b. At some wavelengths like 365 nm the spectrum consists of closely lying transitions. Their separation is close to the resolution of our setup and fitting them with a single Gaussian results in a FWHM value that is much larger than that of neighboring single lines. We therefore use as many Gaussians as the number of known transitions and fix the maxima according to the values given in the datasheet. The resulting FWHM values lie between  $50 \text{ cm}^{-1}$  in the UV and  $100 \text{ cm}^{-1}$  in the visible. This corresponds to a wavelength resolution as low as 0.5 nm. This is more than sufficient for UV/Vis spectroscopy

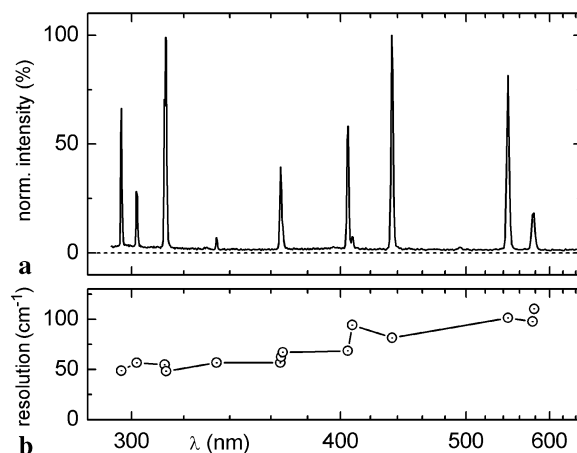


**Fig. 11** (a) Line spectrum of a mercury-neon lamp after the prism-based polychromator measured with the CCD camera. (b) Determined line widths (FWHM) from Gaussian fits to the atomic transitions. For closely lying transitions the centers of the Gaussian fits were fixed to the established values

in solution were typical bands have widths on the order of  $2000\text{ cm}^{-1}$ .

## 5 Representative data and modeling of the experimental recordings

### 5.1 Transient spectroscopy of naphthalene bisimide upon visible excitation

To illustrate the use of the new broadband pump-probe spectrometer for molecular dynamics we show data on a core-substituted naphthalene bisimide (NBI) after visible excitation in Fig. 12. The transient spectra were recorded with the PDA-based camera at 370 delay line positions between  $-15$  and  $300$  ps and are an average of three scans. Each spectrum in these scans is computed from 2500 pairs of white light pulses with and without excitation. The optical density of the sample solution at the excitation wavelength was set to  $\sim 0.2$  at a thickness of  $120\text{ }\mu\text{m}$ . This corresponds to a concentration of  $0.8\text{ mmol/l}$ . The energy of the pump light centered at  $620\text{ nm}$  was limited to  $80\text{ nJ}$  and focused to a

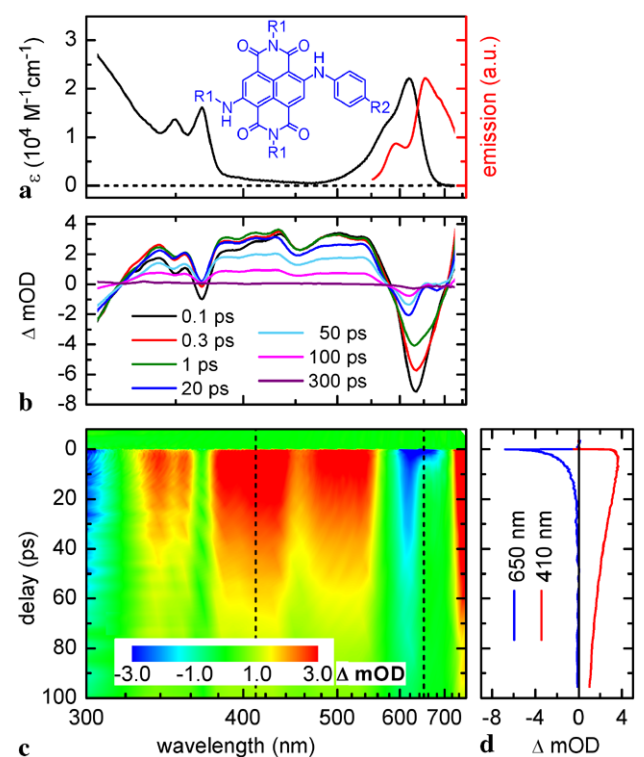


**Fig. 12** (a) Steady state absorption (black) and emission (red) of a core-substituted NBI dissolved in chloroform: R1=C<sub>8</sub>H<sub>17</sub>, R2=C<sub>4</sub>H<sub>9</sub>. (b) Transient spectra at selected delay times detected with the PDA-based camera after excitation with 20 fs pulses centered at 620 nm. The spectra represent horizontal slices out of the 2D data shown in (c). Two kinetic traces in the excited state absorption band at 410 nm and the stimulated emission band at 650 nm (dashed lines) are shown in (d)

diameter of  $150\text{ }\mu\text{m}$ . The stray light of the pump amounted to about 30% of the full molecular signal and was subtracted from the transient data using its signature at negative delay times.

Under these conditions, less than 10% of the molecules inside the pump volume are excited resulting in absorption changes between  $-7$  and  $+3\text{ mOD}$ . Although these changes are quite small, the high sensitivity of the setup still allows for a very good signal-to-noise ratio of, e.g., 75:1 at  $400\text{ nm}$ .

Due to the ultrabroad range of the CaF<sub>2</sub> white light we not only observe the ground state bleach of the first excited state around  $620\text{ nm}$ , but also the signature of the second electronic transition at  $368\text{ nm}$  and the onset of higher transitions below  $320\text{ nm}$ . In these spectral regions the ground state bleach does not overlap with the stimulated emission and is not distorted by stray light from the pump. By comparison to the excited state absorption (ESA) signal in spectral regions without ground state absorption, an unambiguous determination of the dynamics of the ground state recovery is therefore possible. This is especially helpful in two important situations. If an optically dark photoproduct is irreversibly generated, a residual bleach signal can allow for an accurate calculation of its quantum yield. A differing decay of the ground state bleach and the ESA indicates long lived intermediates.

The inspection of the data in Fig. 12 reveals that the kinetics indeed differs significantly for well separated spectral regions. Between  $380$  and  $550\text{ nm}$  the signal is dominated by a fairly structureless ESA. As seen in the red curve of Fig. 12d, the major contribution to the ESA signal appears instantaneously with the optical excitation and rises only slightly to its maximum within a few picoseconds. The most prominent dynamics is given by a large amplitude decay on the time scale of tens of picoseconds. In contrast, the decay in the region of the stimulated emission around  $650\text{ nm}$  occurs predominantly on the few picosecond time scale. This finding explains the unusual steady state fluorescence spectrum shown in Fig. 12a which features a contribution from higher vibrational levels of the S<sub>1</sub> state at  $590\text{ nm}$ : The electronic excitation decays before the vibrational cooling is completed and therefore resonance emission is comparable to the vibrationally relaxed one. Situations of this kind clearly show the importance of multichannel detection for the gain of a complete picture of the excited state dynamics of the molecular system under investigation.

### 5.2 Ultrafast photochemistry of diphenylmethyl chloride upon UV excitation

In a second showcase example we performed measurements on diphenylmethyl chloride (DPMC) in acetonitrile solution. These data were recorded with the CCD camera in three scans between  $-100$  and  $+1900\text{ ps}$  each with  $2000$

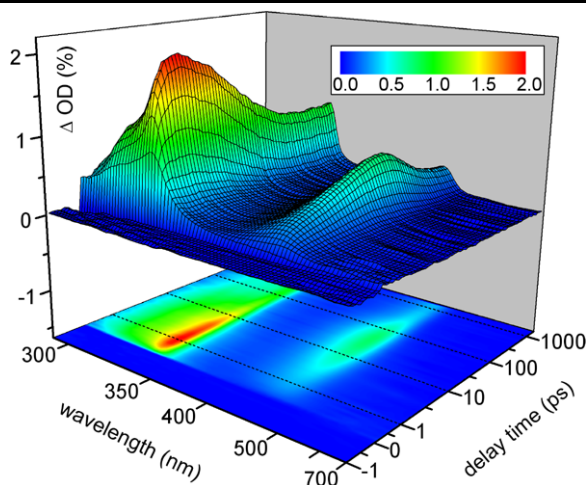


**Fig. 13** Transient absorption spectra of diphenylmethyl chloride in acetonitrile after 270 nm excitation detected with the CCD camera. The delay time axis is linear between  $-1$  and  $+1$  ps and logarithmic between  $1$  and  $1900$  ps. The coherent artifact around time zero has been omitted from the graph. The absorption band at  $330$  nm is assigned to the radical pair and the one at  $435$  nm to the formation of an ion pair

averages per spectrum. The pump wavelength was tuned to the first absorption band at  $270$  nm. Since this transition is much weaker than the one pumped in NBI—the extinction coefficient at  $270$  nm is only  $400 \text{ l mol}^{-1} \text{ cm}^{-1}$ —the pump photon density has to be increased. We therefore focused  $140$  nJ of the UV light down to a beam diameter of  $80 \mu\text{m}$  in the sample leading to an excitation probability of roughly  $0.5\%$ . The concentration  $c_{\text{DPMC}} = 40 \text{ mmol/l}$  also had to be chosen much higher to reach an optical density of  $0.2$  in the  $120 \mu\text{m}$  flow cell.

The transient spectra are depicted in Fig. 13 as a pseudo-3D plot which shows two induced absorption bands with maxima at  $330$  and  $435$  nm, well outside the absorption spectrum of DPMC. They correspond to the diphenylmethyl radical and the benzhydrylium cation that are formed by the photo-induced dissociation of DPMC. The rise of the bands in the first few hundred femtoseconds monitors the cleavage of the C–Cl bond, the first step of the photochemical reaction. The native ratio of ion pair to radical pair is subsequently increased by an intermolecular electron transfer from the diphenylmethyl radical to the chlorine radical. This is seen in the concerted decay (radical) and rise (cation) of the two bands on the time scale of  $20$  ps. At larger delay times above  $100$  ps, the decay of the cation band reflects the geminate recombination with the chloride anion. A more detailed analysis of the dynamics will be given in a future publication.

This example shows again the importance of a spectrally broad probe window as this allows one to fully resolve the signatures of all relevant photoproducts. Since the reaction dynamics has contributions from the femtosecond to the nanosecond regime, the implementation of the non-linear

sampling time scale is a key point for a direct understanding of the underlying processes. In addition, the multichannel detection in combination with the high spectral resolution enables us to observe and quantitatively treat shifts and spectral narrowing of bands that occur, e.g., due to solvation or vibrational cooling. A thorough analysis of the cation band indeed reveals such a shift by about  $5$  nm. Since transient absorption spectroscopy is a method that provides absolute values, knowing the relevant experimental parameters allows for a precise quantitative analysis and in this case is capable of supplying absolute quantum yields of the ultrafast photodissociation.

### 5.3 Post-processing of multichannel data: analysis of the ultrafast molecular dynamics

The availability of a 2D data set from the multichannel detection permits and requires a different post-processing than in the case of single-channel spectra or kinetic curves. The analysis we perform does not just aim at the full parameterization of the data obtained but rather follows a spectroscopy oriented approach. That means we use the available knowledge, e.g., from own steady state measurements or the literature to stepwise gain full insight into the mechanisms of the ultrafast processes on the molecular level.

To achieve this goal, at first we study the dynamics at distinguished positions throughout the whole spectrum like the maxima of the radical and ion bands in Fig. 13, but also in between for the determination of the ESA contribution. We have therefore developed a LabView routine that allows us to perform fits of kinetic traces which we obtain by averaging the data from a freely selectable number of neighboring pixels. Thus, step by step we can gather first hints of the relevant time scales for the different processes we observe. The fit function  $F(t)$  we employ can thereby change according to the model we assume. In case of a simple rate model it can be written as:

$$F(t) = \text{IRF} \otimes \left\{ \theta(t) \cdot \left[ \sum_i A_i \exp\left(\frac{-t}{\tau_i}\right) + \text{const} \right] \right\} + \text{artifact}. \quad (6)$$

It consists of the instrumental response function IRF convoluted with the product of the step function  $\theta$  and a sum of exponentials. If necessary, the fit function in our program can be augmented with damped oscillations or stretched exponentials [87].

Our LabView code also includes the calculation of the correlation matrix of all possible pairs of fit parameters. If one of the off-diagonal elements in this matrix approaches  $\pm 1$ , the correlation of the two parameters is very high leading to compensation effects. This is an indication that more free parameters are used than are supported by the data. We

therefore use the correlation matrix to avoid too many exponential functions to characterize the observed dynamics. This approach is comparable to other proposed methods like singular value decomposition [39, 88], however less affected by noise in the data.

The fits of kinetic traces at single spectral positions often result in a systematic variation of the locally determined time constants. This can have technical reasons like varying contributions of the noise in the data, but it can more importantly be a consequence of an incomplete model. For example, the overwhelmingly used rate models do not include solvation, internal vibrational redistribution or vibrational cooling. These processes lead to spectral shifts as well as narrowing and broadening of bands. If these contributions are small compared to the absorption changes due to the population dynamics, a global fit can be used to find a unique set of decay time constants for the whole system. Our global analysis is based on the formalism developed by Fita et al. [89] which extracts decay associated difference spectra [90] from the transient data. The consistency of the obtained results can be checked with the help of qualitative data visualization methods like the logarithmic differentiation of the absorption changes [88].

If however the spectral shifts become dominant, then the evaluation of band integrals helps to disentangle electronic dynamics from solvation and vibrational relaxation. This method is best suited for isolated bands in the transient absorption spectra like the cation and the radical band in Fig. 13. Then, the integral  $\int d\lambda \frac{OD}{\lambda}$  is proportional to the transition dipole moment squared [91, 92] and to the population of the absorbing electronic state. Therefore, the temporal evolution of the integral allows one to directly evaluate the population transfer between electronic states or chemical species. In some cases, the spectral shift itself is the quantity of interest, as it can for instance yield information on solvation dynamics [63, 93, 94]. Then, a spectral decomposition into the different contributing signals such as excited state absorption and stimulated emission can be used to quantify the shift of the individual bands [73].

These examples demonstrate that the multichannel data in the broad detection range between 290 and 720 nm lend themselves to a wealth of post-processing strategies that put the interpretation and modeling on solid ground. The quality of the final picture is closely related to the understanding and correct implementation of the technical and spectroscopic concepts presented in this paper. Almost all of these issues have been previously assessed by other groups. However, only the appropriate combination of all of them renders the described state-of-the-art spectrometer.

Changes in different directions are always possible, e.g., shifting the probe supercontinuum further towards the mid IR [45], using more advanced compression techniques to obtain even shorter excitation pulses [47] or replacing the

flow cell with a liquid jet [95]. The exact implementation depends on the particular requirements of the investigated sample. By combining tunable excitation with highly sensitive broadband detection and a simple but thoroughly conceived optical design the spectrometer as presented here allows for the investigation of a large variety of spectroscopic problems whilst keeping the technical flexibility necessary to address even more challenging systems.

**Acknowledgements** A large number of previous members of the group have made significant contributions to the development of the setup to its present state, namely Prof. S. Lochbrunner, Dr. U. Schmidhammer, Dr. V. deWaele, Dr. C. Elsner, A. Arsenyev, M. Schlosser, J. Piel, S. Schindlbeck and A. Böck. We also thank Prof. W. Zinth and his coworkers as well as Prof. N. Ernsting for many valuable suggestions and comments. We thank Prof. B. Lang for his advice concerning the CCD camera. Furthermore, we thank Prof. F. Würthner for supplying us with the NBI samples. Last but not least we gratefully acknowledge financial support from the International Max Planck Research School on Advanced Photon Science (U.M.), the Alexander von Humboldt Stiftung (I.P.), the SFB 749 (Dynamics and Intermediates of Molecular Transformations) and the DFG-Cluster of Excellence: Munich-Centre for Advanced Photonics.

## References

1. A.H. Zewail, *J. Phys. Chem. A* **104**, 5660 (2000)
2. R. Danielius, A. Piskarskas, A. Stabinis, G.P. Banfi, P. Di Trapani, R. Righini, *J. Opt. Soc. Am. B* **10**, 2222 (1993)
3. P. Hamm, C. Lauterwasser, W. Zinth, *Opt. Lett.* **18**, 1943 (1993)
4. F. Seifert, V. Petrov, M. Woerner, *Opt. Lett.* **19**, 2009 (1994)
5. V. Petrov, F. Rotermund, F. Noack, *J. Opt. A* **3**, R1 (2001)
6. T. Wilhelm, J. Piel, E. Riedle, *Opt. Lett.* **22**, 1494 (1997)
7. E. Riedle, M. Beutter, S. Lochbrunner, J. Piel, S. Schenkl, S. Spörlein, W. Zinth, *Appl. Phys. B* **71**, 457 (2000)
8. J. Piel, M. Beutter, E. Riedle, *Opt. Lett.* **25**, 180 (2000)
9. G. Cerullo, S. De Silvestri, *Rev. Sci. Instrum.* **74**, 1 (2003)
10. A.J. Wurzer, T. Wilhelm, J. Piel, E. Riedle, *Chem. Phys. Lett.* **299**, 296 (1999)
11. K. Stock, T. Bizjak, S. Lochbrunner, *Chem. Phys. Lett.* **354**, 409 (2002)
12. V. de Waele, M. Beutter, U. Schmidhammer, E. Riedle, J. Daub, *Chem. Phys. Lett.* **390**, 328 (2004)
13. A. Baltuska, T. Kobayashi, *Appl. Phys. B* **75**, 427 (2002)
14. M. Zavelani-Rossi, D. Polli, G. Cerullo, S. de Silvestri, L. Gallmann, G. Steinmeyer, U. Keller, *Appl. Phys. B* **74**, S245 (2002)
15. P. Baum, S. Lochbrunner, E. Riedle, *Opt. Lett.* **29**, 1686 (2004)
16. G. Cerullo, C. Manzoni, L. Lüer, D. Polli, *Photochem. Photobiol. Sci.* **6**, 135 (2007)
17. D. Polli, M.R. Antognazza, D. Brida, G. Lanzani, G. Cerullo, S. De Silvestri, *Chem. Phys.* **350**, 45 (2008)
18. R.R. Alfano, *The Supercontinuum Laser Source* (Springer, Berlin, 2005)
19. A. Lochschmidt, N. Eilers-Knig, N. Heineking, N.P. Ernsting, *J. Phys. Chem. A* **103**, 1776 (1999)
20. A. Sugita, T. Furuhi, M. Yamashita, T. Kobayashi, *J. Phys. Chem. A* **106**, 581 (2002)
21. G. Duvanel, N. Banerji, E. Vauthey, *J. Phys. Chem. A* **111**, 5361 (2007)
22. D.B. Spry, A. Goun, M.D. Fayer, *J. Phys. Chem. A* **111**, 230 (2007)
23. V. Nagarajan, E. Johnson, P. Schellenberg, W. Parson, R. Windeler, *Rev. Sci. Instrum.* **73**, 4145 (2002)

24. R. Huber, T. Köhler, M.O. Lenz, E. Bamberg, R. Kalmbach, M. Engelhard, J. Wachtveitl, *Biochemistry* **44**, 1800 (2005)
25. A.N. Tarnovsky, W. Gawelda, M. Johnson, C. Bressler, M. Chergui, *J. Phys. Chem. B* **110**, 26497 (2006)
26. A.V. Zamyatin, A.V. Soldatova, M.A.J. Rodgers, *Inorg. Chim. Acta* **360**, 857 (2007)
27. J.L. Pérez Lustres, A.L. Dobryakov, A. Holzwarth, M. Veiga, *Angew. Chem. Int. Ed.* **46**, 3758 (2007)
28. T.A. Zeidan, Q. Wang, T. Fiebig, F.D. Lewis, *J. Am. Chem. Soc.* **129**, 9848 (2007)
29. V. Karunakaran, K. Kleiner, R. Improta, S.A. Kovalenko, *J. Am. Chem. Soc.* **131**, 5839 (2009)
30. C. Ley, J. Brazard, F. Lacombat, P. Plaza, M.M. Martin, G.A. Kraus, J.W. Petrich, *Chem. Phys. Lett.* **457**, 82 (2008)
31. P.Z. El-Khoury, A.N. Tarnovsky, *Chem. Phys. Lett.* **453**, 160 (2008)
32. M. Seel, E. Wildermuth, W. Zinth, *Meas. Sci. Technol.* **8**, 449 (1997)
33. T. Hirsch, H. Port, H.C. Wolf, B. Miehl, F. Effenberger, *J. Phys. Chem. B* **101**, 4525 (1997)
34. R. Croce, M.G. Müller, R. Bassi, A.R. Holzwarth, *Biophys. J.* **80**, 901 (2001)
35. A. Maciejewski, R. Naskrecki, M. Lorenc, M. Ziolk, J. Karolczak, J. Kubicki, M. Matysiak, M. Szymanski, *J. Mol. Struct.* **555**, 1 (2000)
36. M. Raytchev, E. Pandurski, I. Buchvarov, C. Modrakowski, T. Fiebig, *J. Phys. Chem. A* **107**, 4592 (2003)
37. S. Laimgruber, H. Schachenmayr, B. Schmidt, W. Zinth, P. Gilch, *Appl. Phys. B* **85**, 557 (2006)
38. D. Polli, L. Lüer, G. Cerullo, *Rev. Sci. Instrum.* **78**, 103108 (2007)
39. N.P. Ernsting, S.A. Kovalenko, T. Senyushkina, J. Saam, V. Farztdinov, *J. Phys. Chem. A* **105**, 3443 (2001)
40. L. Boilet, G. Buntinx, C. Lefumeux, O. Poizat, *J. Photochem. Photobiol. A* **163**, 529 (2004)
41. A.C. Moskun, S.E. Bradforth, J. Thøgersen, S. Keiding, *J. Phys. Chem. A* **110**, 10947 (2006)
42. H.C. Wang, Y.C. Lu, C.Y. Chen, C.C. Yang, *Opt. Express* **15**, 3417 (2007)
43. M.K. Reed, M.K. Steiner-Shepard, M.S. Armas, D.K. Negus, *J. Opt. Soc. Am. B* **12**, 2229 (1995)
44. J.B. Ashcom, R.R. Gattass, C.B. Schaffer, E. Mazur, *J. Opt. Soc. Am. B* **23**, 2317 (2006)
45. M. Bradler, P. Baum, E. Riedle, *Appl. Phys. B* (2009, submitted)
46. C. Schrieffer, S. Lochbrunner, E. Riedle, D.J. Nesbitt, *Rev. Sci. Instrum.* **79**, 13107 (2008)
47. P. Baum, S. Lochbrunner, E. Riedle, *Appl. Phys. B* **79**, 1027 (2004)
48. P. Baum, M. Breuer, E. Riedle, *Opt. Lett.* **31**, 2220 (2006)
49. I.Z. Kozma, P. Baum, S. Lochbrunner, E. Riedle, G. Steinmeyer, *Opt. Express* **11**, 3110 (2003)
50. I.Z. Kozma, P. Baum, U. Schmidhammer, S. Lochbrunner, E. Riedle, *Rev. Sci. Instrum.* **75**, 2323 (2004)
51. T. Bizjak, J. Karpiuk, S. Lochbrunner, E. Riedle, *J. Phys. Chem. A* **108**, 10763 (2004)
52. B. Schmidt, C. Sobotta, S. Malkmus, S. Laimgruber, M. Braun, W. Zinth, P. Gilch, *J. Phys. Chem. A* **108**, 4399 (2004)
53. J. Savolainen, D. van der Linden, N. Dijkhuizen, J.L. Herek, *J. Photochem. Photobiol. A* **196**, 99 (2008)
54. J.M. Klopff, P. Norris, *Appl. Surf. Sci.* **253**, 6305 (2007)
55. G. Buntinx, R. Naskrecki, O. Poizat, *J. Phys. Chem.* **100**, 19380 (1996)
56. R. Huber, H. Satzger, W. Zinth, J. Wachtveitl, *Opt. Commun.* **194**, 443 (2001)
57. P. Tzankov, I. Buchvarov, T. Fiebig, *Opt. Commun.* **203**, 107 (2002)
58. C. Nagura, A. Suda, H. Kawano, M. Obara, K. Midorikawa, *Appl. Opt.* **41**, 3735 (2002)
59. J.M. Dudley, G. Genty, S. Coen, *Rev. Mod. Phys.* **78**, 1135 (2006)
60. P.B. Corkum, C. Rolland, T. Srinivasan-Rao, *Phys. Rev. Lett.* **57**, 2268 (1986)
61. S.A. Trushin, S. Panja, K. Kosma, W.E. Schmid, W. Fuß, *Appl. Phys. B* **80**, 399 (2005)
62. E. Goulielmakis, S. Koehler, B. Reiter, M. Schultze, A.J. Verhoef, E.E. Serebryannikov, A.M. Zheltikov, F. Krausz, *Opt. Lett.* **33**, 1407 (2008)
63. V. Karunakaran, M. Pfaffe, I. Ioffe, T. Senyushkina, S.A. Kovalenko, R. Mahrwald, V. Farztdinov, H. Sklenar, N.P. Ernsting, *J. Phys. Chem. A* **112**, 4294 (2008)
64. I. Buchvarov, A. Trifonov, T. Fiebig, *Opt. Lett.* **32**, 1539 (2007)
65. V. Kartazayev, R.R. Alfano, *Opt. Commun.* **281**, 463 (2008)
66. R.S.S. Kumar, K.L.N. Deepak, D.N. Rao, *Phys. Rev. A* **78**, 43818 (2008)
67. A. Brodeur, S.L. Chin, *J. Opt. Soc. Am. B* **16**, 637 (1999)
68. V.P. Kandidov, O.G. Kosareva, I.S. Golubtsov, W. Liu, A. Becker, N. Akozbek, C.M. Bowden, S.L. Chin, *Appl. Phys. B* **77**, 149 (2003)
69. V.M. Farztdinov, A.L. Dobryakov, V.S. Letokhov, Y.E. Lozovik, Y.A. Matveets, S.A. Kovalenko, N.P. Ernsting, *Phys. Rev. B* **56**, 4176 (1997)
70. M. Kandyala, T. Shih, E. Mazur, *Phys. Rev. B* **75**, 214107 (2007)
71. H. Marciniak, M. Fiebig, M. Huth, S. Schiefer, B. Nickel, F. Selmaier, S. Lochbrunner, *Phys. Rev. Lett.* **99**, 176402 (2007)
72. U. Schmidhammer, U. Megerle, S. Lochbrunner, E. Riedle, J. Karpiuk, *J. Phys. Chem. A* **112**, 8487 (2008)
73. U. Megerle, F. Selmaier, C. Lambert, E. Riedle, S. Lochbrunner, *Phys. Chem. Chem. Phys.* **10**, 6245 (2008)
74. M. Barbatti, A.J.A. Aquino, H. Lischka, C. Schrieffer, S. Lochbrunner, E. Riedle, *Phys. Chem. Chem. Phys.* **11**, 1406 (2009)
75. W. Zinth, U. Zinth, *Optik* (Oldenbourg, München, 2009)
76. E.A. Juban, J.K. McCusker, *J. Am. Chem. Soc.* **127**, 6857 (2005)
77. V.I. Klimov, D.W. McBranch, *Opt. Lett.* **23**, 277 (1998)
78. S.A. Kovalenko, N.P. Ernsting, J. Ruthmann, *Chem. Phys. Lett.* **258**, 445 (1996)
79. S. Ruhman, A.G. Joly, K.A. Nelson, *J. Chem. Phys.* **86**, 6563 (1987)
80. S.A. Kovalenko, A.L. Dobryakov, J. Ruthmann, N.P. Ernsting, *Phys. Rev. A* **59**, 2369 (1999)
81. W. Wohlleben, T. Backup, J.L. Herek, R.J. Cogdell, M. Motzkus, *Biophys. J.* **85**, 442 (2003)
82. M. Rasmusson, A.N. Tarnovsky, E. Akesson, V. Sundström, *Chem. Phys. Lett.* **335**, 201 (2001)
83. I.Z. Kozma, P. Krok, E. Riedle, *J. Opt. Soc. Am. B* **22**, 1479 (2005)
84. M. Ziolk, M. Lorenc, R. Naskrecki, *Appl. Phys. B* **72**, 843 (2001)
85. K. Ekvall, P. van der Meulen, C. Dhollande, L.-E. Berg, S. Pommeret, R. Naskrecki, J.-C. Mialocq, *J. Appl. Phys.* **87**, 2340 (2000)
86. M. Lorenc, M. Ziolk, R. Naskrecki, J. Karolczak, J. Kubicki, A. Maciejewski, *Appl. Phys. B* **74**, 19 (2002)
87. G. Williams, D.C. Watts, *Trans. Farad. Soc.* **66**, 80 (1970)
88. H. Satzger, W. Zinth, *Chem. Phys.* **295**, 287 (2003)
89. P. Fita, E. Luzina, T. Dziembowska, C. Radzewicz, A. Grabowska, *J. Chem. Phys.* **125**, 184508 (2006)
90. I.H.M. van Stokkum, D.S. Larsen, R. van Grondelle, *Biochim. Biophys. Acta* **1657**, 82 (2004)
91. S.J. Strickler, R.A. Berg, *J. Chem. Phys.* **37**, 814 (1962)
92. A.P. Thorne, *Spectrophysics* (Chapman and Hall, London, 1974)
93. M.L. Horng, J.A. Gardecki, A. Papazyan, M. Maroncelli, *J. Phys. Chem.* **99**, 17311 (1995)
94. J.L. Pérez Lustres, S.A. Kovalenko, M. Mosquera, T. Senyushkina, W. Flasche, N.P. Ernsting, *Angew. Chem. Int. Ed.* **44**, 5635 (2005)
95. M.J. Tauber, R.A. Mathies, X. Chen, S.E. Bradforth, *Rev. Sci. Instrum.* **74**, 4958 (2003)





## **Appendix A2**

### **Laboratory apparatus for the accurate, facile and rapid determination of visible light photoreaction quantum yields**

*U. Megerle, R. Lechner, B. König, E. Riedle*

Photochemical & Photobiological Sciences 9, 1400-1406 (2010)



# Laboratory apparatus for the accurate, facile and rapid determination of visible light photoreaction quantum yields†

Uwe Megerle,<sup>a</sup> Robert Lechner,<sup>b</sup> Burkhard König<sup>b</sup> and Eberhard Riedle<sup>\*a</sup>

Received 25th June 2010, Accepted 13th August 2010

DOI: 10.1039/c0pp00195c

A novel setup for the direct determination of the quantum yield in photocatalytic and photochemical processes is reported. It combines the opto-electronic measurement of the absorbed amount of light with established quantitative chemical analysis of the products. High power visible LEDs are found to be convenient light sources for the illumination without the need for spectral filtering. The LED output can be imaged efficiently and in a controlled fashion into the sample. The residual transmitted light is continuously monitored by a dedicated and calibrated solar cell. The setup can be used under the conditions of a chemical synthesis laboratory. All information needed for the assembly and operation of the device is made available. The performance is validated by comparison to standard chemical actinometry and by the determination of quantum yields for reactions reported by others and ones investigated in our own laboratory.

## 1. Introduction

Solar irradiation is the only sustainable energy source on earth. Its utilization to generate electric power in silicon based solar cells has reached high technical levels and found broad commercial application. Only recently the less explored use of visible light to drive endothermic processes or to accelerate chemical reactions has found widespread interest.<sup>1</sup> Besides the more classical photochemical processes the application of chemical photocatalysts is rapidly gaining importance.<sup>2–9</sup> For all photochemical conversions the quantum yield will eventually, beside the chemical yield, determine the commercial success and the importance of a given process. Only for a high quantum yield, *i.e.* a large fraction of absorbed photons leading to the desired product, the use of light as a reagent will be justified. However, many reports claiming the sustainable utilization of solar energy for chemical reactions lack an accurate determination of their photoefficiency. Therefore it is most important to have a readily available laboratory procedure to measure the quantum yield.<sup>10,11</sup>

Recently, Maschmeyer and Che emphasized the importance of a simple and practical way to normalize the performance of photocatalysts.<sup>12</sup> The situation may be particularly complex for heterogeneous catalytic systems, but also for homogeneous catalysis only a few determinations of the quantum yield are found. The reason for this deficit could well be that the classical chemical actinometric procedures as standardized by IUPAC<sup>13–15</sup> and newly developed ones<sup>16–18</sup> are often laborious and in most instances only suitable for the UV. Even the use of dye solutions in combination with suitable detection electronics as photon counters<sup>19</sup> needs

a complicated calibration if not only the variation of the yield with wavelength is to be determined. We report here a novel opto-electronic device for the rapid and facile determination of absolute quantum yields for visible light photoreactions under the conditions of a chemical synthesis laboratory. The method builds on the documented preparative use of high power LEDs<sup>5,6,20</sup> and just adds the quantitative determination of the two relevant factors determining the process quantum yield, the absorbed amount of light and the amount of product.

## 2. LED-based setup for quantitative irradiation

### 2.1 High power LEDs for illumination

A number of classical light sources have been established for photochemistry and photocatalysis. They include mercury lamps, halogen lamps or lately energy-saving light bulbs. For selection of desired wavelength regions, solid state or solution filters are added or the spectrum is limited by a polychromator. For more fundamental studies aimed at a precise understanding of processes laser sources are used. Green chemistry tries to utilize all or a sizable part of the solar spectrum.

Recently it has been suggested to use a photon source as similar to sunlight as possible for standardization of photocatalytic systems.<sup>12</sup> This is certainly the proper choice in terms of normalization and possible technical applications, whereas a more detailed and optically oriented approach will help to enhance the understanding at the molecular level. Photocatalytic chromophores absorb only selected parts of the visible spectrum. A typical example is flavin which is found as cofactor in many enzymes but is also used in synthetic photocatalysis.<sup>3,4</sup> If the absorption spectrum of flavin (Fig. 1(a)) is compared to the solar irradiance at the earth surface<sup>21</sup> (Fig. 1(c)), it is obvious that a large fraction of the light intensity is lost and the determination of the number of actually absorbed photons is difficult. The same holds for mercury lamps, halogen lamps or energy-saving light bulbs. In addition, it is not at all easy to collect and direct the light from these sources into the sample cell in a defined way.

<sup>a</sup>Lehrstuhl für BioMolekulare Optik, Ludwig-Maximilians-Universität (LMU), Oettingenstr. 67, 80538 München, Germany. E-mail: riedle@physik.lmu.de; Fax: +49 89 2180 9202; Tel: +49 89 2180 9210

<sup>b</sup>Institut für Organische Chemie, Fakultät für Chemie und Pharmazie, Universität Regensburg, D-93040 Regensburg, Germany

† Electronic supplementary information (ESI) available: Design drawings, hints for assembly and adjustment of the device. See DOI: 10.1039/c0pp00195c

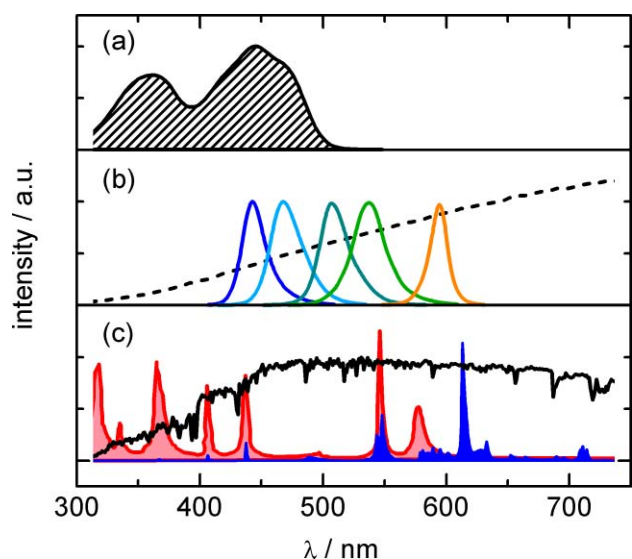


**Fig. 1** (a) Absorption spectrum of riboflavin tetra acetate in MeCN–H<sub>2</sub>O (50:50) solution. (b) Emission spectrum of a “100 W” halogen light bulb (nominal electrical consumption, dashed line) and typical high power LEDs (solid lines): LXHL-LR3C, LXHL-LB3C, LXHL-LE3C, LXHL-MM1C, LXHL-ML1C (from left to right). (c) Light sources: “100 W” Hg lamp (red line), “15 W” energy-saving light bulb (blue) and sun light at the earth surface (black line).

An alternative is to use modern high power light emitting diodes (LEDs). They can provide high photon fluxes at a variety of well defined spectral bands which allows the choice of the optimized light source for a given visible light photoreaction.<sup>4-6,22</sup> UV sources with comparable properties will likely be available quite soon. As shown in Fig. 1(b), the width of each spectrum matches well typical molecular absorption bands in solution. This avoids the need for spectral filtering and allows a uniform illumination without bleaching effects or restrictions to strong atomic lines. Blocking of undesired spectral regions, in particular near infrared and “heat”, which has to be explicitly performed for classical lamps, is automatically ensured with LEDs.

Commercial high power LEDs are available at the level of 1, 3 or 5 W electrical power. The optical output is about 10%, so a nominal 3 W LED supplies 300 mW of light. This total optical power is emitted with Lambertian characteristic, additional molded optics are sometimes added to reduce the viewing angle of 140° to smaller values.

## 2.2 Imaging with a photographic lens

In preliminary experiments we compared the possibility of imaging and utilizing the output of various LEDs. We found that the initial advantage of small viewing angles provided by the on-device optics is more than offset by the reduced beam quality. With the basic Lambertian units a good optical imaging is in principal possible. Due to the small size of the die (the emitting semiconductor chip), the imaging of the LED emission is greatly simplified compared to light bulbs.

For the imaging optics we compared singlet lenses and simple lens combinations, condenser arrangements, aspheric lenses and commercially available photographic lenses. Interestingly and most welcome, the least expensive photographic lenses proved

to be by far superior to all other options typically used in an optics laboratory. With its achromatic design for the whole visible spectrum, an extremely large numerical aperture, compact build and nearly perfect anti-reflection coating, a photographic lens is the ideal solution. It even provides an integrated adjustable and reproducible aperture for the regulation of the throughput and the focusing mechanics for the fine adjustment of the imaging. The lens materials and AR coatings allow the use from 380 to 800 nm.

A scheme of the resulting LED-based irradiation setup is shown in Fig. 2 together with a photograph of the assembled device. The light from a 3 W LED (Luxeon LXHL series; Philips Lumileds Lighting Company<sup>23</sup>) is imaged into the sample contained in a standard 10 mm cuvette with a fast photographic lens of  $f = 50$  mm (Nikkor AF-S 50/1.4 G; Nikon GmbH,<sup>23</sup> sold at about €300). The large aperture of  $f/1.4$  together with the high imaging quality (aplanatic design) of the photographic lens ensures an efficient utilization of the available photons and a high degree of control and reproducibility of the illumination. The fine structure of the die can be clearly resolved at the image plane in the center of the cuvette.<sup>24</sup>

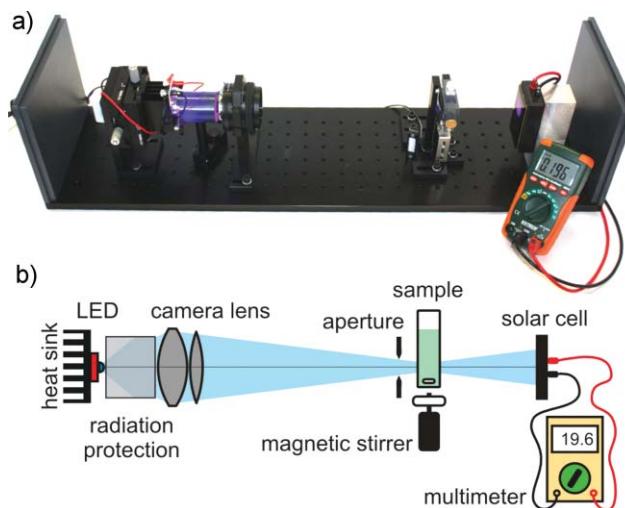


**Fig. 2** (a) Photograph of the compact and portable setup for quantitative irradiation. (b) Schematic of the setup with a high-power light emitting diode as light source and a multimeter connected to a solar cell as light detector.

An optimum distance between the LED and the sample can be found that keeps the image of the die to less than the 10 mm aperture of the cuvette and collects as large a solid angle of the emitted light as possible. Most of the light is collected if the spacing between the LED and the lens is close to the focal length. This does, however, place the image and thereby the smallest irradiated area far away from the lens. Consequently the image is much larger than the available aperture and light is lost. Conversely, tight imaging leads to a larger LED–lens distance and a smaller collection angle. The light not properly imaged by the lens is blocked by a cylindrical radiation protection between the LED and the lens and a rectangular aperture in front of the cuvette. Overall we succeeded in imaging nearly 10% of the LED output into the sample.

### 2.3 Absolute power detection with a solar cell

The defined, near perpendicular incidence of the radiation on the sample allows for an accurate determination of the number of absorbed photons by measuring the radiant power in the transmitted beam with and without sample (see section 2.4). In laser optics, the standard way to do this is by using a rather expensive commercial powermeter based on a photodiode or a thermopile. However, available units with sufficient sensitivity suffer from small apertures on the order of 10 mm diameter. To measure the transmitted power, the detector has to be placed behind the sample cell where the beam profile typically covers an area of more than  $10 \times 10 \text{ mm}^2$ . We therefore searched for an alternative and found that the geometrical constraints can be circumvented with the use of a commercially available solar cell as detector.

When no current is drawn from the cell, the voltage across a sufficiently illuminated photocell is given roughly by the bandgap of the material, usually Si with an open circuit voltage of 0.7 V. Increase of the illumination does not change this voltage. The cell can, however, also be operated as a current source and the current converted into a voltage drop across a resistor with a small resistance. This illumination dependent voltage drop can then be displayed with a readily available multimeter.

We chose a model 191281-EB photocell (active area of  $2 \times 3 \text{ cm}^2$ ; Conrad Electronic SE<sup>23</sup>) with a rated voltage of 0.5 V at a rated current of 400 mA. A termination of around  $50 \Omega$  was found suitable (see below). With 20 mW light at the sample and illuminating an area of at least  $10 \times 10 \text{ mm}^2$  on the photocell placed slightly behind the sample cell, the irradiance (intensity) on the photocell is less than  $200 \text{ W m}^{-2}$ . This is well below the solar irradiation at the earth surface of  $710 \text{ W m}^{-2}$  (AM1.5 direct normal, 280–1100 nm; ASTM standard G173-03).<sup>21</sup> Therefore the irradiation condition is well within the operational limits and the produced current is a good measure for the irradiance. We experimentally find a sensitivity of the cell of 260 mA per W of 443 nm light from the LED, corresponding to a yield of  $1.6 \times 10^{18}$  electrons per second from  $2.2 \times 10^{18}$  photons per second, *i.e.* a quantum efficiency of 73%. The 20 mW light finally result in a voltage drop of about 200 mV, well below the rated voltage.

For the absolute calibration and a test of the linearity we compared the voltage across the terminating resistor for different illumination levels. The radiant power was measured with a calibrated thermopile powermeter (PowerMax-USB PS19Q; Coherent Inc.<sup>23</sup>) placed directly in the image plane. We found the response (see circles in Fig. 3) to be linear with a deviation of less than 5% in the range between 0.2 and 20 mW. This is the standard range accessible with our setup using LEDs driven with 3 W of electrical power. The slope of the linear fit (blue dashed line) can be adjusted with the resistance on the solar cell to 10 mV per mW, in our example with a value of  $44 \Omega$ . Thus, one can read off the significant digits of the radiant power directly from the multimeter, for the highest powers a small correction factor should be applied that can be readily evaluated from Fig. 3.

We repeated the calibration for five LEDs emitting at different wavelengths and found a very similar behavior for all of them. Only the sensitivity of the solar cell changed slightly and was compensated by a small variation of the resistor. Long time measurements with both the solar cell and the powermeter show

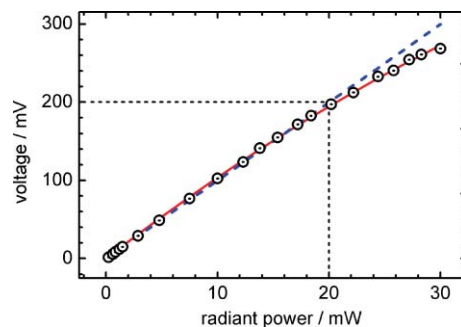


**Fig. 3** Solar cell output voltage across a  $44 \Omega$  resistor (circles) plotted against the effectively used radiant power of a 3 W LED (LXHL-LR3C;  $\lambda_c = 443 \text{ nm}$ ). Blue dashed line: linear least squares fit between 0.2 and 20 mW with fixed zero intercept; red solid line: 2nd order polynomial fit between 0.2 and 30 mW with fixed zero intercept.

that (a) the solar cell does not change its performance and (b) the LED driven with the used power supply renders the same light output for many hours in continuous operation and many weeks with repeated turn-on. As power supply we used a 675 mA constant current source (model LT-1088; LED-TECH.DE optoelectronics<sup>23</sup>). The combination of the power supply and the intrinsic performance of the LED together with a good heat sinking capability<sup>24</sup> render the observed stability of the sample irradiance without extra feedback effort.

For repeated measurements with the same LED, the solar cell detector will be much more convenient on a day-to-day basis than classical chemical actinometry. For example, it allows checking if the catalytic chromophore shows bleaching during the irradiation. Using the f-stops on the aperture ring of the photographic lens, it is also straightforward to adjust the light intensity quantitatively according to the experimental requirements. The chemical actinometer does, however, provide an excellent possibility for an absolute check of the calibration at times.<sup>15</sup>

### 2.4 Measurement protocol

We propose and tested the following procedure to perform a reproducible illumination experiment and quantify the number of photons absorbed by the sample.

(1) The LED light is blocked by putting the front cover on the photographic lens. This allows the determination of the radiant power  $P_0$  of the ambient light on the detector and its subtraction from all further power measurements.

(2) The cover is removed and a reference cuvette with pure solvent is inserted. The transmitted radiant power  $P_{\text{ref}} = P_{\text{ref}}^{\text{meas}} - P_0$  is noted.

(3) The reference is exchanged with the sample cuvette and a timer is started. This marks the beginning of the illumination period.

(4) The transmitted power  $P_{\text{sample}} = P_{\text{sample}}^{\text{meas}} - P_0$  is noted. If long illumination times ( $\sim$ hours) are necessary, it is reasonable to check at regular intervals that  $P_{\text{sample}}$  does not change, *e.g.* due to photobleaching of the sample. Similarly, the performance of the LED output can be checked by shortly exchanging the sample with the reference cuvette and comparing the transmitted power with  $P_{\text{ref}}$ .

(5) After a selected illumination time, the sample (or an aliquot of it) is taken to the chemical analysis to measure the final product concentration (see section 2.5).

The quantum yield  $\Phi$  of the overall photoreaction is generally defined as the number  $N_{\text{prod}}$  of formed product molecules divided by the number of absorbed photons  $N_{\text{ph,abs}}$ .<sup>10</sup> The latter quantity is directly proportional to the absorbed radiant power  $P_{\text{abs}}$ :

$$\Phi = \frac{N_{\text{prod}}}{N_{\text{ph,abs}}} = N_{\text{A}} h c \frac{c_{\text{prod}} V}{P_{\text{abs}} \Delta t \lambda_{\text{LED}}} \quad (1)$$

Here,  $N_{\text{A}}$  is the Avogadro constant,  $h$  is Planck's constant,  $c$  is the speed of light,  $c_{\text{prod}}$  is the product concentration,  $V$  is the sample volume,  $\Delta t$  is the illumination time and  $\lambda_{\text{LED}}$  is the central wavelength of the LED. The term quantum yield is most informative for monochromatic light.<sup>25</sup> For a broad spectral distribution of the light source, the emission spectrum and the absorption spectrum of the sample are convoluted and the determined quantum yield will depend on both. However, in most cases LED emission spectra are comparatively narrow and symmetric around the central wavelength (see Fig. 1). Since we measure the absorbed power, the error resulting from the finite bandwidth only originates from the wavelength dependent photon energy. In good approximation,  $\lambda_{\text{LED}}$  can be used to determine the total number of absorbed photons from the measured radiant power.

The absorbed radiant power  $P_{\text{abs}}$  can be calculated from  $P_{\text{ref}}$  and  $P_{\text{sample}}$  recorded during step 2 and 4 of the protocol:

$$P_{\text{abs}} = (P_{\text{ref}} - P_{\text{sample}})f = (P_{\text{ref}} - P_{\text{sample}}) \frac{1 + R \frac{P_{\text{sample}}}{P_{\text{ref}}}}{1 - R} \quad (2)$$

The small correction factor  $f$  results from back reflection with coefficient  $R$  from the terminal glass/air interface that leads to additional absorption. For a fused silica cuvette and  $\lambda = 443$  nm the reflectivity amounts to  $R = 0.036$ , so if  $P_{\text{sample}}$  is  $\sim 0$  mW,  $f = 1.037$ , *i.e.* a correction of 3.7% is to be used, for  $P_{\text{sample}} = 0.5P_{\text{ref}}$  one obtains  $f = 1.056$ . It should be noted that the reflectivity at the glass/solvent interface is more than one order of magnitude smaller and can be neglected in this context, just like multiple reflections between any two interfaces.

After the well defined illumination of the reaction mixture the sample should be transported and handled with as little additional irradiation as possible. This is best achieved by transporting and storing it in a dark environment. Needed further processing should be done under safe light that is not absorbed by the sample, *e.g.* red light for the described visible light photocatalysis and with only visible light for UV sensitive catalysts.

## 2.5 Quantification of the chemical conversion with gas chromatography

Any suitable and established analytical technique for the determination of the chemical product yields can be used to quantify the outcome of the irradiation. The proper choice depends on the chemical properties of the examined species, for example high performance liquid chromatography (HPLC) or NMR spectroscopy might be the method of choice. We chose standard and readily available gas chromatography (GC 5890 Series II from Hewlett–Packard, capillary column J+W Scientific—DB-5MS/30 m  $\times$  0.25

mm/0.25  $\mu\text{m}$  film) and a flame ionization detector (FID) for the investigated systems.

The temperature of the injector was 200 °C and the detector was heated to 310 °C. For the measurement of methoxybenzyl alcohol and methoxybenzyl aldehyde, the following temperature program was applied to achieve an adequate separation of the substances. The column temperature was first kept at 40 °C for 3 min. Then, the temperature was ramped up to 140 °C at 8 °C min<sup>-1</sup> and afterwards to 280 °C with 25 °C min<sup>-1</sup>, followed by keeping it at 280 °C for 5 min to ensure a complete release of the sample.

Typical results are shown in Fig. 4. In a reference measurement we used 0.01 M toluene as an internal standard in an equimolar mixture with methoxybenzyl alcohol and methoxybenzyl aldehyde. Retention times of 3.7, 14.6 and 14.1 min are found in agreement with the known behavior (see Fig. 4(a)). A 2.0 ml sample of 80  $\mu\text{mol}$  methoxybenzyl alcohol and 8  $\mu\text{mol}$  riboflavin tetraacetate (the photocatalyst) dissolved in a 50/50 volume-mixture of water and acetonitrile was illuminated for 100 min with 20.2 mW of 443 nm light and the GC trace shown in Fig. 4(b) was recorded. We do not find a signal from the flavin and assume that it stays in the stationary phase. From the integrals (dashed lines) it can be clearly seen that only a fraction of 9.2% of the initially applied alcohol is converted to the aldehyde. For a 6.4 times smaller concentration of substrate and catalyst and proportionally shorter illumination of 15.5 min the conversion

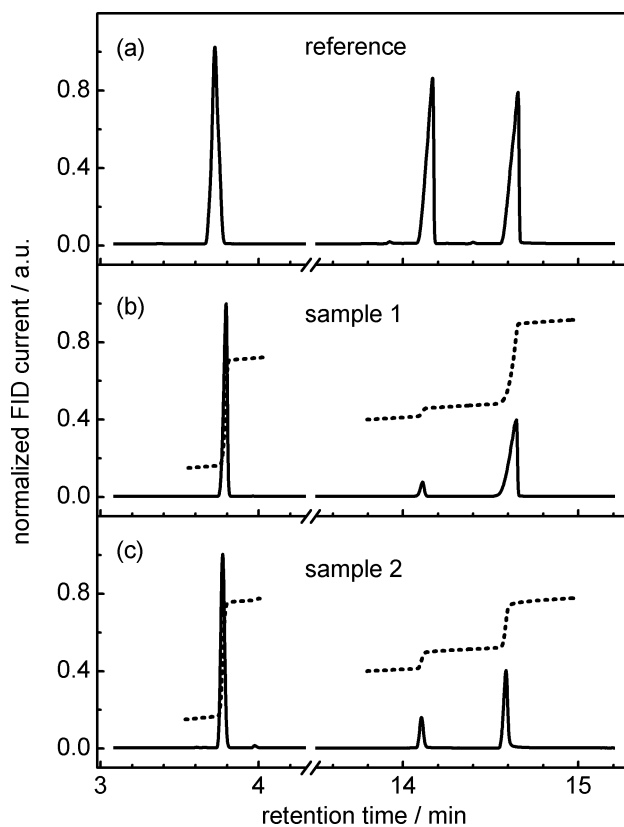


**Fig. 4** Typical gas chromatography traces used for the quantitative determination of the chemical yield after defined LED illumination. (a) Reference of known fractions of toluene (at about 3.7 min), methoxybenzyl aldehyde (14.1 min) and methoxybenzyl alcohol (14.6 min). (b) and (c) Samples with concentrations to be determined. For the evaluation the integrals over the respective peaks (dotted lines) are used.

was 22.4%. The higher value is directly seen from the experimental trace and the integral in Fig. 4(c).

The shown examples demonstrate that a significant chemical transformation due to the photocatalysis is needed for an accurate quantitative determination. Accordingly, suitable illumination times have to be chosen. The examples in this work range from 2 to 100 min. With the high degree of stability of the setup in general and in particular the LED source driven by a current stabilized power supply, even durations of some hours do not pose any problem.

### 3. Quantum yield test measurements

To test our apparatus we determined the quantum yield of ferrous production in the classical potassium ferrioxalate actinometry<sup>13</sup> under irradiation with 443 nm light at room temperature. The potassium ferrioxalate actinometry measurements have been performed as described in ref. 14. The following four stock solutions were prepared:

(1) Ferric sulfate solution: 1.47 g  $\text{Fe}_2(\text{SO}_4)_3$  pentahydrate in 5.5 mL conc.  $\text{H}_2\text{SO}_4$  was diluted with water up to 10 mL.

(2) Potassium oxalate solution: 2.76 g potassium oxalate monohydrate was dissolved in water up to 10 mL.

(3) 1,10-Phenanthroline solution: 0.2% (w/w) 1,10-phenanthroline in water.

(4) Buffer solution: 0.82 g NaOAc trihydrate in 1 mL conc.  $\text{H}_2\text{SO}_4$  was diluted with water up to 10 mL.

A mixture of 1 ml of (1) and 1 ml of (2) were pipetted into a 10 mL fused silica cuvette. The solution was irradiated for 2 min with 443 nm light. With an absorbed radiant power  $P_{\text{abs}}$  of 20.2 mW, this corresponds to the absorption of  $5.4 \times 10^{18}$  photons. After the illumination, 4 ml of (3) and 0.5 ml of (4) were added to 0.1 ml of the irradiated sample and the solution was diluted to 10 mL with water. In parallel, a blank sample was prepared following the same procedure as described above but omitting irradiation.

The amount of ferrous production can be measured *via* spectrophotometric determination of its 1,10-phenanthroline complex at 510 nm. Therefore, the absorbance  $A$  at 510 nm of the irradiated sample *versus* water was measured and corrected for the absorbance of the blank sample. From this and the number of absorbed photons  $N_{\text{ph,abs}}$ , the quantum yield of ferrous production  $\Phi_{443\text{nm}}$  can be calculated:<sup>14</sup>

$$\Phi_{443\text{nm}} = \frac{AV_2V_3N_A}{\epsilon dV_1N_{\text{ph,abs}}} \quad (3)$$

Here,  $V_1 = 0.1$  ml is the volume of irradiated sample withdrawn for the complexation with 1,10-phenanthroline,  $V_3 = 10$  ml is the volume used for the dilution of  $V_1$ ,  $V_2 = 2$  ml is the total volume of irradiated sample solution,  $d = 1$  cm is the path length of the cuvette used to measure the absorbance  $A$  of the 1,10-phenanthroline complex and  $\epsilon = 1.11 \times 10^4$  L mol<sup>-1</sup> cm<sup>-1</sup> is the extinction coefficient of the complex at 510 nm.

From three repeated measurements we obtained an average value of  $\Phi_{443\text{nm}} = 0.99$  with a standard deviation of 0.08. This is in perfect agreement with the reported quantum yield of 1.00 at 442 nm.<sup>14</sup>

As an example from ongoing research we measured the photocatalytic enantioselective alkylation reaction of aldehydes recently reported by MacMillan and coworkers.<sup>9</sup> They used ruthenium

**Table 1** Results of the photooxidation of 4-methoxybenzyl alcohol (MBA) to 4-methoxy-benzaldehyde catalyzed by riboflavin tetraacetate (2 mM)

[MBA]/mM	Solvent	Illumination time	Chemical yield (%)	Quantum yield $\Phi$ (%)
2	MeCN/DMSO (98 : 2, v/v)	3 h	4.20	0.021
2		5 h	10.3	0.031
2		10 h	31.0	0.047
Average				0.033 ± 0.013
2	MeCN-H <sub>2</sub> O (50 : 50, v/v)	5 min	10.1	1.80
5		12.5 min	13.8	2.46
10		25 min	16.0	2.85
20		50 min	17.1	3.05
40		100 min	14.7	2.62
200		8.3 h	5.90	1.05

tris(bipyridine) as the redox active photocatalyst and a 15 W energy-saving light bulb with a not precisely described imaging geometry for irradiation. To the best of our knowledge, no quantum efficiency of the reaction has been reported so far. With our new setup we determined the quantum yield of this reaction to 49%.

A sample of 2.7 ml *N,N'*-dimethylformamide solution containing 0.963 mmol bromodiethyl malonate, 1.93 mmol octanal and a mixture of 0.193 mmol imidazolidinone and 0.0048 mmol Ru(bpy)<sub>3</sub>Cl<sub>2</sub> as photocatalyst in the presence of 1.93 mmol 2,6-lutidin was irradiated for 60 min with 20.5 mW of 443 nm light. The yield of the enantioenriched  $\alpha$ -alkylated aldehyde was quantified by GC using chlorobenzene as an internal standard. The aldehyde peak was well separated from that of any other components of the reaction mixture. Thus, the chemical yield could be accurately measured to 14%, corresponding to the quantum yield of 49%. For longer irradiation times of 120 and 180 min, somewhat lower quantum yields of 47% and 42% were determined, reflecting the substrate consumption in the course of the reaction.

The same blue emitting LED was also used to drive the aerobic photooxidation of methoxybenzyl alcohol in the presence of flavin acting as photocatalyst as described above.<sup>3,4</sup> Beyond the example presented above, we found a strong dependence of the reaction quantum yield on the substrate concentration as well as on the solvent. By adding water to the originally used solvent acetonitrile, the quantum yield increased by two orders of magnitude. All results are summarized in Table 1. For the smallest quantum yields the very long time of irradiation leads to a somewhat increased relative uncertainty due to badly known side processes. In the presence of water, the nontrivial optimal concentration of the benzyl alcohol was found to be 20 mM. This illustrates how the facile determination of the quantum yield can be used as a tool to optimize the efficiency of a photoreaction.

To estimate the overall accuracy of our method for the determination of reaction quantum yields, we consider the major contributions to the uncertainty. With proper care and chemical experience in the sample preparation and handling, the concentration and volume of the solution should be determinable to about 1%. The physical measurement of the absorbed radiant power is precise to better than 5%, limited in practice by the calibration of the solar cell *via* the laser powermeter. In addition, the overlap of the sample absorption with the LED emission spectrum has to be considered. Last but not least, we estimate the quantitative

chemical analysis of the product to be accurate to about 5% from our experience and discussions with colleagues in the field. In summary, this amounts to about a 10% accuracy for the whole procedure.

#### 4. Conclusions and outlook

In summary, the described device allows the facile and exact determination of quantum yields for visible light chemical reactions in a synthesis research laboratory environment. It is built from carefully selected, commercially available optical, electronic and mechanical components with moderate financial cost. Chemical actinometry is avoided and the use of selected LED light sources ensures controlled and reproducible irradiation conditions over weeks without repeated calibration. The absorbed amount of light, *i.e.* the number of photons, is directly related to the chemical yield determined by established analytic methods, *i.e.* the number of product molecules.

The use of a solar cell with a low resistance termination allows to determine the radiative power of the large light beam and is a rugged and affordable alternative to expensive and delicate laser powermeters. The continuous electronic determination of the transmitted radiant power over the course of the reaction provides a detailed picture of stability and possible degradation processes and facilitates reaction condition optimization. Once the yield has been determined at one or a few wavelength bands, the yield for solar irradiation can be directly calculated with the help of the known absorption spectrum and compared to the determination of the apparent quantum yield with a solar simulator.<sup>12</sup> The use of a LED provides the additional possibility to differentiate between the changes in inherent efficiency as opposed to spectral shifts when the solar harvesting system is optimized.

The purely opto-electronic measurement of the number of absorbed photons avoids the tedious and precisely to be performed chemical actinometer procedures used so far. These methods are less well established in the visible, where green chemistry and the excellent availability of high-power LEDs nicely combine. The calibration of various lamp/filter combinations needed in classical actinometry is replaced by the simple powermeter based calibration of the various LEDs monitored by the same solar cell. The all-optical “photon counting” is particularly advantageous for low QY systems that require very long illumination times. Under these circumstances multiple chemical actinometer measurements are typically performed to monitor any relevant changes,<sup>11</sup> whereas our approach only requires reading-off the multimeter.

Further extensions according to specific needs should pose no serious problem due to the open layout of the new setup. Ongoing developments of high power LEDs will make the UV range progressively accessible. Since only one wavelength range at a time is used, the camera lens does not have to be fully achromatic, but only adjusted by a small amount. At the same time, UV sensitive “solar” cells are already at hand.

Since the product yield and the stability of the reactants can be expected to be temperature dependent, a temperature controlled sample seems like a valuable extension. This would also compensate for possible heating during the illumination. For investigations of heterogeneous catalysis the LED light might be severely scattered and the use of an Ulbricht sphere for the determination of the illumination is suggested. Last but not least, a

computer interfaced recording of the solar cell reading will allow to monitor a changing transmission of the sample and to incorporate this information into the final evaluation.<sup>26</sup>

We recommend the simple and low cost device not only to chemists applying photocatalysis for synthesis to quickly evaluate and improve their methods, but also to researchers interested in many other photo-initiated processes. All necessary details needed for the assembly and operation are provided in the ESI.†

#### Acknowledgements

We thank the Deutsche Forschungsgemeinschaft (GRK 1626 and SFB 749) for support of our research. We gratefully acknowledge financial support from the International Max Planck Research School on Advanced Photon Science (U.M.). S. Kümmel provided valuable technical help.

#### References

- 1 D. Ravelli, D. Dondi, M. Fagnoni and A. Albini, Photocatalysis. A multi-faceted concept for green chemistry, *Chem. Soc. Rev.*, 2009, **38**, 1999–2011.
- 2 J. M. R. Narayanan, J. W. Tucker and C. R. J. Stephenson, Electron-Transfer Photoredox Catalysis: Development of a Tin-Free Reductive Dehalogenation Reaction, *J. Am. Chem. Soc.*, 2009, **131**, 8756–8757.
- 3 H. Schmaderer, P. Hilgers, R. Lechner and B. König, Photooxidation of Benzyl Alcohols with Immobilized Flavins, *Adv. Synth. Catal.*, 2009, **351**, 163–174.
- 4 J. Svoboda, H. Schmaderer and B. König, Thiourea-Enhanced Flavin Photooxidation of Benzyl Alcohol, *Chem.–Eur. J.*, 2008, **14**, 1854–1865.
- 5 J. P. Ghosh, C. H. Langford and G. Achari, Characterization of an LED Based Photoreactor to Degrade 4-Chlorophenol in an Aqueous Medium Using Coumarin (C-343) Sensitized TiO<sub>2</sub>, *J. Phys. Chem. A*, 2008, **112**, 10310–10314.
- 6 J. P. Ghosh, R. Sui, C. H. Langford, G. Achari and C. P. Berlinguette, A comparison of several nanoscale photocatalysts in the degradation of a common pollutant using LEDs and conventional UV light, *Water Res.*, 2009, **43**, 4499–4506.
- 7 K. Zeitler, Photoredox Catalysis with Visible Light, *Angew. Chem., Int. Ed.*, 2009, **48**, 9785–9789.
- 8 J. Du and T. P. Yoon, Crossed Intermolecular [2+2] Cycloadditions of Acyclic Enones via Visible Light Photocatalysis, *J. Am. Chem. Soc.*, 2009, **131**, 14604–14605.
- 9 D. A. Nicewicz and D. W. C. MacMillan, Merging Photoredox Catalysis with Organocatalysis: The Direct Asymmetric Alkylation of Aldehydes, *Science*, 2008, **322**, 77–80.
- 10 M. B. Rubin and S. E. Braslavsky, Quantum yield: the term and the symbol. A historical search, *Photochem. Photobiol. Sci.*, 2010, **9**, 670–674.
- 11 R. R. Sauers, S. D. van Arnum and A. A. Scimone, Green chemistry analytical method development: a revisit on the use of potassium ferrioxalate as a chemical actinometer, *Green Chem.*, 2004, **6**, 578–582.
- 12 T. Maschmeyer and M. Che, Catalytic Aspects of Light-Induced Hydrogen Generation in Water with TiO<sub>2</sub> and Other Photocatalysts: A Simple and Practical Way Towards a Normalization?, *Angew. Chem., Int. Ed.*, 2010, **49**, 1536–1539.
- 13 C. A. Parker, A new sensitive chemical actinometer I. Some trials with potassium ferrioxalate, *Proc. R. Soc. London, Ser. A*, 1953, **220**, 104–116.
- 14 S. L. Murov, I. Carmichael, G. L. Hug, *Handbook of Photochemistry*, Marcel Dekker, New York, 2nd edn, 1993, ch. 13.
- 15 H. J. Kuhn, S. E. Braslavsky and R. Schmidt, Chemical actinometry, *Pure Appl. Chem.*, 2004, **76**, 2105–2146.
- 16 J. J. Jankowski, D. J. Kieber and K. Mopper, Nitrate and Nitrite Ultraviolet Actinometers, *Photochem. Photobiol.*, 1999, **70**, 319–328.
- 17 R. O. Rahn, Potassium Iodide as a Chemical Actinometer for 254 nm Radiation: Use of Iodate as an Electron Scavenger, *Photochem. Photobiol.*, 1997, **66**, 450–455.
- 18 R. G. Zepp, M. M. Gumz, W. L. Miller and H. Gao, Photoreaction of Valerophenone in Aqueous Solution, *J. Phys. Chem. A*, 1998, **102**, 5716–5723.



- 
- 19 W. Amrein, J. Gloor and K. Schaffner, An electronically integrating actinometer for quantum yield determinations of photochemical reactions, *Chimia*, 1974, **28**, 185–188.
- 20 X. Huang, H. Wang, S. Yin, X. Chen, W. Chen and H. Yang, Sterilization system for air purifier by combining ultraviolet light emitting diodes with TiO<sub>2</sub>, *J. Chem. Technol. Biotechnol.*, 2009, **84**, 1437–1440.
- 21 <http://rredc.nrel.gov/solar/standards/am1.5/>.
- 22 U. Schmidhammer, S. Roth, E. Riedle, A. A. Tishkov and H. Mayr, Compact laser flash photolysis techniques compatible with ultrafast pump–probe setups, *Rev. Sci. Instrum.*, 2005, **76**, 093111.
- 23 Mention of vendor names and model numbers is for technical communication purposes only and does not necessarily imply recommendation of these units, nor does it imply that comparable units from another vendor would be less suitable for this application.
- 24 Further details can be found in the ESI†.
- 25 S. E. Braslavsky, Glossary of terms used in photochemistry 3rd edition, *Pure Appl. Chem.*, 2007, **79**, 293–465.
- 26 J. Tonne, H. Prinzbach and J. Michl, Double actinometry for rigorous evaluation of quantum yields of clean photoreversible photochemical reactions, *Photochem. Photobiol. Sci.*, 2002, **1**, 105–110.



# Laboratory apparatus for the accurate, facile and rapid determination of visible light photoreaction quantum yields

Uwe Megerle,<sup>a</sup> Robert Lechner,<sup>b</sup> Burkhard König<sup>b</sup> and Eberhard Riedle<sup>a</sup> \*

<sup>a</sup> *Lehrstuhl für BioMolekulare Optik, Ludwig-Maximilians-Universität (LMU),  
Oettingenstr. 67, 80538 München, Germany*

<sup>b</sup> *Institut für Organische Chemie, Fakultät für Chemie und Pharmazie,  
Universität Regensburg, D-93040 Regensburg, Germany*

\* Corresponding author:

*e-mail: riedle@physik.lmu.de, Tel.: +49 89 2180 9210 Fax: +49 89 2180 9202*

-----

## Supporting Information

-----

## *S1 High power LEDs for illumination*

To assure a maximum in light output, efficiency and lifetime of the LEDs, an adequate heat management is essential. We use LEDs with a metal base and mount them on aluminum disks of 25 mm in diameter with thermally conductive adhesive pads. The disks themselves are then thermally connected to a larger heat sink (Sk-189-50sa, Fischer Elektronik)<sup>1</sup>. On the one hand this ensures effective heat dissipation while on the other hand the LED can still be freely rotated. For a square shape of the semiconductor die of the LED this allows optimal matching of the imaged beam profile to the aperture of the cuvette.

Besides the rotation, the possibility to move the LED horizontally and vertically is also essential for the alignment. A displaced LED is imaged less precisely and with less efficiency by the photographic lens. As shown in Figure S1, we implement this by mounting the heat sink on two perpendicular translation stages (DT25/M, Thorlabs GmbH (see footnote 1)).

To allow for a simple and quick change of the LEDs, short wires with pin plugs are soldered to each individual LED. They can directly be connected to the constant current source (675 mA, LT-1088, LED-tech (see footnote 1)).

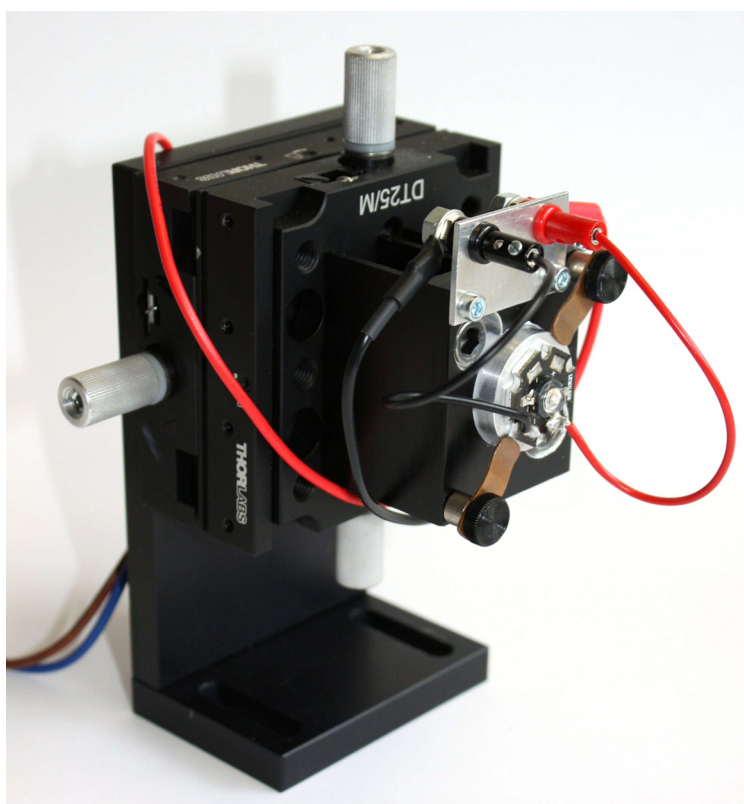


**Fig. S1** Image of the assembled LED stage.

---

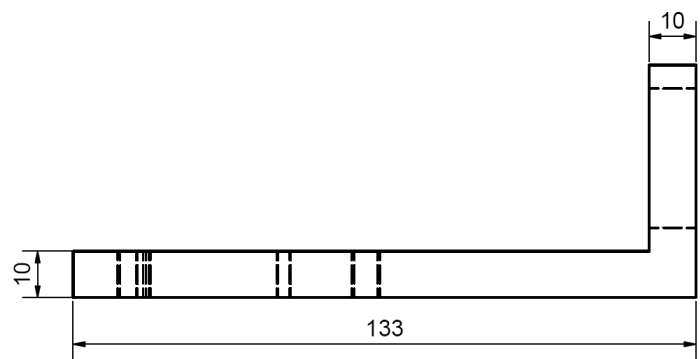
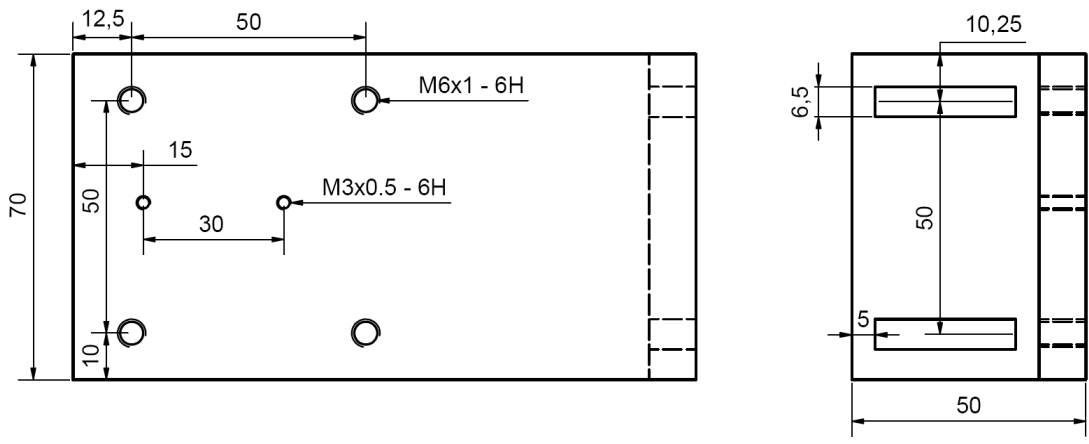
<sup>1</sup> Mention of vendor names and model numbers is for technical communication purposes only and does not necessarily imply recommendation of these units, nor does it imply that comparable units from another vendor would be any less suitable for this application.

## *S2 Adjusting the sample cell*

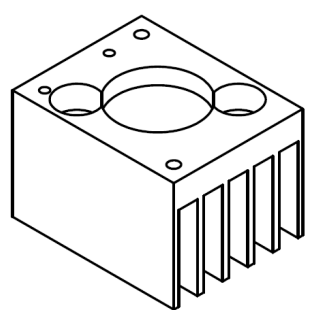
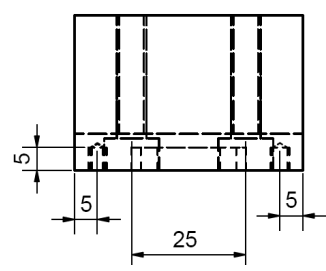
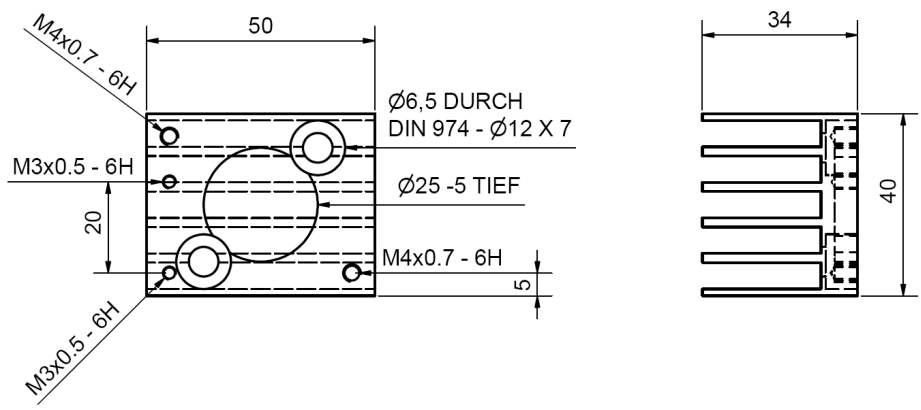
We use 1-cm absorption cuvettes (e.g., 110 QS, Hellma Optik GmbH (see footnote 1)). This ensures reproducibility and a favorable near perpendicular incidence of the radiation. The whole cuvette mount is adjustable in height. If sufficient sample solution is available, the cell can be shifted downwards to insert a magnetic stir bar. A convenient and inexpensive solution for rotating the stir bar is to use a magnet on a DC motor (1524B024S-R-15A, Faulhaber GmbH (see footnote 1)) whose speed can be adjusted with a switchable AC adapter.

A thin aperture placed in front of the sample cell is helpful for both alignment and blocking of stray light that might disturb the measurement. In our case, a square aperture of 8 x 8 mm is used according to the square shape of the semiconductor die of the LEDs. During the adjustment, we replace the sample cell with an equally sized "dummy cuvette" that has a white card or semitransparent paper in the middle. This little device acts as screen for the image of the LED die. It allows checking whether the LED is properly aligned and oriented and no light is cut by the aperture or the side walls of the cuvette.

S3 Design drawings<sup>2</sup>

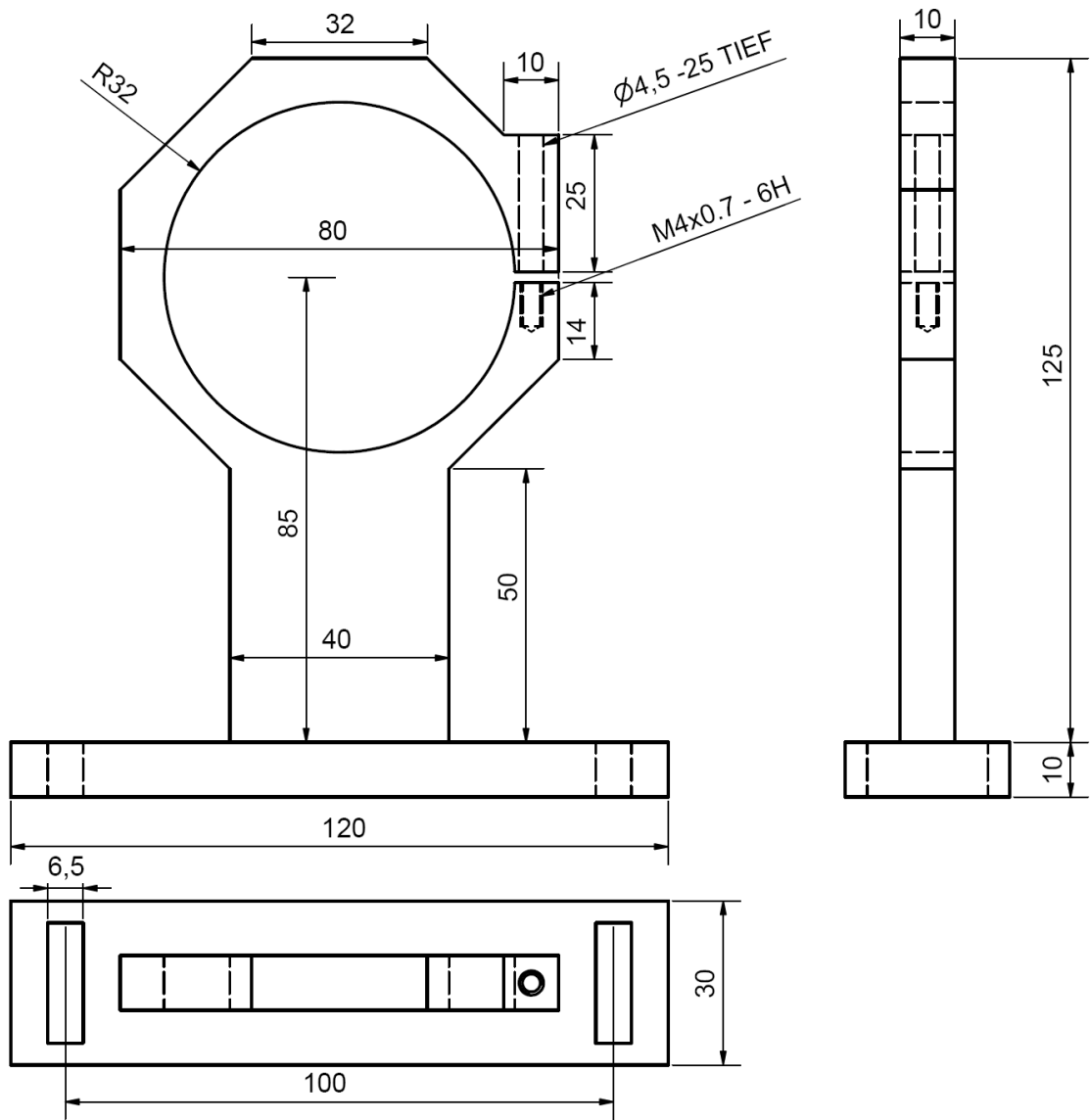


base for LED stage,  
black anodized aluminum

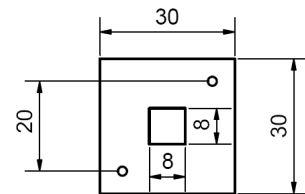
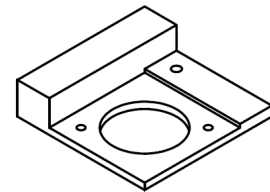
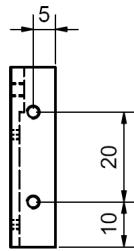
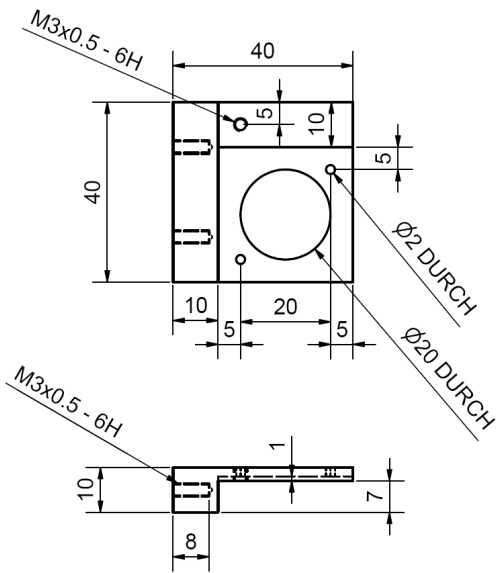
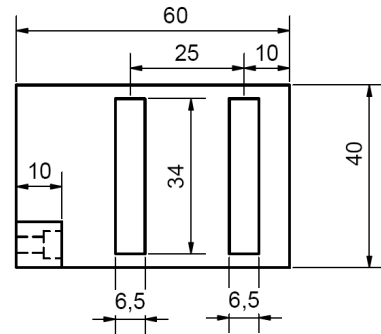
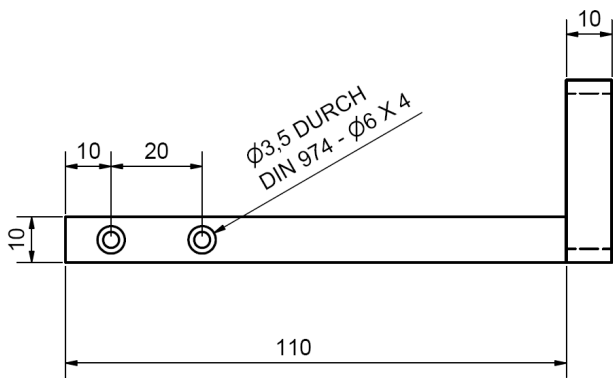


heat sink (Sk-189-50sa, black anodized aluminum) with connections for LED

<sup>2</sup> Electronic CAD files of the mechanical components can be requested from the authors.

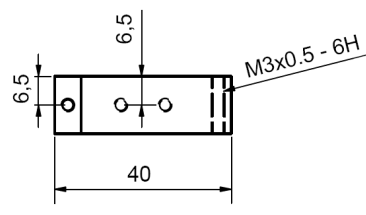
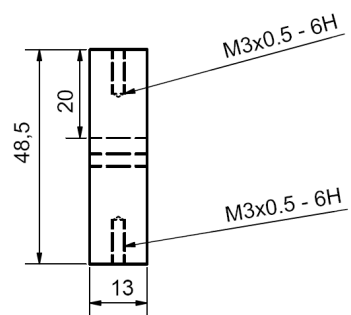
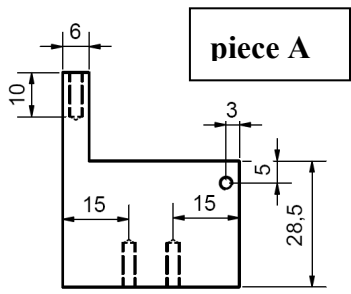
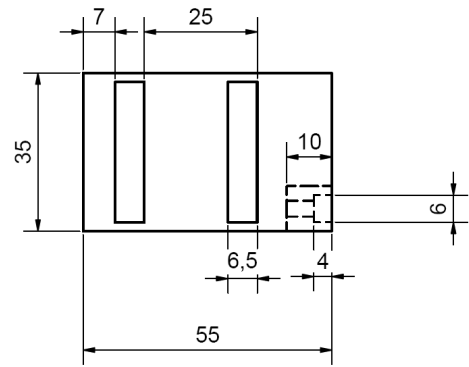
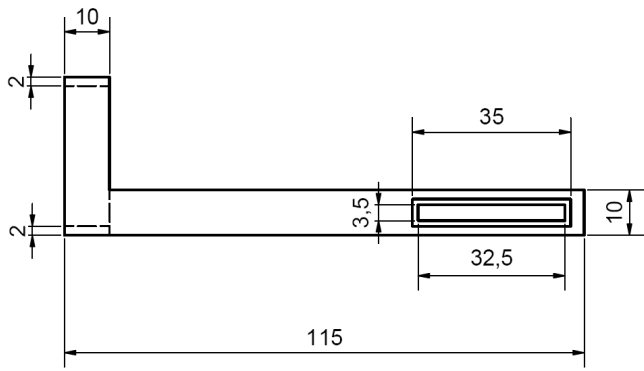


mount for the photographic lens (black anodized aluminum)

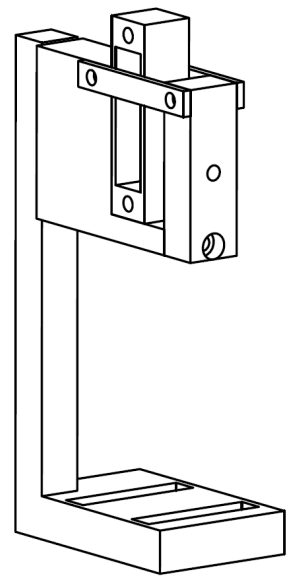
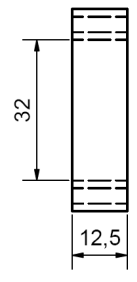
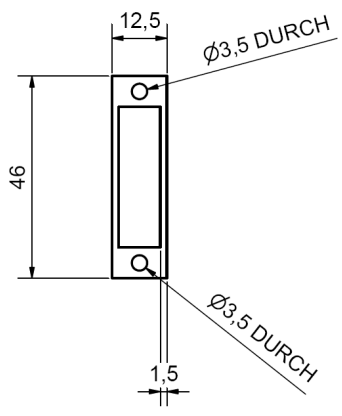
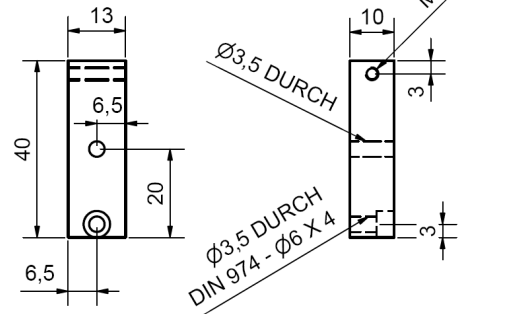


base for the removable aperture in front of the cuvette (black anodized aluminum)



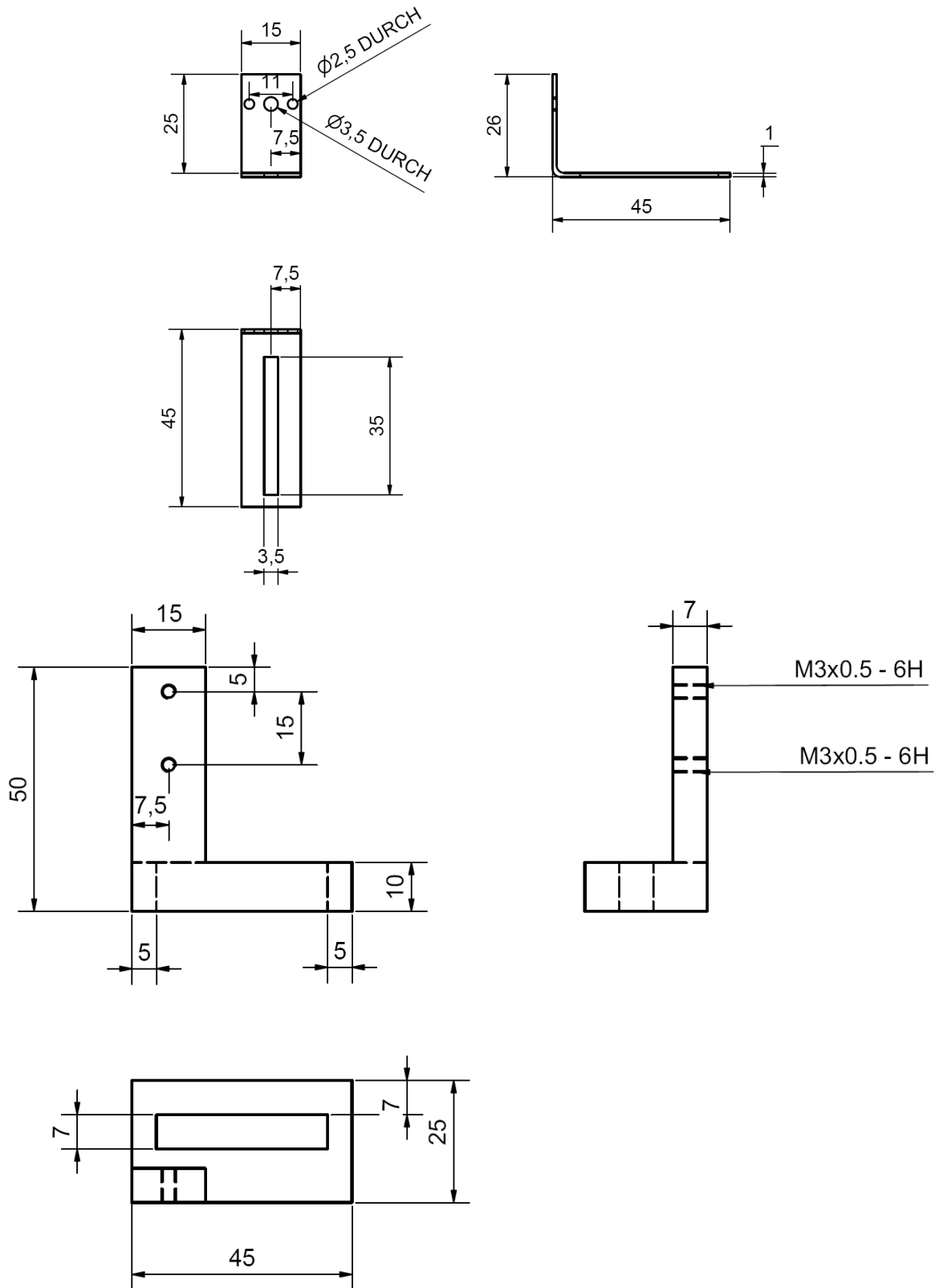


**piece B**



cuvette mount + dummy cuvette

(black anodized aluminum, except for pieces A+B: PVC)



base for magnetic stirrer motor (black anodized aluminum)

## **Appendix A3**

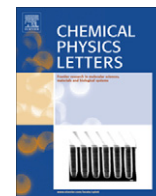
### **Influence of core-substitution on the ultrafast charge separation and recombination in arylamino core-substituted naphthalene diimides**

*I. Pugliesi, U. Megerle, S.-L. Suraru, F. Würthner, E. Riedle, S. Lochbrunner*

Chemical Physics Letters 504, 24-28 (2011)

Reprinted with permission from Elsevier.





## Influence of core-substitution on the ultrafast charge separation and recombination in arylamino core-substituted naphthalene diimides

Igor Pugliesi<sup>a</sup>, Uwe Megerle<sup>a</sup>, Sabin-Lucian Suraru<sup>b</sup>, Frank Würthner<sup>b</sup>, Eberhard Riedle<sup>a,\*</sup>, Stefan Lochbrunner<sup>c,\*</sup>

<sup>a</sup> Lehrstuhl für BioMolekulare Optik, Ludwig-Maximilians-Universität München, Oettingenstr. 67, 80538 München, Germany

<sup>b</sup> Institut für Organische Chemie, Universität Würzburg, Germany

<sup>c</sup> Institut für Physik, Universität Rostock, Universitätsplatz 3, 18055 Rostock, Germany

### ARTICLE INFO

#### Article history:

Received 22 December 2010

In final form 14 January 2011

Available online 18 January 2011

### ABSTRACT

We study the charge separation and recombination of two arylamino core-substituted naphthalene diimides by transient absorption. Both compounds show a 3 ps relaxation from the initially excited partial to the full charge transfer state. Quantum chemical calculations show that this process is associated with a twisting of the arylamino substituent. In the twisted conformation the energy gap between ground and excited state is 0.7 eV for two amino core-substituents and 0.5 eV for one amino and one chloro core-substituent. The larger energy gap leads to a six-fold increase in the lifetime of the fully charge separated state from 11 to 70 ps.

© 2011 Elsevier B.V. All rights reserved.

### 1. Introduction

Brilliant colors and intense fluorescence characterize core-substituted naphthalene diimides (NDIs). Only small structural changes are required to make them absorb or fluoresce across the whole visible spectral range. NDIs have thus been utilized in multicolor light harvesting architectures, supramolecular n/p heterojunctions and organic solar cells [1,2].

Fluorescence quantum yields between 0.5 and 0.8 have been reported for alkylamino and alkoxy core-substituted NDIs [3] and more recently also for alkylsulfanyl core-substituents [4]. In contrast, arylamino core-substituted NDIs have extremely low quantum yields [5]. Intramolecular hydrogen bonding of the amino hydrogen to the adjacent C=O group has been considered as a major pathway for the radiationless deactivation of the excited state. On the other hand Mayor and coworkers [4] have recently shown that also phenoxy and phenylsulfanyl core-substituted NDIs without the possibility of H-bonding are extremely weakly fluorescent. Odobel and coworkers [6] observed fluorescence quenching in a similar situation by directly attaching phenyl rests or phenylethynyl groups to the naphthyl core of naphthalene diimides.

For the larger perylene diimides low fluorescence quantum yields are observed in polar solvents if electron rich aryl groups are attached to the naphthyl subunits at bay positions. The fluorescence quenching was shown to be either due to a combination of

conformational changes and reversible charge transfer processes (for dyes bearing less electron rich substituents) or an irreversible charge transfer with subsequent decay into the ground state (for dyes bearing more electron rich substituents). The latter process occurred on a 150 ps time scale in the less polar solvent toluene and on a 50 ps time scale in the more polar solvent tetrahydrofuran [7].

In a recent publication [8] some of us have shown that in the case of phenylsulfanyl core-substituted NDIs the ultrafast fluorescence quenching is also due to a photoinduced charge transfer (CT) from the substituent to the NDI chromophore. However, in contrast to the perylene diimide case, the CT is directly coupled to an asymmetric conformational change. The emerging full CT state has a lifetime of only a few picoseconds before the system returns to the ground state. The mechanism explains the observed large differences in fluorescence quantum yield between alkyl and aryl attachments on the sulfur core-substituent.

In this work we investigate the effects due to variation of the core-substituent itself on the CT mechanism. For this purpose we performed femtosecond pump-probe experiments and *ab initio* calculations on the two arylamino core-substituted NDIs Cl-NDI-NAr and N-NDI-NAr, as shown in Figure 1. While both molecules have the same carbon scaffold and an arylamino core-substituent in common, they differ by the second core-substituent. In one case it is a chlorine atom, in the other an alkylamino group. The steady state properties of both compounds have been characterized by Würthner and coworkers [5], who showed them to have a negligible fluorescence quantum yield. The absorption and fluorescence bands of N-NDI-NAr were found to be redshifted by ~90 nm with respect to Cl-NDI-NAr as a consequence of the different core sub-

\* Corresponding authors. Fax: +49 89 2180 9202 (E. Riedle), +49 381 498 6802 (S. Lochbrunner).

E-mail addresses: [riedle@physik.lmu.de](mailto:riedle@physik.lmu.de) (E. Riedle), [stefan.lochbrunner@uni-rostock.de](mailto:stefan.lochbrunner@uni-rostock.de) (S. Lochbrunner).

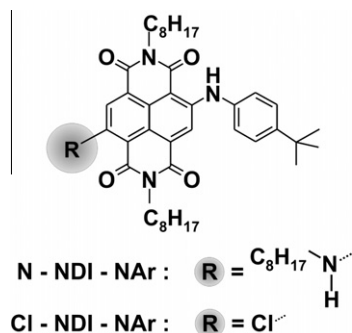


**Figure 1.** Chemical structure of the two investigated arylamino core-substituted naphthalene diimides.

stituents. Our work unravels the CT mechanism and explains the significant differences in the charge recombination dynamics leading back to the ground state. The results and their comparison to the case of phenylsulfanyl substituents are useful to develop concepts for a tailored design of NDIs in electron-transfer cascades.

## 2. Experimental and theoretical methods

The synthesis of the investigated molecules has been reported in Ref. [5]. For the transient absorption study the compounds were dissolved in chloroform of spectroscopic grade. The solutions were pumped through a flow cell of 120  $\mu\text{m}$  thickness and had an optical density of  $\sim 0.2$  at the excitation wavelength. The broadband transient spectrometer has been described in detail in Ref. [9]. For Cl-NDI-NAr pump pulses at 520 nm and for N-NDI-NAr at 620 nm were employed, corresponding to the respective maxima of the visible absorption bands. The pulses had energies around 100 nJ and were focused down to a diameter of 150  $\mu\text{m}$  FWHM inside the sample. A CaF<sub>2</sub> continuum spanning from below 300 nm to 750 nm and polarized at the magic angle was used as probe light. The temporal resolution was better than 100 fs, well below all observed decay rates.

For the *ab initio* calculations the C<sub>8</sub>H<sub>17</sub> alkyl chains and tert-butyl groups of Cl-NDI-NAr and N-NDI-NAr were replaced by hydrogen atoms to reduce computational time. Full geometry optimizations for the neutral ground ( $S_0$ ) state have been carried out using the DFT methodology and the B3-LYP functional. To ensure that true minima were found, additional frequency calculations were performed.

To validate the CT mechanism observed experimentally we also performed calculations on the singly charged NDI anions. Here additionally the aryl group of Cl-NDI-NAr and N-NDI-NAr was replaced by a hydrogen atom. Geometry optimizations and vertical transition energies were calculated in the unrestricted framework using the B3-LYP functional.

The first singlet excited ( $S_1$ ) state of the neutral molecules was optimized with the TDDFT methodology using the B3-LYP functional. In the calculations presented only single excitations have been considered. The Karlsruhe split valence basis set [10,11] augmented with a polarization function (SVP) was used in all calculations, which have been performed using the DFT and TDDFT [12] routines implemented in the TURBOMOLE 5.9.1 *ab initio* suite [13,14].

## 3. Results and discussion

Figure 2a shows the evolution of the transient absorption spectrum of N-NDI-NAr in chloroform after excitation at 620 nm. At early delay times ( $< 1$  ps) we find a broad excited state absorption

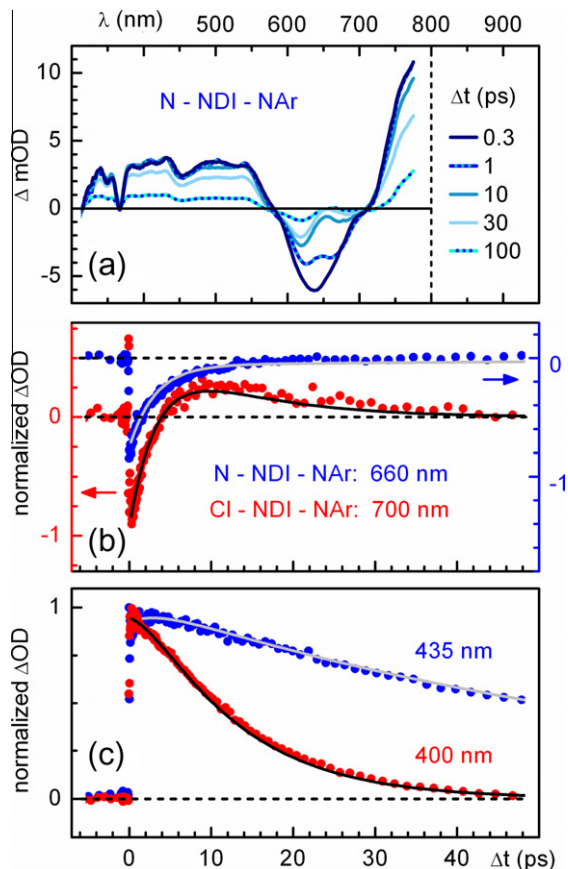


**Figure 2.** (A) Transient absorption spectra of N-NDI-NAr in chloroform solution after excitation at 620 nm. (b) Temporal evolution of the absorbance changes in the region of the stimulated emission and (c) the excited state absorption for N-NDI-NAr (blue circles) and Cl-NDI-NAr (red circles). The global fits are shown as solid lines. In panel (b) the curves are vertically shifted for better visibility.

(ESA) that dominates the spectrum below 575 nm and above 710 nm. Only between 600 and 700 nm a negative absorption change is observed. This signature arises from both ground state bleach (GSB) and stimulated emission (SE). The ESA bands and the GSB appear within the cross-correlation time and decay synchronously on a timescale of several tens of picoseconds (see also blue dots in Figure 2c). In contrast, the long wavelength portion of the negative  $\Delta\text{OD}$  signal due to the SE shows a much faster decay within a few picoseconds (see blue dots in Figure 2b). This fast emission quenching dynamics is in agreement with the almost negligible fluorescence quantum yield reported in Ref. [5]. The significantly longer presence of ESA and GSB compared to the SE implies that the population of the optically excited state is transferred to an intermediate state before the final relaxation to the ground state.

For Cl-NDI-NAr the same qualitative behavior of fast SE quenching and slower GSB and ESA relaxation is observed although the signatures in the transient absorption spectra are more strongly dominated by ESA. The temporal behavior of the transient signal is shown as red data points for a selected wavelength in the range of the SE (Figure 2b) and of the ESA (Figure 2c). The results indicate that an analogous quenching mechanism is at work in both compounds. A complete view of the multichannel data is provided in Figure S1 for N-NDI-NAr and Figure S2 for Cl-NDI-NAr.

We quantify the relaxation dynamics with a global fit procedure [15] based on a rate model. For both molecules a bi-exponential model is required and sufficient to achieve a satisfactory agreement between experiment and simulations. Figure 2b shows the fit curves

of the time traces at 660 nm for N-NDI-NAr and at 700 nm for Cl-NDI-NAr where the SE dominates over the ESA. The synchronous decay of the SE is reflected in almost identical time constants of 3.1 ps (N-NDI-NAr) and 3.4 ps (Cl-NDI-NAr). The sign change at  $\Delta t = 4$  ps in the time trace of Cl-NDI-NAr (red dots in Figure 2b) is a consequence of the superposition of ESA and SE at this spectral position. Figure 2c shows the fit curves at 435 nm for N-NDI-NAr and at 400 nm for Cl-NDI-NAr reflecting the ESA decay and the return to the ground state. Here we find significantly different dynamics between the two NDIs. While the ESA of Cl-NDI-NAr decays with 11 ps, the N-NDI-NAr has a roughly sixfold longer excited state lifetime of 70 ps.

To gain further insight into the quenching mechanism and in particular the differences in the excited state lifetimes we invoke the aid of *ab initio* calculations. The ground state geometry optimization was carried out using a starting geometry similar to that found with semiempirical methods [5], i.e. with the aryl group twisted slightly out of the plane of the central NDI chromophore. In contrast to the sulfanyl core-substituted NDIs [8], the optimized  $S_0$  state structure of both amino-substituted NDIs retains this quasi-planar conformation. Here the extension of the chromophore  $\pi$ -system onto the aryl substituent leads to a lower molecular energy than the minimization of the steric repulsion between the NDI hydrogens and the aryl substituent.

The calculated vertical transition energies for the quasi-planar structures of N-NDI-NAr and Cl-NDI-NAr are shown in Figure 3a and c. They are in very good agreement with the steady state absorption bands. This validates our choice of the computational method. The calculated first vertical transition ( $S_0-S_1$ ) is of  $\pi\pi^*$  character for both molecules and can be assigned to the absorption band in the visible. The high oscillator strength of around 0.2 reflects the large extinction coefficient of  $\sim 20,000 \text{ M}^{-1}\text{cm}^{-1}$ . The orbitals involved in the transition are shown in the left panel of Figure 4a for N-NDI-NAr. The orbitals for Cl-NDI-NAr are essentially identical as can be seen in Figure S3. Within the linear response formalism of TDDFT, the  $\pi\pi^*$  transition is described to 98% by a single electron excitation from the HOMO to the LUMO. While the HOMO is delocalized over the NDI chromophore (NDI- $\pi$ ) and the aryl substituent (NAr- $\pi$ ), the LUMO is a pure NDI- $\pi^*$

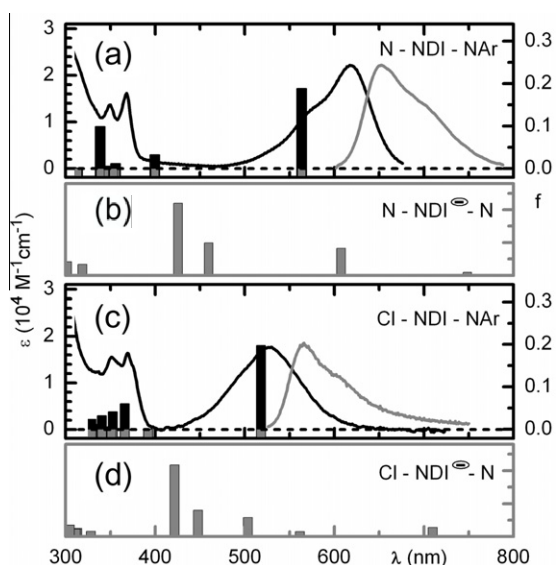


**Figure 3.** Absorption and emission spectrum of N-NDI-NAr (a) and Cl-NDI-NAr (c) in chloroform solution. The calculated vertical transitions from the neutral electronic ground state are shown as black bars. In (b) and (d) the corresponding transitions of the anionic ground states are shown.

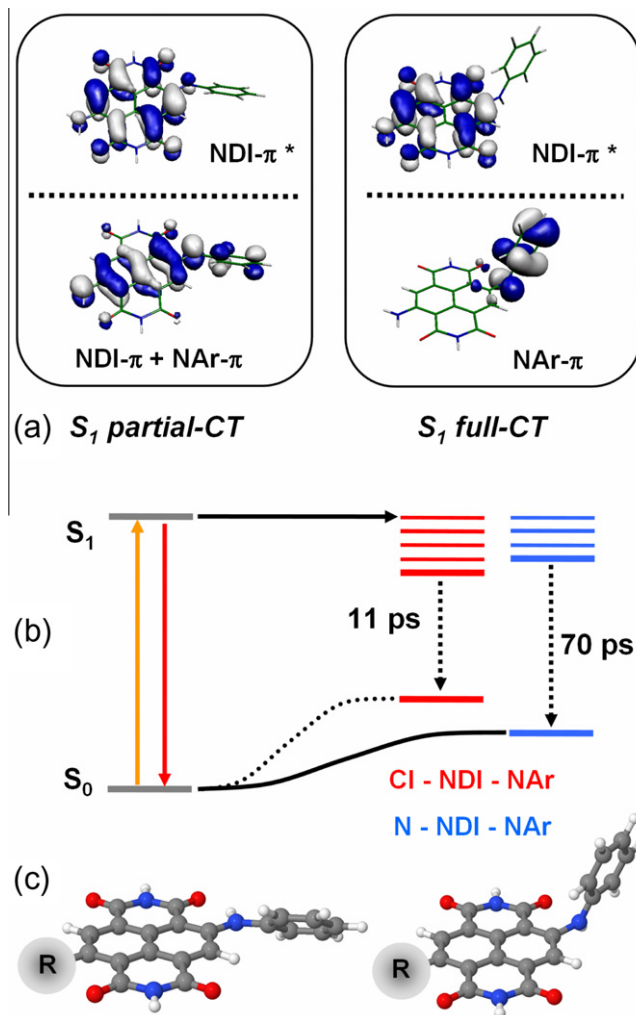


**Figure 4.** (A) Molecular orbitals describing the two CT states. (b) Relative energies of the electronic states involved in the CT process for N-NDI-NAr (blue lines) and Cl-NDI-NAr (red lines). (c) Minimum energy geometries for the ground state and the full CT state.

orbital. Thus the  $S_0-S_1$  transition is of partial CT character from the substituent to the core.

For both N-NDI-NAr and Cl-NDI-NAr the geometry optimization of the  $S_1 \pi\pi^*$  state leads to a structure where the whole arylamino substituent is twisted by  $90^\circ$  out of the NDI chromophore plane (see Figure 4c). Thus in analogy to the phenylsulfanyl core-substituted NDIs [8], the initially excited partial-CT state is at best a local minimum of the  $S_1$  potential energy surface. In the twisted structure the character of the lower lying SOMO orbital changes from NDI- $\pi$  + NAr- $\pi$  to a pure NAr- $\pi$ . The calculated fluorescence oscillator strength to the  $S_0$  state of  $7.8 \times 10^{-4}$  is more than two orders of magnitude smaller than the value for the  $S_1$  partial-CT state, as the NAr- $\pi$  orbital is conformationally decoupled from the NDI- $\pi$ -system.

From the theoretical analysis, for both NDIs the quenching of the SE is due to a charge transfer driven conformational change of the arylamino substituent relative to the NDI chromophore. After electronic excitation into the  $S_1$  partial CT state, the molecule follows during the first 3 ps an adiabatic pathway to the  $S_1$  full CT state. Thereby the whole arylamino substituent twists out of the plane of the NDI chromophore. The combination of the rapid conversion from the partial to the full CT and the low oscillator strength of the latter results in efficient emission quenching and the negligible fluorescence quantum yield.

Spectro-electrochemical measurements [6] on the singly charged anion of an NDI with two alkylamino core-substituents support the proposed CT mechanism. The NDI radical anion shows two strong absorption bands to the red and the blue of the neutral NDI absorption band. In accordance with these experimental results, the *ab initio* calculations on the N–NDI–N anion shown in Figure 3b yield strong absorptions with a difference of 0.2 eV to the red and 0.5–0.7 eV to the blue of the calculated  $S_0$ – $S_1$  transition of N–NDI–NAr. This can be compared to the transient spectra of N–NDI–NAr that feature broad ESA signatures on both sides of the GSB + SE band (see Figure 2a). Thus the ESA observed after the full charge separation can be assigned to the absorption of the NDI anion generated by photoinduced electron transfer. The charge separation process itself causes only marginal changes in the ESA. This can be rationalized by assuming that the observed ESA bands result from transitions of the electron in the upper SOMO to higher orbitals. These transitions are little affected by the character change of the lower lying SOMO during the charge separation. For the Cl–NDI–N anion the calculations predict a stronger overlap between the anion and the neutral absorption bands (Figure 3d). This is reflected in the above mentioned more dominant contribution of the ESA in the spectral region of the GSB and SE (see Figure S2).

The most interesting result obtained from the *ab initio* calculations is the significantly different energy gap between the  $S_1$ -full-CT and the ground state obtained for the two NDIs (Figure 4b). For Cl–NDI–NAr, the energy difference is 0.5 eV while for N–NDI–NAr it is raised by 40% to 0.7 eV. On the basis of the energy gap law [16], this explains the experimentally found difference in transition probability for the relaxation to the ground state. The exponential dependence of the rate on the energy gap leads to the six-fold slower decay time of N–NDI–NAr. In analogy to [16], the charge recombination rate  $k$  is written in dependence of the gap energy  $E_g$  as  $k = A \times \exp(-\gamma E_g / \hbar\omega)$ .  $\omega$  is the mean frequency of the energy accepting vibrational modes and  $\gamma$  a factor that depends weakly on the energy gap and the vibronic structure of the molecule. We obtain  $\gamma / \hbar\omega = 1 / (870 \text{ cm}^{-1})$  from the ratio of the rates and a frequency factor  $A = 9.3 \times 10^{12} \text{ s}^{-1}$ . The frequency factor is in the range expected for the weak coupling limit [16]. Typical vibrational frequencies for the accepting modes between 1000 and  $3000 \text{ cm}^{-1}$  result in values for  $\gamma$  between 1.1 and 3.4. Similar values have been reported for carotenoids [17] and azulene [16]. These findings support the applicability of the energy gap law.

#### 4. Conclusions

In this work the influence of core substituents on the electronic relaxation of NDIs due to CT processes is investigated by femtosecond absorption spectroscopy. The work is thereby complementary to the more frequently studied CT mechanism of NDIs with electron donors attached to the N-termini [18–21]. We observe for the two compounds N–NDI–NAr and Cl–NDI–NAr an ultrafast charge separation with  $\sim 3$  ps after optical excitation into the  $S_1$  partial CT state. This step is found to be rather insensitive to the second substituent opposite to the donor moiety. This is in stark contrast to the charge recombination step leading back into the electronic ground state which takes 70 ps in the case of N–NDI–NAr and 11 ps in the case of Cl–NDI–NAr. To rationalize these findings *ab initio* calculations were performed. The calculated energy gap between the fully charge separated and the electronic ground state of N–NDI–NAr is 0.2 eV larger than in the case of Cl–NDI–NAr and the energy gap rule can account for the variation of the dynamics.

In our previous work on alkyl and arylsulfanyl core-substituted NDIs we found that full charge separation between the NDI chromophore and the aryl substituent occurs on the picosecond time scale via a two step process [8]. The first step corresponds to a planarization of the substituents and an associated partial electron transfer. In the second step the phenylsulfanyl substituent twists out of the NDI plane leading to a full charge transfer within 6–7 ps. The first step is not necessary in the case of the amino substituents studied here since the optically excited state has already a partial CT character and a quasi planar configuration. This is a result of the quasi planar equilibrium structure of the ground state due to an intramolecular hydrogen bond between the amino group and the vicinal carbonyl oxygen. The step to complete charge separation is very similar in both systems. The timescales are comparable and the process is associated with a twisting motion of the donor moiety out of the chromophore plane. It indicates that this scenario is general for core substituted NDIs while the atom linking the donor to the chromophore influences the initial phase of the charge separation via the equilibrium geometry in the ground state. In [8] we were able to change the coupling of the optically excited with the charge separated state and the speed of the corresponding electron transfer process by introducing a methylene spacer between the linker atom and the electron donor. In the present work the speed of the charge recombination process is strongly changed by varying the energy gap to the ground state via a second substituent. This indicates that the coupling and the energy gap represent two handles of the system, which allow tuning the charge separation and recombination process more or less independently from each other.

These findings should be helpful for the application of NDIs. For instance, NDIs are promising building blocks for electron transfer cascades with potential applications in artificial solar energy conversion [22]. Thereby efficient and fast charge separation and successive stabilization of the charges are important issues. This can be achieved using an assembly of molecules [23] or by making use of conformational changes within one molecule which trap the charge separated state [24]. Substituted NDIs might here be of interest if it is possible to increase the energy gap for recombination from 0.7 eV to about 1.2 eV. In this case the lifetime of the charge separated state should be in the nanosecond range due to the exponential dependence on the gap energy. On the other hand the fast charge separation process should be only little affected.

These findings should be helpful for the application of NDIs. For instance, NDIs are promising building blocks for electron transfer cascades with potential applications in artificial solar energy conversion [22]. Thereby efficient and fast charge separation and successive stabilization of the charges are important issues. This can be achieved using an assembly of molecules [23] or by making use of conformational changes within one molecule which trap the charge separated state [24]. Substituted NDIs might here be of interest if it is possible to increase the energy gap for recombination from 0.7 eV to about 1.2 eV. In this case the lifetime of the charge separated state should be in the nanosecond range due to the exponential dependence on the gap energy. On the other hand the fast charge separation process should be only little affected.

#### Acknowledgements

This work was supported by the Austrian Science Fund within the framework of the Special Research Program F16 (Advanced Light Sources), the SFB749, the DFG-Cluster of Excellence: Munich-Centre for Advanced Photonics and the BMBF (project OPV-Hybride). UM thanks the International Max Planck Research School on Advanced Photon Science for financial support. The Alexander von Humboldt Stiftung is gratefully acknowledged for a fellowship (IP), the Leibniz-Rechenzentrum LRZ Munich for computing time and access to TURBOMOLE.

#### Appendix A. Supplementary data

Supplementary data associated with this article can be found, in the online version, at doi:10.1016/j.cpllett.2011.01.038.

#### References

- [1] N. Sakai, J. Mareda, E. Vauthey, S. Matile, Chem. Commun. 46 (2010) 4225.
- [2] A.L. Sisson, N. Sakai, N. Banerji, A. Fürstenberg, E. Vauthey, S. Matile, Angew. Chem. Int. Edit. 47 (2008) 3727.
- [3] F. Würthner, S. Ahmed, C. Thalacker, T. Debaerdemaeker, Chem. Eur. J. 8 (2002) 4742.
- [4] A. Błaszczyk, M. Fischer, C. von Hänisch, M. Mayor, Helv. Chim. Acta 89 (2006) 1986.



- [5] C. Thalacker, C. Röger, F. Würthner, *J. Org. Chem.* 71 (2006) 8098.
- [6] S. Chopin, F. Chaignon, E. Blart, F. Odobel, *J. Mater. Chem.* 17 (2007) 4139.
- [7] E. Fron et al., *Photochem. Photobiol. Sci.* 7 (2008) 1509.
- [8] I. Pugliesi, P. Krok, S. Lochbrunner, A. Błaszczuk, C. von Hänisch, M. Mayor, E. Riedle, *J. Phys. Chem. A* 114 (2010) 12555.
- [9] U. Megerle, I. Pugliesi, C. Schrieber, C.F. Sailer, E. Riedle, *Appl. Phys. B* 96 (2009) 215.
- [10] A. Schäfer, H. Horn, R. Ahlrichs, *J. Chem. Phys.* 97 (1992) 2571.
- [11] A. Schäfer, C. Huber, R. Ahlrichs, *J. Chem. Phys.* 100 (1994) 5829.
- [12] F. Furche, R.J. Ahlrichs, *Chem. Phys.* 117 (2002) 7433.
- [13] O. Treutler, R. Ahlrichs, *J. Chem. Phys.* 102 (1995) 346.
- [14] R. Ahlrichs, M. Bär, M. Häser, H. Horn, C. Kölmel, *Chem. Phys. Lett.* 162 (1989) 165.
- [15] P. Fita, E. Luzina, T. Dziembowska, Cz. Radzewicz, A. Grabowska, *J. Chem. Phys.* 125 (2006) 184508.
- [16] R. Englman, J. Jortner, *Mol. Phys.* 18 (1970) 145.
- [17] V. Chynwat, H.A. Frank, *Chem. Phys.* 194 (1995) 237.
- [18] M.P. Debreczeny, W.A. Svec, M.R. Wasielewski, *Science* 274 (1996) 584.
- [19] A. Osuka, R. Yoneshima, H. Shiratori, T. Okada, S. Taniguchi, N. Mataga, *Chem. Commun.* (1998) 1567.
- [20] P. Ganesan, J. Baggerman, H. Zhang, E.J.R. Sudhölter, H. Zuilhof, *J. Phys. Chem. A* 111 (2007) 6151.
- [21] F. Chaignon, F. Buchet, E. Blart, M. Falkenstrom, L. Hammerstrom, F. Odobel, *New J. Chem.* 33 (2009) 408.
- [22] C. Röger, M.G. Müller, M. Lysetska, Y. Miloslavina, A.R. Holzwarth, F. Würthner, *J. Am. Chem. Soc.* 128 (2006) 6542.
- [23] B.P. Fingerhut, W. Zinth, R. De Vivie-Riedle, *Phys. Chem. Chem. Phys.* 12 (2010) 422.
- [24] H.A. Meylemans, J.T. Hewitt, M. Abdelhaq, P.J. Vallett, N. Damrauer, *J. Am. Chem. Soc.* 132 (2010) 11464.



## Supplementary data

# Influence of core-substitution on the ultrafast charge separation and recombination in aryl-core-substituted naphthalenediimides

Igor Pugliesi,<sup>a</sup> Uwe Megerle,<sup>a</sup> Frank Würthner,<sup>b</sup> Eberhard Riedle,<sup>a,\*</sup>  
Stefan Lochbrunner<sup>c,\*</sup>

<sup>a</sup> Lehrstuhl für BioMolekulare Optik, Ludwig-Maximilians-Universität München,  
80538 München, Germany

<sup>b</sup> Institut of Organic Chemistry, Universität Würzburg, Germany

<sup>c</sup> Institut für Physik, Universität Rostock, Germany

\* Corresponding authors:

*e-mail:* riedle@physik.lmu.de, *Tel.:* +49 89 2180 9210

*e-mail:* stefan.lochbrunner@uni-rostock.de, *Tel.:* +49 381 498 6960

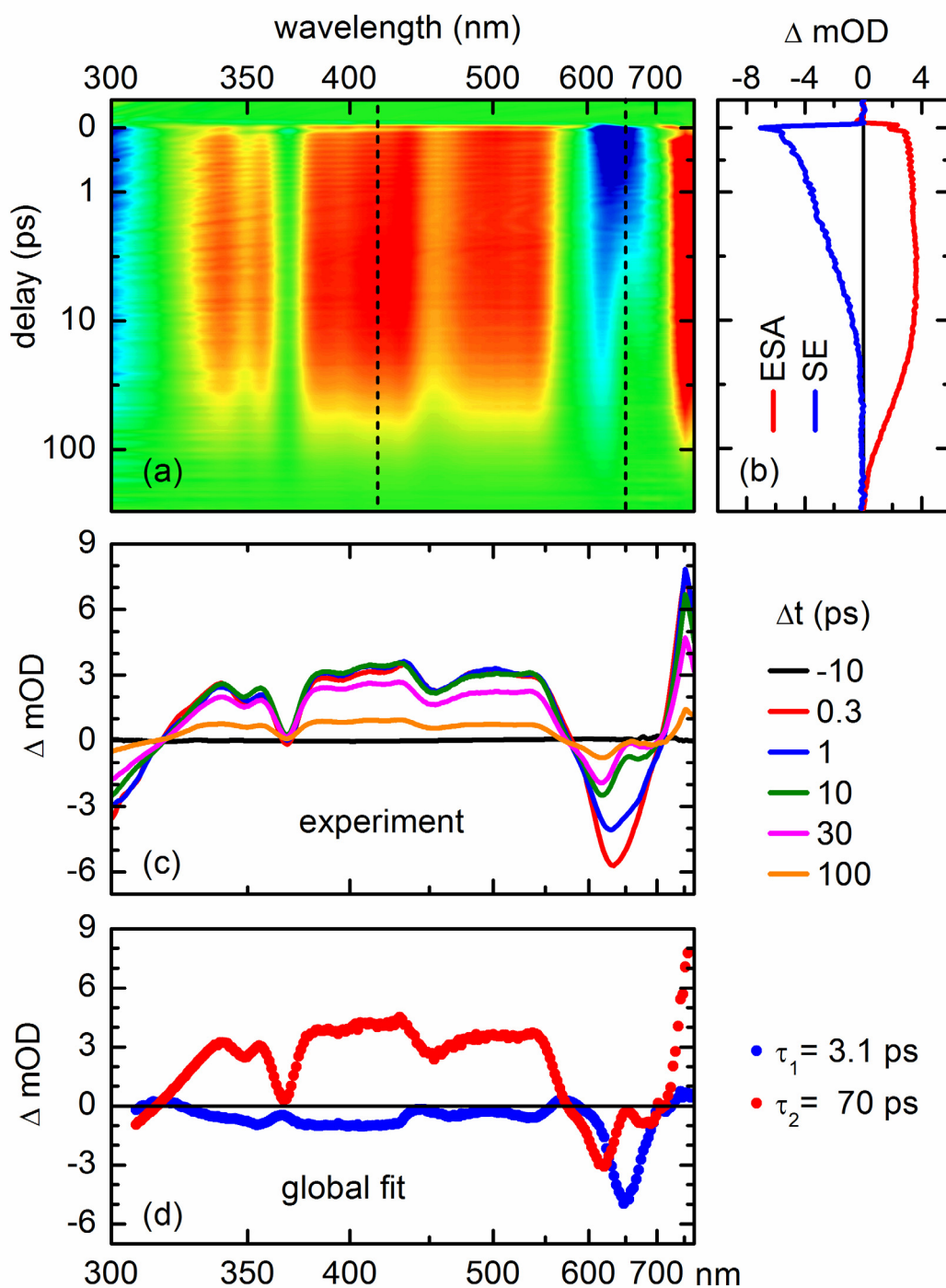


**Fig. S1** (a) Color map of the transient absorption of N-NDI-NAr in chloroform after optical excitation at 620 nm; warm colors represent positive and cold colors negative absorption changes. The time axis is linear up to 1 ps and logarithmic for longer delays. (b) Time traces at the spectral position of the ESA and SE (dotted lines in (a)). (c) Spectral cuts at selected delay times. (d) Decay associated difference spectra of the biexponential global fit.

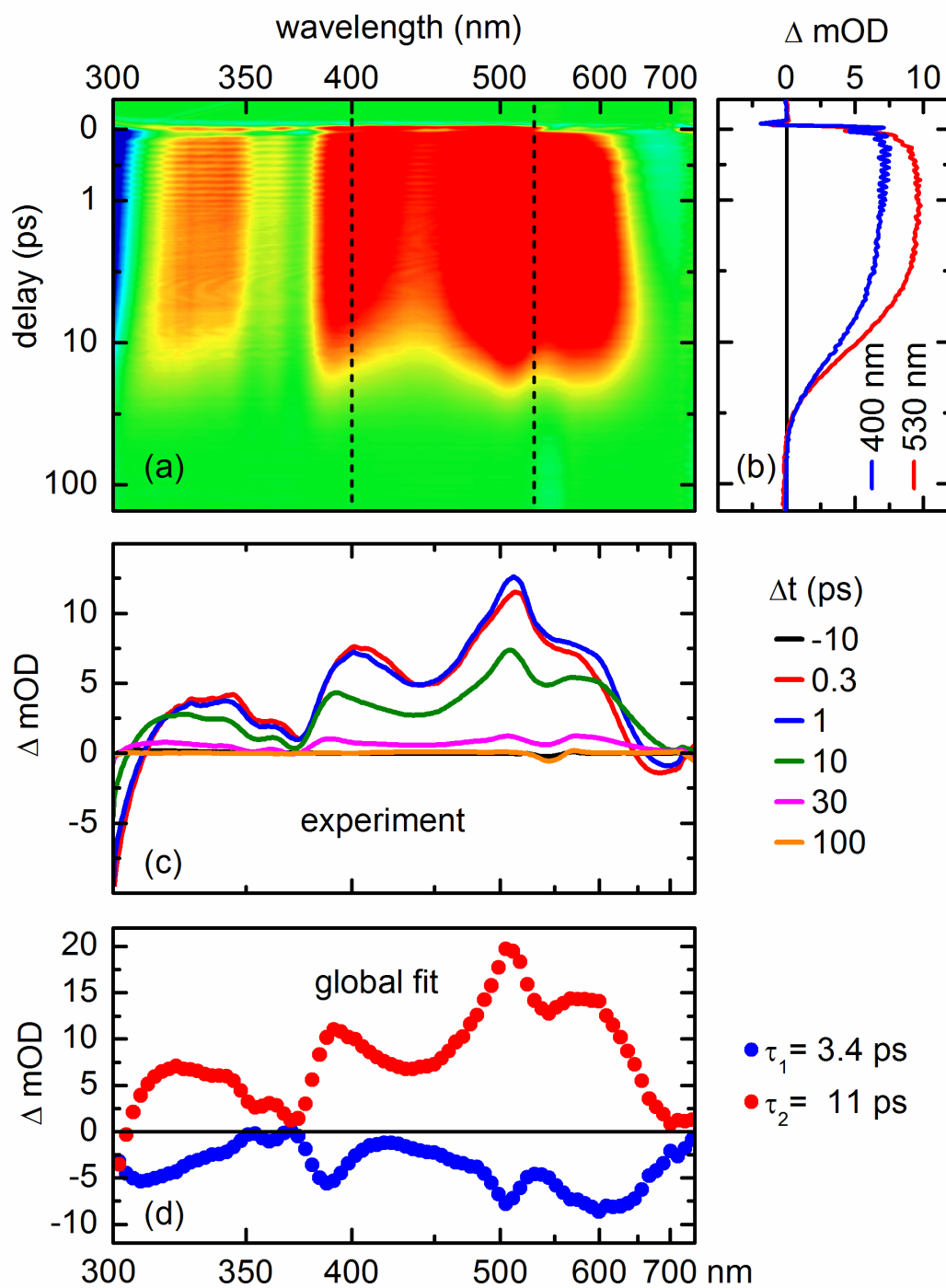


**Fig. S2** (a) Color map of the transient absorption of Cl-NDI-NAr in chloroform after optical excitation at 520 nm; warm colors represent positive and cold colors negative absorption changes. The time axis is linear up to 1 ps and logarithmic for longer delays. (b) The time traces demonstrate the dominant character of the ESA even at the spectral position of GSB (530 nm). (c) Spectral cuts at selected delay times. (d) Decay associated difference spectra of the biexponential global fit.

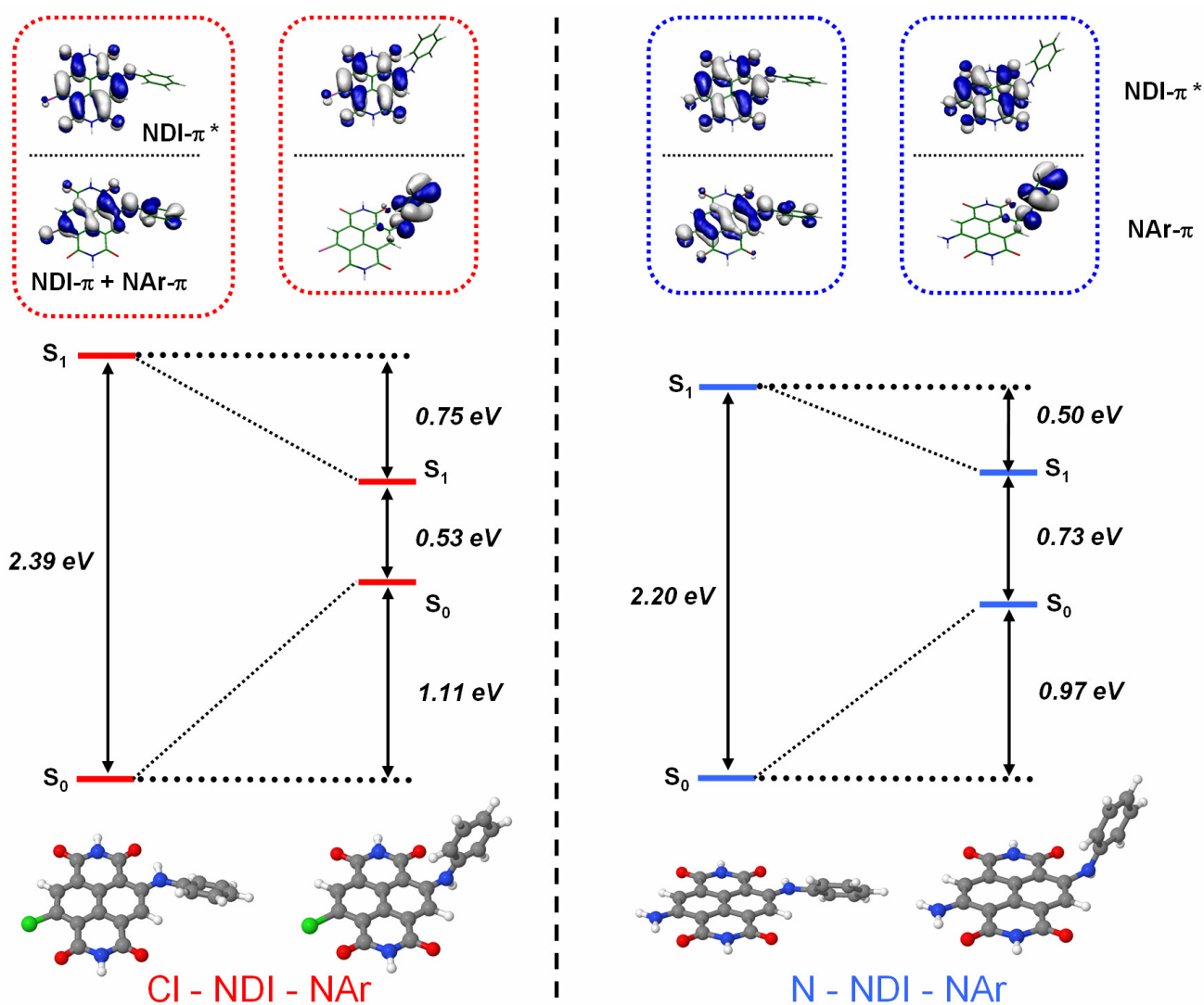


**Fig. S3** *Ab-initio* results for Cl-NDI-NAr and N-NDI-NAr obtained at the DFT and TDDFT / SVP level of theory. The upper panels show the molecular orbitals involved in the S<sub>1</sub> partial to S<sub>1</sub> full CT process. The energy level diagram shown in the middle is to scale. The lower panel shows the optimized geometries of the quasi-planar ground and the twisted S<sub>1</sub> full CT state.

## **Appendix A4**

### **Symmetry-dependent solvation of donor-substituted triarylboranes**

*U. Megerle, F. Selmaier, C. Lambert, E. Riedle, S. Lochbrunner*

Physical Chemistry Chemical Physics 10, 6245-6251 (2008)





# Symmetry-dependent solvation of donor-substituted triarylboranes

Uwe Megerle,<sup>\*a</sup> Florian Selmaier,<sup>a</sup> Christoph Lambert,<sup>b</sup> Eberhard Riedle<sup>a</sup> and Stefan Lochbrunner<sup>c</sup>

Received 11th April 2008, Accepted 3rd July 2008

First published as an Advance Article on the web 9th September 2008

DOI: 10.1039/b806131a

Donor-substituted triarylboranes are investigated by femtosecond absorption spectroscopy to study the influence of molecular symmetry on solvation. In solvents of varying polarity and differently fast solvation response, the solvation dynamics of a highly symmetric triple carbazole-substituted triarylborane (TCB) is compared to a single carbazole-substituted triarylborane (CB). The decomposition of the transient absorption spectra allows us to measure the solvation time by means of the time-dependent solvatochromic shift of the excited-state absorption (ESA) and the stimulated emission (SE). For all polar solvents under study we find an accelerated solvation process for TCB compared to the less symmetric CB. The difference is particularly large for solvents with a slow response. In order to explain these findings we propose that the electronic excitation is mobile in the symmetric molecule and can change between the three carbazole chromophores probably by a hopping mechanism. The excited-state dipole moment of TCB can thereby respond to the solvent relaxation and changes its direction according to the local field of the solvation shell. Thus, in a symmetric solute the possibility of an intramolecular charge delocalization over equivalent sites accelerates the approach of the minimum-energy configuration.

## 1. Introduction

The interaction of a molecule with its environment is a key aspect regarding the functionality of the molecule in a multi-component material.<sup>1,2</sup> In particular, if electronic excitations are involved, solvation processes resulting from such interactions have a strong impact on the dynamic material response.<sup>3</sup> A fascinating way of possibly altering solvation processes is to make the charges or excitations mobile within the solute. This can elegantly be achieved in highly symmetric molecules with several equivalent active sites.<sup>4,5</sup> Solvation has been investigated intensively in terms of solvent properties and electronic dipole changes in the solute.<sup>6–9</sup> However, almost no data is available about the influence of molecular symmetry on the solute/solvent-correlated dynamics.<sup>10,11</sup> We investigate this aspect by analyzing the ultrafast solvation dynamics of the triple carbazole-substituted triarylborane (TCB) which consists of three chromophores and whose equilibrium structure has a threefold rotation symmetry around the central boron atom (Fig. 1). The dynamics of TCB in several solvents with different polarity and response speed is compared to the single carbazole-substituted triarylborane (CB) which has only one active site.

A prerequisite for an excitation transfer between different subchromophores and thereby for an intramolecular contribution to the solvation process is effective electronic coupling.

Such a coupling between the transition moments of the subchromophores of TCB was indeed proposed by one of us.<sup>12</sup> Within the framework of the exciton coupling theory,<sup>13</sup> one

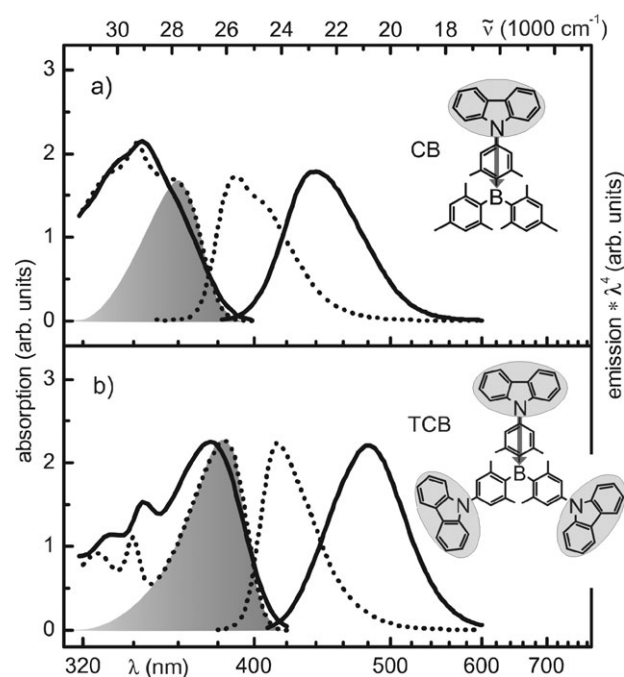


**Fig. 1** Steady-state absorption and emission spectra of (a) CB and (b) TCB in cyclohexane (dotted lines) and benzonitrile (solid lines). All solutions were excited at  $\lambda = 340$  nm. The CT-absorption band of both compounds in cyclohexane is shaded. It corresponds to a transfer of electron density from the carbazole moiety (gray ellipse) to the boron center as indicated by the arrow in the chemical structure.

<sup>a</sup> Lehrstuhl für BioMolekulare Optik, Ludwig-Maximilians-Universität München, Oettingenstr. 67, 80538 München, Germany.

E-mail: Uwe.Megerle@physik.uni-muenchen.de

<sup>b</sup> Institut für Organische Chemie, Julius-Maximilians-Universität Würzburg, Am Hubland, 97074 Würzburg, Germany

<sup>c</sup> Institut für Physik, Universität Rostock, Universitätsplatz 3, 18055 Rostock, Germany

can explain the  $1600\text{ cm}^{-1}$  redshift of the charge transfer (CT) absorption band of TCB compared to that of CB (shaded area in Fig. 1).

The unusual opposite solvatochromic shifts of the absorption and emission bands of both CB and TCB show that the photoexcitation leads to an inversion and increase of the static dipole moment in both compounds. The absorption of a photon is associated with a charge transfer from the nitrogen to the boron center (arrows in Fig. 1), resulting in a static dipole moment of 10 D for the excited state of CB and 9 D for that of TCB.<sup>12</sup>

In the case of TCB, the  $D_3$  symmetry of the ground state is slightly broken due to interactions with the environment and the electronic excitation induced by absorption of a photon is predominantly localized on one subchromophore.<sup>12</sup> The symmetry breaking can be concluded from the ground-state dipole moment of TCB (1.7 D), which is very similar to that of CB (1.8 D). Without symmetry breaking, the net dipole moment of TCB would vanish and no blueshift of the absorption band should be found. For both compounds, the direction of the ground-state dipole moment with a partially positive boron and a partially negative nitrogen center is opposite to that of the excited state.<sup>12</sup> The resulting difference of roughly 11 D between the static dipole moment of the ground and the excited state can be seen from the fact that for both molecules the redshift of the emission with increasing polarity is much stronger than the blueshift of the absorption. In polar solvents, this strong increase and reversal of the dipole moments of CB and TCB upon photoexcitation initiate a strong rearrangement of the solvation shell.

In the following section 2 we describe the femtosecond absorption experiments on CB and TCB dissolved in cyclohexane, benzonitrile, dichloromethane, chloroform and tetrahydrofuran. The experimental results together with a procedure to analyze the time-dependent shift of the absorption and emission bands are presented in section 3. On the basis of this evaluation the speed of solvation of TCB is compared to CB and finally the influence of mobile excitations on the solvation dynamics of the symmetric compound is discussed in section 4.

## 2. Experimental concept and implementation

In order to measure the solvation dynamics of the two donor-substituted triarylboranes, we apply transient absorption (TA) spectroscopy on the femtosecond timescale. In the past, methods like fluorescence upconversion<sup>14–16</sup> or Kerr-gating<sup>17,18</sup> have been successfully used to monitor the time-dependent emission following the optical excitation. For the upconversion method, the evaluation of the spectral shift of broad bands requires a very careful calibration of the sensitivity on the detection wavelength. In our particular case, the spectral range of the emission is in the blue and UV and thereby poses additional experimental challenges. Kerr-gating on the other hand suffers from high noise if applied to samples with long fluorescence lifetimes. Therefore we find it attractive to apply TA spectroscopy, which has also already been used to elucidate solvation dynamics.<sup>19,20</sup> This method intrinsically renders absolute numbers for the transmission change without

calibration of the sensitivity and one can achieve high signal-to-noise ratios larger than  $100:1$ .<sup>21</sup> The use of  $\text{CaF}_2$  as the medium for the white-light generation allows us to access easily the spectral region around  $400\text{ nm}$ <sup>20</sup> where the stimulated emission is expected. In general, TA signals consist of contributions from stimulated emission, ground-state bleaching and excited-state absorption (ESA). However, we will show that a proper analysis of the data allows a decomposition of the transient spectra and an accurate determination of the spectral shifts (see section 3.2).

In our experiment, a regenerative Ti:sapphire amplifier system (CPA 2001, Clark MXR) was used to pump a two-stage noncollinearly phase-matched optical parametric amplifier (NOPA)<sup>22</sup> delivering pulses of a few  $\mu\text{J}$  at  $720\text{ nm}$  with a repetition rate of  $1\text{ kHz}$ . Compression with SF10 prisms and subsequent frequency doubling in a BBO (beta barium borate) crystal yielded sub-100 fs pump pulses at  $360\text{ nm}$ . They were focused into a  $1\text{ mm}$  quartz cuvette containing the sample with a focus diameter of  $100\ \mu\text{m}$ . The pump energy was limited to  $\sim 100\text{ nJ}$  in order to avoid nonlinear effects such as multiphoton ionization of the solvent. By focusing another part of the Ti:sapphire beam (typically  $1\ \mu\text{J}$ ) into a rotating  $\text{CaF}_2$  plate of  $4\text{ mm}$  thickness, a supercontinuum was generated and used as probe. The fundamental wavelength ( $775\text{ nm}$ ) and the neighboring, strongly modulated spectral region were filtered out by a custom-made dielectric mirror. The probe was focused into the sample with a spherical mirror to a focus diameter of  $70\ \mu\text{m}$  and subsequently recollimated. Then, the probe light was dispersed with a fused silica prism and reflected by a spherical mirror mounted on a computer-controlled rotation stage. Transient spectra with a spectral resolution of  $100\text{--}200\text{ cm}^{-1}$  and a time resolution of  $\sim 200\text{ fs}$  were recorded by moving the dispersed beam over a photodiode (PDI-400-1-UV; Becker&Hickl GmbH) behind a slit. The temporal dispersion of the continuum was corrected for during the measurements by adjusting the delay line of the excitation pulses synchronously with the wavelength. The relative polarizations between pump and probe were set to the magic angle ( $54.7^\circ$ ) by a half-wave plate in the pump-beam path.

The synthesis of CB and TCB has been described previously.<sup>12</sup> The solvents cyclohexane, dichloromethane, chloroform and tetrahydrofuran were obtained from Merck and benzonitrile from Sigma-Aldrich in spectroscopic quality. The concentrations of CB and TCB were chosen such that the optical densities of the solutions were below 0.5 for a  $1\text{ mm}$  layer. The steady-state absorption spectra were recorded with a PerkinElmer Lambda 19 spectrophotometer and the fluorescence was measured with a Spex Fluorolog 2 spectrofluorometer with an excitation wavelength of  $340\text{ nm}$ . The cw (continuous wave) fluorescence spectra were multiplied by a factor of  $\lambda^4$  to obtain the spectral shape of the stimulated emission in the transient absorption spectra.<sup>23</sup>

## 3. Results

### 3.1 Femtosecond transient absorption: solvation dynamics

Fig. 2 shows the transient absorption spectra of TCB in cyclohexane and benzonitrile after photoexcitation. In the

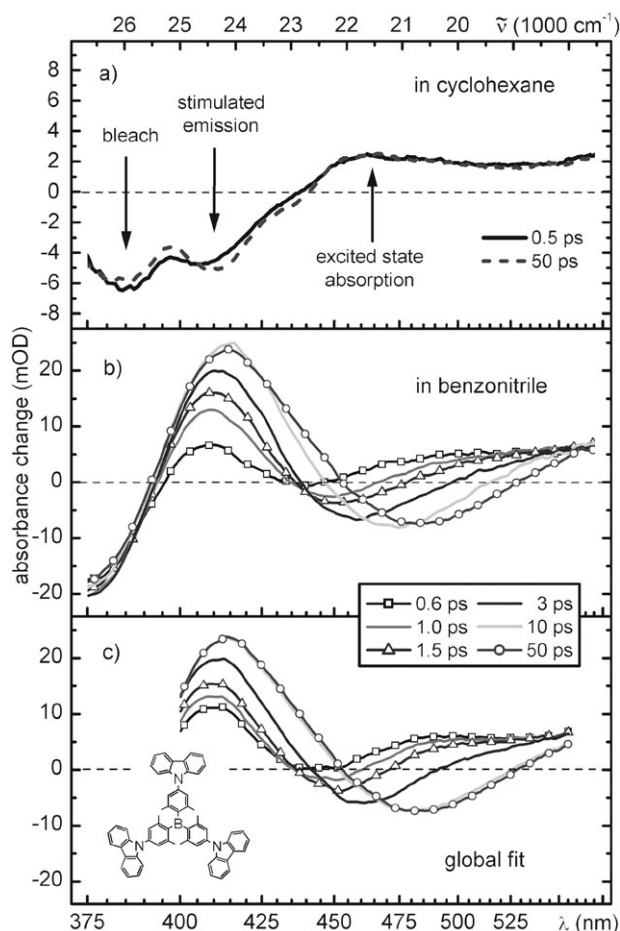


**Fig. 2** TA spectra of TCB (a) in cyclohexane after excitation at 340 nm and (b) in benzonitrile after excitation at 360 nm. (c) The spectra from (b) are simulated between 400 and 555 nm according to the global-fit routine described in the text.

nonpolar cyclohexane they remain unchanged on the timescale of several tens of picoseconds (see Fig. 2a). Only for larger delay times, approaching the fluorescence lifetime of a few nanoseconds, does the decay to the ground state cause the signal to decrease. A comparison with the cw spectra (Fig. 1) identifies the local minimum at 385 nm as a signature of the ground-state bleach, while the minimum at 410 nm corresponds to the maximum of the stimulated emission (SE). Both signatures are overlaid with the excited-state absorption (ESA) that contributes a positive change to the optical density and dominates for wavelengths above 440 nm.

This static behavior of the TA spectra is completely changed when TCB is dissolved in a polar solvent like benzonitrile (see Fig. 2b). Now a pronounced evolution of the spectra between 0 and  $\sim 50$  ps delay is found. Again, a minimum is observed at the position of the ground-state absorption maximum (375 nm) and a second local minimum due to the stimulated emission. For increasing delay times, the latter shifts from 440 nm to about 480 nm, which corresponds to the peak of the cw fluorescence in this solvent. This shift arises unambiguously from the solvation of the highly polar excited state of TCB. However, the observed local minimum cannot be directly identified with the position of the SE maximum. The ESA

strongly distorts the spectral shape and in addition experiences a solvation-dependent shift. The spectral distortion caused by the ESA can be seen for example by the fact that the optical density (OD) value of the local minimum in the visible changes by about 7 mOD between 0.6 and 50 ps delay.

In the case of CB (Fig. 3), the overall picture seen in the TA spectra is similar to TCB. While practically no dynamics of the spectral signatures are found for the nonpolar solvent cyclohexane (see Fig. 3a), the TA changes drastically during the first tens of picoseconds in polar solvents like benzonitrile (see Fig. 3b). In cyclohexane, the local minimum at  $\sim 390$  nm agrees well with the cw emission peak (see Fig. 1) and no significant spectral shift is observed. In benzonitrile, the TA spectra at early delay times show a local minimum around 400 nm that shifts to longer wavelengths until a delay time of  $\sim 2$  ps. Again, the signature of the SE is distorted by the band structure of the ESA. In contrast to TCB, the superposition of SE and ESA even causes the local minimum to disappear in the spectra of CB for certain delay times, e.g. 3 ps. For delay times between 5 and 50 ps, a minimum is found again shifting from 445 to 455 nm respectively. Since the cw emission of CB in benzonitrile has a maximum at 440 nm, it is obvious that a direct identification of the time-dependent spectral position of

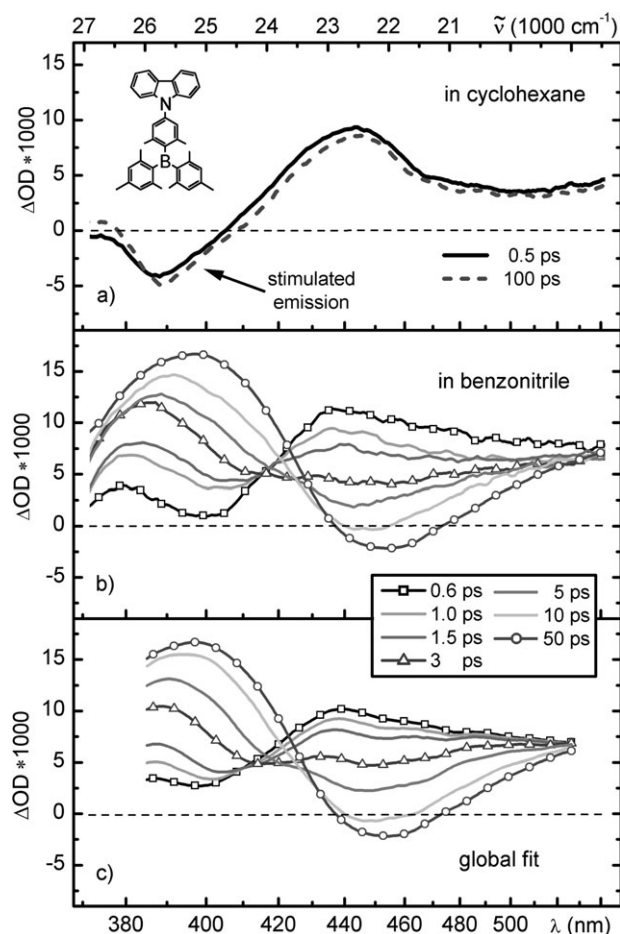


**Fig. 3** TA spectra of CB (a) in cyclohexane after excitation at 340 nm and (b) in benzonitrile after excitation at 360 nm. (c) The spectra from (b) are simulated between 385 and 525 nm according to the global-fit routine described in the text.

the SE in the transient spectra is not possible. Thus, kinetic traces at fixed probe wavelengths would not allow one to quantify the solvation dynamics. Nevertheless, the time-dependent Stokes shift can be measured by modeling the transient spectra with a global-fit routine.

### 3.2 Global fit: decomposition of the TA spectra

In the visible (above  $\sim 400$  nm) region, only two signals contribute to the TA spectra: the ESA and the SE. Both signals depend on the delay time  $t$  and on the wavenumber  $\tilde{\nu}$ :

$$\text{TA}(t, \tilde{\nu}) = \text{ESA}(t, \tilde{\nu}) + \text{SE}(t, \tilde{\nu}) \quad (1)$$

From the time invariance of the spectra in cyclohexane we conclude that solvation is the only driving force for the spectral changes in polar solvents as it is discussed below. We assume an evolution of both the  $\text{ESA}(t, \tilde{\nu})$  and the  $\text{SE}(t, \tilde{\nu})$  that comprises an exponential shift of the spectral bands with time on the energy scale as depicted in Fig. 4 and given in eqn (2) and (3):

$$\text{ESA}(t, \tilde{\nu}) = \text{ESA}(\infty, [\tilde{\nu} - \Delta\tilde{\nu}_{\text{ESA}} \cdot e^{-t/\tau}]) \quad (2)$$

$$\text{SE}(t, \tilde{\nu}) = \text{SE}(\infty, [\tilde{\nu} - \Delta\tilde{\nu}_{\text{SE}} \cdot e^{-t/\tau}]) \quad (3)$$

$\Delta\tilde{\nu}_{\text{ESA}}$  and  $\Delta\tilde{\nu}_{\text{SE}}$  are the total shifts of the ESA and SE signatures and  $\tau$  is the common time constant reflecting the averaged solvation dynamics of the system. In this case, we use  $t = \infty$  for delay times larger than the solvation timescale but much lower than the nanosecond fluorescence lifetime,<sup>12</sup> *i.e.* when the system is in quasi-equilibrium. Then, the SE signature must coincide with the known steady-state emission spectrum in the respective solvent (lower solid line in Fig. 4). The spectral shape of the ESA for large delay times can then be inferred from the final transient spectrum by subtracting the cw emission spectrum with a proper scaling factor. The result is typically a broad ESA band with a maximum around 420 nm (upper solid line in Fig. 4).

For small delay times the SE is blueshifted, accounting for the unfavorable energetic situation before full solvation of the

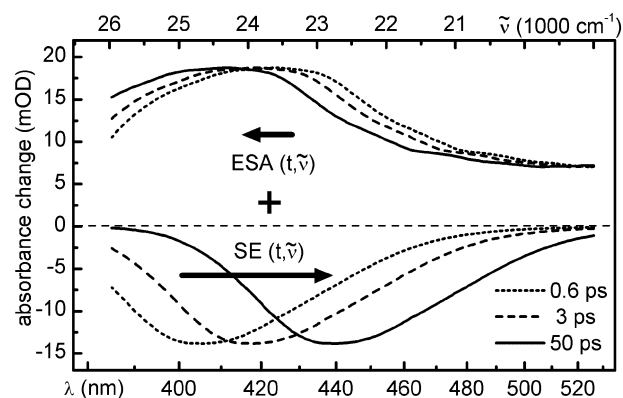


**Fig. 4** Simulation (global fit) of the transient spectra of CB in benzonitrile (compare Fig. 3b): the spectral evolution is described by a small shift of the calculated ESA (upper part,  $\Delta\tilde{\nu}_{\text{ESA}} = -790 \text{ cm}^{-1}$ ) in combination with a strongly shifting SE (lower part,  $\Delta\tilde{\nu}_{\text{SE}} = 2180 \text{ cm}^{-1}$ ). The optimal shift amplitudes as well as the corresponding exponential time constant  $\tau = 5.04$  ps were found by a least-squares fit to the transient absorption data.

system. As a consequence,  $\Delta\tilde{\nu}_{\text{SE}}$  in eqn (3) will always have a positive sign. Since the dipole of the higher electronic states contributing to the ESA band is unknown at first,  $\Delta\tilde{\nu}_{\text{ESA}}$  can in principle have both signs. However, the dynamics of the shift should be the same as for the SE and therefore the same  $\tau$  can be used in eqn (2) and (3). The shifted ESA and SE at early delay times are shown as dashed and dotted lines in Fig. 4.

With a least-squares fit algorithm we optimized the shift amplitudes  $\Delta\tilde{\nu}_{\text{ESA}}$  and  $\Delta\tilde{\nu}_{\text{SE}}$  as well as the corresponding time constant  $\tau$  for best agreement between the simulated TA spectra according to eqn (1) and the experimental data. The obtained fit parameters for CB and TCB in four polar solvents are given in Table 1 together with the average solvation times from the literature. An additional variable in the fit algorithm was the absolute scaling of the cw emission spectrum. However, since this parameter depends on the experimental conditions in the steady-state measurement, it is not of general interest and was not included in the Table. In all cases, the correlations between the fit variables were well below unity which proves, for example, that  $\Delta\tilde{\nu}_{\text{ESA}}$  is not a redundant parameter in our model.

To rule out significant contributions from the ground-state bleach, the global fit was restricted to the spectral region from 25 000 to 18 000  $\text{cm}^{-1}$  for TCB and from 26 000 to 19 000  $\text{cm}^{-1}$  for CB. For the solvent benzonitrile, the spectra simulated in such a manner are shown in Fig. 2c and 3c for TCB and CB respectively. The agreement with the experimental curves in Fig. 2b and 3b is very good. This again justifies our assumption that only solvatochromic shifts are responsible for the pronounced evolution of the TA spectra. It is noteworthy that this minimal parameter model which contains only one time constant can reproduce with a high accuracy the complex behavior of the CB spectra in polar solvents (Fig. 3c). On the contrary, fits to kinetic traces at fixed wavelengths comprise one to three exponential components with strongly varying time constants depending on the probe wavelength. Therefore, they are not suitable for describing the solvation dynamics.

Usually multiple time constants are used to describe solvation.<sup>8</sup> We find it sufficient to use a single time constant to reproduce our experimental results. It should be compared to the weighted average of the multiple time constants. In this approach the fast inertial components might not be fully taken into account. However, the good agreement with the experimental data shows that our model reflects the dominant solvation effects.

The shift amplitudes of a few thousand  $\text{cm}^{-1}$  found for the SE of CB and TCB compare reasonably well with the steady-state spectra. The solvatochromic shift can be related in a first approximation to the difference between the Stokes shift in a nonpolar and a polar solvent. This difference ranges roughly from 2000 to 4000  $\text{cm}^{-1}$ .<sup>12</sup> A more detailed comparison of the solvent- and solute-dependent trends is complicated by the somewhat arbitrary assignment of the CT absorption maximum of CB, which is superimposed on a local carbazole transition. Additionally, we might not resolve the full solvatochromic shift in our TA spectra due to a limited time resolution. We only want to stress that the values for  $\Delta\tilde{\nu}_{\text{ESA}}$  are typically much lower than  $\Delta\tilde{\nu}_{\text{SE}}$  for both solutes. This implies a much weaker change of the static dipole moment for the  $S_1 \rightarrow S_n$  transition than for the  $S_0 \rightarrow S_1$  excitation.

**Table 1** Global-fit parameters in several polar solvents.  $\Delta\tilde{\nu}_{\text{ESA}}$ : shift of the excited-state absorption;  $\Delta\tilde{\nu}_{\text{SE}}$ : shift of the stimulated emission;  $\tau$ : solvation time. Values for TCB are in bold for convenience. For comparison, the average solvation times for coumarin 153 from ref. 8 are given in the last column

Solvent	$\Delta\tilde{\nu}_{\text{ESA}}/\text{cm}^{-1}$		$\Delta\tilde{\nu}_{\text{SE}}/\text{cm}^{-1}$		$\tau/\text{ps}$		$\langle\tau_{\text{solv}}\rangle/\text{ps}$ Ref. 8
	TCB	CB	TCB	CB	TCB	CB	
Benzonitrile	<b>100</b>	−790	<b>3130</b>	2180	<b>2.97</b>	5.04	5.1
Chloroform <sup>a</sup>	<b>460</b>	−1080	<b>1040</b>	970	<b>4.27</b>	8.26	2.8
Tetrahydrofuran	<b>80</b>	−650	<b>3220</b>	2110	<b>1.10</b>	1.48	0.94
Dichloromethane	<b>−140</b>	−780	<b>2190</b>	1940	<b>1.06</b>	1.30	0.56

<sup>a</sup> The quality of the data and the fit are inferior in this solvent. For details see text.

## 4. Discussion

The goal of this work is to investigate the intramolecular contributions to the overall solvation dynamics. In this respect, the most interesting variable in the global analysis of the TA spectra is the time for the spectral shifts of the ESA and the SE. It is interpreted as the average solvation time of the system. Table 1 clearly reveals an accelerated solvation for TCB when compared to CB in the same solvent. In all four cases, the larger, symmetric molecule is solvated faster than the smaller one with lower symmetry.

The evaluated solvation times are in the same regime as the average solvation timescales obtained with a coumarin solute,<sup>8</sup> which affirms our global-fit routine. However, we are aware that an average solvent relaxation time of a given solvent is not a universal constant but depends on the specific solvent–solute combination and the method of measurement.<sup>24</sup> The largest deviation of the solvation times is found for CB in chloroform, but in this solvent both our data and those of ref. 8 have the lowest quality. Additional difficulties for the interpretation of these data and their comparison to the other solvents arise from the fact that the chloroform solutions were excited at 340 nm instead of 360 nm. Nevertheless, these data also confirm the general trend of shorter solvation times for TCB than for CB.

Interestingly, these differences become smaller in solvents with fast relaxation times. In dichloromethane and tetrahydrofuran, the solvation time of TCB is only 20–25% below that of CB ( $\Delta\tau < 400$  fs), while *e.g.* for benzonitrile the acceleration amounts to over 40% or a difference of about 2 ps. Fig. 5a shows the evaluated solvation rates (*i.e.* the inverse of the solvation times  $\tau$ ) for CB and TCB in the four polar solvents under study.

There are several experimental and theoretical studies investigating the influence of the solute on the solvation dynamics. For instance, a dependence on the multipole order of the photo-induced charge distribution was predicted.<sup>25</sup> This effect should cause no significant difference in the solvation dynamics of CB and TCB since the charge distributions are very similar. Molecular dynamics simulations also suggest a decrease of the solvation timescale for an increasing distance from the solute.<sup>26</sup> However, it was argued that for dipolar solutes no remarkable dependence on the solute size should result.<sup>27</sup> On the other hand, theoretical studies indicate that a solute which can easily translate and rotate experiences a faster solvation than a less mobile molecule.<sup>28</sup> From this one might expect a slightly slower solvation for the larger TCB. In

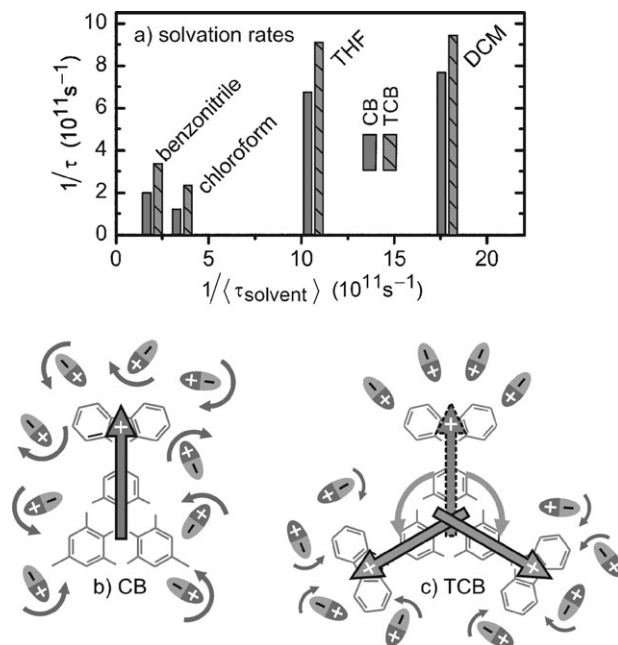


**Fig. 5** (a) Solvation rates (inverse solvation times  $\tau$ ) from the global-fit analysis for CB and TCB in polar solvents (THF: tetrahydrofuran; DCM: dichloromethane). The x-axis represents the average solvation rates from ref. 8. Lower part: schematic representation of the different solvation processes of (b) CB and (c) TCB. Optical excitation leads to an inverted static dipole moment (arrow on top of the chemical structure) initially localized on one branch in both compounds. For CB as solute, only the solvent molecules (elliptic dipoles) respond by translation or rotation to reach the solvated quasi-equilibrium state. For TCB as solute, intramolecular excitation transfer between the subchromophores can occur in addition.

accordance with this, experimental studies indeed find a somewhat slower solvation for larger molecules.<sup>29,30</sup>

In order to explain the consistently higher rates of TCB, we propose different solvation processes for CB and TCB as depicted schematically in Fig. 5b and c. Based on the fact that the three subchromophores of TCB are electronically coupled,<sup>12,31</sup> we suggest an intramolecular charge transfer in the excited state from one carbazole moiety to another. The excitation transfer would be driven by the fact that the charge-accepting carbazole is situated in a more favorably oriented solvent shell. This hypothesis requires an unsymmetrical solvation of TCB in the ground state. This is supported by static

fluorescence and absorption measurements which indicate a symmetry-broken ground state for TCB.<sup>12</sup> Thus, the complete system of the solute and the surrounding solvent dipoles possesses an additional pathway to reach a minimum-energy configuration. This process might be supported by an increased planarity in the excited state, as has been proposed for similar multichromophores.<sup>32</sup>

In principle, other intramolecular processes might also contribute to accelerated spectral shifts in the transient spectra of TCB. Intramolecular vibrational redistribution can result in spectral redshifts and might be faster in larger molecules with more internal degrees of freedom. This should also be observed to a certain degree in nonpolar solvents. We do not observe a significant evolution of the transient spectra in cyclohexane (see Fig. 2 and 3). This indicates that vibrational redistribution processes have only little impact on the spectral evolution of CB and TCB. In particular they cannot be responsible for the strong variations between the two molecules in polar solvents. Because of the flexible moieties of TCB, the influence of conformational changes on the solvation dynamics also has to be considered. However, the excited-state dipole moments of CB and TCB are very similar<sup>12</sup> indicating that in TCB the charge redistribution is essentially restricted to a single branch. Therefore, a geometric rearrangement of the three branches will not directly contribute to the observable solvation dynamics.

The intramolecular charge transfer during solvation most likely proceeds *via* a site-to-site hopping process<sup>33,34</sup> rather than a delocalization of the wavefunction over the subchromophores.<sup>35</sup> Otherwise, the solvation times of TCB would be much faster. In this case, no approach to the solvation dynamics of CB would be found for solvents with fast relaxation times (<1 ps). We therefore assume that the charge hopping occurs with a rate of about  $10^{12} \text{ s}^{-1}$ , *i.e.* on the timescale of  $\sim 1$  ps, in addition to the usual solvation. The latter is governed by motions of the solvent molecules and is the only available process in the case of simple chromophores such as CB (see Fig. 5b). For TCB however, the intramolecular charge redistribution plays an important role in the overall solvation process (see Fig. 5c).

## 5. Conclusions

We showed that the symmetry of a multi-chromophore solute can have a significant impact on its solvation dynamics. The availability of several active sites opens up the possibility of intramolecular excitation or charge transfer in addition to the intermolecular response by the solvent shell after photoexcitation. Thereby, the static dipole moment of the excited state is essentially mobilized and can hop between the branches of the symmetric molecule. This leads to an accelerated energy relaxation in comparison to a model compound with only one active site.

The study shows also that TA spectroscopy is a powerful tool to characterize these processes. This holds in particular if a global-fit procedure is applied that accounts directly for the spectral shifts of the involved ESA and SE bands.

In general, our study is an example for the significant dependence of the solvation dynamics on the solute. This fact

is often neglected in the literature, especially for aprotic solvents, and most experimental studies focus on the solvent dependence of the dynamics.<sup>36,37</sup> On the other hand, the accelerated response of symmetric solutes can be used to stabilize excited states faster and more efficiently. Multichromophores designed in such a way can therefore be interesting for applications in functional organic materials, since in general their other properties differ only slightly from their single-site counterparts.

## Acknowledgements

Financial support from the International Max Planck Research School on Advanced Photon Science (U. M.) is gratefully acknowledged.

## References

- 1 C. D. Entwistle and T. B. Marder, *Chem. Mater.*, 2004, **16**, 4574–4585.
- 2 A. Painelli, F. Terenziani and Z. G. Soos, *Theor. Chem. Acc.*, 2007, **117**, 915–931.
- 3 M. Glasbeek and H. Zhang, *Chem. Rev.*, 2004, **104**, 1929–1954.
- 4 O. Varnavski, T. Goodson III, L. Sukhomlinova and R. Twieg, *J. Phys. Chem. B*, 2004, **108**, 10484–10492.
- 5 C. Le Droumaguet, O. Mongin, M. H. V. Werts and M. Blanchard-Desce, *Chem. Commun.*, 2005, 2802–2804.
- 6 P. F. Barbara and W. Jarzēba, *Adv. Photochem.*, 1990, **15**, 1–68.
- 7 M. Maroncelli, *J. Mol. Liq.*, 1993, **57**, 1–37.
- 8 M. L. Horng, J. A. Gardecki, A. Papazyan and M. Maroncelli, *J. Phys. Chem.*, 1995, **99**, 17311–17337.
- 9 J. L. Pérez Lustres, S. A. Kovalenko, M. Mosquera, T. Senyushkina, W. Flasche and N. P. Ernstring, *Angew. Chem., Int. Ed.*, 2005, **44**, 5635–5639.
- 10 A. T. Yeh, C. V. Shank and J. K. McCusker, *Science*, 2000, **289**, 935–938.
- 11 A. Bhaskar, G. Ramakrishna, Z. Lu, R. Twieg, J. M. Hales, D. J. Hagan, E. Van Stryland and T. Goodson III, *J. Am. Chem. Soc.*, 2006, **128**, 11840–11849.
- 12 R. Stahl, C. Lambert, C. Kaiser, R. Wortmann and R. Jakober, *Chem.–Eur. J.*, 2006, **12**, 2358–2370.
- 13 M. Kasha, H. R. Rawls and M. A. El-Bayoumi, *Pure Appl. Chem.*, 1965, **11**, 371–392.
- 14 R. Schanz, S. A. Kovalenko, V. Kharlanov and N. P. Ernstring, *Appl. Phys. Lett.*, 2001, **79**, 566–568.
- 15 L. J. Zhao, J. L. P. Lustres, V. Farztdinov and N. P. Ernstring, *Phys. Chem. Chem. Phys.*, 2005, **7**, 1716–1725.
- 16 A. Cannizzo, O. Bräm, G. Zgrablic, A. Tortschanoff, A. A. Oskouei, F. van Mourik and M. Chergui, *Opt. Lett.*, 2007, **32**, 3555–3557.
- 17 B. Schmidt, S. Laimgruber, W. Zinth and P. Gilch, *Appl. Phys. B: Lasers Opt.*, 2003, **76**, 809–814.
- 18 S. Arzhantsev and M. Maroncelli, *Appl. Spectrosc.*, 2005, **59**, 206–220.
- 19 S. A. Kovalenko, N. Eilers-König, T. A. Senyushkina and N. P. Ernstring, *J. Phys. Chem. A*, 2001, **105**, 4834–4843.
- 20 U. Schmidhammer, U. Megerle, S. Lochbrunner, E. Riedle and J. Karpiuk, *J. Phys. Chem. A*, 2008, DOI: 10.1021/jp800863u.
- 21 C. Schriever, S. Lochbrunner, E. Riedle and D. J. Nesbitt, *Rev. Sci. Instrum.*, 2008, **79**, 013107-1–013107-9.
- 22 E. Riedle, M. Beutter, S. Lochbrunner, J. Piel, S. Schenk, S. Spörlein and W. Zinth, *Appl. Phys. B: Lasers Opt.*, 2000, **71**, 457–465.
- 23 G. Angulo, G. Grampp and A. Rosspeintner, *Spectrochim. Acta, Part A*, 2006, **65**, 727–731.
- 24 R. Maksimenka, M. Margraf, J. Köhler, A. Heckmann, C. Lambert and I. Fischer, *J. Chem. Phys.*, 2008, **347**, 436–445.

- 
- 25 K. Nishiyama, T. Yamaguchi, F. Hirata and T. Okada, *J. Solution Chem.*, 2004, **33**, 631–639.
- 26 M. Maroncelli, E. W. Castner, Jr., B. Bagchi and G. R. Fleming, *Faraday Discuss. Chem. Soc.*, 1988, **85**, 199–210.
- 27 D. F. Parsons, M. V. Vener and M. V. Basilevsky, *J. Phys. Chem. A*, 1999, **103**, 1171–1178.
- 28 F. Ingrosso, B. M. Ladanyi, B. Mennucci, M. D. Elola and J. Tomasi, *J. Phys. Chem. B*, 2005, **109**, 3553–3564.
- 29 S. G. Su and J. D. Simon, *J. Phys. Chem.*, 1989, **93**, 753–758.
- 30 W. Jarzeba, G. C. Walker, A. E. Johnson and P. F. Barbara, *Chem. Phys.*, 1991, **152**, 57–68.
- 31 C. Lambert, W. Gaschler, E. Schmälzlin, K. Meerholz and C. Bräuchle, *J. Chem. Soc., Perkin Trans.*, 1999, **2**, 577–587.
- 32 W. Verbouwe, L. Viaene, M. Van der Auweraer, F. C. De Schryver, H. Masuhara, R. Pansu and J. Faure, *J. Phys. Chem. A*, 1997, **101**, 8157–8165.
- 33 L. Latterini, G. De Belder, G. Schweitzer, M. Van der Auweraer and F. C. De Schryver, *Chem. Phys. Lett.*, 1998, **295**, 11–16.
- 34 W. Verbouwe, M. Van der Auweraer, F. C. De Schryver, J. J. Piet and J. M. Warman, *J. Am. Chem. Soc.*, 1998, **120**, 1319–1324.
- 35 J. J. Piet, W. Schuddeboom, B. R. Wegewijs, F. C. Grozema and J. M. Warman, *J. Am. Chem. Soc.*, 2001, **123**, 5337–5347.
- 36 C. F. Chapman, R. S. Fee and M. Maroncelli, *J. Phys. Chem.*, 1995, **99**, 4811–4819.
- 37 K. Nishiyama, F. Hirata and T. Okada, *J. Chem. Phys.*, 2003, **118**, 2279–2285.





## **Appendix A5**

### **The key role of solvation dynamics in intramolecular electron transfer: time-resolved photophysics of crystal violet lactone**

*U. Schmidhammer, U. Megerle, S. Lochbrunner, E. Riedle, J. Karpiuk*

Journal of Physical Chemistry A 112, 8487-8496 (2008)



# The Key Role of Solvation Dynamics in Intramolecular Electron Transfer: Time-Resolved Photophysics of Crystal Violet Lactone

Uli Schmidhammer,<sup>§,†</sup> Uwe Megerle,<sup>†</sup> Stefan Lochbrunner,<sup>ll,†</sup> Eberhard Riedle,<sup>\*,†</sup> and Jerzy Karpiuk<sup>\*,‡</sup>

Lehrstuhl für BioMolekulare Optik, Ludwig-Maximilians-Universität (LMU), Oettingenstr. 67, 80538 München, Germany, and Institute of Physical Chemistry, Polish Academy of Sciences, Kasprzaka 44/52, 01-224 Warsaw, Poland

Received: January 29, 2008; Revised Manuscript Received: June 7, 2008

The intramolecular electron-transfer reaction in crystal violet lactone in polar aprotic solvents is studied with femtosecond transient absorption spectroscopy. The initially excited charge transfer state  ${}^1\text{CT}_A$  is rapidly converted into a highly polar charge transfer state  ${}^1\text{CT}_B$ . This ultrafast electron transfer is seen as a solvent-dependent dual fluorescence in steady-state spectra. We find that the electron-transfer process can be followed by a change from a double-peaked transient absorption spectrum to a single-peak one in the low picosecond range. The transient absorption kinetic curves are multiexponential, and the fitted time constants are solvent dependent but do not reproduce the known solvation times. For 6-dimethylaminophthalide, the optically active constituent of crystal violet lactone, only a small temporal evolution of the spectra is found. To explain these findings, we present a model that invokes a time-dependent electron-transfer rate. The rate is determined by the instantaneous separation of the two charge-transfer states. Because of their differing dipole moments, they are dynamically lowered to a different extent by the solvation. When they temporarily become isoenergetic, equal forward and backward transfer rates are reached. The intrinsic electron-transfer ( ${}^1\text{CT}_A \rightarrow {}^1\text{CT}_B$ ) reaction is probably as fast as that in the structurally analogous malachite green lactone (on the 100 fs time scale). The key element for the dynamics is therefore its control by the solvent, which changes the relative energetics of the two states during the solvation process. With further stabilization of the more polar state, the final equilibrium in state population is reached.

## I. Introduction

Excited molecules in solution and their chemical reactions are often considerably affected by the interaction with the environment. The dynamical behavior of the solvent molecules can lead to significant charge redistribution and the population of charge-transfer (CT) states that are inaccessible in the absence of solute–solvent interactions. The dynamics of such solvent-controlled electron-transfer (ET) processes reflects the interplay between intramolecular and solvation dynamics. Generally, a two-dimensional reaction coordinate is used in the description to include both the vibronic couplings and the solvent degrees of freedom.<sup>1</sup> The kinetics of solvent-controlled ET processes has been extensively studied theoretically,<sup>2,3</sup> but the existing body of time-dependent studies demonstrating the dynamic solvent control of ET<sup>3–11</sup> still leaves important fundamental questions open. In this paper, we want to experimentally clarify the impact of solvation on the ET dynamics and how the progress of the solvation influences the ET.

So far, little experimental effort has been made on separating the two components of the reaction coordinate and exploring the mechanism of solvent control. This is a consequence of focusing on a limited number of molecular systems and of

inherent characteristics of the ET processes in these systems. A specific ET process to be used to visualize the solvent control should be driven by a strong enough electronic coupling such that for suitable energetics of the donor and acceptor levels, the ET process will be much faster than the response of the solvent. To the best of our knowledge, molecular systems with documented strong coupling and suitable influence of the solvent on the energetics have not yet been described in the literature.

Early investigations linked the ET processes to the longitudinal dielectric relaxation time ( $\tau_L$ ) of the solvent.<sup>2,12</sup> When ET reactions faster than  $\tau_L$  were reported,<sup>13,14</sup> it became clear that the rate of both intramolecular<sup>15–20</sup> and intermolecular<sup>21,22</sup> ET processes can by far exceed  $\tau_L$ . Extremely rapid ET processes with predicted rates up to  $10^{14} \text{ s}^{-1}$  have been proposed,<sup>23,24</sup> but until now experimental reports on intramolecular ET on this time scale are still very scarce.<sup>17–20</sup> Recently, we approached this limit by showing that intramolecular ET in phenolphthalein is accomplished within 50 fs,<sup>25</sup> in accord with a few other reports presenting sub-100 fs ET processes.<sup>26,27</sup>

The understanding of solvation dynamics<sup>28–33</sup> and the effects it may exert on the CT processes relies heavily on time-resolved solvation data.<sup>34</sup> The solvation occurs on multiple time scales ranging from less than 100 fs to several picoseconds.<sup>29,30,34</sup> The studies of the solvent response and of the mechanism of solvation used a variety of simple dyes and experiments based on time-dependent Stokes-shift measurements.<sup>34</sup> This method is believed to provide a linear image of the solvation process; the application is, however, limited to highly fluorescing probe molecules, and it is based on a number of assumptions<sup>34</sup> such

\* Corresponding authors. E-mail: riedle@physik.uni-muenchen.de and karpiuk@ichf.edu.pl

<sup>†</sup> Ludwig-Maximilians-Universität.

<sup>‡</sup> Polish Academy of Sciences.

<sup>§</sup> Present address: Laboratoire de Chimie Physique, ELVSE, UMR8000, CNRS, Université Paris-Sud, bâtiment 349, 91405 Orsay cedex, France.

<sup>ll</sup> Present address: Institut für Physik, Universität Rostock, Universitätsplatz 3, 18055 Rostock, Germany.

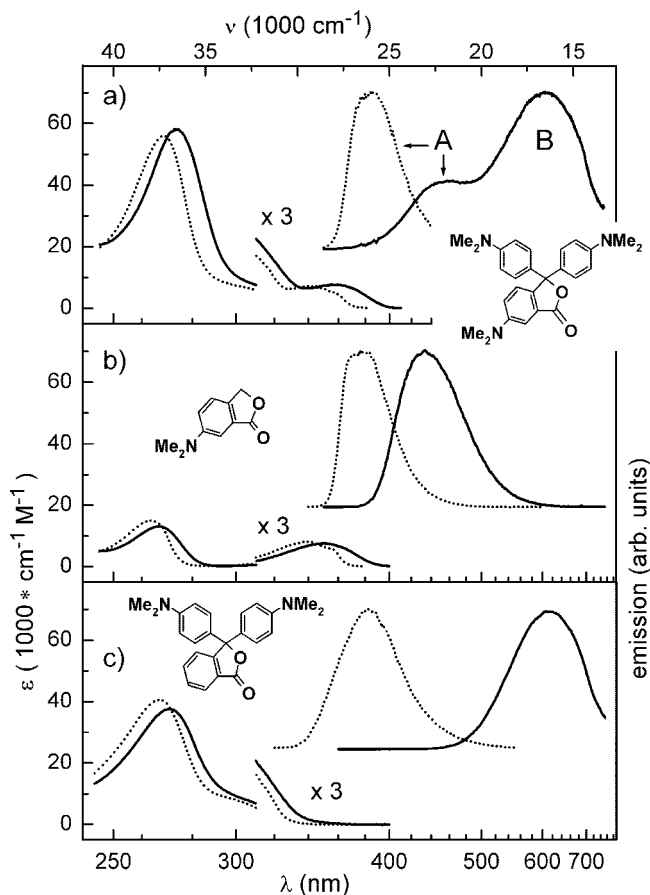


**Figure 1.** Steady-state absorption and emission spectra of (a) CVL, (b) 6-DMAPd, and (c) MGL in ACN (solid lines) and *n*-hexane (dotted lines). All solutions were excited in the first absorption band ( $\lambda_{\text{exc}} = 353$  nm for CVL and 6-DMAPd,  $\lambda_{\text{exc}} = 310$  nm for MGL). Note that the dual fluorescence spectrum (bands A and B) of CVL in ACN is approximately the sum of the spectra of 6-DMAPd and MGL.

as the absence of electronic relaxation in the probe molecule and vibrational relaxation being much faster than solvation.

Up to now, experimental investigations of the dynamical solvent effect on the reaction dynamics have focused on small organic molecules,<sup>4,6,7,9,26,35</sup> metal complexes,<sup>18,36,37</sup> and CT to solvent states.<sup>38</sup> To clearly separate the influence of the solvation from the intramolecular properties that determine the speed of ET, molecules are needed which allow ET under favorable conditions faster than the solvation time scale. A very promising class of molecules in this context are lactone forms of triaryl-methane dyes (LTAM), well-defined molecular systems with donor and acceptor units built around a tetrahedral carbon atom. Such an arrangement of donor and acceptor results in a weak donor–acceptor electronic coupling in the ground state so that the absorption transitions in LTAMs in the lower energy region are localized on their structural subunits. Moreover, an appropriate substitution of the donor or acceptor subunits allows for tuning of the ET process and even for observation of qualitatively new phenomena such as, for instance, the newly discovered population of two polar excited states displaying dual fluorescence in crystal violet lactone (CVL).<sup>39</sup>

CVL is a colorless lactone derivative of the triarylmethane dye crystal violet. The CVL molecule is composed of two dimethylaniline (DMA) groups attached via a tetrahedral carbon atom to 6-dimethylaminophthalide (6-DMAPd) at position 3 (see Figure 1). The lowest state populated in absorption is localized on the 6-DMAPd moiety. In moderately and highly polar aprotic

solvents, CVL emits fluorescence from two different polar excited states: (i) the optically populated, moderately polar state localized on 6-DMAPd and (ii) a highly polar CT state populated upon ET from one of the DMA groups to the lactone ring of the 6-DMAPd subunit.<sup>39</sup>

For LTAMs with a CT state approximately degenerate to or below any locally excited state,<sup>40</sup> we have found that the ET proceeds faster than the ultrafast solvation. In malachite green lactone (MGL), it takes 150 fs upon excitation to the  $S_2$  state, and in phenolphthalein, it takes 50 fs upon excitation to the  $S_1$  state.<sup>25</sup> Here, we study the dynamics of CVL, which is the dimethylamino derivative of MGL (see Figure 1). Contrary to MGL, the optically excited state of CVL lies below the highly polar CT state, and the latter becomes accessible only after sufficient solvation. From steady-state spectroscopy, we have argued that the kinetics in CVL involves two processes: lowering the energy of the CT state by solvation and the actual intramolecular ET. Based on the analogy with MGL, one expects that the latter occurs on the time scale of 100 fs once the CT state becomes energetically accessible. Observation of an ET product on the ultrafast time scale will give a direct proof of the suggested model and determine the actual speed of the process.

It has been shown by low-temperature studies in MGL that possible large-amplitude motions of the DMA groups do not have any significant effect on the charge separation.<sup>41</sup> This conclusion is also supported by investigations on the structurally related but rigid lactone form of rhodamine 101.<sup>42</sup> Here, twisting motions are even impossible for promoting the highly efficient ET. Because of the very similar nature of the  $CT_B$  state in CVL and the CT state in MGL, we extend this conclusion to CVL. As a consequence, a possible motion of the DMA groups should also not be relevant for the ET dynamics in CVL.

The present paper reports a femtosecond pump–probe study of the photoinduced ET in CVL and in 6-DMAPd in polar aprotic solvents with differing dielectric response. The time evolution of the transient absorption (TA) allows us to identify the emerging electronic structure and to follow the kinetics of the transformation. The excited-state dynamics of CVL are compared with those of the substructures of CVL (6-DMAPd and MGL), and the results lead to a detailed picture of the CT process in CVL and its dependence on the stage of solvation.

## II. Experimental Section

CVL (Aldrich) was crystallized twice from acetone. MGL was synthesized as described by Fischer<sup>43</sup> and subsequently repeatedly recrystallized from 1-propanol. 6-DMAPd was synthesized as described by Stanetty et al.<sup>44</sup> and purified by repeated crystallization from methanol. The solvents *n*-hexane, butyl ether, ethyl acetate, acetonitrile (ACN), and dimethylsulfoxide (DMSO) were of spectroscopic quality. Propylene carbonate (PC) was of analytical purity grade. All measurements were performed at room temperature.

For fluorescence measurements, the optical densities of the samples were 0.1–0.15 at the excitation wavelengths (1 cm layer). For the femtosecond experiments, the concentrations of CVL and 6-DMAPd were chosen such that the optical density of a 1 mm layer was 0.3–0.5. Absorption spectra were recorded with Shimadzu UV 3100 and Perkin-Elmer Lambda 19 spectrophotometers, and the fluorescence spectra were measured with an Edinburgh Analytical Instruments FS900 spectrofluorimeter. The raw fluorescence spectra were corrected by subtraction of the background due to the solvent and for the instrumental response. The fluorescence spectra were recorded as a function

of wavelength and subsequently multiplied by a factor  $\lambda^2$  to convert counts per wavelength interval into counts per wave-number interval. The absorption spectra of CVL and 6-DMAPd did not change during the laser measurements, which proves the photostability of both compounds under the experimental conditions of this work.

The femtosecond TA measurements were performed with a broadband pump–probe setup. A Ti:sapphire amplifier system (CPA 2001; Clark-MXR) was used to pump a two-stage noncollinear optical parametric amplifier (NOPA) delivering  $\sim 7 \mu\text{J}$  pulses at 740 nm. Frequency doubling in a 140  $\mu\text{m}$  BBO crystal yielded 370 nm pump pulses that were compressed to  $\sim 80$  fs. By focusing another part of the Ti:sapphire laser (typically 1  $\mu\text{J}$ ) into a rotating  $\text{CaF}_2$  disk (4 mm thickness), a supercontinuum was generated and used as probe. The fundamental wavelength (775 nm) was blocked by a dielectric mirror with high transmittance ( $>80\%$ ) between 300 and 700 nm and high reflectance around 800 nm. The pump and the probe pulses were focused into the sample with spherical mirrors. After the interaction in the sample, the probe beam was dispersed with a motorized monochromator with a spectral resolution of 6 nm and detected with a photodiode module (PDI-400–1–P-UV; Becker&Hickl GmbH). The temporal dispersion of the continuum due to the filter, the entrance window of the fused silica cell, and the sample amounted to about 800 fs between 350 and 700 nm. It was corrected while measuring the transient spectra. The temporal resolution was determined to be better than 300 fs. The pump energy was limited to about 270 nJ per pulse to avoid nonlinear effects such as multiphoton ionization of the solvent. The polarizations of the pump and probe pulses were set to the magic angle.

### III. Results

**III.1. Ground-State Absorption and Solvent-Dependent Emission of CVL.** Steady-state absorption and fluorescence spectra of CVL, MGL, and 6-DMAPd in *n*-hexane and in ACN are shown in Figure 1. The absorption spectra did not show any absorption in the visible, both before and after the fluorescence and TA measurements, indicating that only the colorless lactone forms and no colored ionic forms (e.g., crystal violet cation,  $\text{CV}^+$ ,<sup>45</sup> or malachite green cation,  $\text{MG}^+$ <sup>46</sup>) were present. The spectrum of CVL at wavelengths above 250 nm is a superposition of the contributions from the *N,N'*-dimethylaniline and 6-DMAPd moieties in both solvents. Such additivity of absorption transitions localized on structural parts of the molecule was earlier reported for MGL<sup>47</sup> and for other leuco forms of triarylmethanes<sup>48</sup> and was explained by weak ground-state conjugation of the chromophores forming the molecule. The lowest-energy, low-intensity absorption band shows (both in CVL and in 6-DMAPd) a red shift with increasing solvent polarity (for CVL, 1600  $\text{cm}^{-1}$  from hexane to DMSO) and has been ascribed to a CT transition localized on 6-DMAPd.<sup>39,49</sup> This means that only the 6-DMAPd subunit of CVL is excited in the pump–probe experiments with 370 nm excitation.

Depending on the solvent polarity, CVL emits in aprotic solvents at room temperature single (A band, low polar solvents) or dual (A and B bands, medium and highly polar solvents) fluorescence (see Figure 1a). Strong solvatochromic shifts of both fluorescence bands prove a significant charge redistribution in both emitting states, hereinafter referred to as  ${}^1\text{CT}_\text{A}$  and  ${}^1\text{CT}_\text{B}$ . A comparison with 6-DMAPd and MGL shows that the A band emanates from a polar excited state localized within the 6-DMAPd subunit ( ${}^1\text{CT}_\text{A}$ ,  $\mu_\text{e} = 10.7$  D), and the B band emanates from a highly polar state ( ${}^1\text{CT}_\text{B}$ ,  $\mu_\text{e} = 25.2$  D) formed

after full ET from one of the dimethylaniline groups to the 6-DMAPd moiety.<sup>39</sup> Because of the symmetry and spiro-like architecture of CVL, the two dimethylaniline groups are equivalent.

The fluorescence spectra of 6-DMAPd and MGL consist of a single band each (Figure 1b,c) that shows pronounced red shifts with increasing solvent polarity. A comparison of the spectral position and width of the fluorescence band of 6-DMAPd with the short wavelength A band of CVL strongly suggests that in both molecules, the emission comes from the same chromophore. The approximate mirror symmetry of the absorption and emission spectra<sup>50</sup> of CVL in low polar solvents proves that both the first absorption band and the fluorescence band belong to the same electronic transition. The excited-state dipole moment of 6-DMAPd is significantly larger ( $\mu_\text{e} = 11.2$  D)<sup>51</sup> than that in the  $\text{S}_0$  state ( $\mu_\text{g} = 6.55$  D) and indicates sizable charge redistribution upon excitation. The angular displacement of the  $\vec{\mu}_\text{e}$  vector against  $\vec{\mu}_\text{g}$  ( $34.8^\circ$ ) indicates CT from the dimethylamino group toward the meta position of the benzene ring in 6-DMAPd.<sup>49</sup>

The B band in CVL is very similar to the fluorescence band of MGL in terms of half-width, spectral position, and solvatochromic shift of the fluorescence maximum (see Figure 1). The spectral similarity implies that these two bands come from excited states with very similar electronic structures. The fluorescence of MGL shows a very large Stokes shift (exceeding 16 000  $\text{cm}^{-1}$  in DMSO) and a strong solvatochromic effect and has been assigned to emanate from a highly polar CT state ( $\mu_\text{e} = 25.0$  D) with an electron transferred from the dimethylaminophenyl ring to the phthalide moiety.<sup>41</sup> In light of the analogies between CVL and MGL and equal dipole moments in the CT state of MGL and the  ${}^1\text{CT}_\text{B}$  state of CVL, the same conclusion holds for CVL, and the long-wavelength fluorescence is assigned to a radiative back ET from the  ${}^1\text{CT}_\text{B}$  state to the ground state.<sup>39</sup>

**III.2. Solvation Equilibrated TA of CVL and 6-DMAPd.** Time-resolved absorption spectra of CVL and 6-DMAPd after excitation with 370 nm pulses were measured between 380 and 700 nm. Even at the short wavelength edge of this range and for the most polar solvents, the ground-state absorption of all investigated molecules is negligible compared to the excited-state absorption. For delay times larger than 100 ps, no changes of the spectral shape and positions were found. The eventual decrease of the TA signal in the nanosecond range is due to the electronic relaxation back to the ground state. The TA spectra of CVL in ACN and in butyl ether at a delay time of 100 ps (Figure 2a) agree well with those reported for a nanosecond TA study<sup>39</sup> and prove that the absorbing species are already the products of a solvent-dependent excited-state process occurring on a time scale shorter than 100 ps. The spectra show only TA throughout the visible and no indication of stimulated emission. This is also true for all other transient spectra reported below. At first sight, this is surprising because the fluorescence of the molecules is also observed in the visible (see Figure 1). The first absorption band of CVL (and also 6-DMAPd) is quite weak ( $\epsilon \approx 2500 \text{ cm}^{-1} \text{ M}^{-1}$ ) because of its CT character. The electronic transition corresponding to the A band of the fluorescence can be expected to be equally weak, and by comparison, we find the same to be true for the B band. This means that the stimulated emission signal will also be weak. In contrast, any transition from the excited state to higher electronic states is most likely much stronger, and the resulting excited-state absorption will totally mask the weak stimulated emission signal.

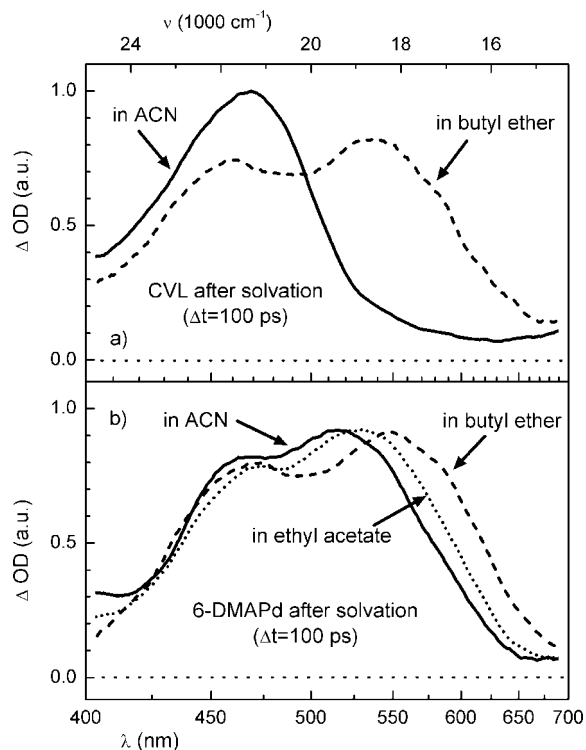


**Figure 2.** TA spectra of (a) CVL and (b) 6-DMAPd in low (butyl ether), intermediate (ethyl acetate), and high polarity (ACN) solvents. The spectra were recorded for  $\lambda_{\text{exc}}=370$  nm and at a 100 ps delay. At this time, all solvation and ET processes are completed, and no further change of the spectral shape and positions can be found.

The TA spectrum of CVL in the low polarity butyl ether consists of two absorption bands with maxima at 460 and 540 nm. Because the steady-state emission spectrum of CVL in butyl ether (spectrum not shown) does not show dual-band character or a significant Stokes shift,<sup>39</sup> it can be concluded that after 100 ps, the system is still in the optically excited state ( $^1\text{CT}_A$ ). The observation of the double-peak TA spectrum can therefore serve as indication that CVL is in the  $^1\text{CT}_A$  state. Additional strong support for this proposition comes from the close similarity of the CVL spectrum with the TA spectrum of 6-DMAPd (see Figure 2b). In 6-DMAPd, no additional CT process can occur after the optical excitation, and the same holds for CVL in low polarity solvents. Only a weak shift of the double peaked TA spectrum with the solvent polarity is observed for 6-DMAPd. This shows that the influence of solvation on the TA spectrum is weak for a given electronic state.

The TA spectrum recorded for CVL in the highly polar ACN differs strongly and consists of a single large band with a maximum at 470 nm. We suggest to take this spectral signature as indication that ET has occurred and the  $^1\text{CT}_B$  state is populated. The TA band of CVL in ACN at 100 ps agrees very well with the absorption band of the radical cation of DMA,<sup>52</sup> which proves the radical ion pair nature of the  $^1\text{CT}_B$  state<sup>39</sup> responsible for the single-peak TA spectrum.

The strong dependence of the TA spectra on solvent polarity indicates that in low polarity solvents, the photophysics of CVL is confined to the 6-DMAPd subunit, whereas in moderately and highly polar ones, the product of a fast excited-state ET process is observed on the 100 ps time scale.

**III.3. Femtosecond Transient Spectra and Kinetics in Polar Solvents.** In the preceding sections, we identified signatures of the TA spectra that can serve as indications for the electronic state that CVL and 6-DMAPd occupy. We now

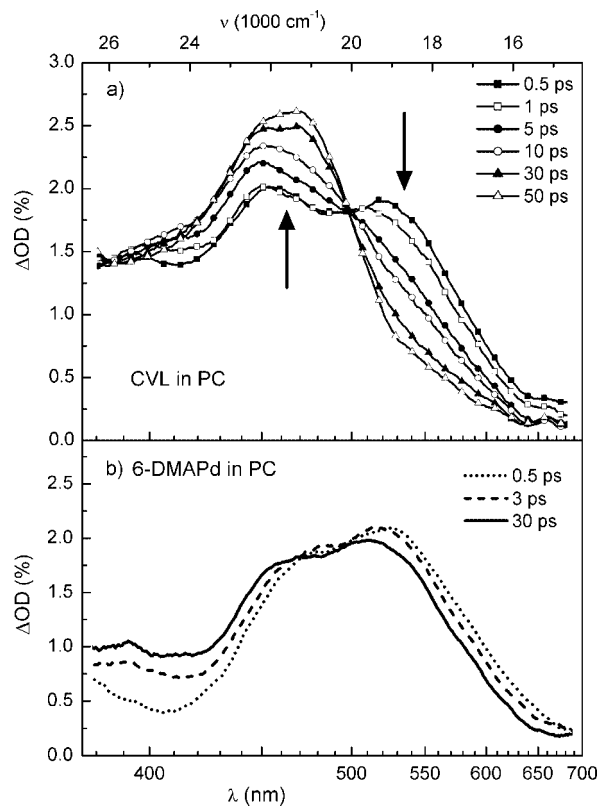


**Figure 3.** TA spectra recorded at various delay times after 370 nm excitation of (a) CVL and (b) 6-DMAPd in PC. Note the isosbestic point found for the CVL spectra.

turn to the temporal evolution of the systems between the optical excitation and the quasi-equilibrium achieved after 100 ps.

TA spectra of CVL and 6-DMAPd in the highly polar PC are shown in Figure 3. For 6-DMAPd, only extremely small shifts are found (Figure 3b) that can be assigned to solvation of the only accessible CT state and possibly some intramolecular vibrational relaxation (IVR). In contrast, the spectra for CVL change from the double-peaked initial form to the single-peaked form typical for the  $^1\text{CT}_B$  state. The change reflects the direct observation of the ultrafast transition from the optically excited  $^1\text{CT}_A$  state to the  $^1\text{CT}_B$  state. The very pronounced isosbestic point signals the direct interconversion of only two participating states.

The temporal evolution can best be investigated at the maximum of the  $^1\text{CT}_B$  peak and in the red slope of the  $^1\text{CT}_A$  spectrum. The TA kinetic traces shown in Figure 4a demonstrate this point. At 470 nm, the optical density increases and signals the developing population of the  $^1\text{CT}_B$  state, whereas the optical density decreases at 580 nm and signals the decay of the  $^1\text{CT}_A$  population.

To quantify the temporal evolution, we have fitted the experimental curves with biexponential functions and a constant signal to account for the long time quasi-equilibrium. The time constants represent a parametrization of the observed kinetic traces and cannot be directly identified with solvation times (see discussion below).

For 6-DMAPd also, a slight rise of the TA signal at short wavelengths and a slight decrease at long wavelengths is found (Figure 4b). These curves can be fitted with single-exponential functions. The time constants give an indication for the solvation of the only accessible CT state and possibly IVR.

In ACN, each compound displays a behavior of the TA very similar to that found for PC (see Figure 5). Again, an isosbestic

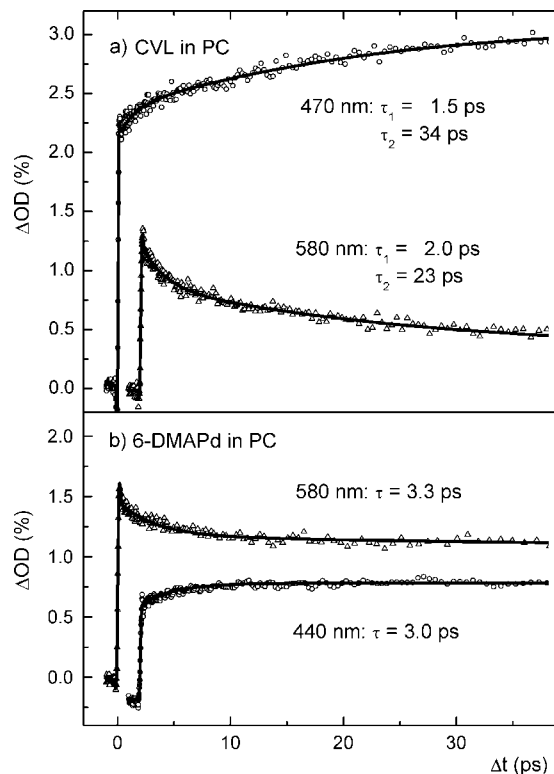


**Figure 4.** TA kinetic curves for (a) CVL and (b) 6-DMAPd in PC after excitation at 370 nm. For better visibility, one curve in each panel is slightly shifted. The solid lines are double-exponential functions (for CVL) and single-exponential functions (for 6-DMAPd) fitted to the data. The sharp peak observed at  $t = 0$  is due to a coherent artifact.

point is observed for the CVL spectra and indicates the straight population transfer between only two states. A closer look shows that the temporal evolution in ACN is faster than that in PC. This tendency matches the well-documented faster solvation of ACN.<sup>34</sup>

The temporal evolution of the TA signals of CVL in ACN was monitored at 470 and 550 nm (see Figure 6). Again, at the blue maximum of the single-peaked TA spectrum, a strong rise is found, and in the red slope, a corresponding decrease is found. The fits render a nearly single-exponential behavior, but a close inspection also reveals a weak contribution in the range of hundreds of femtoseconds. The slow component is about three times faster than that in PC.

All fitted parameters are collected in Table 1. For each time constant, the associated preexponential factor  $a_i$  is given in addition. The latter values are normalized to the initial amplitude  $a_0$  of the signal after the optical excitation.<sup>53</sup> In addition to the solvents ACN and PC explicitly shown in this work, we also measured the ET dynamics in DMSO and include the obtained exponential constants in Table 1.

#### IV. Discussion and Modeling

**IV.1. Observation of the ET by TA.** The established method for the characterization of ET processes is the analysis of the changes in the emission spectrum with solvent polarity and time. From a large Stokes shift, a strong change of the dipole moment in the electronically excited state is typically deduced. To obtain a quantitative understanding of the excited-state dynamics, however, the solvation-dependent rise of the ground-state energy has to be considered, and the observed spectral shift cannot be simply ascribed to a lowering of the excited state. Moreover, the concurrence of solvation and ET processes cause a high degree of complexity.

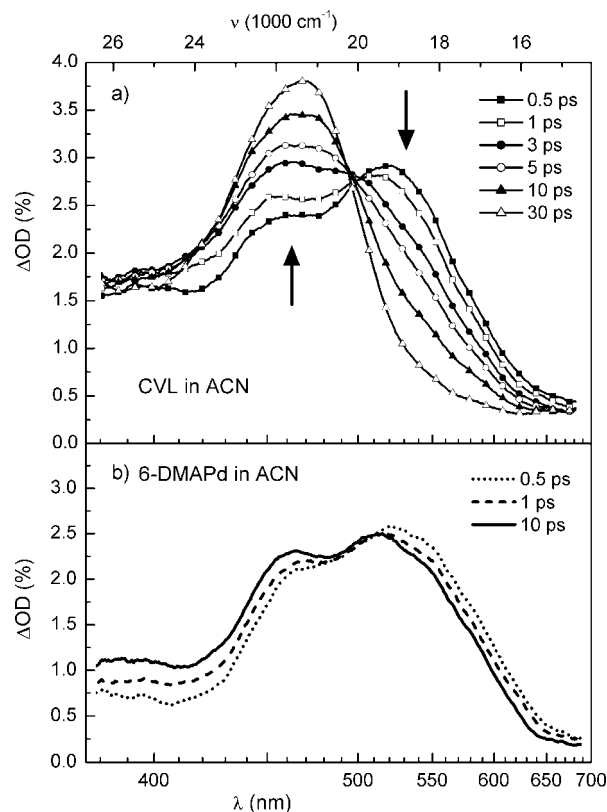


**Figure 5.** TA spectra recorded at various delay times after 370 nm excitation of (a) CVL and (b) 6-DMAPd in ACN. Note the isosbestic point found for the CVL spectra. Compared to Figure 3, shorter times are shown, reflecting the faster dynamics in ACN.

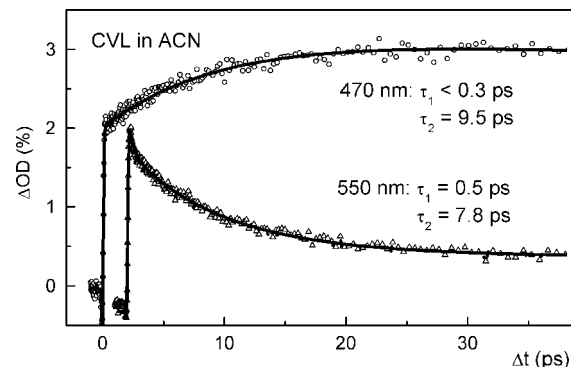


**Figure 6.** TA kinetic curves of CVL in ACN after excitation at 370 nm. For better visibility, the curve at 550 nm is slightly shifted.

In this work, we use the TA spectrum to analyze the ultrafast ET process. The recording of the time-resolved emission is quite difficult or even impossible for molecules with a weak electronic transition from the considered excited state to the ground state. Such a weak transition is quite common for a CT state with its largely changed electronic wave function. On the contrary, there is most likely some higher electronic state with a good transition strength, and in the investigated CVL molecule, such a transition is actually found in the experimentally accessible spectral range. The fact that neither the polarity of the solvent nor the solvation changes the TA bands significantly allows for the straightforward interpretation of the observed changes as ET dynamics. The TA measurement also does not suffer from the decrease of emission yield with the decreasing energy gap between the solvated CT state and the ground state for strongly polar solvents.<sup>39</sup>

**TABLE 1: Time Constants Obtained from Fitting of Kinetic Curves of CVL and 6-DMAPd in ACN, DMSO, and PC<sup>a</sup>**

CVL		6-DMAPd			
		acetonitrile			
$\tau_1$ (ps)	$a_1/a_0$	$\tau_1$ (ps)	$a_1/a_0$		
<0.3		0.7	-0.55	rise	
0.5	0.16	1.0	0.15	decay	
$\tau_2$ (ps)	$a_2/a_0$	$\tau_2$ (ps)	$a_2/a_0$		
9.5	-0.61			rise	
7.8	0.55			decay	
		dimethylsulfoxide			
$\tau_1$ (ps)	$a_1/a_0$	$\tau_1$ (ps)	$a_1/a_0$		
1.4	-0.12	1.8	-0.13	rise	
1.4	0.19	1.7	0.12	decay	
$\tau_2$ (ps)	$a_2/a_0$	$\tau_2$ (ps)	$a_2/a_0$		
12	-0.25	6.1	-0.08	rise	
15	0.31	7.5	0.05	decay	
		propylene carbonate			
$\tau_1$ (ps)	$a_1/a_0$	$\tau_1$ (ps)	$a_1/a_0$		
1.5	-0.11	3.0	-0.24	rise	
2.0	0.28	3.3	0.20	decay	
$\tau_2$ (ps)	$a_2/a_0$	$\tau_2$ (ps)	$a_2/a_0$		
34	-0.61			rise	
23	0.42			decay	

<sup>a</sup> A rise of the TA is found at short wavelengths and a decay at long wavelengths. The amplitudes  $a_1$  and  $a_2$  of the two exponential contributions are given relative to the signal amplitude  $a_0$  directly after the excitation pulse.

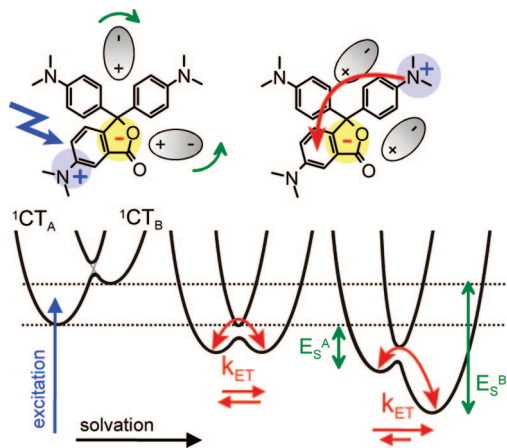


**Figure 7.** Snapshots of the excited energy levels of CVL during solvation. Left: after optical excitation. Middle: during solvation of the molecule, when the  ${}^1\text{CT}_A$  and  ${}^1\text{CT}_B$  state are in energetic resonance. Right: when solvation is completed.  $k_{\text{ET}}$  is the rate of ET. The molecular cartoons depict the charge reorganization, and the red arrows refer to the transfer of the electron.

#### IV.2. Solvent-Dependent Temporal Evolution of the ET.

From the time-dependent TA spectra of CVL reported in Section III, we directly get information on the depopulation of the optically excited  ${}^1\text{CT}_A$  state and the population of the  ${}^1\text{CT}_B$  state. The isobestic point observed for all solvents (compare Figures 3 and 5) proves that there is no additional state involved in the transfer. The rise of the TA signal at the maximum of the single-peaked band assigned to the  ${}^1\text{CT}_B$  state and the decrease in the red wing that best monitors the  ${}^1\text{CT}_A$  state occur with the same time constants for each solvent within the experimental accuracy.

Our fit parameters (Table 1) are in the subpicosecond and picosecond range just as the solvation times reported by Maroncelli and co-workers.<sup>34</sup> There is, however, no close match between these measured solvation times and our fitted time constants for the ET in CVL. What we do find is a reasonable correlation with the dielectric response and solvation energy as well as the viscosity as we go from ACN to DMSO and PC. We also find a similar trend for the solvation of 6-DMAPd. Overall, the ET times are in the picosecond regime and thereby markedly slower than the 50–150 fs time constants that we have reported for phenolphthalein and MGL.<sup>25</sup>

The structurally related molecules MGL and CVL are both set up around a tetrahedral carbon atom and are characterized by a nearly orthogonal arrangement of the electron-donating groups relative to the acceptor moiety. The structural difference between MGL and CVL—the presence of the amino group at the phthalide ring—results in a huge difference in the photo-physics that has to be explained together with the observed dependence on the solvent.

**IV.3. CVL Energetics and Population Transfer to the  ${}^1\text{CT}_B$  State.** In MGL, the optically excited state is localized on one of the dimethylamino groups, and the ET shifts the electron to the phthalide moiety. Because this ET proceeds on the time scale of vibrational motions in polar as well as nonpolar solvents, we can conclude that the CT state is already energetically accessible right after the excitation.

In nonpolar solvents, no ET is seen for CVL, and we can conclude that the optically excited  ${}^1\text{CT}_A$  state (localized on the 6-DMAPd moiety) is lower than the  ${}^1\text{CT}_B$  state that is delocalized over the whole molecule and similar in electronic structure to the CT state of MGL. For sufficiently polar solvents, the ET sets in, and we conclude that the solvation lowers the  ${}^1\text{CT}_B$  state strongly enough to energetically allow the transfer and build up a significant population in the  ${}^1\text{CT}_B$  state. A model that explicates this situation for the different steps during the solvation process is shown in Figure 7.

In the classical Marcus theory, the intramolecular coordinates relevant to the ET and the intermolecular coordinates of solvent distance and orientation are unified in a single generalized coordinate. Numerous time-resolved emission studies investigating solvation from an optically activated, nonequilibrated distribution clearly show that the emission band shifts with time and only changes its width to a smaller degree.<sup>29,32,34</sup> From this, it can be concluded that there is a separation of time scales between the intramolecular and pure solvation degrees of freedom, and it is meaningful to use two separate coordinates to describe the solvation of a single excited state.<sup>33</sup> The time-dependent spectral position of the emission band is equal to the momentary difference between the lowered excited-state energy and the rising ground-state energy. The width is given mainly by the Franck–Condon structure and the rapid solvent fluctuations and, to a lesser degree, by the inhomogeneous distribution of solvent environments. In this sense, we believe that it is appropriate in the investigated situation to use a quasi-two-dimensional description with one combined coordinate for the intramolecular degrees of freedom and the rapid fluctuations and a second slow solvation coordinate. The sketches in Figure 7 are to be understood as selected cross sections of this 2D potential energy surface for a given time and therefore extent of the solvation.

This picture of a single excited state has to be extended to the two excited states of CVL. Even in a highly polar solvent, the  ${}^1\text{CT}_B$  state lies above the  ${}^1\text{CT}_A$  state as long as the molecule is in the ground state with its low dipole moment and the



associated dynamic arrangement of the solvent molecules. The excitation of the  ${}^1\text{CT}_A$  state instantaneously increases the molecular dipole moment and solvation, that is, the partial alignment of the polar solvent molecules, sets in. This lowers the  ${}^1\text{CT}_A$  state but even more the highly polar  ${}^1\text{CT}_B$  state with its similar localization of the negative charge. We therefore augment the sketches in Figure 7 by a second parabola for the  ${}^1\text{CT}_B$  state with a time- (solvation) dependent crossing of the parabola describing the  ${}^1\text{CT}_A$  state.

Eventually, the two CT states come close in energy, and assisted by the thermal fluctuations, the ET becomes possible. The strong electronic coupling in CVL that we infer from the 100 fs ET in the closely related MGL does then indeed lead to the ET. At this point in time, the reaction rates in forward and backward direction are equal. The ongoing solvation shifts the dynamic equilibrium between the  ${}^1\text{CT}_A$  and  ${}^1\text{CT}_B$  state toward the latter. The final equilibrium is established when the states are lowered from the initial energies by  $E_S^A$  and  $E_S^B$ . The described interplay of the solvation and the ET leads to the experimentally observed solvent control of the ET, concerning both the extent and the speed.

**IV.4. Modeling of the ET During Solvation.** For a more quantitative description of the solvent-dependent ET, a suitable model has to be applied, and for this, a number of microscopic quantities have to be determined. We have to know the initial separation of the CT states and the total amount of energetic lowering (solvation energy) caused by each of the solvents. An estimate for the solvation times has to be accepted, and finally, the local heating has to be taken into account. The proper combination of these considerations leads to a knowledge of the energetics at each point in time and therefore allows the application of the Marcus theory<sup>54,55</sup> to determine a time-dependent ET rate.

**Initial Separation of the CT States in Vacuum.** As discussed in Section III.1, all of the CVL fluorescence originates from the  ${}^1\text{CT}_A$  state for low polarity solvents and most from the  ${}^1\text{CT}_B$  state for high polarity ones. Equal fluorescence decay times in both bands can be taken as an indication that the particular solvent leads to the equilibration of the two states at long times. Single intensive ( $\Phi_{\text{fl}} = 0.44$ ) fluorescence in tetrahydrofuran ( $\epsilon = 7.6$ ) indicates the first case, and an intense second fluorescence band in the slightly more polar dichloromethane ( $\epsilon = 8.9$ , total  $\Phi_{\text{fl}} = 0.27$ ,  $\tau_{\text{fl}} = 22.4$  ns in both the A and B bands) allows us to locate the  $\epsilon$  value needed for the equilibration between these values. To estimate the separation of the CT states in vacuum, we start from the experimentally observed energetic situation in quasi-equilibrium, that is, after solvation, and then use calculated solvation energies to reconstruct the energetics of the isolated molecule.

For the calculation of the solvation energies  $E_S^X$ , we neglect the polarizability of the solute and use the Onsager solution for the dipolar reaction field:<sup>56</sup>

$$E_S^X = \frac{1}{4\pi\epsilon_o} \frac{\mu_X^2}{a_X^3} \frac{\epsilon - 1}{2\epsilon + 1} \quad (1)$$

Here,  $a_X$  is the effective radius of the spherical Onsager cavity of the  ${}^1\text{CT}_X$  state, its charge separation is represented by its dipole moment  $\mu_X$ , and  $\epsilon$  is the static dielectric constant of the solvent. For the  ${}^1\text{CT}_A$  and  ${}^1\text{CT}_B$  states of CVL, we use cavity radii of 3.6 and 5.8 Å, respectively,<sup>57</sup> and the experimentally determined values of the dipole moments of 10.7 and 25.2 D.<sup>39</sup> For the above-discussed situation of energetic equilibration after solvation (found between tetrahydrofuran and dichloromethane),

the difference in solvation energies  $\Delta E_S = E_S^B - E_S^A$  equals the sought energy gap without solvation.

$\Delta E_S$  rises from 1640  $\text{cm}^{-1}$  in tetrahydrofuran to 1690  $\text{cm}^{-1}$  in dichloromethane. From this, we estimate a value of  $\Delta E_0^{\text{vac}} = 1660$   $\text{cm}^{-1}$  for the separation of the  ${}^1\text{CT}_A$  and  ${}^1\text{CT}_B$  states in vacuum. We further identify the energy gap between the two states with the Gibbs free energy change  $\Delta G^0$  for the Marcus description of the CT.

**Total Energetic Lowering Due to Solvation.** For ACN, DMSO, and PC, the value of  $\Delta E_S$  is determined at 1930, 1960, and 1970  $\text{cm}^{-1}$ . These values lead to the conclusion that the  ${}^1\text{CT}_B$  state is finally stabilized to  $-\Delta G^0(t=\infty) = 270$ , 300, and 310  $\text{cm}^{-1}$  below the  ${}^1\text{CT}_A$  state. Considering the thermal energy of about 200  $\text{cm}^{-1}$  in the room temperature experiment, a nontrivial distribution between the states is reached according to

$$K_{\text{eq}} = \frac{[{}^1\text{CT}_B]}{[{}^1\text{CT}_A]} = \exp(-\Delta G^0/k_B T) \quad (2)$$

For ACN, this amounts to  $K_{\text{eq}} = 3.86$ , that is, an almost 4-fold larger population of the  ${}^1\text{CT}_B$  state. The equilibrium persists until the electronic ground state is reached by back ET on the nanosecond time scale.<sup>39</sup>

**Solvation Dynamics and Time-Dependent Energetics.** The lowering of the two CT states and the establishment of the  ${}^1\text{CT}_A \rightleftharpoons {}^1\text{CT}_B$  equilibrium during solvation is a dynamic process. The energetics of educt and product are controlled by the dielectric relaxation properties of the solvent, as has been proposed for instance in the case of *t*-stilbene.<sup>58</sup> In detail, the energy separation of the states in vacuum  $\Delta E_0^{\text{vac}}$  corrected for the difference  $\Delta E_{S,\text{el}}$  of the instantaneous electronic part of the total solvation energy gives the initial energy separation  $\Delta G^0(t=0)$  of the states in solution:

$$\Delta G^0(t=0) = \Delta E_0^{\text{vac}} - \Delta E_{S,\text{el}} = \Delta E_0^{\text{vac}} - \frac{1}{4\pi\epsilon_o} \left( \frac{\bar{\mu}_B^2}{a_B^3} - \frac{\bar{\mu}_A^2}{a_A^3} \right) \frac{n^2 - 1}{2n^2 + 1} \quad (3)$$

Here,  $n$  is the refractive index of the solvent. The remaining part  $\Delta E_{S,\text{or}} = \Delta E_S - \Delta E_{S,\text{el}}$  of the solvation energy, that is, the one due to the reorientation of the solvent molecules, is time dependent. The relevant time scales  $\tau_i$  and amplitudes  $a_i$  in the different solvents can be taken from the known solvation parameters.<sup>34</sup> The Gibbs free energy change  $\Delta G^0$  for the ET can then be written as

$$\Delta G^0(t) = \Delta G^0(0) - \Delta E_{S,\text{or}} \left[ 1 - \sum_i a_i \exp(-t/\tau_i) \right] \quad (4)$$

We performed simulations of the time-dependent energy separation for ACN, DMSO, and PC and for comparison also for methanol. The results are shown in Figure 8a. For all four solvents, the energy gap crosses zero within at most a few picoseconds, corresponding to resonance between the two states. For ACN with its known fast solvation, this occurs already after a few 100 fs, for DMSO and for PC at about 1.5 ps. From this time on, the ET can proceed effectively. The relation of the stabilization capability  $\Delta E_{S,\text{or}}$  to the initial energy gap  $\Delta G^0(t=0)$  is the very reason why the solvent-controlled ET does not show the same time constants as the pure solvation. Methanol is included here to demonstrate the fact that an early ET can occur even in a solvent with slower reorganization.<sup>59</sup>

The description of the time-dependent change of the energy gap suggests a smooth and monotonic process. This is certainly

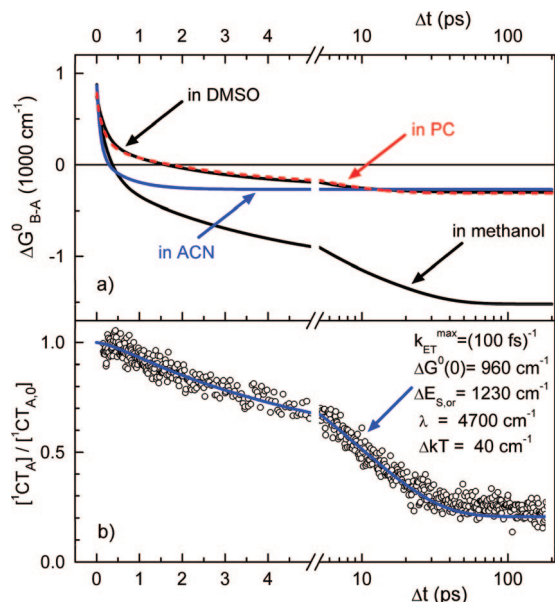


**Figure 8.** (a) Calculated change of the driving force  $\Delta G^0(t)$  during the solvation process for the reaction from  ${}^1\text{CT}_A$  to  ${}^1\text{CT}_B$  for CVL in different solvents according to eq 4. (b) Normalized population of the  ${}^1\text{CT}_A$  state (circles) in ACN after 370 nm excitation obtained from the kinetic curve at 470 nm probe wavelength (see Figure 7 upper curve). The solid line shows the simulation of the  ${}^1\text{CT}_A$  population according to the kinetic model described in the text (eqs 5 and 6).

only a crude approximation because only a quasi-equilibrium can be expected at any point in time. The solvation is actually accomplished via statistical fluctuations of the solvent polarization around the average.<sup>60</sup> Occasionally, an arrangement of solvent molecules will occur that will equate the energies of the  ${}^1\text{CT}_A$  and  ${}^1\text{CT}_B$  states enabling the ET.

**Application of Marcus Theory.** Equation 4 implies that the reaction barrier for ET becomes time dependent and consequently also the ET rate. Time-dependent reaction barriers have been proposed for instance by Simon<sup>61</sup> for solvent nonequibrated ET processes and for photoisomerization reactions by Mohrschladt et al.<sup>62</sup> To model the overall process, we apply the Marcus theory with the time-dependent driving force from eq 4 and the reorganization energy  $\lambda$ :

$$k_{\text{ET}}(t) = k_{\text{ET}}^{\text{max}} \exp\left(\frac{-(\lambda \pm \Delta G^0(t))^2}{4\lambda k_{\text{B}}T}\right) \quad (5)$$

The plus sign refers to the forward and the minus sign to the backward ET.  $k_{\text{ET}}^{\text{max}}$  is the preexponential factor that gives an upper limit for the ET in the case of a vanishing barrier. It is determined by the electronic coupling. Because of the similarity of MGL and CVL, we adapt the experimental value of  $(100 \text{ fs})^{-1}$  found for MGL for the present study on CVL.

With the time-dependent ET rates given by eq 5, we numerically determine the time dependence of the population of the two CT states. The forward and backward reaction rates are explicitly considered via the usual equation:

$$\frac{d[{}^1\text{CT}_A]}{dt} = -k_{\text{ET}}^+(t)[{}^1\text{CT}_A] + k_{\text{ET}}^-(t)(1 - [{}^1\text{CT}_A]) \quad (6)$$

This result can be directly compared to the experimental recordings if we normalize the experimental data to the initial population of the  ${}^1\text{CT}_A$  state. A typical result for the depopulation of the  ${}^1\text{CT}_A$  state is shown in Figure 8b. The small offset at long times is due to the persistent equilibrium population

discussed above. It is important to note that all kinetic information used in the model is taken from independent experiments. The time constants given in Table 1 did not enter the final model and have to be regarded as rough indications of the relevant time scales only.

For the good agreement between modeling and experiment, two further details were important. First, the value of  $\lambda$  had to be adjusted to match the observation at long times. The value of  $4700 \text{ cm}^{-1}$  is in a typical range for comparable systems.<sup>63,64</sup> We can also compare this value to the reorganization contribution of the solvent which can be estimated according to a derivation by Marcus<sup>55</sup> to  $4470 \text{ cm}^{-1}$ .<sup>65</sup> As expected for a solvation-controlled reaction, the intramolecular component plays only a minor role.

Second, we noticed that the assumption of a constant temperature did not allow the desired quality of the modeling. It is reasonable to assume that the molecule is slightly heated because of the optical excitation that includes some vibrational excess energy. Because of the optical selection rules and the fact that the internal vibrational redistribution is far from complete within the first picosecond, a highly nonstatistical distribution has to be assumed. Accordingly, the temperature in relevant modes can easily deviate from the limited value that one would calculate from full statistics. The increase in local temperature (corresponding to an empirical value of  $40 \text{ cm}^{-1}$ , in good agreement with ref 66) will decay exponentially on a picosecond time scale. We used reported cooling times for ACN<sup>67</sup> to derive the time-dependent temperature  $k_{\text{B}}T(t) = [200 + 40(0.6 e^{-t/2.6 \text{ ps}} + 0.4 e^{-t/11 \text{ ps}})] \text{ cm}^{-1}$ .

At the moment, the model does not allow for a precise and detailed prediction of the solvent driven ET dynamics because the applied values of several parameters are rough estimations and the obtained dynamics is quite sensitive to these values. However, the good agreement between the modeled and the measured time-dependent CT populations demonstrates that it reflects the key features of the dynamics. They result from the variation of the ET rate with time because of the changes of the CT energetics caused by the ongoing solvation.

Strictly speaking, the Marcus theory was originally formulated for a quasi-equilibrium situation. In the situation discussed in this work, this condition is only fulfilled marginally because the intrinsic ET rate is somewhat faster than the solvation. Sumi and Marcus expanded the theory to dynamical effects and derived algebraic formulas to describe this more complicated situation.<sup>68</sup> However, because of the various additional contributions to the spectroscopic observations and the limited applicability of simple analytic ET models,<sup>69</sup> we presently restrain ourselves from the direct application of such formalisms. In future work, full molecular dynamics simulations<sup>70,71</sup> incorporating modern analytic aspects<sup>72,73</sup> should be used to model the combined solvation and ET dynamics without artificial separation of coordinates and time scales.

## V. Conclusions

The photophysics of CVL are strongly influenced by the surrounding medium. The solvent polarity dynamically determines the energetics of both CT states and controls the availability of the various deactivation pathways. In this work, we focused on the effect that the solvation dynamics has on the photoinduced ET reaction in CVL and addressed the question of how it enables and controls ET. In a fs pump–probe study of the CVL photophysics in solvents of different polarity, we found a strong connection between the solvation dynamics and the observable  ${}^1\text{CT}_A \rightarrow {}^1\text{CT}_B$  population transfer. The  ${}^1\text{CT}_B$  state

is populated with a time-dependent rate, and the observed CT dynamics is significantly affected by the competition between solvent relaxation and reaction. In ionic solvents, it has recently been found that the ET of CVL shows strong environmental heterogeneity<sup>74</sup> instead of the temporal evolution found by us for the polar organic solvents.

We used TA measurements instead of the more usual time-resolved emission. At least for the present case of CVL, TA proves to be a very sensitive and informative probe for the CT process. We want to point out that TA spectroscopy has already been used by others quite successfully to even study solvation without any additional reactive process.<sup>33</sup>

Even though it might seem trivial, the energetic position of the educt and product is not explicitly treated in many of the theoretical and experimental studies concerning the solvent-controlled ET regime. It can, however, explain the strong variation of time constants attributed to solvation-controlled ET in different molecular systems in a straightforward fashion. These time constants cannot be uniformly correlated to the solvation dynamics because the energetics between donor and acceptor vary with the molecular systems. Similarly, the theoretical approaches only consider the influence of the solvent on the preexponential factor and implicitly assume the energetic configuration to be independent of time.<sup>68,75</sup> The experimental findings in CVL clearly show that it is not only the solvation dynamics that is decisive for the control of the ET but also the amount of stabilization that is achieved on a certain time scale. Without sufficient energetic stabilization of the product state, no ET is found at all.

We believe that the present results and conclusions are relevant for a wide range of spiro-like donor–acceptor molecules with one bond mediating an ultrafast intramolecular ET process. For a large body of spiro-type molecules with both theoretical and practical relevance, such as, for example, photochromic spiropyranes and spirooxazines, CVL can be considered as a molecule that visualizes the CT processes underlying their photophysics and photochemistry.

The formation of the <sup>1</sup>CT<sub>B</sub> state from the <sup>1</sup>CT<sub>A</sub> is due to ET from the DMA group to the 6-DMAPd subunit with formation of an intramolecular exciplex. Directly after optical excitation, the energy separation is so large that we suggest to call the ET nonadiabatic at this early time. When the lowering of both states due to solvation leads to energetic equilibration, the ET turns into an adiabatic reaction.<sup>75</sup> The latter situation resembles the ET processes occurring faster than diffusive solvation both in intra-<sup>7</sup> and in intermolecular<sup>63,76–78</sup> CT reactions involving dimethylaniline as electron donor. Both CVL and the related MGL offer a number of advantages and may be used as model systems in controversies concerning ET rates<sup>17,78</sup> in such systems. In both LTAMs, the electron donor is in direct contact (via a covalent bond) with the acceptor, so that no diffusional translation and reorientation is needed to induce ET. The ET process proceeds intramolecularly in a well-defined geometry, allowing one to study the ET kinetics and dynamics with only one mutual donor–acceptor orientation and distance. The experimental findings will consequently be much more directly comparable to theoretical studies without the need for extensive averaging.

**Acknowledgment.** Financial support from Grant 3T09A06929 from the Polish Ministry of Science and Higher Education and European Community Grant G5MA-CT-2002-04026 (J.K.) and The International Max Planck Research School on Advanced Photon Science (U.M.) is gratefully acknowledged. The collaboration was supported by a travel grant from the Deutsche

Forschungsgemeinschaft and by the SFB 749 (Dynamik und Intermediate molekularer Transformationen).

## References and Notes

- (1) Bagchi, B.; Gayathri, N. *Adv. Chem. Phys.* **1999**, *107*, 1.
- (2) Zusman, L. D. *Chem. Phys.* **1980**, *49*, 295.
- (3) For a review see Jortner, J.; Bixon, M., Eds. *Electron transfer: from isolated molecules to biomolecules*. *Adv. Chem. Phys.*; J. Wiley: New York 1999; Vols. 106–107.
- (4) Weaver, M. J. *Chem. Rev.* **1992**, *92*, 463.
- (5) (a) Kang, T. J.; Kahlow, M. A.; Giser, D.; Swallen, S.; Nagarajan, V.; Jarzaba, W.; Barbara, P. F. *J. Phys. Chem.* **1988**, *92*, 6800. (b) Kang, T. J.; Jarzaba, W.; Barbara, P. F.; Fonseca, T. *Chem. Phys.* **1990**, *149*, 81. (c) Tominaga, K.; Walker, G. C.; Kang, T. J.; Barbara, P. F.; Fonseca, T. *J. Phys. Chem.* **1991**, *95*, 10485.
- (6) Horng, M. L.; Dahl, K.; Jones, G., II; Maroncelli, M. *Chem. Phys. Lett.* **1999**, *315*, 363.
- (7) Tominaga, K.; Walker, G. C.; Jarzaba, W.; Barbara, P. F. *J. Phys. Chem.* **1991**, *95*, 10475.
- (8) Barthel, E. R.; Martini, I. B.; Schwartz, B. J. *J. Phys. Chem. B* **2001**, *105*, 12230.
- (9) Saleh, N.; Kauffman, J. F. *J. Phys. Chem. A* **2004**, *108*, 7139.
- (10) Glasbeek, M.; Zhang, H. *Chem. Rev.* **2004**, *104*, 1929.
- (11) Grabowski, Z. R.; Rotkiewicz, K.; Rettig, W. *Chem. Rev.* **2003**, *103*, 3899.
- (12) Kosower, E. M.; Huppert, D. *Annu. Rev. Phys. Chem.* **1986**, *37*, 127.
- (13) Kahlow, M. A.; Kang, T. J.; Barbara, P. F. *J. Phys. Chem.* **1987**, *91*, 6452.
- (14) Kobayashi, T.; Takagi, Y.; Kandori, H.; Kemnitz, K.; Yoshihara, K. *Chem. Phys. Lett.* **1991**, *180*, 416.
- (15) Pöllinger, F.; Heitele, H.; Michel-Beyerle, M. E.; Anders, C.; Füscher, M.; Staab, H. A. *Chem. Phys. Lett.* **1992**, *198*, 645.
- (16) Walker, G. C.; Åkesson, E.; Johnson, A. E.; Levinger, N. E.; Barbara, P. F. *J. Phys. Chem.* **1992**, *96*, 3728.
- (17) Baigar, E.; Gilch, P.; Zinth, W.; Stöckl, M.; Härter, P.; von Feilitzsch, T.; Michel-Beyerle, M. E. *Chem. Phys. Lett.* **2002**, *352*, 176.
- (18) Son, D. H.; Kambhampati, P.; Kee, T. W.; Barbara, P. F. *J. Phys. Chem. A* **2002**, *106*, 4591.
- (19) Mataga, N.; Chosrowjan, H.; Taniguchi, S.; Shibata, Y.; Yoshida, N.; Osuka, A.; Kikuzawa, T.; Okada, T. *J. Phys. Chem. A* **2002**, *106*, 12191.
- (20) Giaimo, J. M.; Gusev, A. V.; Wasielewski, M. R. *J. Am. Chem. Soc.* **2002**, *124*, 8530.
- (21) Yoshihara, K.; Yartsev, A.; Nagasawa, Y.; Kandori, H.; Douhal, A.; Kemnitz, K. *Pure Appl. Chem.* **1993**, *65*, 1671.
- (22) Iwai, S.; Murata, S.; Tachiya, M. *J. Chem. Phys.* **1998**, *109*, 5963.
- (23) (a) Jortner, J.; Bixon, M.; Heitele, H.; Michel-Beyerle, M. E. *Chem. Phys. Lett.* **1992**, *197*, 131. (b) Bixon, M.; Jortner, J. *J. Phys. Chem.* **1993**, *97*, 13061.
- (24) Bixon, M.; Jortner, J. *Adv. Chem. Phys.* **1999**, *106*, 35.
- (25) Bizjak, T.; Karpiuk, J.; Lochbrunner, S.; Riedle, E. *J. Phys. Chem. A* **2004**, *108*, 10763.
- (26) Kovalenko, S. A.; Pérez Lustres, J. L.; Ernsting, N. P.; Rettig, W. *J. Phys. Chem. A* **2003**, *107*, 10228.
- (27) Kubo, M.; Mori, Y.; Otani, M.; Murakami, M.; Ishibashi, Y.; Yasuda, M.; Hosomizu, K.; Miyasaka, H.; Imahori, H.; Nakashima, S. *J. Phys. Chem. A* **2007**, *111*, 5136.
- (28) Rosenthal, S. J.; Xie, X.; Du, M.; Fleming, G. R. *J. Chem. Phys.* **1991**, *95*, 4715.
- (29) Maroncelli, M. *J. Mol. Liq.* **1993**, *57*, 1.
- (30) Barbara, P. F.; Jarzaba, W. *Adv. Photochem.* **1990**, *15*, 1.
- (31) Jimenez, R.; Fleming, G. R.; Kumar, P. V.; Maroncelli, M. *Nature* **1994**, *369*, 471.
- (32) Ruthmann, J.; Kovalenko, S. A.; Ernsting, N. P.; Ouw, D. *J. Chem. Phys.* **1998**, *109*, 5466.
- (33) Pérez Lustres, J. L.; Kovalenko, S. A.; Mosquera, M.; Senyushkina, T.; Flasche, W.; Ernsting, N. P. *Ang. Chem., Int. Ed.* **2005**, *44*, 5635.
- (34) Horng, M. L.; Gardecki, J. A.; Papazyan, A.; Maroncelli, M. *J. Phys. Chem.* **1995**, *99*, 17311.
- (35) Åkesson, E.; Walker, G. C.; Barbara, P. F. *J. Chem. Phys.* **1991**, *95*, 4188.
- (36) Londergan, C. H.; Salsman, J. C.; Ronco, S.; Dolkas, L. M.; Kubiak, C. P. *J. Am. Chem. Soc.* **2002**, *124*, 6236.
- (37) Wang, Ch.; Mohny, B. K.; Akhremitchev, B. B.; Walker, G. C. *J. Phys. Chem. A* **2000**, *104*, 4314.
- (38) Martini, I. B.; Barthel, E. R.; Schwartz, B. J. *Science* **2001**, *293*, 462.
- (39) Karpiuk, J. *J. Phys. Chem. A* **2004**, *108*, 11183.
- (40) Karpiuk, J.; Karolak, E.; Nowacki, J. *Pol. J. Chem.* **2008**, *82*, 865.
- (41) Karpiuk, J. *J. Phys. Chem. Chem. Phys.* **2003**, *5*, 1078.
- (42) Karpiuk, J.; Grabowski, Z. R.; De Schryver, F. C. *J. Phys. Chem.* **1994**, *98*, 3247.

- (43) Fischer, O. *Chem. Ber.* **1879**, 12, 1685.
- (44) Stanetty, P.; Rodler, I.; Krumpak, B. *J. prakt. Chem.* **1993**, 335, 17.
- (45) Duxbury, D. F. *Chem. Rev.* **1993**, 93, 381.
- (46) Nagasawa, Y.; Ando, Y.; Kataoka, D.; Matsuda, H.; Miyasaka, H.; Okada, T. *J. Phys. Chem. A* **2002**, 106, 2024.
- (47) Kuzuya, M.; Miyake, F.; Okuda, T. *Chem. Pharm. Bull.* **1983**, 31, 791.
- (48) Jarikov, V. V.; Neckers, D. C. *Adv. Photochem.* **2001**, 26, 1, and references cited therein.
- (49) Karpiuk, J.; Svartsov, Y. N.; Nowacki, J. *Phys. Chem. Chem. Phys.* **2005**, 7, 4070.
- (50) Marcus, R. A. *J. Phys. Chem.* **1989**, 93, 3078.
- (51) The values of  $\mu_e = 11.2$  D derived from a steady-state solvatochromic study and of the angle between  $\vec{\mu}_e$  and  $\vec{\mu}_g$  ( $34.8^\circ$ ) used here differ from those published earlier (ref 39) for 6-DMAPd (9.7 D,  $32^\circ$ ) because of different  $\mu_g$  values assumed (5.9 D from AM1 calculations in ref 39 instead of 6.55 D in ref 49 from the DFT method).
- (52) Shida, T. *Electronic absorption spectra of radical ions*; Elsevier: New York, 1988.
- (53) De Waele, V.; Beutter, M.; Schmidhammer, U.; Riedle, E.; Daub, J. *Chem. Phys. Lett.* **2004**, 390, 328.
- (54) Marcus, R. A. *J. Chem. Phys.* **1956**, 24, 966.
- (55) Marcus, R. A.; Sutin, N. *Biochim. Biophys. Acta* **1985**, 811, 265.
- (56) Onsager, L. *J. Am. Chem. Soc.* **1936**, 58, 1486.
- (57) The choice of different Onsager radii for both CT states has been discussed in detail in ref 39.
- (58) Hicks, J. M.; Vandersall, M. T.; Sitzmann, E. V.; Eisenthal, K. B. *Chem. Phys. Lett.* **1987**, 135, 413.
- (59) In protic solvents, the solvation (as overall stabilization resulting from interactions with the solvent) of CVL comprises a contribution due to hydrogen bonding.
- (60) Calef, D. F.; Wolynes, P. G. *J. Phys. Chem.* **1983**, 87, 3387.
- (61) Simon, J. D. *Pure Appl. Chem.* **1990**, 62, 2243.
- (62) Mohrschladt, R.; Schroeder, J.; Schwarzer, D.; Troe, J.; Vöhringer, P. *J. Chem. Phys.* **1994**, 101, 7566.
- (63) Nad, S.; Pal, H. *J. Phys. Chem. A* **2000**, 104, 673.
- (64) Nad, S.; Pal, H. *J. Chem. Phys.* **2002**, 116, 1658.
- (65) For a bimolecular ET reaction with a given distance  $r_{DA}$  between a spherical donor ( $r_D$ ) and acceptor ( $r_A$ ), the reorganization energy is given by  $\lambda_0 = e^2/4\pi\epsilon_0[1/(2r_D) + 1/(2r_A) - 1/r_{DA}](1/n^2 - 1/\epsilon)$ . Here,  $n$  and  $\epsilon$  are the refractive index and dielectric constant of the solvent, respectively. In analogy to ref 39, we used  $r_D = 3$  Å,  $r_A = 3.6$  Å, and  $r_{DA} = 4.3$  Å.
- (66) Maroncelli, M. *J. Chem. Phys.* **1991**, 94, 2084.
- (67) Kovalenko, S. A.; Schanz, R.; Hennig, H.; Ernsting, N. P. *J. Chem. Phys.* **2001**, 115, 3256.
- (68) Sumi, H.; Marcus, R. A. *J. Chem. Phys.* **1986**, 84, 4894.
- (69) Barbara, P. F.; Walker, G. C.; Smith, T. P. *Science* **1992**, 256, 975.
- (70) Hilczer, M.; Tachiya, M. *J. Mol. Liq.* **2000**, 86, 97.
- (71) Scherer, P. O. J.; Tachiya, M. *J. Chem. Phys.* **2003**, 118, 4149.
- (72) Denny, R. A.; Bagchi, B.; Barbara, P. F. *J. Chem. Phys.* **2001**, 115, 6058.
- (73) Burghardt, I.; Bagchi, B. *Chem. Phys.* **2006**, 329, 343.
- (74) Jin, H.; Li, X.; Maroncelli, M. *J. Phys. Chem. B* **2007**, 111, 13473.
- (75) Gladkikh, V.; Burshtein, A. I. *J. Phys. Chem. A* **2005**, 109, 4983.
- (76) Yoshihara, K.; Tominaga, K.; Nagasawa, Y. *Bull. Chem. Soc. Jpn.* **1995**, 68, 696.
- (77) Castner, E. W., Jr.; Kennedy, D.; Cave, R. J. *J. Phys. Chem. A* **2000**, 104, 2869.
- (78) Morandeira, A.; Fürstenberg, A.; Gumy, J.-C.; Vauthey, E. *J. Phys. Chem. A* **2003**, 107, 5375.

## **Appendix A6**

### **Unraveling the flavin-catalyzed photooxidation of benzylic alcohol with transient absorption spectroscopy from sub-pico- to microseconds**

*U. Megerle, M. Wenninger, R.-J. Kutta, R. Lechner, B. König, B. Dick, E. Riedle*

Physical Chemistry Chemical Physics 13, 8869-8880 (2011)



Cite this: *Phys. Chem. Chem. Phys.*, 2011, **13**, 8869–8880

www.rsc.org/pccp

PAPER

## Unraveling the flavin-catalyzed photooxidation of benzylic alcohol with transient absorption spectroscopy from sub-pico- to microseconds

Uwe Megerle,<sup>a</sup> Matthias Wenninger,<sup>a</sup> Roger-Jan Kutta,<sup>b</sup> Robert Lechner,<sup>c</sup> Burkhard König,<sup>c</sup> Bernhard Dick<sup>b</sup> and Eberhard Riedle<sup>\*a</sup>

Received 21st January 2011, Accepted 23rd February 2011

DOI: 10.1039/c1cp20190e

Flavin-mediated photooxidations have been described for applications in synthetic organic chemistry for some time and are claimed to be a route to the use of solar energy. We present a detailed investigation of the involved photophysical and photochemical steps in methoxybenzyl alcohol oxidation on a timescale ranging from sub-picoseconds to tens of microseconds. The results establish the flavin triplet state as the key intermediate for the photooxidation. The initial step is an electron transfer from the alcohol to the triplet state of the flavin catalyst with  ${}^3k_{\text{ET}} \approx 2 \times 10^7 \text{ M}^{-1} \text{ s}^{-1}$ , followed by a proton transfer in  $\sim 6 \mu\text{s}$ . In contrast, the electron transfer involving the singlet state of flavin is a loss channel. It is followed by rapid charge recombination ( $\tau = 50 \text{ ps}$ ) without significant product formation as seen when flavin is dissolved in pure benzylic alcohol. In dilute acetonitrile/water solutions of flavin and alcohol the electron transfer is mostly controlled by diffusion, though at high substrate concentrations  $> 100 \text{ mM}$  we also find a considerable contribution from preassociated flavin–alcohol-aggregates. The model including a productive triplet channel and a competing singlet loss channel is confirmed by the course of the photooxidation quantum yield as a function of substrate concentration: We find a maximum quantum yield of 3% at 25 mM of benzylic alcohol and significantly smaller values for both higher and lower alcohol concentrations. The observations indicate the importance to perform flavin photooxidations at optimized substrate concentrations to achieve high quantum efficiencies and provide directions for the design of flavin photocatalysts with improved performance.

### 1. Introduction

Riboflavin, vitamin B<sub>2</sub>, is an important biological redox cofactor capable of two subsequent one electron transfers.<sup>1</sup> Due to its reasonably strong absorption up to 500 nm and the redox properties of its excited states it has been used as a chemical photocatalyst operating with visible light. Flavin-based photoredox systems were inspired by the biological model of photolyase, a light driven bacterial enzyme repairing thymine dimer DNA lesions by photoinduced single electron transfer. Its mode of action has been investigated and mimicked by several model systems. The studies revealed the photocatalytic one electron repair mechanism and the dependence of the efficiency on the distance of the reduced flavin and additional sensitizing chromophores.

Preparative flavin-mediated photooxidations<sup>2,3</sup> were investigated by Shinkai,<sup>4,5</sup> Fukuzumi<sup>6–8</sup> and others.<sup>9–12</sup> To enhance the photocatalytic efficiency and photocatalyst stability, heterocyclic substrate binding sites or flavin transition metal complexes have been used. The redox properties of flavin were modulated by hydrogen bonding and transition metal complexation.<sup>13–16</sup> Scandium complexes of flavin without a detailed described structure were used by Fukuzumi to investigate photophysical parameters and propose a mechanistic scheme of the process. Some of us have used zinc-cyclen appended flavins for the photooxidation of benzyl alcohols<sup>17</sup> and recently extended the synthetic scope to photocatalytic cleavage of benzyl protection groups and photooxidation of activated hydrocarbons by flavin tetraacetate and blue light.<sup>18</sup>

Flavin photocatalysts reported so far were designed on the assumption that close proximity of the substrate and flavin chromophore will enhance the efficiency and selectivity of the photooxidation process. This assumption is based on the well known distance dependence of electron transfer as described by the Marcus theory and successful examples from template photochemistry.<sup>19</sup> However, our preliminary quantum yield determinations of the flavin photooxidation at different substrate

<sup>a</sup> Lehrstuhl für BioMolekulare Optik, Ludwig-Maximilians-Universität München, 80538 München, Germany. E-mail: riedle@physik.lmu.de; Fax: +49 89 2180 9202; Tel: +49 89 2180 9210

<sup>b</sup> Institut für Physikalische und Theoretische Chemie, Universität Regensburg, D-93040 Regensburg, Germany

<sup>c</sup> Institut für Organische Chemie, Universität Regensburg, D-93040 Regensburg, Germany

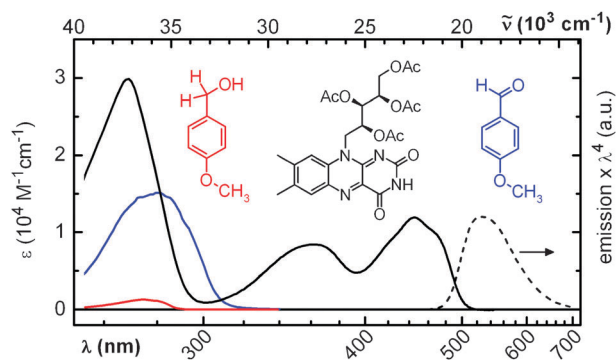


**Fig. 1** Steady state absorption spectra of the oxidized form of riboflavin tetraacetate (RFTA, black), 4-methoxybenzyl alcohol (MBA, red) and 4-methoxy-benzaldehyde (blue) dissolved in MeCN/H<sub>2</sub>O (50 : 50, v/v). The emission spectrum of RFTA is shown as a dashed line. The wavelength scale is reciprocal to render a linear energy scale shown at the top.

concentrations indicated that this assumption is not generally valid.<sup>20</sup> Therefore it seems necessary to reinvestigate the flavin mediated benzyl alcohol photooxidation with state-of-the-art time resolved spectroscopic methods.

The photophysical properties of flavins have been studied for almost a century.<sup>21,22</sup> In the past decade, transient absorption studies with picosecond to microsecond resolution have been carried out in solution<sup>23–26</sup> and in protein environment<sup>27–33</sup> to gain insight into the excited state dynamics of flavin-based systems. The experimental studies have been assisted by various *ab initio* calculations.<sup>34–40</sup> In many cases, the first step of the photo-initiated dynamics consists of an ultrafast electron transfer from a donor to the excited flavin.

In the present paper we aimed at gaining a complete understanding of the photooxidation mechanism of 4-methoxybenzyl alcohol (MBA) to the corresponding aldehyde using riboflavin tetraacetate (RFTA) as catalyst (Fig. 1). We found that relevant processes during the reaction occur both in the singlet and triplet manifold of RFTA states. Therefore, the timescales for the productive reactions and loss channels range from sub-picoseconds to several microseconds. To measure the fast singlet dynamics we used a setup based on a femtosecond white light pulse as a probe, while the slower triplet dynamics were monitored with a Streak camera using a pulsed Xe-flashlamp to generate the probe light. This unique combination of state-of-the-art spectrometers renders a detailed picture of the flavin photoreaction and thereby helps to derive structural design guidelines for photocatalysts with improved performance.

## 2. Experimental section

Riboflavin tetraacetate (RFTA) was synthesized as previously reported.<sup>12</sup> 4-methoxybenzyl alcohol (MBA) was obtained from Acros and distilled before use. The solvents acetonitrile (MeCN), water and DMSO were of spectroscopic quality. The steady state spectra were recorded with a Perkin-Elmer Lambda 19 spectrophotometer and a Spex Fluorolog 2 spectrofluorometer at room temperature. For the fluorescence measurements, the optical density of the sample in a 1 cm cuvette was 0.05 at the excitation wavelength of 420 nm. The fluorescence

spectrum was corrected for the instrument response and multiplied by a factor of  $\lambda^4$  to obtain the spectral shape of the stimulated emission in the time resolved absorption spectra.<sup>41</sup>

### Femtosecond transient absorption measurements

The femtosecond spectrometer has been described in detail.<sup>42</sup> A Ti:sapphire amplifier system (CPA 2001; Clark MXR) was used to pump a noncollinear optical parametric amplifier tuned to 480 nm. The pulses were compressed to  $\sim 50$  fs and attenuated to 400 nJ at the sample position. By focusing another part of the Ti:sapphire laser into a moving CaF<sub>2</sub> disk (4 mm thickness), a probe white light was generated ranging from below 300 nm to 750 nm. A computer controlled delay line was used to set pump–probe delays up to 1 ns. The pump and probe pulses were focused into the sample to spot sizes of 120  $\mu\text{m}$  and 30  $\mu\text{m}$  FWHM using spherical mirrors. After the interaction in the sample, the probe beam was dispersed with a fused silica prism and detected with a photodiode array of 512 pixels. The relative polarizations between the pump and probe were set to the magic angle (54.7°) by a half-wave plate in the pump-beam path. The  $\sim 1.5$  ps chirp of the white light was corrected for prior to the data analysis using the coherent artifact as an indicator for time zero at each wavelength. Throughout the probe range, the spectral resolution was better than 100  $\text{cm}^{-1}$  and the temporal resolution was better than 150 fs. For the experiments in MeCN/H<sub>2</sub>O (50 : 50, v/v) solution, the temperature of the sample was set to 300 K. A flow cell with 1 mm thickness was used and the flavin concentration was 0.5 mM. The measurements in pure MBA and in MeCN/DMSO (98 : 2, v/v) were performed with a flow cell of 120  $\mu\text{m}$  thickness at ambient temperature. Here, the flavin concentration was 2 mM.

### Microsecond transient absorption measurements

To measure transient spectra in the range from nanoseconds to 20  $\mu\text{s}$  the sample was excited with 8–10 ns pulses at 450 nm from a 10 Hz Optical Parametric Oscillator (OPO, Continuum) pumped by the third harmonic of a Nd:YAG laser (Surelite II, Continuum). A pulsed 150 W Xe flashlamp (MSP-05, Müller Elektronik-Optik) was used as probe light and the full time range was monitored at once with a streak camera (C7700, Hamamatsu Photonics).<sup>32</sup> RFTA was dissolved in MeCN/H<sub>2</sub>O (50 : 50, v/v) at a concentration of 40.9  $\mu\text{M}$ , which gave an optical density of about 0.5 at 450 nm with a path length of 10 mm. A fused silica flow cuvette with 10 mm of optical path length for excitation and 10 mm for probe light was used. Including the storage vessel and the peristaltic pump, the overall volume was 10 mL. The excitation light was focused into the sample with a cylindrical lens ( $f = 150$  mm), and the pulse energy was adjusted to about 8 mJ per pulse at the sample. Mechanical shutters were used to select pump and probe pulses. The probe light with a very flat intensity profile of 2 ms duration was refocused three times by a series of toric mirrors: on a mechanical shutter to block the continuous light from the Xe flashlamp, on the sample cell, and on the entrance slit of the imaging spectrograph (Bruker 200is, grating 100 grooves per mm) in front of the streak camera.



The streak camera converts the coupled spectral and temporal information into two-dimensional images of the intensity distribution of the probe white light. Each transient absorption data set was calculated from four images taken with a frequency of 0.5 Hz: an image ( $D_{FL}$ ) with both flash lamp and laser, an image ( $D_0$ ) without any incoming light, an image ( $D_F$ ) only with the flash lamp, and an image ( $D_L$ ) only with the laser. Results represent the average of 100 individual measurement sequences with a time window of 10  $\mu$ s and a time resolution of 20 ns. The transient absorption is calculated from these data as  $\log[(D_F - D_0)/(D_{FL} - D_L)]$ . The fluorescence of RFTA can be very strong, much brighter than the white light pulse. In this case the fluorescence is not cancelled well in the difference  $D_{FL} - D_L$  and we used  $D_0$  instead of  $D_L$  as the background for the data  $D_{FL}$ . The data analysis then yields the fluorescence spectrum as an additional component with unresolved decay time. All described measurements were performed at ambient temperature.

### Data analysis

Data were analyzed with homemade software to obtain decay associated difference spectra (DADS). This analysis corresponds to the least-squares fit:

$$|\Delta OD(t, \lambda) - \sum_k^N f_k(t) \text{DADS}_k(\lambda)|^2 = \min, \quad (1)$$

where  $\Delta OD(t, \lambda)$  is the measured data matrix and the  $f_k(t)$  are exponential (or more complex) decay functions convoluted with a Gaussian function as the apparatus response function  $g(t)$

$$f_k(t) = g(t) \otimes \exp(-(t - t_0)/\tau_k). \quad (2)$$

For each manifold  $\{f_k\}$  the DADS display the spectral changes associated with the particular decay times  $\tau_k$ . This procedure does not assume a specific kinetic model assigning the rates to reaction steps, but is compatible with all models that involve only unimolecular reaction steps. The DADS are in turn linear combinations of the species spectra. The linear coefficients depend on the particular kinetic model, *e.g.*, a linear decay sequence or models involving parallel reactions and branching. After a kinetic model has been chosen, the system of linear equations can be solved for the species spectra.

### Quantum yields

Relative product quantum yields (QY) for different MBA concentrations in MeCN/H<sub>2</sub>O (50 : 50, v/v) were determined by the change in the absorbance in the region of 305 to 325 nm. In this region the absorbance of the product 4-methoxybenzaldehyde is much larger than that of MBA, and the contribution of RFTA is constant (compare Fig. 1). Photoexcitation was performed in fused silica cuvettes with a 2 mm by 10 mm cross section. Two high-power LEDs (Luxeon III Emitter LXHL-PBO9, Philips, 150 mW at 460 nm) were mounted at 1 cm distance to each other on opposite sides of the cuvette. The path length for monitoring the changing absorption was 10 mm, for photoexcitation 2 mm. A custom-designed power supply was used to apply light pulses of reproducible length and intensity. Absorption spectra were

measured with a Perkin Elmer Lambda-9 spectrometer. The temperature of the cuvette was held at 20 °C by a thermostat.

Absolute values for the product QYs were obtained by calibration of the maximum value at 25 mM MBA using an LED-based apparatus described in detail elsewhere.<sup>20</sup> Here, the RFTA concentration was set to 2 mM as in the femto-second experiments. After a defined irradiation time with 20.2 mW of 443 nm light, the chemical yield of 4-methoxybenzaldehyde was determined by quantitative gas chromatography. From the number of absorbed photons and the resulting chemical conversion, the absolute reaction quantum yield was determined.

## 3. Results and discussion

The spectroscopic study of the flavin-catalyzed photooxidation of benzylic alcohol relies on the differing spectra of the various redox and protonation states of flavin. All existing models assume that essentially only the catalyst and the substrate contribute to the reaction steps. Consequently we can deduce the oxidation mechanism from the time resolved observation of the evolving flavin transformation.

### 3.1 Femtosecond dynamics of riboflavin tetraacetate in pure methoxybenzyl alcohol

The simplest and seemingly clearest approach to study the photocatalytic oxidation is to bring the substrate MBA and the catalyst RFTA in direct contact. Typically, one would assume that this system shows the most effective conversion of alcohol to aldehyde since the reactants are inevitably in close proximity. However, we find that the experimental results contradict this assumption.

Even so MBA solidifies at room temperature, the lowering of the melting point by the solute is already sufficient to turn it into a highly viscous liquid that easily dissolves RFTA in mM concentrations. Thus, we could perform transient absorption measurements at ambient temperature in a flow cell without any additional solvent. Fig. 2a shows the transient absorption spectra of RFTA dissolved in pure MBA between -1 and 1000 ps after excitation at 480 nm, the first absorption maximum of flavin. The spectra consist of three major contributions that can all be assigned to RFTA transitions. Two bands with negative changes of the optical density indicate the ground state bleach (GSB) of RFTA around 450 nm and the stimulated emission (SE) around 560 nm. These bands are partially overlaid with the excited state absorption (ESA) that contributes a positive absorption change and has its maximum around 370 nm. All of these signatures decay to the baseline within the observed time window indicating a complete deactivation back to the ground state of RFTA on the timescale of several tens of picoseconds.

A closer inspection of the data reveals a significantly faster decay of the SE around 560 nm than of the ESA or GSB bands. This is clearly seen in Fig. 2b. The few ps decay of the stimulated emission goes along with an apparent redshift of the ESA band by  $\sim 10$  nm. The GSB, however, shows no significant dynamics on this timescale. Except for minor shifts and the missing SE band, the transient spectrum after the fluorescence quenching (at a delay time  $\Delta t = 10$  ps) is similar

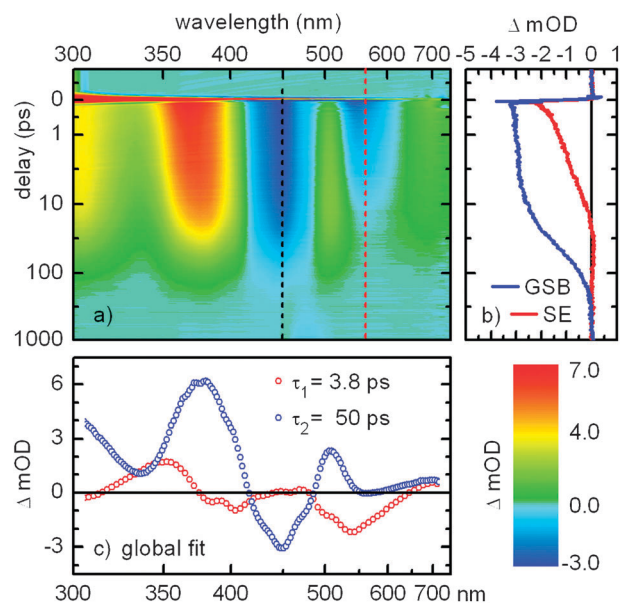


**Fig. 2** (a) Transient absorption of RFTA dissolved in pure methoxybenzyl alcohol after excitation at 480 nm. The delay time axis is linear between  $-1$  and  $1$  ps and logarithmic between  $1$  and  $1000$  ps. (b) Kinetic traces show a faster decay in the band of the stimulated emission (SE,  $560$  nm, red line) than in the ground state bleach (GSB,  $450$  nm, blue line). (c) Decay associated difference spectra from a biexponential global fit.

to the transient spectrum of the  $S_1$  state ( $\Delta t = 0$  ps). This situation is frequently found when the quenching mechanism is an electron transfer to the excited chromophore. Typically, the low energy transitions from the  $S_1$  state involve the promotion of the electron from the highest SOMO (corresponding to the LUMO of the equilibrium molecule) to higher unoccupied orbitals. In first approximation, these transitions are not affected when an additional electron is transferred to the lower lying SOMO of the  $S_1$  state (corresponding to the HOMO). Consistently, the observed spectral features agree well with the absorption spectrum of the flavin radical anion.<sup>43</sup>

This proves that the first step of the photoinduced dynamics is an electron transfer (ET) from one of the surrounding MBA molecules to  $^1\text{RFTA}^*$  yielding the radical anion  $\text{RFTA}^{\bullet-}$  and the radical cation  $\text{MBA}^{\bullet+}$ . The weak signature of the radical cation expected around  $440$  nm<sup>44–46</sup> is not observed spectroscopically as it is masked by the much stronger ground state bleach of flavin. The absence of any residual signals at long delay times indicates a full charge recombination by back electron transfer from  $\text{RFTA}^{\bullet-}$  to  $\text{MBA}^{\bullet+}$ .

In a precise description, the ET process described above changes the ESA band of  $^1\text{RFTA}^*$  into a very similar product absorption of  $\text{RFTA}^{\bullet-}$ . Due to the spectral similarity and the nearly identical intensity, we choose to use the term “ESA band” for the denomination of both.

To quantify the dynamics of the ET processes, we perform a least square global analysis using a biexponential fit function. We find that the spectral evolution can be well reproduced with two decay time constants of  $3.8$  and  $50$  ps. The decay associated difference spectra shown in Fig. 2c underline the qualitative description given above. The fast time constant is

negligible in the region of the GSB, but forms the strongest contribution in the SE band. The dispersive shape of the amplitude spectrum around  $370$  nm again shows the fast spectral shift of the ESA band. In contrast, the decay associated difference spectrum of the  $50$  ps component has a very low amplitude in the SE band, but reflects the concerted decay of ESA and GSB.

Thus, after photoexcitation, the system of RFTA in pure MBA performs a nonproductive cycle of fast forward ET ( $\sim 4$  ps), but also rapid back-ET ( $50$  ps) that restores the reactants RFTA and MBA to the ground state. It is noteworthy that the triplet state  $^3\text{RFTA}$  does not play a role under these conditions as the known rate of intersystem crossing<sup>39,47</sup> is about three orders of magnitude smaller than the competing  $S_1$  quenching rate of  $\sim (4 \text{ ps})^{-1}$ . The fast back-reaction essentially rules out any further electron or proton transfer steps from MBA to RFTA needed to convert the alcohol to aldehyde. From the photocatalytic point of view, dissolving RFTA directly in the substrate MBA inhibits an effective utilization of photons, *i.e.* a good photoreaction quantum yield. The results from the ultrafast spectroscopic analysis explain why practically no conversion of MB-alcohol to MB-aldehyde can be observed even under long-time irradiation. To reach traceable aldehyde concentrations in an alcohol environment requires so many excitations per RFTA molecule that the flavin will likely degrade before.

### 3.2 Femtosecond dynamics in a dilute solution of MeCN/DMSO

As shown in the previous section, a direct contact between MBA and RFTA is not desirable for efficient photocatalysis. To circumvent this we used the “inert” solvent acetonitrile (MeCN) to dissolve RFTA and MBA in chosen concentrations. For better solubility of RFTA (up to  $2$  mM), we added  $2$  vol.% of DMSO to MeCN. By changing the MBA concentration one can then tune the average distance between the reactants. Based on the strong distance dependence of electron transfer one can also expect the rates to decrease significantly.

The transient absorption spectra of RFTA in solution are very similar to the ones in pure MBA. As shown in Fig. 3a, they consist of the same signatures, most prominently a strong ESA band around  $360$  nm, the negative GSB around  $440$  nm and the negative SE band around  $550$  nm. Small differences in the shape and position of these bands with respect to the ones observed in pure MBA can be explained by the lower polarity of the MeCN/DMSO mixture.<sup>48</sup>

In the absence of MBA, our time window of  $1$  ns allows for the observation of only the onset of a slow decay of all signals. This decay reflects the photophysical lifetime of the  $S_1$  state of flavin. With time correlated single photon counting we can determine the fluorescence lifetime of RFTA with higher accuracy and find a value of  $6.0$  ns, very similar to other flavins in solution.<sup>26</sup> Upon addition of MBA in concentrations of several hundred mM, one observes an increasingly faster decay of all signatures. For example, at  $300$  ps delay and  $400$  mM MBA, the amplitude of the RFTA signals has dropped to  $50\%$  of the initial value directly after excitation (Fig. 3a).

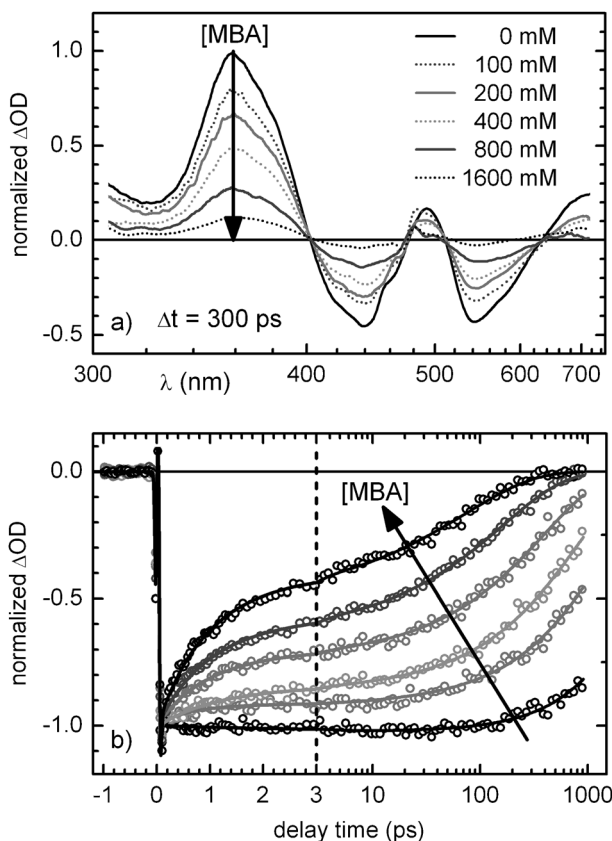


**Fig. 3** (a) TA spectra of RFTA in MeCN/DMSO (98 : 2, v/v) for different MBA concentrations at 300 ps delay. The spectra have been normalized to the initial amplitude of the ESA band after photo-excitation. (b) Decay of the SE of RFTA in MeCN/H<sub>2</sub>O (50 : 50, v/v) for the same MBA concentrations as in (a). The kinetic traces are obtained from band integrals (525–625 nm, circles). The fit functions according to the diffusion model described in the text are shown as solid lines. The delay time axis is linear between –1 and 3 ps and logarithmic between 3 and 1000 ps.

In contrast to the situation in pure MBA, the SE now decays on the same timescale as the other signatures. The reason for this is that the reaction of <sup>1</sup>RFTA\* with MBA is now a two-stage process: first, the reactants have to approach from a large separation distance to close proximity by diffusion and then the ET and all subsequent steps occur in this close configuration. If the concentration of MBA is not extremely high (< 1 M), the rate to form an encounter pair of <sup>1</sup>RFTA\* and MBA is much smaller than the first-order rate coefficient <sup>1</sup>k<sub>ET</sub> = (4 ps)<sup>-1</sup> of the ET and also smaller than the back reaction rate <sup>1</sup>k<sub>b-ET</sub> = (50 ps)<sup>-1</sup> (see Section 3.1). Hence, the observed dynamics are governed by the diffusion limited formation of <sup>1</sup>RFTA\*–MBA-encounter pairs that lead to a non-productive deactivation of <sup>1</sup>RFTA\* by an ET cycle like in pure MBA. Again, this model is qualitatively confirmed by the absence of any product signals at long delays for the highest MBA concentrations.

For a quantitative modeling of the diffusion dynamics, the use of single or multi-exponential fit functions is generally not justified. In the case of diffusive quenching, the intensity decay becomes non-exponential due to a time dependence of the reaction rate.<sup>49,50</sup> The transient effect originates from a changing concentration of MBA quenchers around the excited RFTA molecules.

The concentration is directly related to the average distance between the reactants and thereby to the time needed for an encounter after a random walk. Following excitation, the RFTA chromophores with nearby quenchers from the statistical distribution will react first. At later times, the ensemble of left over excited flavins faces a smaller effective MBA concentration and reacts with a smaller rate. At some point, the depletion of the MBA density around the remaining RFTA\* molecules is balanced by the diffusion of bulk MBA molecules towards RFTA\*. Thus, the reaction rate decreases from an initially high value to a constant that depends on the mutual diffusion coefficient *D* and the interaction distance *R*<sub>int</sub> of the molecules.

The derivation of the mathematical description of this model follows ref. 49. It starts from Fick's law of diffusion for the MBA quencher molecules:

$$\frac{\partial \rho_{\text{MBA}}(r, t)}{\partial t} = D \nabla^2 \rho_{\text{MBA}}(r, t) \quad (3)$$

The concentration of MBA quencher molecules is described by the normalized density distribution  $\rho_{\text{MBA}}$  around a spherical RFTA\* molecule at  $r = 0$ . The diffusion equation contains three partial derivatives, the general solution therefore requires one initial condition at fixed time and two boundary conditions for fixed space coordinates. In the Smoluchowski theory, the initial condition is used that at the moment of excitation  $\rho_{\text{MBA}}$  is homogeneous around any RFTA molecule, *i.e.*  $\rho_{\text{MBA}}(r, t = 0) = 1$  for  $r > R_{\text{int}}$ , but no reactant separation smaller than the interaction distance  $R_{\text{int}}$  is possible, *i.e.*  $\rho_{\text{MBA}}(r, t = 0) = 0$  for  $r \leq R_{\text{int}}$ . One boundary condition is obtained by assuming that the bulk concentration of quenchers far away from the excited chromophore is not affected by the reaction, *i.e.*  $\rho_{\text{MBA}}(r \rightarrow \infty, t) = 1$ . The second boundary condition follows from the fact that no quencher molecules are found at a distance  $R_{\text{int}}$  from the excited chromophores at any time, *i.e.*  $\rho_{\text{MBA}}(R_{\text{int}}, t) = 0$ .

Solving eqn (3) under these conditions and substituting the result into the particle current of MBA molecules through a surface of area  $4\pi R_{\text{int}}^2$  yields the reaction rate of MBA quenchers with the excited RFTA\* molecules:<sup>49</sup>

$$\begin{aligned} -\frac{d[\text{RFTA}^*]}{dt} &= 10^3 N_A 4\pi R_{\text{int}} D \left( 1 + \frac{R_{\text{int}}}{\sqrt{\pi D t}} \right) [\text{MBA}]_0 [\text{RFTA}^*] \\ &= k_{\text{diff}}(t) [\text{MBA}]_0 [\text{RFTA}^*] \end{aligned} \quad (4)$$

$[\text{MBA}]_0$  and  $[\text{RFTA}^*]$  are the initial concentrations of MBA and excited RFTA molecules in the solution. The multiplication with  $10^3 N_A$  where  $N_A$  is Avogadro's number is needed to convert  $k_{\text{diff}}(t)$  to units of M<sup>-1</sup> s<sup>-1</sup>.

The change in optical density  $\Delta\text{OD}(t)$  observed in our transient experiments is proportional to  $[\text{RFTA}^*](t)$ . Integrating eqn (4) therefore yields an expression that can be used directly to model the diffusion controlled fluorescence quenching:

$$\begin{aligned} \Delta\text{OD}(t) &= \Delta\text{OD}(0) \exp \left\{ -\frac{t}{\tau_{\text{fl}}} - 10^3 N_A 4\pi R_{\text{int}} D [\text{MBA}]_0 \left( 1 + \frac{2R_{\text{int}}}{\sqrt{\pi D t}} \right) t \right\} \end{aligned} \quad (5)$$

**Table 1** Results of the fit to the femtosecond TA data for varying MBA concentrations in two solvent mixtures using the diffusion model. The exponential contribution from pre-associated aggregates yielded  $\tau_{\text{fast}}(\text{SE}) = 4.5$  ps and  $\tau_{\text{fast}}(\text{ESA}) = 36$  ps in MeCN/DMSO and  $\tau_{\text{fast}}(\text{SE}) = 0.9$  ps and  $\tau_{\text{fast}}(\text{ESA}) = 6.4$  ps in MeCN/H<sub>2</sub>O. The resulting interaction radii were 3.8 Å and 6.0 Å, respectively.

[MBA]/mM	100	200	400	800	1600
MeCN/DMSO (98 : 2)					
$A_{\text{fast}}/A_{\text{diff}}$	0.05	0.06	0.09	0.16	0.25
$D/\text{Å}^2 \text{ ns}^{-1}$	160	130	110	100	90
$\tau_{\text{fl,eff}}/\text{ps}$	1100	740	420	230	87
$\Phi_{\text{ISC}}/\Phi_{\text{ISC},0}$ (%)	18	12	7.0	3.8	1.5
MeCN/H <sub>2</sub> O (50 : 50)					
$A_{\text{fast}}/A_{\text{diff}}$	0.07	0.17	0.32	0.57	0.95
$D/\text{Å}^2 \text{ ns}^{-1}$	59	60	56	52	42
$\tau_{\text{fl,eff}}/\text{ps}$	1400	700	310	120	45
$\Phi_{\text{ISC}}/\Phi_{\text{ISC},0}$ (%)	23	12	5.2	2.0	0.75

Here,  $\tau_{\text{fl}}$  is the fluorescence lifetime of RFTA, and  $D = D_{\text{RFTA}} + D_{\text{MBA}}$  is the mutual diffusion constant.

The Smoluchowski diffusion model provides a consistent description of the predominant contribution to the dynamics for all MBA concentrations and over the whole spectral range. For the quantitative modeling, we preferred band integrals over transients at individual wavelengths. This minimizes the influence of spectral diffusion caused for instance by solvation or vibrational cooling. For a given MBA concentration, the diffusion dynamics in all three major bands (ESA, GSB and SE) could be described by one common set of parameters. The obtained values are given in Table 1.

In MeCN/DMSO solution, the mutual diffusion constant  $D$  of RFTA and MBA was found to lie between 90 and 160 Å<sup>2</sup> ns<sup>-1</sup>. This is in good agreement with the values estimated from the Stokes–Einstein relationship for spherical particles with radius  $R$  in a solution of viscosity  $\eta$  at the absolute temperature  $T$ :

$$D = \frac{k_{\text{B}}T}{6\pi\eta} \left( \frac{1}{R_{\text{RFTA}}} + \frac{1}{R_{\text{MBA}}} \right) \geq \frac{k_{\text{B}}T}{6\pi\eta R_{\text{MBA}}}. \quad (6)$$

From its bulk properties,  $R_{\text{MBA}}$  can be estimated to 3.7 Å, while  $\eta$  of pure MeCN at room temperature is 0.34 mPa s<sup>51</sup> yielding  $D \geq 170$  Å<sup>2</sup> ns<sup>-1</sup>. In the presence of DMSO and upon addition of MBA, the viscosity of the solution rises and  $D$  decreases accordingly (see Table 1).

As expected, the interaction distance  $R_{\text{int}}$  was not found to change for different MBA concentrations within the accuracy of our experiment. Interestingly, the obtained value of 3.8 Å is significantly smaller than the sum of the molecular radii of RFTA and MBA. This indicates that a specific orientation, most likely a face-to-face geometry, is required for an efficient electron transfer.<sup>52,53</sup>

For low MBA concentrations, the agreement between the diffusion model and our transient data is quite satisfactory. However, at higher MBA concentrations we observe an additional very fast component in the flavin kinetics. Since the Smoluchowski theory already poses an upper bound for the reaction rate at contact,<sup>54</sup> this cannot be due to the simplifying assumptions of the diffusion fit function. For a consistent modeling at all MBA concentrations, we therefore added an exponential term with a ps decay time to the fit function.

As shown in Table 1, the relative amplitude  $A_{\text{fast}}$  of this component rises with the MBA concentration. It can therefore be assigned to preassociated RFTA–MBA aggregates<sup>54,55</sup> which are not subject to diffusion control.

This assignment is supported by the characteristic decay time  $\tau_{\text{fast}}$  obtained from the fit: it is not dependent on the MBA concentration and it is smaller in the spectral region of the SE (4.5 ps) than in the ESA band (36 ps). This reflects the forward and backward electron transfer times in the aggregates, in agreement to the situation of RFTA dissolved in pure MBA. From the relative aggregate contribution at different MBA concentrations, one can calculate an association constant of  $K = 0.2 \text{ M}^{-1}$  for RFTA–MBA-complexes in MeCN/DMSO solution. This value is even smaller than the weak association constants around  $1 \text{ M}^{-1}$  found for other aromatic molecules of similar size in MeCN solution.<sup>56</sup> We assume that the aggregates consist of a  $\pi$ -stacked configuration of RFTA and MBA whose driving force is the hydrophobicity of the chromophores.

A careful check of the steady state absorption spectrum at varying MBA concentration in the RFTA solution did not render significant changes relative to the variation induced by changes in the polarity of the solvent. This is not unexpected considering the weak association constant and the large energy difference between the lowest RFTA excitation and the lowest MBA excitation.

Overall, the Smoluchowski diffusion model extended by the contribution from preassociated aggregates completely describes the observed dynamics of RFTA and MBA in dilute solution. Thus, no indications for a significant catalytic photo-oxidation of MBA to the aldehyde can be found, at least not for the MBA concentrations that are compatible with ultrafast spectroscopy. The higher this concentration, the faster the quenching of the S<sub>1</sub> state of RFTA by ET from MBA, which is then followed by rapid charge recombination.

### 3.3 Changes to the femtosecond dynamics upon the addition of water

From earlier studies<sup>17</sup> it is known that the quantum yield of flavin-catalyzed photooxidation of benzylic alcohol can rise significantly in the presence of water. We therefore performed a series of additional measurements in MeCN/H<sub>2</sub>O (50 : 50, v/v) solution. Overall, we find similar spectral signatures and dynamics as in MeCN/DMSO. Again, an increase of the MBA concentration leads to a faster quenching of the RFTA fluorescence and an essentially concerted decay of all other transient signatures. The same diffusion model with an additional contribution from preassociated RFTA–MBA aggregates could be used to reach a consistent quantitative description of the dynamics (see Fig. 3b). However, the set of parameters had to be altered in comparison to the MeCN/DMSO solution.

First, the contribution of preassociated RFTA–MBA aggregates is now considerably higher. At 1600 mM MBA, the ratio of RFTA molecules in aggregates to free ones approaches 1 : 1 (see Table 1). The obtained association constant of  $K' = 0.6 \text{ M}^{-1}$  is three times higher than in the absence of water. This confirms the hydrophobic effect as a driving force for the aggregation: this effect is of course stronger in the protic and

more polar solvent mixture including water.<sup>56</sup> The characteristic times for the forward (0.9 ps, SE band) and backward ET (6.4 ps, ESA band) inside the aggregates are smaller than in the MeCN/DMSO solution. This might be due to an interaction with the water molecules, *e.g.*, *via* hydrogen bonds that induce a favorable orientation of MBA and RFTA in the aggregates.

Secondly, the parameters of the Smoluchowski diffusion model are also slightly different in the presence of water. We find smaller mutual diffusion constants that indicate a larger effective radius of the moving particles (see eqn (6)). This means that RFTA and MBA probably diffuse together with their solvent shell. A slowed down diffusion of MBA through the last solvent layer around RFTA might add to the effect.<sup>55</sup> The increased amount of “bound” solvent molecules is also supported by the larger interaction distance of 6 Å.<sup>52</sup>

Whereas the obtained parameters from the diffusion model give rich insight into the processes on the molecular level, they are difficult to be interpreted in terms of relevant timescales. To obtain a graspable measure for the reaction dynamics at the different MBA concentrations in both solvent mixtures, we determined an effective fluorescence lifetime  $\tau_{\text{fl,eff}}$  from the normalized integral over the change in signal  $\Delta\text{OD}(\text{SE}; t)$  in the range of the stimulated emission:<sup>57</sup>

$$\tau_{\text{fl,eff}} = \frac{1}{\Delta\text{OD}(\text{SE}; 0)} \int_{t=0}^{\infty} \Delta\text{OD}(\text{SE}; t) dt. \quad (7)$$

This measure is meaningful, as it recovers the decay time for a simple exponential decay as well as the weighted average for a multi-exponential and increases monotonically for longer complex decays. The results are given in Table 1. For technical reasons the values are most reliable for the high MBA concentrations. Their faster dynamics can be observed better within our fixed time window and therefore less extrapolation is required. Nevertheless, the comparison of MeCN/DMSO with MeCN/H<sub>2</sub>O shows that the difference of the reaction speed decreases towards smaller MBA concentrations and eventually changes sign. At 1600 mM, the higher amount of aggregation in the presence of water outweighs the slower diffusion dynamics resulting in half the effective fluorescence lifetime. In contrast, at 100 mM MBA (and below), the contribution from RFTA–MBA-aggregates can be neglected and the speed of the diffusion is the only relevant parameter. Then, the smaller diffusion constants in the aqueous environment lead to a larger fluorescence lifetime than in MeCN/DMSO.

### 3.4 Dynamics involving the triplet state of RFTA

The findings presented above show no photooxidation of MBA as long as the forward and backward ET happen in the singlet manifold. As shown explicitly for RFTA in three different environments (pure MBA, MeCN/DMSO and MeCN/H<sub>2</sub>O), the ET reaction of MBA with <sup>1</sup>RFTA\* is followed by rapid charge recombination. The relevance of this loss channel is lowered when the MBA concentration is decreased. Indeed the chemical conversion was reported at 2 mM,<sup>11</sup> much lower than the concentrations used in the femtosecond measurements. With lower MBA concentration, the probability for intersystem crossing of the excited RFTA rises.

A measure of the quantum yield of triplet formation  $\Phi_{\text{ISC}}$  relative to the intrinsic yield  $\Phi_{\text{ISC},0}$  in the absence of MBA is given by the ratio between  $\tau_{\text{fl,eff}}$  and the native fluorescence lifetime of RFTA of 6.0 ns. As shown in Table 1,  $\Phi_{\text{ISC}}$  is higher in the presence of water for MBA concentrations below 100 mM which could contribute to the increased reaction quantum yield in buffer solution found at low substrate concentrations.<sup>17</sup>

To accentuate the spectral signature of <sup>3</sup>RFTA with our femtosecond setup, we redirected the pump light and omitted the prism compressor and the delay stage. The shortened optical path of the pump pulses resulted in a fixed delay of 12 ns for the white light probe, twice the fluorescence lifetime of flavin. As shown in Fig. 4, the transient spectrum of RFTA in pure MeCN/H<sub>2</sub>O solution measured in this way (dotted line) differs significantly from the S<sub>1</sub> spectrum obtained shortly after excitation ( $\Delta t = 300$  fs, dashed line). On the short wavelength side, the absorption maximum shifts by 2200 cm<sup>-1</sup> from 358 nm to 388 nm. A comparison with the GSB band shows that the extinction coefficient of the ESA band has dropped by roughly a factor of three.

On the long wavelength side above 500 nm, the negative signature from the stimulated emission is largely missing in the 12 ns transient. Instead, a broad absorption is observed with a double peak around 650 and 710 nm and a smaller peak at 510 nm. This is in good agreement with published triplet spectra of similar flavin compounds.<sup>43,58</sup> When MBA is added to the solution (solid line), the amplitude of all signatures decreases, in analogy to the situation at 300 ps delay shown in Fig. 3a. A normalization to the GSB minimum shows that even at 12 ns delay the transient of RFTA without MBA has the expected weak contribution from <sup>1</sup>RFTA\* as seen from the higher absorption around 360 nm and the lower one in the SE region (see Fig. 4) compared to the spectrum with 50 mM MBA.

The dynamics of the triplet state proceed on a nano- to microsecond timescale. This range cannot be covered with the femtosecond setup and transient data were therefore measured with the Streak-camera setup. The obtained spectra at short delay times < 1 μs are identical with the 12 ns spectra

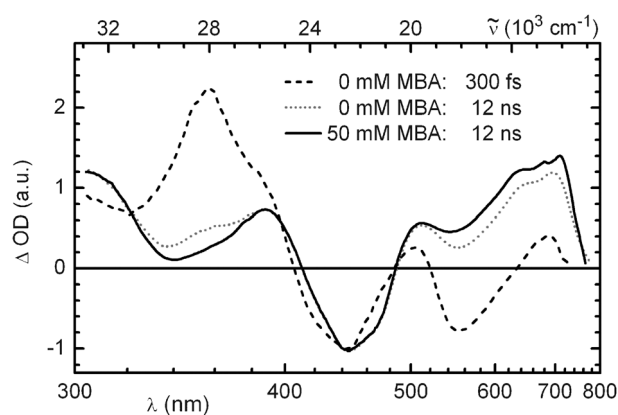


**Fig. 4** Transient absorption spectra of RFTA in MeCN/H<sub>2</sub>O (50 : 50, v/v) directly after excitation (singlet state; dashed line) and after 12 ns delay (triplet state; dotted and solid lines). The spectra have been normalized to the ground state absorption minimum.

from the fs-setup. However, in striking contrast to the unproductive singlet reaction observed in the ultrafast experiments, the  $\mu\text{s}$  measurements reveal a productive reaction between MBA and  $^3\text{RFTA}$  beyond the forward and back-ET. This is most clearly seen as a persistent signature on the 10  $\mu\text{s}$  scale that agrees well with the neutral protonated flavin radical  $\text{RFTA}\cdot^+$  (for details see below).

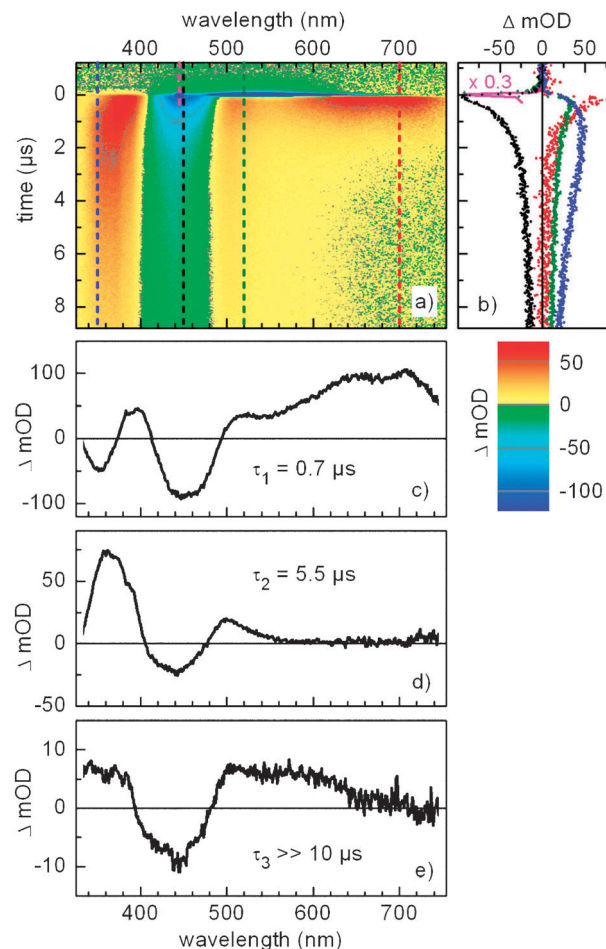
Without MBA in the solution, the TA signal from  $^3\text{RFTA}$  decays monoexponentially with  $\tau = 1.3 \mu\text{s}$  (data not shown). The corresponding rate of  $7.7 \times 10^5 \text{ s}^{-1}$  reflects the diffusional triplet quenching by oxygen in the solution and compares well to similar systems reported in the literature.<sup>24,59,60</sup> Upon addition of MBA, the observed dynamics show significant changes.

Fig. 5 shows the data obtained with 40.9  $\mu\text{M}$  RFTA and 50 mM MBA in MeCN/H<sub>2</sub>O (50 : 50, v/v) solution after excitation at 445 nm. Panel a shows a false colour map of the 2D-transient absorption data matrix. Panel b shows time traces at various wavelengths: the line in magenta represents the time profile of the pump pulse corresponding to the instrument response function. The red dots (700 nm) can be assigned to absorption of the triplet state, decaying with a lifetime of 700 ns. Bleaching at 450 nm (black dots) only recovers partially on this scale. The rise and decay of the green dots (520) and the blue dots (350 nm) indicate the presence of transient intermediates.

A model which contains, in addition to the instrument response function, two exponential functions and one constant term was found suitable to fit the data (Table 2). The fit yields the fluorescence spectrum (associated with the instrument response, not shown) and three decay associated difference spectra (DADS) shown in panels c–e. From the fastest time constant and the intrinsic triplet lifetime in the presence of oxygen we calculated a quenching constant of  $^3k_{\text{ET}} = 1.3 \times 10^7 \text{ M}^{-1} \text{ s}^{-1}$  corresponding to an ET from MBA to  $^3\text{RFTA}$ . The corresponding DADS reflects the conversion of  $^3\text{RFTA}$  to  $\text{RFTA}\cdot^-$  (see Fig. 5c) as seen from the disappearance of the broad long-wavelength absorption and a blueshift of the maximum at  $\sim 370 \text{ nm}$ .<sup>43</sup> The radical ion pair  $\text{RFTA}\cdot^-$  and  $\text{MBA}\cdot^+$  has two deactivation pathways: back-ET to the ground state of the system and the productive proton transfer from MBA to flavin yielding a neutral radical pair. The sum of these two rates was fitted to  $1.8 \times 10^5 \text{ s}^{-1}$ , corresponding to a lifetime of the ion pair of 5.5  $\mu\text{s}$  in accordance with previous studies.<sup>46,61</sup> According to our model, flavin and MBA are in contact—or at least close proximity—after the initial ET. Therefore, the decay of the ion pair should not depend on the substrate concentration. We find a small increase of the effective ion pair lifetime by a factor of 2 when the MBA concentration is increased by a factor of 10 from 50 mM to 500 mM.

In our detection window of up to 20  $\mu\text{s}$ , we observe the signature of a non-decaying species displaying a broad absorption between 500 and 600 nm and a maximum around 350 nm (see Fig. 5e). The signature can be assigned to the neutral protonated flavin radical  $\text{RFTA}\cdot\text{H}^+$ .<sup>43,58,62</sup> This confirms the proposed mechanism of ET followed by a proton transfer between MBA and flavin in the triplet state.

We thus propose that the measurement in the 10  $\mu\text{s}$  range reflects the following reaction steps: The initially populated



**Fig. 5** (a) False colour map of the 2D-transient absorption data matrix measured with 40.9  $\mu\text{M}$  RFTA and 50 mM MBA in MeCN/H<sub>2</sub>O (50 : 50, v/v) solution after excitation at 445 nm. (b) Time traces at various wavelengths. (c–e) Decay associated difference spectra from the global fit.

**Table 2** Results of the global fit to the streak camera measurements for varying MBA concentrations.  $\tau_1 = (k_{\text{b-ISC}} + ^3k_{\text{ET}}[\text{MBA}])^{-1}$ ;  $\tau_2 = (k_{\text{PT}} + ^3k_{\text{b-ET}})^{-1}$ ;  $\tau_3 = (k_{\text{prod}})^{-1}$ . For  $[\text{MBA}] = 0 \text{ mM}$ :  $\tau_1 = (k_{\text{b-ISC}})^{-1} = (7.7 \times 10^5 \text{ s}^{-1})^{-1}$

[MBA]/mM	$\tau_1/\mu\text{s}$	$^3k_{\text{ET}}/\text{M}^{-1} \text{ s}^{-1}$	$\tau_2/\mu\text{s}$	$\tau_3/\mu\text{s}$
0	1.3	—	—	—
2	1.2	$3.2 \times 10^7$	—	—
20	0.92	$1.6 \times 10^7$	4.1	$\gg 10$
50	0.70	$1.3 \times 10^7$	5.5	$\gg 10$
100	0.57	$0.99 \times 10^7$	6.3	$\gg 10$
200	0.31	$1.2 \times 10^7$	8.0	$\gg 10$
500	0.09	$2.1 \times 10^7$	11	$\gg 10$

triplet state decays with a total rate constant  $k_1$ . A fraction  $\alpha$  of this decays into the radical anion  $\text{RFTA}\cdot^-$ , whereas a fraction  $(1 - \alpha)$  decays back to the ground state. Similarly, the total decay of  $\text{RFTA}\cdot^-$  occurs with rate constant  $k_2$  with a fraction  $\beta$  forming the neutral radical  $\text{RFTA}\cdot\text{H}^+$  and a fraction  $(1 - \beta)$  falling back to the ground state. The decay associated difference spectra DADS<sub>1</sub>, DADS<sub>2</sub>, and DADS<sub>3</sub> (see Fig. 5) corresponding to the three rate constants  $k_1$ ,  $k_2$ , and  $k_3 \approx 0$  are then

expressed in terms of the species associated difference spectra  $SADS_{\text{triplet}}$ ,  $SADS_{\text{neutral radical}}$  and  $SADS_{\text{radical anion}}$  by:

$$DADS_1 = SADS_{\text{triplet}} + \frac{\alpha}{k_1 - k_2} (k_2 \beta \cdot SADS_{\text{neutral radical}} - k_1 \cdot SADS_{\text{radical anion}})$$

$$DADS_2 = \frac{\alpha k_1}{k_1 - k_2} (SADS_{\text{radical anion}} - \beta \cdot SADS_{\text{neutral radical}})$$

$$DADS_3 = \alpha \beta \cdot SADS_{\text{neutral radical}} \quad (8)$$

This system of linear equations can be inverted to yield the SADS but the inversion requires knowledge of the fractions  $\alpha$  and  $\beta$ , which cannot be determined by a fit to the data:

$$\begin{aligned} SADS_{\text{triplet}} &= DADS_1 + DADS_2 + DADS_3 \\ SADS_{\text{radical anion}} &= (DADS_3 + DADS_2 (1 - k_2/k_1))/\alpha \\ SADS_{\text{neutral anion}} &= DADS_3/(\alpha\beta) \end{aligned} \quad (9)$$

The fraction  $\alpha$ , however, can be calculated from the total decay rate constants of the triplet in the absence ( $k_0$ ) and in the presence ( $k_1$ ) of MBA as  $\alpha = 1 - k_0/k_1$ . For an MBA concentration of 50 mM we find  $\alpha = 0.46$ . The fraction  $\beta$  only enters in the expression for  $S_{\text{neutral radical}}$  as a scaling parameter. The true species associated spectra (SAS) can be obtained from the SADS by adding the ground state spectrum in an appropriate amount depending on the excitation conditions. Fig. 6 shows the SAS of the three intermediate flavin states obtained from the data at 50 mM MBA and assuming  $\beta = 0.3$ . The SAS are in very good agreement with previously reported absorption spectra of flavin in the triplet state, the semi-quinone radical anion and the protonated neutral radical state.<sup>43</sup>

The proposed sequential electron and proton transfer is also confirmed by experiments at different pH values. Under acidic conditions (addition of 1 mM HCl to the sample solution), we observed no radical anion anymore, but immediately ( $\Delta t \approx 50$  ns) the formation of the neutral radical out of the triplet state. In contrast, under alkaline conditions (addition of 1 mM NaOH to the sample solution) no neutral radical could be seen, but only the radical anion form of RFTA.

In our experiments we cannot yet observe the final step of the reaction yielding the fully reduced flavin and the MB-aldehyde. The required hydrogen atom transfer or disproportionation reactions likely occur on slower timescales up to the ms regime.<sup>63</sup>

### 3.5 Mechanism of the photocatalytic MBA oxidation

From the spectroscopic studies on the various timescales we can compile a detailed scheme of the photooxidation mechanism of MBA in the presence of RFTA (Fig. 7). The rapid, non-productive forward and back-ET from the singlet state of flavin is opposed by the productive stepwise redox reaction involving the triplet state of flavin. The complete picture is confirmed by the non-trivial dependence of the reaction quantum yield (QY) on the substrate concentration shown in Fig. 8. The relative QY for the various concentrations was measured by illumination with a high power LED, the absolute

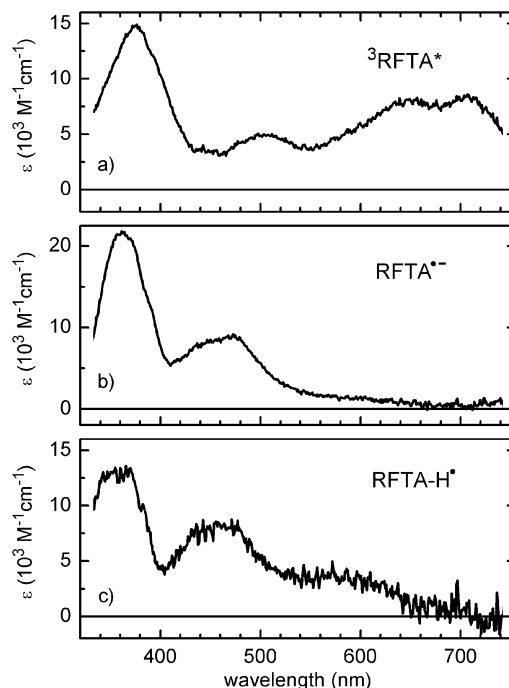


**Fig. 6** Species Associated Spectra (SAS) resulting from the proposed model using the Decay Associated Difference Spectra (DADS) from the global fit analysis. The used parameters were:  $\alpha = 0.46$ ,  $\beta = 0.3$  and  $SAS_{\text{ground state}} = 0.3 S_0$  as the fraction of ground state which was added.

QY by subsequent gas chromatographic detection of the chemical conversion.<sup>20</sup> For a productive singlet channel, one would expect that the QY increases monotonically with the MBA concentration and reaches a constant value at some point.<sup>6–8</sup> However, we find a completely different behavior with a maximum QY of 3% at 25 mM MBA. For both lower and higher MBA concentrations we observe a significant drop of the QY. This can be well understood with our model. At high MBA concentrations, the required ISC to <sup>3</sup>RFTA cannot occur due to fast and non-productive  $S_1$  quenching by MBA. At concentrations below 25 mM, the diffusional approach of MBA and RFTA is becoming slow compared to the intrinsic triplet lifetime. Thus, a balance of the diffusion timescale—*via* the MBA concentration—and the ISC rate is necessary in order to have an encounter of the reactants at the right time: when RFTA is not in the singlet state any more but has not yet relaxed from the triplet state either.

To model quantitatively the dependence of the reaction quantum yield  $\Phi_{\text{tot}}$  on the MBA concentration we use the fit results from the spectroscopic experiments to deduce the QYs of the individual productive steps, *i.e.* intersystem crossing, electron transfer and proton transfer:

$$\begin{aligned} \Phi_{\text{tot}} &\leq \Phi_{\text{ISC}} \Phi_{\text{ET}} \Phi_{\text{PT}} \\ &\leq \frac{k_{\text{ISC}}}{\tau_{\text{T}}^{-1} + k_{\text{ET}}[\text{MBA}]} \frac{k_{\text{ET}}[\text{MBA}]}{k_{\text{ET}}[\text{MBA}] + k_{\text{b-ISC}} k_{\text{b-ET}} + k_{\text{PT}}} \end{aligned} \quad (10)$$

The less than or equal sign in eqn (10) refers to the fact that the last step of the reaction, which at the moment lies beyond our

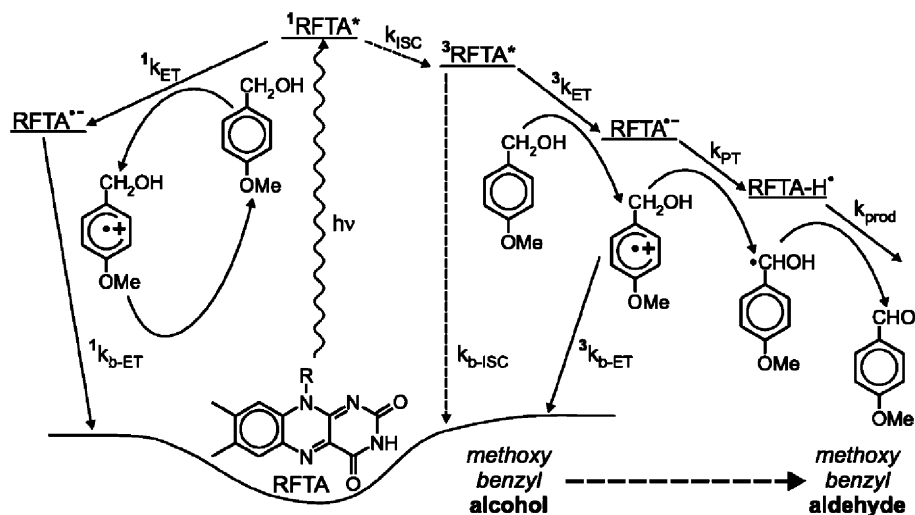


**Fig. 7** Scheme of the oxidation mechanism of MBA. The non-productive singlet channel (left hand side) brings the excited RFTA back to the ground state after diffusion controlled electron transfer from MBA ( $^1k_{ET}$ ) and fast charge recombination ( $^1k_{b-ET}$ ). The encounter of MBA with a triplet flavin (right hand side) can eventually lead to product formation *via* a sequence of electron and proton transfer events. Details see text.

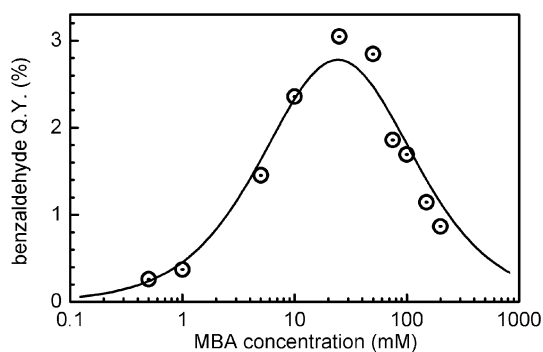


**Fig. 8** Circles: Quantum yield of benzaldehyde production in MeCN/ $H_2O$  (50 : 50, v/v) solution. Solid line: Simulation using the spectroscopically determined reaction rates.

spectroscopically accessible timescale, could further reduce the total QY. The QYs of intersystem crossing  $\Phi_{ISC}$  and electron transfer in the triplet state  $\Phi_{ET}$  depend on the following known rates:

$(\tau_n)^{-1} = (6.0 \text{ ns})^{-1} = 1.7 \times 10^8 \text{ s}^{-1}$  (from a TCSPC measurement of the  $^1RFTA^*$  fluorescence)

$^1k_{ET} = 1.3 \times 10^{10} \text{ M}^{-1} \text{ s}^{-1}$  (from a linear fit to  $\tau_{n,eff}$  at different MBA concentrations)

$^3k_{ET} = 1.7 \times 10^7 \text{ M}^{-1} \text{ s}^{-1}$  (from the  $\mu\text{s}$  decay dynamics at different MBA concentrations)

$k_{b-ISC} = 7.7 \times 10^5 \text{ s}^{-1}$  (from the decay of  $^3RFTA^*$  in the absence of MBA)

The QY of proton transfer  $\Phi_{PT}$  corresponds to the parameter  $\beta = 0.3$  that was used to obtain the SAS (see Section 3.4). Thus,  $k_{ISC}$  is the only free parameter that is not *a priori* known from the spectroscopic analysis. Since it only affects the amplitude of the QY function, the course of  $\Phi_{tot}$  vs. MBA is fixed by the known parameters listed above. As shown in Fig. 8, the derived model (solid line) agrees very well with the measured QYs (circles). This confirms qualitatively and quantitatively the triplet reaction mechanism shown in Fig. 7.

From a least-square fit to the experimental QY data we obtain  $k_{ISC} \geq 1.3 \times 10^8 \text{ s}^{-1}$ . This corresponds to an intrinsic triplet yield of RFTA of 76% in the absence of MBA, which is among the highest values reported for other flavin compounds.<sup>22,37,39</sup> This implies that almost no losses occur in the photooxidation reaction after the first proton transfer step.

For the MeCN/DMSO solvent, *i.e.* in the absence of water, we reported a nearly hundred times lower reaction quantum yield.<sup>20</sup> In the light of the present discussion, we could interpret this as a dramatically reduced probability for proton transfer. It does not seem unlikely that the RFTA radical anion and the MBA radical cation separate by a few solvent molecules between their generation and the proton transfer. In the aqueous environment the hydrogen bond network could still give a good transfer yield, whereas the absence of proton mediators would make this step much more inefficient. One could even speculate that an increased MBA concentration leads to rather far reaching disturbance of the hydrogen network<sup>64</sup> and thereby explains the observed decrease of the proton transfer rate with the rising MBA concentration.

#### 4. Conclusion and outlook

In this work we investigated the flavin-catalyzed photooxidation mechanism of MBA with transient absorption spectroscopy on a timescale ranging from sub-picoseconds to tens of microseconds. The results show that the productive reaction proceeds *via* the triplet state of RFTA and starts with a sequence of an electron and a proton transfer step from MBA to RFTA within 0.1 to 10  $\mu\text{s}$ . In contrast, electron transfer to the singlet excited state of RFTA leads to rapid charge recombination within 50 ps and therefore constitutes a loss channel. Its relevance increases with substrate concentration since diffusion then allows for an encounter of MBA and the excited RFTA before ISC has occurred. In addition, we find a considerable contribution from preassociated RFTA–MBA-aggregates for high MBA concentrations of several 100 mM that also undergo a fast and unproductive



charge separation and recombination cycle. Thus, at high substrate concentrations and especially in pure MBA solution, no significant product formation is observed.

However, if the first ET proceeds after the ISC of RFTA, the charge recombination in the spin correlated radical ion pair is spin forbidden and therefore significantly slowed down.<sup>65</sup> This allows for a higher efficiency of the second reaction step, *i.e.* the proton transfer from  $\text{MBA}^{\bullet+}$  to  $\text{RFTA}^{\bullet-}$ . For a high product QY, the average distance between MBA and RFTA has to be large enough to prevent the likely diffusional encounter within the singlet state lifetime of RFTA which can be achieved by using lower substrate concentrations.

The detailed mechanistic study reveals that the design of a photocatalyst based on the assumption of close proximity of the redox active chromophore and the substrate binding site is not valid for flavins. Instead, other approaches are conceivable to obtain new photocatalysts with improved performance. One possibility is to try to increase the triplet yield by acceleration of the ISC. This might be achieved by exploiting the heavy atom effect through suitable substitution on the flavin chromophore, for instance with sulfur containing groups.<sup>66</sup> Additional substitution of flavin with bulky side chains might impede the aggregation with the substrate by steric hindrance. This would also lead to a higher fraction of excited flavin molecules that can access the triplet state. Another possibility is to use triplet sensitizers<sup>67</sup> that undergo rapid ISC and then transfer their triplet energy to flavin. Thus, the singlet loss channel could be completely circumvented, however with the likely drawback of a higher excitation energy, *i.e.* with the need for UV illumination instead of the desired visible light for the photocatalysis. Performance of the reaction under anaerobic conditions seems tempting, since it would prolong the triplet lifetime. However, oxygen is needed for the reoxidation of RFTA to restore the catalyst. A nearly anaerobic situation might increase the QY at low MBA concentrations, but it would only allow for a very slow overall chemical conversion.

A more promising approach might be to work at high substrate concentrations and render the singlet channel productive. This implies the inhibition of the unproductive back-ET and/or the acceleration of the further productive reaction steps. A concept for this can be found in the general architecture of natural proteins that are involved in redox reactions.<sup>68</sup> There, one frequently finds multiple redox centers in close proximity to each other. By efficient separation of the induced charges along a chain of reaction centers, the charge recombination as well as other deactivation pathways is outpaced. For the flavin photocatalysis, this could imply the attachment of an intermediate electron acceptor unit to the chromophore that also acts as a substrate binding site. After the initial electron transfer from MBA to the intermediate redox center, the negative charge could then be transferred to the flavin. This might slow down the unproductive back electron transfer in favor of subsequent proton and electron transfer events from MBA to the catalyst. Indeed, ten times higher product quantum yields up to 40% were found for the photooxidation of benzylic alcohol using a flavin compound with a covalently linked zinc(II)-cyclen binding site.<sup>17</sup> Further investigations on the details of the reaction mechanism with

this catalyst are needed, as well as an improvement of its photostability. However, the insights from the reaction mechanism of RFTA with MBA described in this work encourage further research along this line to reach higher efficiencies for photocatalytic chemical conversions.

## Acknowledgements

We thank the Deutsche Forschungsgemeinschaft (GRK 1626, SFB 749 and GRK 640) for support of our research. We gratefully acknowledge financial support from the International Max Planck Research School on Advanced Photon Science (U.M.). Discussions with B. Fingerhut and C. F. Sailer were stimulating.

## References

- 1 *Flavins: Photochemistry and Photobiology*, ed. E. Silva and A. M. Edwards, Royal Society of Chemistry, Cambridge, 2006.
- 2 W. Tong, H. P. Ye, H. H. Zhu and V. T. D'Souza, *THEOCHEM*, 1995, **333**, 19–27.
- 3 Y. Yano, *Rev. Heteroat. Chem.*, 2000, **22**, 151–179.
- 4 S. Shinkai, K. Kameoka, K. Ueda, O. Manabe and M. Onishi, *Bioorg. Chem.*, 1987, **15**, 269–282.
- 5 S. Shinkai, K. Kameoka, K. Ueda and O. Manabe, *J. Am. Chem. Soc.*, 1987, **109**, 923–924.
- 6 S. Fukuzumi, S. Kuroda and T. Tanaka, *J. Am. Chem. Soc.*, 1985, **107**, 3020–3027.
- 7 S. Fukuzumi and S. Kuroda, *Res. Chem. Intermed.*, 1999, **25**, 789–811.
- 8 S. Fukuzumi, K. Yasui, T. Suenobu, K. Ohkubo, M. Fujitsuka and O. Ito, *J. Phys. Chem. A*, 2001, **105**, 10501–10510.
- 9 E. Silva, A. M. Edwards and D. Pacheco, *J. Nutr. Biochem.*, 1999, **10**, 181–185.
- 10 A. Mees, C. Behrens, A. Schwöglger, M. Ober and T. Carell, *Eur. J. Org. Chem.*, 2003, 2670–2677.
- 11 J. Svoboda, H. Schmaderer and B. König, *Chem.–Eur. J.*, 2008, **14**, 1854–1865.
- 12 H. Schmaderer, P. Hilgers, R. Lechner and B. König, *Adv. Synth. Catal.*, 2009, **351**, 163–174.
- 13 S. Shinkai, G. X. He, T. Matsuda, A. D. Hamilton and H. S. Rosenzweig, *Tetrahedron Lett.*, 1989, **30**, 5895–5898.
- 14 B. König, M. Pelka, R. Reichenbach-Klinke, J. Schelter and J. Daub, *Eur. J. Org. Chem.*, 2001, 2297–2303.
- 15 M. Gray, A. J. Goodman, J. B. Carroll, K. Bardson, M. Markey, G. Cooke and V. M. Rotello, *Org. Lett.*, 2004, **6**, 385–388.
- 16 A. S. F. Boyd, J. B. Carroll, G. Cooke, J. F. Garety, B. J. Jordan, S. Mabruk, G. Rosair and V. M. Rotello, *Chem. Commun.*, 2005, 2468–2470.
- 17 R. Cibulka, R. Vasold and B. König, *Chem.–Eur. J.*, 2004, **10**, 6223–6231.
- 18 R. Lechner and B. König, *Synthesis*, 2010, 1712–1718.
- 19 J. Svoboda and B. König, *Chem. Rev.*, 2006, **106**, 5413–5430.
- 20 U. Megerle, R. Lechner, B. König and E. Riedle, *Photochem. Photobiol. Sci.*, 2010, **9**, 1400–1406.
- 21 R. Kuhn, P. Gyorgy and T. Wagner-Jauregg, *Ber. Dtsch. Chem. Ges. B*, 1933, **66**, 576–580.
- 22 P. F. Heelis, *Chem. Soc. Rev.*, 1982, **11**, 15–39.
- 23 R. J. Stanley and A. W. MacFarlane, *J. Phys. Chem. A*, 2000, **104**, 6899–6906.
- 24 C. Y. Lu, G. Bucher and W. Sander, *ChemPhysChem*, 2004, **5**, 47–56.
- 25 Y. T. Kao, C. Saxena, T. F. He, L. J. Guo, L. J. Wang, A. Sancar and D. P. Zhong, *J. Am. Chem. Soc.*, 2008, **130**, 13132–13139.
- 26 A. Weigel, A. L. Dobryakov, M. Veiga and J. L. P. Lustres, *J. Phys. Chem. A*, 2008, **112**, 12054–12065.
- 27 C. Aubert, M. H. Vos, P. Mathis, A. P. M. Eker and K. Brettel, *Nature*, 2000, **405**, 586–590.
- 28 D. P. Zhong and A. H. Zewail, *Proc. Natl. Acad. Sci. U. S. A.*, 2001, **98**, 11867–11872.

- 29 T. Kottke, J. Heberle, D. Hehn, B. Dick and P. Hegemann, *Biophys. J.*, 2003, **84**, 1192–1201.
- 30 M. Gauden, I. H. M. van Stokkum, J. M. Key, D. C. Lührs, R. Van Grondelle, P. Hegemann and J. T. M. Kennis, *Proc. Natl. Acad. Sci. U. S. A.*, 2006, **103**, 10895–10900.
- 31 A. Lukacs, A. P. M. Eker, M. Byrdin, K. Brettel and M. H. Vos, *J. Am. Chem. Soc.*, 2008, **130**, 14394–14395.
- 32 T. Langenbacher, D. Immeln, B. Dick and T. Kottke, *J. Am. Chem. Soc.*, 2009, **131**, 14274–14280.
- 33 K. Lanzl, M. von Sanden-Flohe, R. J. Kutta and B. Dick, *Phys. Chem. Chem. Phys.*, 2010, **12**, 6594–6604.
- 34 C. B. Martin, M. L. Tsao, C. M. Hadad and M. S. Platz, *J. Am. Chem. Soc.*, 2002, **124**, 7226–7234.
- 35 C. Neiss, P. Saalfrank, M. Parac and S. Grimme, *J. Phys. Chem. A*, 2003, **107**, 140–147.
- 36 E. Sikorska, I. Khmelinskii, A. Komasa, J. Koput, L. F. V. Ferreira, J. R. Herance, J. L. Bourdelande, S. L. Williams, D. R. Worrall, M. Insińska-Rak and M. Sikorski, *Chem. Phys.*, 2005, **314**, 239–247.
- 37 M. Insińska-Rak, E. Sikorska, J. L. Bourdelande, I. V. Khmelinskii, W. Prukała, K. Dobek, J. Karolczak, I. F. Machado, L. F. V. Ferreira, A. Komasa, D. R. Worrall and M. Sikorski, *J. Mol. Struct.*, 2006, **783**, 184–190.
- 38 K. Sadeghian, M. Bocola and M. Schütz, *J. Am. Chem. Soc.*, 2008, **130**, 12501–12513.
- 39 S. Salzmann, J. Tatchen and C. M. Marian, *J. Photochem. Photobiol., A*, 2008, **198**, 221–231.
- 40 S. Salzmann and C. M. Marian, *Photochem. Photobiol. Sci.*, 2009, **8**, 1655–1666.
- 41 G. Angulo, G. Grampp and A. Rosspeintner, *Spectrochim. Acta, Part A*, 2006, **65**, 727–731.
- 42 U. Megerle, I. Pugliesi, C. Schriever, C. F. Sailer and E. Riedle, *Appl. Phys. B: Lasers Opt.*, 2009, **96**, 215–231.
- 43 M. Sakai and H. Takahashi, *J. Mol. Struct.*, 1996, **379**, 9–18.
- 44 E. Baciocchi, M. Bietti, L. Putignani and S. Steenken, *J. Am. Chem. Soc.*, 1996, **118**, 5952–5960.
- 45 M. Bietti, E. Baciocchi and S. Steenken, *J. Phys. Chem. A*, 1998, **102**, 7337–7342.
- 46 E. Baciocchi, M. Bietti and S. Steenken, *Chem.–Eur. J.*, 1999, **5**, 1785–1793.
- 47 S. D. M. Islam, A. Penzkofer and P. Hegemann, *Chem. Phys.*, 2003, **291**, 97–114.
- 48 C. Reichardt, *Solvents and Solvent Effects in Organic Chemistry*, Wiley-VCH, Weinheim, 3rd edn, 2004.
- 49 S. A. Rice, *Diffusion-limited reactions*, Elsevier Science Publishers B.V., Amsterdam, 1985.
- 50 J. R. Lakowicz, *Principles of fluorescence spectroscopy*, Springer Science + Business Media, New York, 3rd edn, 2006.
- 51 J. H. Dymond, M. A. Awan, N. F. Glen and J. D. Isdale, *Int. J. Thermophys.*, 1991, **12**, 443–477.
- 52 S. G. Ballard and D. C. Mauzerall, *J. Chem. Phys.*, 1980, **72**, 933–947.
- 53 X. Allonas, P. Jacques, A. Accary, M. Kessler and F. Heisel, *J. Fluoresc.*, 2000, **10**, 237–245.
- 54 P. Sreearunothai, S. Asaoka, A. R. Cook and J. R. Miller, *J. Phys. Chem. A*, 2009, **113**, 2786–2795.
- 55 S. Pant, H. Ohtaka-Saiki, M. Takezaki, A. D. Scully, S. Hirayama and T. Tominaga, *J. Phys. Chem. A*, 2008, **112**, 5378–5384.
- 56 M. S. Cubberley and B. L. Iverson, *J. Am. Chem. Soc.*, 2001, **123**, 7560–7563.
- 57 M. N. Berberan-Santos, E. N. Bodunov and B. Valeur, *Chem. Phys.*, 2005, **315**, 171–182.
- 58 T. B. Melø, M. A. Ionescu, G. W. Haggquist and K. R. Naqvi, *Spectrochim. Acta, Part A*, 1999, **55**, 2299–2307.
- 59 C. B. Martin, X. F. Shi, M. L. Tsao, D. Karweik, J. Brooke, C. M. Hadad and M. S. Platz, *J. Phys. Chem. B*, 2002, **106**, 10263–10271.
- 60 B. Branchi, M. Bietti, G. Ercolani, M. A. Izquierdo, M. A. Miranda and L. Stella, *J. Org. Chem.*, 2004, **69**, 8874–8885.
- 61 E. Baciocchi, M. Bietti and S. Steenken, *J. Am. Chem. Soc.*, 1997, **119**, 4078–4079.
- 62 F. Müller, M. Brüstlein, P. Hemmerich, V. Massey and W. H. Walker, *Eur. J. Biochem.*, 1972, **25**, 573–580.
- 63 P. F. Heelis, B. J. Parsons, G. O. Phillips and J. F. McKellar, *Photochem. Photobiol.*, 1981, **33**, 7–13.
- 64 M. Heyden, E. Bründermann, U. Heugen, G. Niehues, D. M. Leitner and M. Havenith, *J. Am. Chem. Soc.*, 2008, **130**, 5773–5779.
- 65 J. W. Verhoeven, *J. Photochem. Photobiol., C*, 2006, **7**, 40–60.
- 66 P. Drössler, W. Holzer, A. Penzkofer and P. Hegemann, *Chem. Phys.*, 2003, **286**, 409–420.
- 67 L. Hviid, W. G. Bouwman, M. N. Paddon-Row, H. J. van Ramesdonk, J. W. Verhoeven and A. M. Brouwer, *Photochem. Photobiol. Sci.*, 2003, **2**, 995–1001.
- 68 C. C. Page, C. C. Moser, X. X. Chen and P. L. Dutton, *Nature*, 1999, **402**, 47–52.

## **Appendix A7**

### **Flavin-induced DNA photooxidation and charge movement probed by ultrafast transient absorption spectroscopy**

*M. Wenninger, D. Fazio, U. Megerle, C. Trindler, S. Schiesser,  
E. Riedle, T. Carell*

ChemBioChem 12, 703-706 (2011)

For copyright reasons, the article is appended in the pre-peer reviewed version.



DOI: 10.1002/cbic.201000730

## Flavin-induced DNA Photooxidation and Charge Movement Probed by Ultrafast Transient Absorption Spectroscopy

Matthias Wenninger, <sup>\*,[a]</sup> Danila Fazio, <sup>\*,[b]</sup> Uwe Megerle, <sup>[a]</sup> Christian Trindler, <sup>[b]</sup> Stefan Schiesser, <sup>[b]</sup> Eberhard Riedle, <sup>[a]</sup> and Thomas Carell <sup>[b]</sup>

Charge transfer processes through DNA have been intensively investigated over the last years using a variety of methods and model systems.<sup>[1-6]</sup> It is now well established that a positive charge moves through the duplex via a hopping mechanism using the purin bases and here particularly dG as stepping stones.<sup>[7]</sup> Under ideal conditions a positive charge can hop over more than 200 bp before it is trapped.<sup>[8]</sup> An excess electron in contrast, which introduces a negative charge into the duplex, hops through the double strand only over about 10-20 bp and in this case the pyrimidine base acts as stepping stones.<sup>[9-16]</sup>

In nature FAD and FMN cofactors, in the oxidized state, are known to photooxidize duplex DNA, which leads to severe oxidative DNA damage particularly at guanine sites.<sup>[17-18]</sup> The fact that UV-A or visible light causes mutations,<sup>[19]</sup> even though DNA features no absorption in this wavelength region, is thought to be caused by such flavin cofactor mediated DNA photooxidation processes.<sup>[20]</sup>

Detailed information on the dynamics and lifetime of flavin dependent photooxidation of DNA as the basis for UV-A photo-carcinogenesis, can be obtained from ultrafast UV/Vis spectroscopy.<sup>[21]</sup> We therefore synthesized and investigated a series of DNA hairpins to gain insight into the flavin triggered photooxidation of selected DNA sequences. For the study the DNA hairpins depicted in Figure 1 were prepared, which all feature the flavin derivative **1** as a capping structure stacking on top of the hairpins.<sup>[22]</sup>

---

[\*] *These authors contributed equally to this work.*

[a] Fakultät für Physik, Lehrstuhl für BioMolekulare Optik  
Ludwigs-Maximilians-Universität München  
Oettingenstraße 67, 80538 München (Germany)

[b] Department of Chemistry and Biochemistry  
Ludwigs-Maximilians-Universität München  
Butenandtstraße 5-13, 81377 München (Germany), Fax: (+49) 89-2189-77756  
E-Mail: [thomas.carell@cup.uni-muenchen.de](mailto:thomas.carell@cup.uni-muenchen.de)

Supporting information for this article is available on the WWW under <http://www.chembiochem.org> or from the authors.

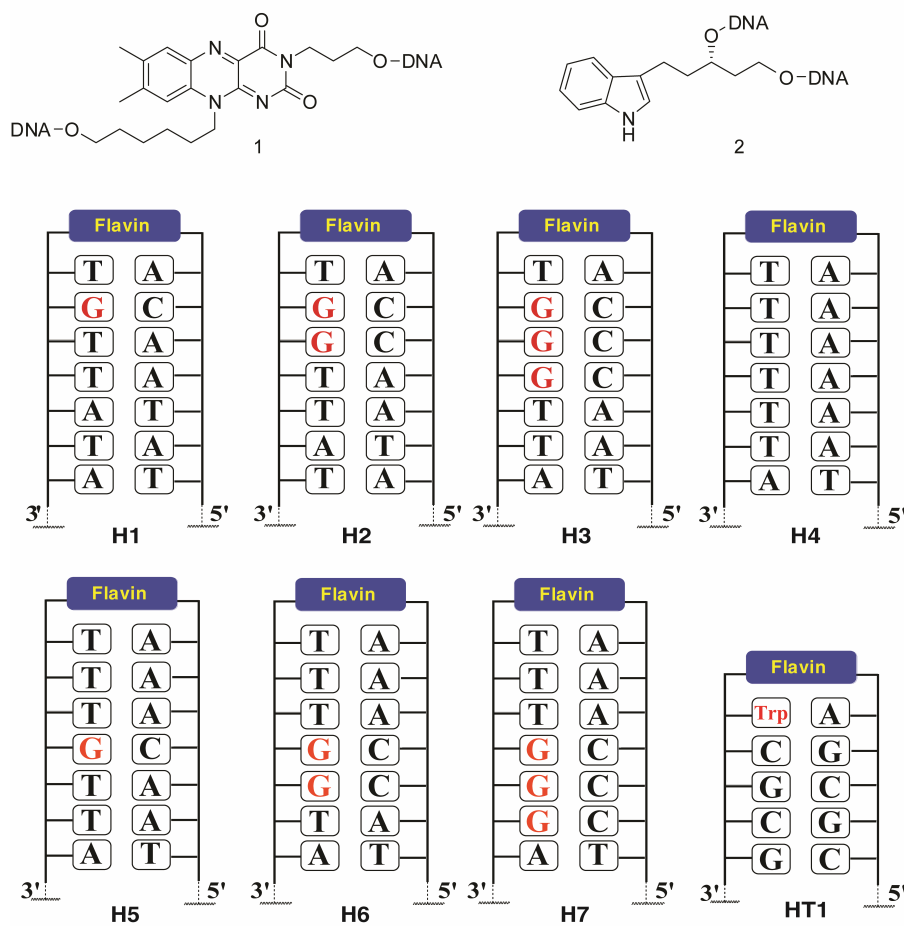


**Figure 1.** Structures of DNA hairpins **H1** - **H7**. Flavin derivative used as cap (**1**); tryptophan derivative **2** introduced into hairpin **HT1**.

Melting point measurements were performed to ensure that the hairpins (**H1-H7**, **HT1**) are fully closed at room temperature (SI). CD spectra show that the hairpins adopt a B-type DNA double helix structure (SI). The hairpins feature a strong absorption below 280 nm due to the absorption of the DNA bases. The absorption maxima at 360 nm and 450 nm correspond to flavin transitions and allow the selective excitation of the covalently bound chromophore. The intensity of the flavin fluorescence at 550 nm is sequence dependent.

In the first hairpin series **H1-H3** we introduced one AT base pair between the dG electron donors and the flavin acceptor cap. In addition we used instead of a single dG either a (dG)<sub>2</sub> (**H2**) or even a (dG)<sub>3</sub> (**H3**) sequence as the electron donating unit. It is known that the electron donation capability of adenines<sup>[23-24]</sup> is lower compared to guanines and that for guanines it increases with the number of dG bases in a row.<sup>[25-30]</sup> As a reference duplex we synthesized **H4** containing a flavin cap and no dG base. In comparison to the fluorescence intensity measured for compound **1**, the

fluorescence was found to be quenched in all hairpins. The strongest flavin fluorescence was measured for the reference duplex **H4** but even here, the detected fluorescence is significantly lower than that of the free flavin **1**. This suggests that the oxidation potential of the excited state flavin is high enough to oxidize both dG and dA bases, yielding the flavin radical anion and the dA and dG radical cations.<sup>[31]</sup>

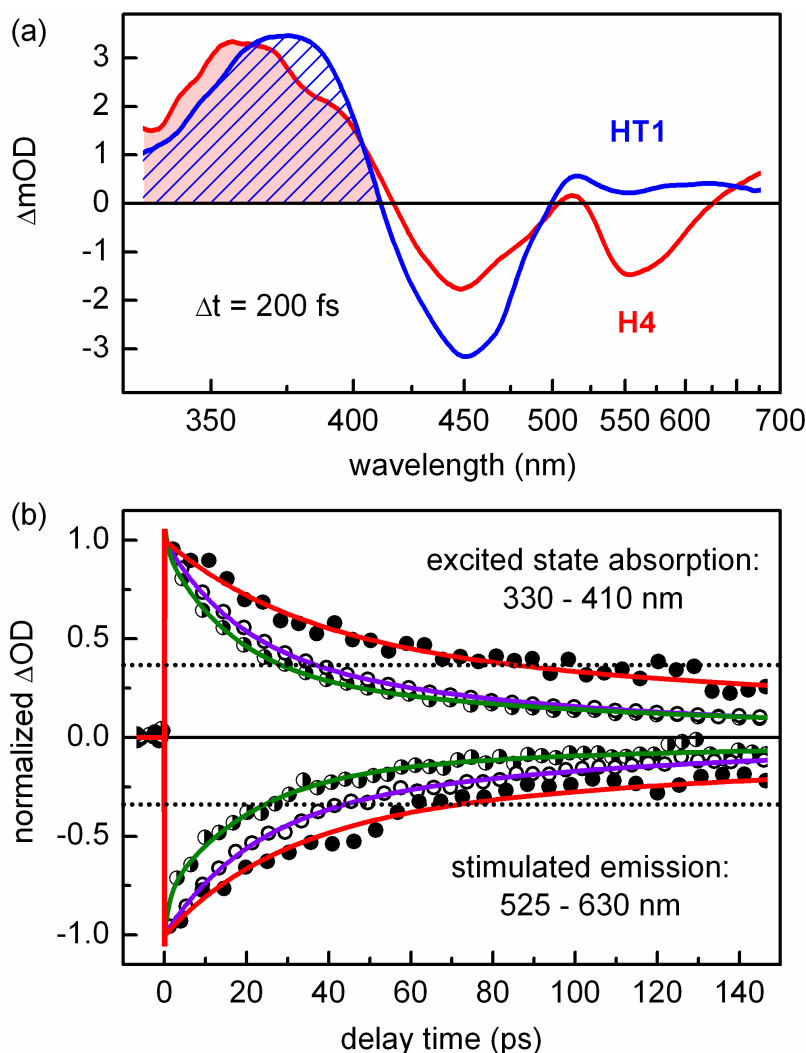


**Figure 2.** (a) Transient absorption spectrum at  $\Delta t = 200$  fs of the hairpins **H4** ( $S_1$  state of flavin) and **HT1** (flavin radical anion). (b) Decay of the transient signal integrated over the spectral region of the excited state absorption (top) and of the stimulated emission (bottom). Red: **H4**; violet: **H1**; green: **H2**; dotted lines:  $1/e$  level of the initial amplitude.

The photoinduced dynamics of the hairpin structures with the flavin cap were measured with a femtosecond broadband pump-probe setup.<sup>[32]</sup> The sample solutions were irradiated with a sub-50 fs pulse at 480 nm to selectively excite the flavin and probed with a white light pulse to obtain the transient absorption in the

spectral region between 300 and 750 nm up to delay times of 1 ns. The transient spectra of all hairpins consist of three major contributions that can be assigned to flavin transitions (Figure 2a). Two bands with negative transient absorption indicate the ground state bleach (around 450 nm) and the stimulated emission (around 550 nm) of the flavin. These bands are partially overlaid with the excited state absorption that contributes a positive absorption change and has a prominent maximum around 370 nm.

For the free flavin compound **1**, the transient signatures decay mono-exponentially with the fluorescence lifetime of  $\tau = 2$  ns (Supporting Information). The decay dynamics of the flavin cap in the hairpin structures are governed by the ultrafast ET from the bases, which quenches the singlet excited state of flavin. The observed dynamics are more complex and require multi-exponential fits.<sup>[33]</sup> Typically, two to three exponential terms and one constant signal lasting beyond the measurement range were necessary for a good parametrization of the data (SI). The complexity of the quenching dynamics prohibits the full and direct interpretation of the obtained time constants. Instead, we use the fit curves to determine the delay times when the signal of the stimulated emission has decayed to  $1/e$  of the initial value at  $\Delta t = 0$ . The  $1/e$  time constants that are compiled in Table 1 are found suitable for a consistent classification of the ET dynamics.

The hairpins **H1-H7** show very similar dynamics, both in the stimulated emission and in the absorption band (see Figure 2b). The first result of this study therefore is that the charge recombination, which proceeds in the Coulomb field established by the  $\text{Fl}^-$  and  $\text{dA}^+/\text{dG}^+$  ions, is faster than the initial forward ET process. In order to measure the hidden charge recombination rate we replaced the electron donating dG unit by a stronger donating tryptophane unit<sup>[34]</sup> We had to insert additional dG:dC base pairs in the stem to ensure proper closing of the hairpin, which we found otherwise too unstable. In the hairpin **HT1**, we measured indeed an extremely fast forward ET within 100 fs allowing us to decipher the rate of charge recombination to about 1 ps. This experiment allowed us in addition to identify the spectral signature of the flavin radical anion (see Figure 2a). The main difference to the flavin  $S_1$  spectrum is the missing stimulated emission around 550 nm. The excited state absorption of the radical around 370 nm is similar in strength but appears slightly red-shifted compared to the  $S_1$  absorption.



**Table 1.** Decay times ( $\tau$ ) of flavin excited state and quantum yields ( $\Phi$ ) for building the long-lived charge separated state (after 1 ns).

Sample	$\tau_{1/e}$ (ps)	$\Phi_{cs}$ (%)
<b>H1</b>	$38 \pm 2$	$< 0.5$
<b>H2</b>	$26 \pm 4$	$< 0.5$
<b>H3</b>	$26 \pm 1$	$< 0.5$
<b>H4</b>	$63 \pm 3$	$< 0.5$
<b>H5</b>	$49 \pm 3$	$3 \pm 1$
<b>H6</b>	$50 \pm 3$	$7 \pm 1$
<b>H7</b>	$52 \pm 3$	$14 \pm 1$
<b>HT1</b>	$0.10 \pm 0.05$	0

In the hairpin structure **H1**, the ET leads to the decay of the flavin excited state on a timescale of 38 ps. If we replace the single dG base by a (dG)<sub>2</sub> or (dG)<sub>3</sub> sequence, the decay time is shorter (26 ps) indicating that the ET is now slightly faster in agreement with the fact that dG bases, stacked in homo-dG sequences, possess a reduced oxidation potential.

In agreement with the steady state fluorescence experiments we observe that the flavin excited singlet state decays even in the dG-free reference hairpin **H4** rather quickly. Here, the electron is donated by the dA base. The time constant for this process is 63 ps, and hence only slightly longer in comparison to the dG containing hairpins (26 ps), showing that dA photooxidation by the excited flavin is only by about a factor of two to three slower.

Due to the short flavin-donor distances we can safely assume that the ET process in the first hairpin series is governed by a direct superexchange based mechanism, in which the charges do not hop over intermediate charge carriers but are directly transferred from the dG nucleobases to the excited flavin and back.<sup>[35-36]</sup> This direct ET based situation changes totally in the hairpin series **H5-H7**, in which a (dA:dT)<sub>3</sub> cassette is situated between the hairpin cap and one, two and three dG electron donors.<sup>[25]</sup> Over the rather large distance of 13.5 Å between the flavin and the first

dG base, electron donation is now dominated by a hopping mechanism.<sup>[35, 37]</sup> We find for all three hairpins identical  $S_1$  decay timescales of 50 ps, not affected by the number of dG bases. We believe that in these systems the charges hop through the spacing dA:dT sequence and that this hopping rate is now governing the rate of flavin photoreduction. The rate of electron donation from the  $(dG)_n$  bases to a putative  $dA^{*+}$  hopping intermediate is clearly slower. The data therefore show that the charge hopping reaction is slower than electron donation from a dG to a close  $dA^{*+}$ .

The  $(dA:dT)_3$  cassette used as a spacer has another important consequence: In the hairpins **H5-H7** we do not observe a complete charge recombination but a partial escape of the injected positive charge. The positive charge in the  $(dA:dT)_3$  cassette hops to the adjacent  $(dG:dC)_n$  cassette. From there, charge recombination is substantially slower because the electron has moved out of the Coulomb field of the flavin radical anion. This process leads to the formation of a long lived charge separated state. Most interestingly, the yield of formation of the charge separated state is influenced by the number of stacking dG bases. To determine the quantum yield of the long-lived charge separation we decomposed the transient absorption spectra at  $\Delta t = 1$  ns into a residual contribution from the flavin  $S_1$  state and the flavin radical anion spectrum known from **HT1**. The integral of the flavin radical signature between 330 nm and 410 nm (Figure 3, shaded area) was used to quantify the quantum yield of the long-lived charge separation. In hairpin **H5** with just one dG electron donor, about 3 % of the flavin is still in the radical anion state at  $\Delta t = 1$  ns. In **H6** with a  $(dG:dC)_2$  sequence the amount has increased to 7 % and in hairpin **H7** possessing a  $(dG:dC)_3$  sequence we even find a fivefold increase to 14 % (Table 1).

In summary, by using short time spectroscopy we were able to decipher the dynamics of flavin-induced photooxidation of DNA, which is one factor contributing to UV-A induced photo-carcinogenesis.<sup>[38-39]</sup> Finally we were able to show that in special sequences long lived charge separated state can be created using the flavin as photooxidant.<sup>[25]</sup> This requires fast forward electron transfer by hopping through dA:dT sequences followed by charge trapping in dG:dC sequences.

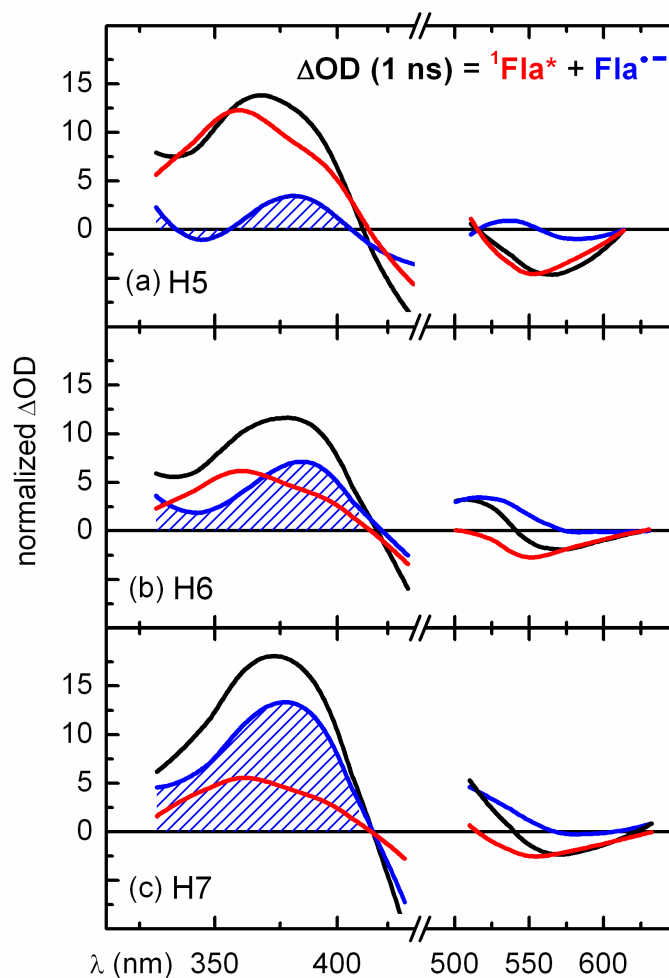


**Figure 3.** Decomposition of the transient absorption spectrum at  $\Delta t = 1$  ns (black line): The residual contribution from the  $S_1$  state of flavin (from  $\Delta t < 200$  fs, red line) is subtracted to obtain the contribution from the long-lived radical anion of flavin (blue line). The spectra have been normalized to the initial amplitude directly after excitation.

## Experimental Section

**DNA synthesis and purification:** The synthesis of the oligonucleotides containing the flavin *H*-phosphonate was performed on an Expedite 8900 DNA synthesizer using a mixed phosphoramidite/ *H*-phosphonate / phosphoramidite coupling protocol. For a full oxidation of the flavin an additional oxidation step was necessary at the end of the synthesis using  $I_2$  in MeCN and *N*-Methylmorpholine in water as first oxidation solution and  $I_2$  in MeCN and  $NEt_3$  in water as the second one. Oligonucleotides were cleaved from the solid support and deprotected using conc. ammonia/ethanol 3:1 for 20 h at room temperature. Analytical and preparative HPLC were performed on  $C_{18}$ -reversed phase columns by Macherey-Nagel and 0.1 M  $NHEt_3OAc$  in water: acetonitrile as eluent. The strands were further characterized by

MALDI-TOF-MS. MALDI spectra were recorded on a Bruker Autoflex mass spectrometer using 3-hydroxypicolinic acid as matrix substance and measuring in negative polarity mode.

**Melting point experiments:** Melting temperature ( $T_m$ ) were measured on a Cary 100 UV/Vis spectrometer using 1 mL quartz cuvettes with 1cm path length. Absorption at 260 nm of equimolar DNA complements (3  $\mu$ M in 150 mM NaCl, 10 mM Tris-HCl, pH 7.4) were measured. For every strand four temperature cycles from 5 °C to 90 °C were recorded, the average melting points are depicted in supporting information.

**CD experiments:** CD spectra were recorded at room temperature on a Jasco J-810 spectropolarimeter equipped with a Peltier temperature controller using 1 mL quartz cuvettes with 1 cm path length. The samples contained 150 mM NaCl, 10 mM Tris-HCl (pH 7.4) and 3  $\mu$ M of the hairpin structures.

**Femtosecond transient absorption:** The femtosecond broadband pump-probe setup has been described in detail elsewhere.<sup>[32]</sup> Briefly, a Ti:sapphire amplifier system (CPA 2001; Clark-MXR) with a repetition rate of 1 kHz was used to pump a noncollinear optical parametric amplifier delivering pump pulses at  $\lambda = 480$  nm with a length of 40 fs. The pump pulses were focused into a 250  $\mu$ m flow cell containing the cooled sample (10 °C) with a spot size of 150  $\mu$ m. The pump energy was limited to < 1  $\mu$ J to avoid nonlinear effects. By focusing another part of the Ti:sapphire laser into a rotating CaF<sub>2</sub> disk a supercontinuum (300 – 750 nm) was generated and used as probe. The polarizations of the pump and probe pulses were set to magic angle (54.7°). After the interaction in the sample, the probe light was dispersed with a fused silica prism and detected with a 512 pixel photodiode array. The chirp of the white light was corrected for prior to data analysis and the resulting temporal resolution was better than 100 fs.

### **Acknowledgements**

*We thank the SFB 749 and the Excellence Cluster NIM (Nano Initiative Munich). M.W. thanks the GRK 1626 Chemical Photocatalysis for a fellowship.*

**Keywords:** Charge transfer · DNA · Flavins · Oxidative damage · Photomutagenesis

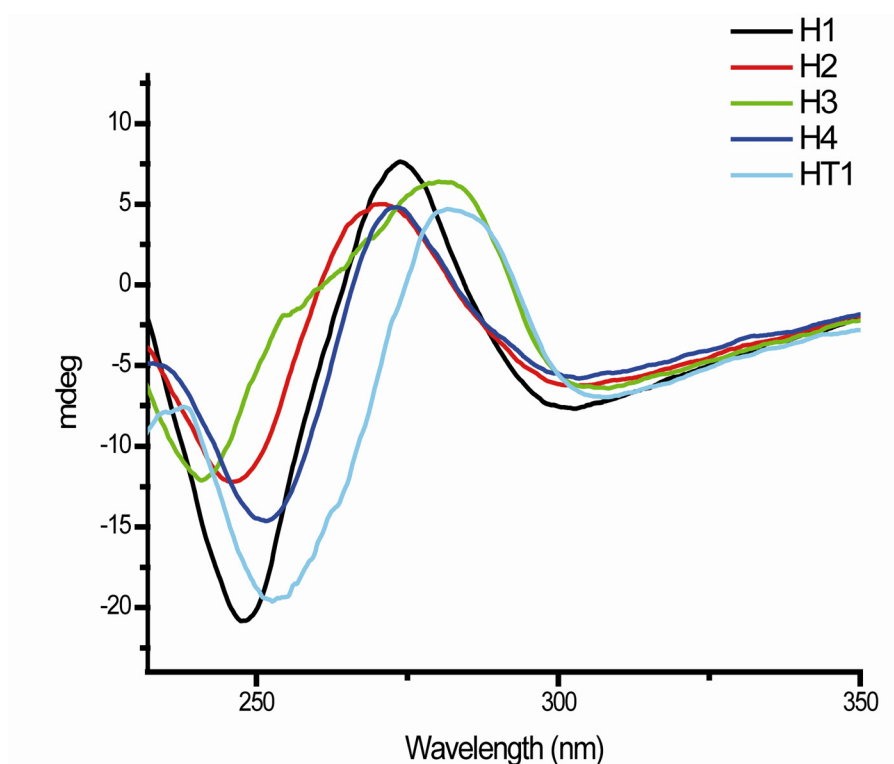
- [1] J. C. Genereux, J. K. Barton, *Chem. Rev.* **2009**, *110*, 1642-1662.
- [2] B. Giese, *Ann. Rev. Biochem.* **2002**, *71*, 51-70.
- [3] G. B. Schuster, *Acc. Chem. Res.* **2000**, *33*, 253-260.
- [4] F. D. Lewis, R. L. Letsinger, M. R. Wasielewski, *Acc. Chem. Res.* **2000**, *34*, 159-170.
- [5] M. Pavanello, L. Adamowicz, M. Volobuyev, B. Mennucci, *J. Phys. Chem. B* **2010**, *114*, 4416-4423.
- [6] T. Takada, M. Fujitsuka, T. Majima, *PNAS* **2007**, *104*, 11179-11183.
- [7] B. Giese, J. Amaudrut, A.-K. Kohler, M. Spormann, S. Wessely, *Nature* **2001**, *412*, 318-320.
- [8] M. E. Núñez, D. B. Hall, J. K. Barton, *Chem. & Biol.* **1999**, *6*, 85-97.
- [9] C. Behrens, T. Carell, *Chem. Comm.* **2003**, 1632-1633.
- [10] S. Breger, U. Hennecke, T. Carell, *J. Am. Chem. Soc.* **2004**, *126*, 1302-1303.
- [11] H. A. Wagenknecht, *Angew. Chem. Int. Ed.* **2003**, *42*, 2454-2460.
- [12] P. Daublain, A. K. Thazhathveetil, Q. Wang, A. Trifonov, T. Fiebig, F. D. Lewis, *J. Am. Chem. Soc.* **2009**, *131*, 16790-16797.
- [13] K. Siegmund, P. Daublain, Q. Wang, A. Trifonov, T. Fiebig, F. D. Lewis, *J. Phys. Chem. B* **2009**, *113*, 16276-16284.
- [14] C. Wagner, H. A. Wagenknecht, *Chem. Eur. J.* **2005**, *11*, 1871-1876.
- [15] T. Ito, S. E. Rokita, *J. Am. Chem. Soc.* **2004**, *126*, 15552-15559.
- [16] C. Behrens, L. T. Burgdorf, A. Schwögler, T. Carell, *Angew. Chem. Int. Ed.* **2002**, *41*, 1763-1766.
- [17] C.-Y. Lu, S.-D. Yao, N.-Y. Lin, *Chem. Phys. Letters* **2000**, *330*, 389-396.
- [18] W. L. Neeley, J. M. Essigmann, *Chem. Res. Toxicol.* **2006**, *19*, 491-505.
- [19] L. D. McGinty, R. G. Fowler, *Mutation Research* **1982**, *95*, 171-181.
- [20] R. B. Webb, M. M. Malina, *Photochem. Photobiol.* **1970**, *12*, 457-468.
- [21] A. Weigel, A. L. Dobryakov, M. Veiga, J. L. Pérez Lustres, *J. Phys. Chem. A* **2008**, *112*, 12054-12065.
- [22] C. Behrens, M. Ober, T. Carell, *Eur. J. Org. Chem.* **2002**, *2002*, 3281-3289.
- [23] K. Kawai, Y. Osakada, M. Fujitsuka, T. Majima, *Chem. Eur. J.* **2008**, *14*, 3721-3726.
- [24] S. Fukuzumi, H. Miyao, K. Ohkubo, T. Suenobu, *J. Phys. Chem. A* **2005**, *109*, 3285-3294.
- [25] K. Kawai, Y. Osakada, T. Takada, M. Fujitsuka, T. Majima, *J. Am. Chem. Soc.* **2004**, *126*, 12843-12846.
- [26] S. Kanvah, J. Joseph, G. B. Schuster, R. N. Barnett, C. L. Cleveland, U. Landman, *Acc. Chem. Res.* **2009**, *43*, 280-287.
- [27] Y. A. Lee, A. Durandin, P. C. Dedon, N. E. Geacintov, V. Shafirovich, *J. Phys. Chem. B* **2008**, *112*, 1834-1844.
- [28] I. Saito, T. Nakamura, K. Nakatani, Y. Yoshioka, K. Yamaguchi, H. Sugiyama, *J. Am. Chem. Soc.* **1998**, *120*, 12686-12687.
- [29] F. D. Lewis, X. Liu, J. Liu, S. E. Miller, R. T. Hayes, M. R. Wasielewski, *Nature* **2000**, *406*, 51-53.
- [30] Y. A. Lee, B. H. Yun, S. K. Kim, Y. Margolin, P. C. Dedon, N. E. Geacintov, V. Shafirovich, *Chem. Eur. J.* **2007**, *13*, 4571-4581.
- [31] C. E. Crespo-Hernández, D. M. Close, L. Gorb, J. Leszczynski, *J. Phys. Chem. B* **2007**, *111*, 5386-5395.
- [32] U. Megerle, I. Pugliesi, C. Schrieber, C. F. Sailer, E. Riedle, *Appl. Phys. B* **2009**, *96*, 215-231.
- [33] F. D. Lewis, T. Wu, Y. Zhang, R. L. Letsinger, S. R. Greenfield, M. R.

- Wasielewski, *Science* **1997**, *277*, 673-676.
- [34] A. Harriman, *J. Phys. Chem.* **1987**, *91*, 6102-6104.
- [35] K. Kawai, T. Takada, T. Nagai, X. Cai, A. Sugimoto, M. Fujitsuka, T. Majima, *J. Am. Chem. Soc.* **2003**, *125*, 16198-16199.
- [36] Frederick D. Lewis, P. Daublain, B. Cohen, J. Vura-Weis, Michael R. Wasielewski, *Angew. Chem. Int. Ed.* **2008**, *47*, 3798-3800.
- [37] K. Kawai, T. Takada, S. Tojo, T. Majima, *J. Am. Chem. Soc.* **2003**, *125*, 6842-6843.
- [38] A. J. Ridley, J. R. Whiteside, T. J. McMillan, S. L. Allinson, *Int. J. Rad. Biol.* **2009**, *85*, 177-195.
- [39] M. C. Skala, K. M. Riching, A. Gendron-Fitzpatrick, J. Eickhoff, K. W. Eliceiri, J. G. White, N. Ramanujam, *PNAS* **2007**, *104*, 19494-19499.

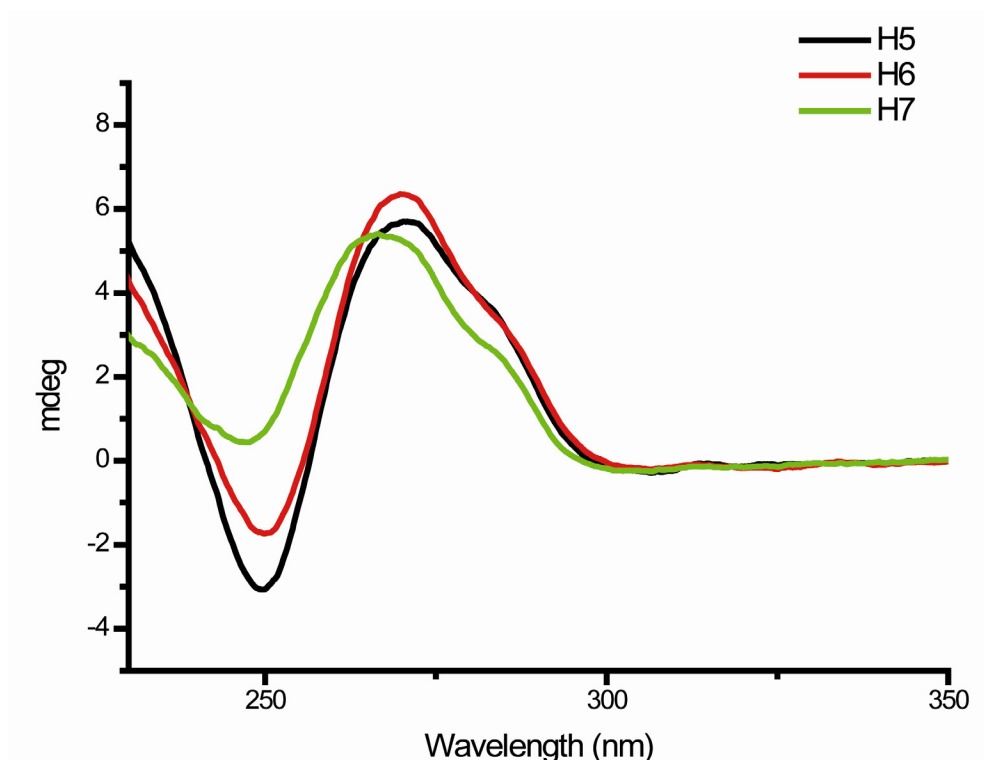
## Supplementary Information

### Flavin-induced DNA Photooxidation and Charge Movement Probed by Ultrafast Transient Absorption Spectroscopy

*Matthias Wenninger, Danila Fazio, Uwe Megerle, Christian Trindler, Stefan Schiesser, Eberhard Riedle and Thomas Carell*



**Supplementary Figure 1.** CD spectra of the investigated DNA hairpins H1, H2, H3, H4, HT1. The minimum at 250 nm and the maximum at 280 nm is indicative of a B-type DNA double helix structure of the hairpin stem [see W. Curtis Johnson Jr, Determination of the Conformation of Nucleic Acids by Electronic CD in Circular Dichroism and the Conformational Analysis of Biomolecules, ed. Gerald D. Fasman, Plenum Press, New York, 1996, pp. 433–468].

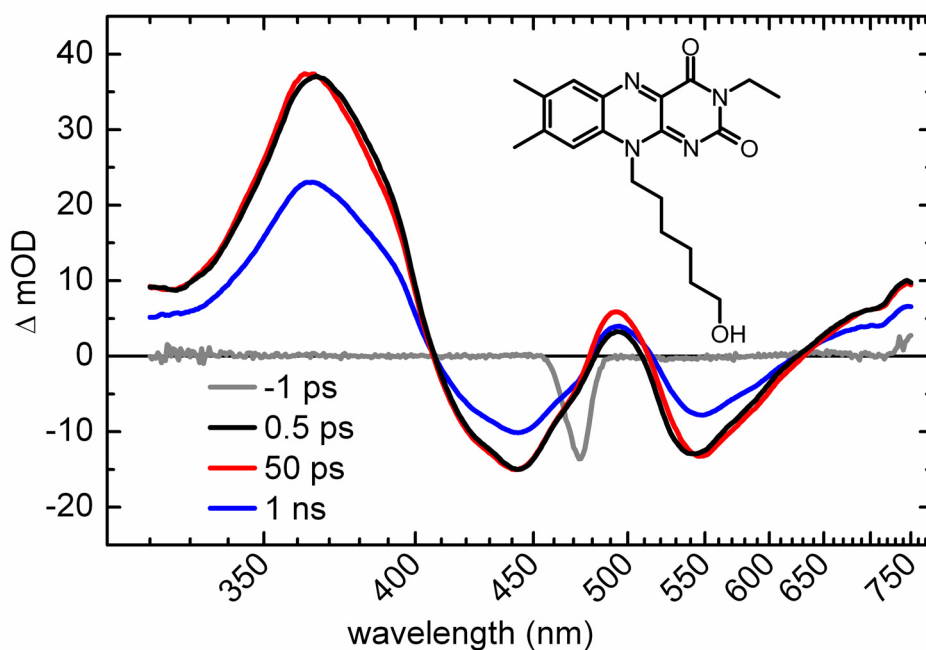


**Supplementary Figure 2.** CD spectra of the investigated DNA hairpins H5, H6, H7. The minimum at 250 nm and the maximum at 280 nm is indicative of a B-type DN double helix structure of the hairpin stem [see W. Curtis Johnson Jr, *Determination of the Conformation of Nucleic Acids by Electronic CD in Circular Dichroism and the Conformational Analysis of Biomolecules*, ed. Gerald D. Fasman, Plenum Press, New York, 1996, pp. 433–468].

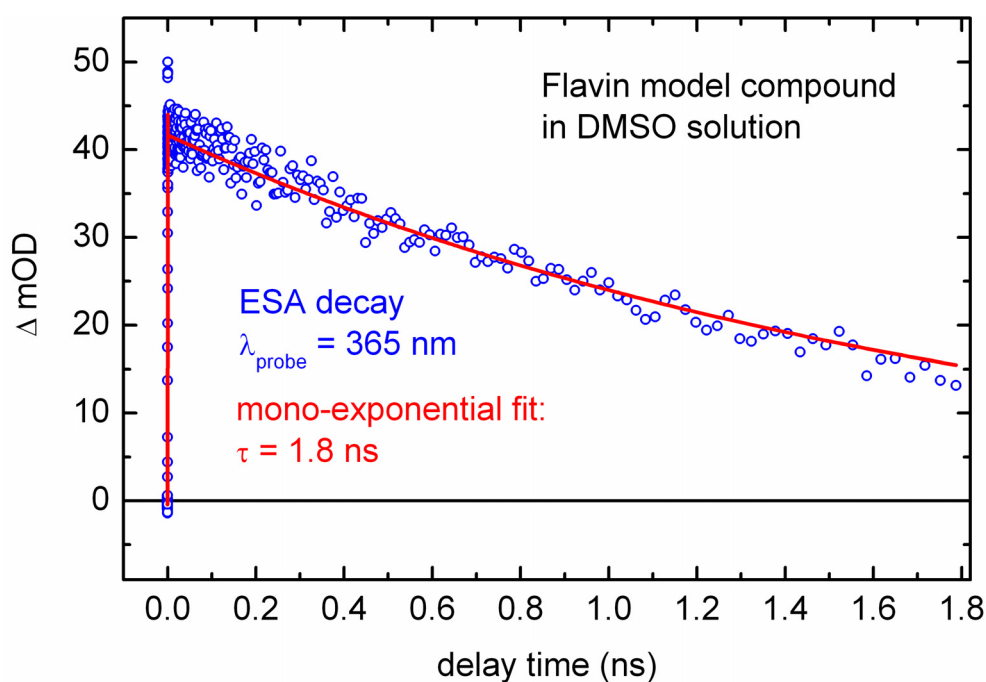
Sample	$T_m$ (°C)
H1	60
H2	65
H3	67
H4	54
H5	60
H6	63
H7	> 90
HT1	> 90

**Supplementary Table 1.** Melting point of the duplexes listed in Figure 1





**Supplementary Figure 3.** Transient absorption spectra of the flavin model compound (inset) dissolved in DMSO after 470 nm excitation. We observe a concerted decay of all signatures on the ns timescale. The stray light peak shown in the trace at  $\Delta t = -1$  ps is corrected for in the other spectra and shows the spectrum of the excitation pulse.



**Supplementary Figure 4.** Decay dynamics of the excited state absorption (365 nm, green circles) and mono-exponential fit (red line). The fits of kinetic traces in the region of the ground state bleach and the stimulated emission yield similar decay times around 2 ns.

	<b>H1</b>		<b>H2</b>		<b>H3</b>		<b>H4</b>	
	A	$\tau$	A	$\tau$	A	$\tau$	A	$\tau$
ESA	3.3	<b>0.6</b>	2.4	<b>0.5</b>	2.0	<b>0.5</b>	--	--
	16.6	<b>22.3</b>	11.8	<b>15.7</b>	8.5	<b>17.0</b>	20.3	<b>33.1</b>
	7.7	<b>111</b>	5.8	<b>99</b>	4.1	<b>111</b>	15.1	<b>187</b>
	0.5	$\infty$	0.6	$\infty$	0.4	$\infty$	3.1	$\infty$
SE	2.5	<b>0.7</b>	3.1	<b>0.9</b>	4.1	<b>0.5</b>	--	--
	18.0	<b>16.2</b>	15.5	<b>16.5</b>	15.6	<b>16.2</b>	20.1	<b>27.9</b>
	13.2	<b>110</b>	5.8	<b>118</b>	6.0	<b>115.2</b>	12.7	<b>192</b>
	0	$\infty$	0.9	$\infty$	0.9	$\infty$	1.2	$\infty$

	<b>H5</b>		<b>H6</b>		<b>H7</b>		<b>H8</b>	
	A	$\tau$	A	$\tau$	A	$\tau$	A	$\tau$
ESA	32.7	<b>47.1</b>	21.1	<b>23.9</b>	26.2	<b>40.9</b>	8.5	<b>0.7</b>
	9.8	<b>540</b>	26.2	<b>106</b>	10.6	<b>230</b>	1.1	<b>5.6</b>
	5.2	$\infty$	7.5	$\infty$	8.6	$\infty$		
SE	20.7	<b>22.9</b>	14.5	<b>10.9</b>	30.1	<b>27.9</b>	4.5	<b>0.1</b>
	6.7	<b>98</b>	28.5	<b>69.7</b>	12.2	<b>237</b>	-2.9	<b>0.9</b>
	1.7	$\infty$	2.2	$\infty$	1.6	$\infty$		

**Supplementary Table 2.** Fit parameters of multi-exponential fit curves for stimulated emission (SE, 525-625 nm) and excited state absorption (ESA, 325-415 nm). Units are arbitrary for the pre-exponential amplitudes A and ps for time constants  $\tau$ . A value of  $\tau = \infty$  corresponds to a socket of the signal lasting beyond the measurement range of 1 ns.

## List of LabView programs

In the framework of this thesis, the following LabView codes have been used for the post-processing and evaluation of the experimental results. They are saved on the local network of the institute (R:\Dissertationen\Diss\_Megerle,Uwe\LabView\_programs) and can be requested by email from Prof. Riedle (riedle@physik.lmu.de):

- **Post-processing of TA data**

- “*broadband\_postprocessing.vi*” consisting of
  - *00\_view\_multi\_measurements.vi*
  - *10\_split\_multi\_measurements\_into\_filter+data.vi*
  - *20\_average\_multiple\_files.vi*
  - *30\_wavelength\_calib\_Sellmaier.vi*
  - *40\_manual\_time\_zero.vi*
  - *60\_apply\_chirp\_correction.vi*
  - *70\_append\_wavelength.vi*
  - *80\_transmission\_to\_OD.vi*
  - *90\_subtract\_stray\_light.vi*
- “*chirp\_correction\_v6*” (previously used version of the broadband post-processing suite)
- “*2D\_SG\_smooth.vi*” (data smoothing using a 2-dimensional Savitzky-Golay filter)
- “*single\_channel\_processing*” (for older TA data obtained in single-channel mode)

- **Data evaluation and fit routines**

- “*LDAC.vi*” (logarithmic differentiation of absorption changes)
- “*global\_fit*”
- “*global\_fit\_2010*” (newest version including numerical convolution, in test)
- “*DADS\_to\_SAS.vi*” (calculate species spectra from decay associated spectra)
- “*decomposition.vi*” (decomposition of TA spectra into ESA, GSB and SE using steady state spectra)
- “*Fit\_2D\_data\_single-channel\_v2.4*” (for fitting individual channels of multichannel TA data)
- “*band\_integral.vi*” (including fit of the kinetics)
- “*anisotropy.vi*”
- “*FWHM.vi*” (full-width-half-maximum of TA bands and corresponding fit of the kinetics)
- “*band\_maxima.vi*” (including fit of the kinetics)
- “*fit\_single\_channel*” (for fitting of single-channel TA data)
- “*fit\_shift*” (global fit routine for band shifts used for the TABs data of section 3.2)

- **Additional tools**

- “*emission\_correction.vi*” (process steady-state emission spectra)
- “*sensitivity.vi*” (evaluate the standard deviation of the baseline in a TA data set)
- “*demo\_scan.vi*” (simulation of data acquisition using previously measured TA spectra)
- “*generate\_test\_data.vi*”



## Danksagung

Diese Arbeit hätte ohne die Hilfe und Unterstützung vieler Leute nicht entstehen können. Mein herzlicher Dank gebührt deshalb:

**Prof. Eberhard Riedle** für sein leidenschaftliches Engagement und die nie nachlassende aktive Unterstützung meiner wissenschaftlichen Tätigkeit. Ich verdanke ihm viele entscheidende Einsichten, Ideen und Impulse, auch weit über das Physikerdasein hinaus. Insbesondere möchte ich mich auch für die Flexibilität und finanzielle Großzügigkeit im Zusammenhang mit meiner Elternteilzeit bedanken.

**Prof. Wolfgang Zinth** für das lebendige Interesse an meiner Arbeit, die aufschlussreichen Diskussionen im Rahmen vieler Seminarvorträge und die stets offene Tür bei allerlei Fragen wie z.B. nach den Details der LDAC Anwendung.

**Prof. Joachim Rädler** für die sofortige Bereitschaft, das Zweitgutachten für meine Arbeit zu übernehmen. Darüber hinaus möchte ich mich auch für das Verständnis in Bezug auf unsere elterlichen Pflichten bedanken, von dem ich indirekt über Judith oft genug profitieren durfte.

**Prof. Stefan Lochbrunner**, der mir in der Anfangsphase und selbst nach seinem Ruf nach Rostock unzählige wertvolle Tipps und Hilfestellungen bei meinen Projekten gegeben hat.

**Dr. Igor Pugliesi** und **Dr. Christian Schriever**, die mir vor allem bei den diversen Lab-View Programmen enorm geholfen haben, angefangen von kleinen Programmiertipps bis hin zur Überlassung ganzer Module. Darüber hinaus waren Igers *ab initio* Rechnungen bei vielen Projekten von unschätzbarem Wert, genauso wie die häufigen Diskussionen verschiedenster Zusammenhänge rund um die Spektroskopie.

allen externen Kooperationspartnern aus dem Chemiebereich, deren interessante Proben und Fragestellungen unsere Technikentwicklungen nicht nur sinnvoll gemacht, sondern oft auch konkret angestoßen haben. Im Einzelnen danke ich den Arbeitsgruppen um **Prof. Thomas Carell** aus München, **Prof. Burkard König** und **Prof. Bernhard Dick** aus Regensburg, **Prof. Christoph Lambert** und **Prof. Frank Würthner** aus Würzburg, sowie **Dr. Jerzy Karpiuk** aus Warschau. Für die gute und intensive Zusammenarbeit auf Augenhöhe möchte ich mich speziell bei **Roger-Jan Kutta**, **Dr. Robert Lechner** und **Danila Fazio** bedanken.

„meinen“ Diplomanden **Florian Selmaier** und **Matthias Wenninger** sowie dem Bachelor-Kandidaten **Matthias Bock** für ihre Ausdauer beim Messen und die gute Vorarbeit bei der Zusammenstellung der Daten für ihre Ausarbeitungen. In diesem Zusammenhang danke ich auch **Anton Arsenyev** für die Überwindung vieler technischer Schwierigkeiten bei der Inbetriebnahme der PDA-Kamera.

**Dr. Uli Schmidhammer** für die Starthilfe in dieses Forschungsgebiet während der Diplomarbeit und die spätere z.T. länderübergreifende Zusammenarbeit am CVL-Projekt.

**Rudi Schwarz**, **Christian Hausmann** und **Alfons Stork**, die alles an Mechanik machen können, was man im Laborbetrieb braucht. Was sie nicht machen können, braucht man auch nicht, z.B. eckige Langlöcher. Ähnliches gilt im Optikbereich für **Harald Hoppe**.

allen aktuellen und ehemaligen Kollegen am BMO, die selbst in stressigen Phasen dafür gesorgt haben, dass man gerne ins Institut kommt. Neben den schon erwähnten sind dies insbesondere meine alten Studienkollegen **Christian Homann, Florian Lederer, Andreas Böck** und **Stefan Schindlbeck**, meine (zeitweiligen) Zimmergenossen **Patrizia Krok, Christian Sailer** und **Michael Mikhailov**, die PC-Beauftragten **Dr. Karl-Heinz Mantel, Markus Breuer** und **Max Bradler**, sowie der stets hilfsbereite und spendable **Prof. Peter Gilch**. Ebenso danke ich **Dr. Subrata Mahanta** und **Dr. Rupashree Balia Singh** für das letzte Korrekturlesen mit der Aufmerksamkeit von „bear eyes“.

**Frau Monika Wild** stellvertretend für die gesamte **IMPRS-APS**, der ich neben einem Stipendium viele interessante Seminare vor noch interessanterer Kulisse verdanke.

meiner **Familie**, insbesondere meinen Eltern und Schwiegereltern und allen voran natürlich meiner wunderbaren Frau **Judith**, die durch ihren Beistand und nicht zuletzt durch ausführliches Babysitten während des Endspurts meine Dissertation enorm unterstützt haben. Gleichzeitig erinnern sie mich jeden Tag aufs Neue daran, welche Vielfalt an Schätzen es auch außerhalb der Physik noch zu finden gibt.

# Curriculum vitae

## PERSONAL DETAILS

---

Last name: Megerle  
First name: Uwe  
Date of birth: 17.04.1980  
Place of birth: Bucarest, Romania  
Nationality: German  
Marital status: married, 1 child

## EDUCATION

---

1986 – 1990 German primary school in Lugoj, Romania  
1990 – 1996 Kreisgymnasium Riedlingen, Baden-Württemberg  
1996 – 1999 Gymnasium of the Liebfrauenschule Sigmaringen  
06/1999 Abitur with grade 1.0  
10/2000 – 09/2002 Undergraduate studies in physics at the LMU München  
09/2002 – 06/2003 Erasmus year at the University of Kent at Canterbury, UK;  
awarded “Diploma with Distinction” in Physics  
06/2003 – 10/2006 Graduate studies in physics at the LMU München  
10/2006 Diploma in physics with grade “very good”  
since 11/2006 PhD student at the chair of BioMolecular Optics, LMU München